A Measurement of Electron Neutrino Appearance in the MINOS Experiment After Four Years of Data

A dissertation presented by

Steven Cavanaugh

to

The Department of Physics

in partial fulfillment of the requirements

for the degree of

Doctor of Philosophy

in the subject of

Physics

Harvard University

Cambridge, Massachusetts

May 2010

© 2010 - Steven Cavanaugh

All rights reserved.

Thesis advisor

Professor Gary Feldman

Author

Steven Cavanaugh

A Measurement of Electron Neutrino Appearance in the MINOS Experiment After Four Years of Data

Abstract

This work attempts to measure or set a limit on $\sin^2(2\theta_{13})$, the parameter which describes $\nu_\mu \rightarrow \nu_e$ oscillations. The MINOS detectors at Fermilab are used to perform a search for the oscillations utilizing a beam of ν_μ neutrinos created in the NuMI beamline by the collisions of 120 GeV protons with a carbon target. These collisions create $\pi^\pm$ and $K^\pm$ which are focused with magnetic horns, are allowed to decay, and result in a beam of ν_μ in the energy range of 1 to 30 GeV. Two functionally identical steel-scintillator calorimetric detectors are utilized to measure the interactions of the generated neutrinos. A detector close to the NuMI beam, located 104 m underground and 1040 m from the target, is used to measure the properties of the neutrino beam, including the flux, composition, and energy spectrum. This information is used in part to generate a predicted spectrum of neutrinos in absence of $\nu_\mu \rightarrow \nu_e$ oscillations in the detector located far from the target, at a distance of 705 m underground and 735.5 km from the target. An excess of predicted ν_e charged current events in this far detector will be interpreted as $\nu_\mu \rightarrow \nu_e$ oscillations, and a measurement of $\sin^2(2\theta_{13})$ will be made using a Feldman-Cousins analysis.

The measurement of $\nu_\mu \rightarrow \nu_e$ requires the separation of ν_e candidates from background events. New reconstruction software was developed with a focus on identifying ν_e candidate events in order to reduce systematic errors. The event parameters measured by this software were used as an input to an artificial neutral network event discriminator. The details of this reconstruction software and the other steps of the analysis necessary to

making the measurement will be discussed.

This work builds on a previous measurement made with this experiment. After two years of running with 3.14×10^{20} protons-on-target (POT), a limit was set at $\delta_{CP} = 0$ for the normal (inverted) hierarchy of $\sin^2(2\theta_{13}) < 0.29$ (0.42) at 90% C.L. This study finds after four years of data with an accumulated intensity of 7×10^{20} POT that $\sin^2(2\theta_{13}) < 0.12$ (0.20) with $\delta_{CP} = 0$ at 90% C.L. for the normal (inverted) hierarchy.

Contents

Title Page i
Abstract iii
Table of Contents v
List of Figures ix
List of Tables xii
Acknowledgments xiv
Dedication xvi

1 Introduction and Summary **1**

2 The Theory of Neutrino Oscillations **3**
2.1 A Brief History 3
2.2 Neutrinos and The Standard Model 9
2.2.1 Review of Field Theories 11
2.2.2 The Weak Force 17
2.2.3 Leptons and the Weak Force 20
2.2.4 Cabibbo, Kobayashi, and Maskawa 22
2.2.5 Neutrino Interaction Variables 23
2.2.6 Oscillations 26
2.2.7 CP Violation 29
2.2.8 Lepton Mass 33
2.2.9 Matter Effects 34
2.3 Experimentally Measured Properties of Neutrinos 39
2.3.1 Neutrino Mass 40
2.3.2 Oscillation Parameters 40

3 The MINOS Experiment **43**
3.1 The NuMI Beamline 43
3.2 The MINOS Detectors 50
3.2.1 Detector Technology 50
3.2.2 Physics of the Detector Technology 57
3.2.3 Calibration 57
3.2.4 Cross Talk 65

3.2.5 Storing Data . . . 66
3.3 Simulated Data . . . 66
3.3.1 Simulating the Neutrino Beam . . . 67
3.3.2 Simulating Interactions in the Detectors . . . 68
3.3.3 Modeling the Detector Response . . . 72
3.3.4 Oscillation Weights . . . 74
3.4 Batch Processing and Standard Data Reconstruction . . . 75
3.5 Considerations for the Measurement . . . 76

4 The Analysis **79**
4.1 The Procedure . . . 79
4.2 Preparing the Data . . . 80
4.2.1 Data Quality . . . 80
4.2.2 Fiducial Volume Restriction . . . 81
4.3 ν_e Candidate Event Energy Calibration . . . 82
4.4 Signal Selection . . . 83

5 Event Identification **87**
5.1 Event Variables . . . 87
5.2 Identifying Signal Events with an Artificial Neural Network . . . 89
5.3 Quantifying the ANN's Signal from Background Separation Ability . . . 92
5.4 ANN11 - The Primary PID . . . 94
5.5 ANN14 - A Cross Check PID . . . 95

6 An Alternative Event Reconstruction and Analysis **97**
6.1 Motivation . . . 97
6.2 The ParticlePID Algorithm . . . 98
6.2.1 Data Input and Preparation . . . 98
6.2.2 Objects Used in this Algorithm . . . 99
6.2.3 Dynamic Clustering . . . 101
6.2.4 Long Track Identification . . . 102
6.2.5 Shower Component Identification . . . 106
6.2.6 Making a Particle3D Object . . . 109
6.3 Oscillated ν_e Event Selection . . . 116
6.3.1 Useful Variables for Event Identification . . . 117
6.3.2 Training the Neural Network . . . 118
6.3.3 Examining the Selected Sample . . . 124
6.3.4 Variable Stability . . . 130
6.4 Other Details . . . 136
6.4.1 PID Overlap . . . 136
6.4.2 Reconstruction of the Electromagnetic Shower Fraction . . . 140
6.4.3 Vertex Resolution . . . 143
6.4.4 Other Attempts . . . 148

7 An Additional Tool - Muon Removal **149**
7.1 Muon Removed ν_μ CC (MRCC) Events . . . 149
7.1.1 Method . . . 150
7.1.2 Uses . . . 150
7.1.3 Muon Removed ν_μ CC with Monte Carlo Electron Events (MRE) . 151

8 Predicting the Far Detector Data **153**
8.1 Overview of the Extrapolation Method . . . 153
8.2 Near Detector Decomposition . . . 155
8.2.1 Horn On-Off Method . . . 156
8.2.2 MRCC Method . . . 165
8.2.3 Near Data Decomposition Method Summary . . . 165
8.3 Far Detector Prediction . . . 166

9 Understanding Systematics **170**
9.1 Systematics of the Beam Simulation . . . 171
9.1.1 Uncertainty on the Data Based Adjustment to the Simulated Flux . 171
9.1.2 Flux Simulation . . . 172
9.1.3 Target Degredation . . . 172
9.2 Uncertainties of the Physics Simulation in the Detectors . . . 173
9.2.1 Cross Section . . . 173
9.2.2 Hadronization Model . . . 174
9.2.3 INTRANUKE . . . 177
9.3 Uncertainties in Detector Response . . . 178
9.3.1 Absolute Energy Scale . . . 178
9.3.2 Hadronic versus EM Energy Scale . . . 178
9.4 Extrapolation Effects . . . 178
9.4.1 Normalization . . . 179
9.4.2 Calibration . . . 179
9.4.3 Preselection . . . 181
9.4.4 Cross Talk Modeling . . . 182
9.4.5 Near Detector Event Intensity . . . 183
9.5 Far Detector Systematics for ν_τ and Signal ν_e Events . . . 184
9.5.1 ν_μ CC Systematics . . . 184
9.5.2 Signal Efficiency . . . 184
9.6 Systematics - Detailed Tables . . . 185
9.6.1 Near Detector . . . 187
9.6.2 Far Detector . . . 190
9.6.3 Extrapolation Systematics NC + ν_μ CC + Beam ν_e . . . 193
9.6.4 Extrapolation Systematics ν_τ . . . 196
9.6.5 Extrapolation Systematics Signal ν_e . . . 198
9.7 Cosmic Backgrounds . . . 201
9.8 Summary . . . 201

10 Verification of the Methods **204**
10.1 Anti-PID 204
10.2 MRCC 207
10.3 MRE 232
10.4 Summary 232

11 Far Detector Signal Region Prediction and Results **233**
11.1 How to Make a Measurement 233
11.2 Possible Sensitivities 237
11.3 Results 239
11.4 Conclusion 244

12 Future Steps **246**
12.1 The Future of MINOS 246
12.2 Future Experiments 246

Bibliography **248**

List of Figures

2.1 Measurement of the number of neutrino flavors from LEP 7
2.2 The two weak interactions of the neutrino. 22
2.3 The kinematics of the general neutrino interaction 25
2.4 The neutrino mass hierarchy 30
2.5 The oscillation probability for ν_μ disappearance in MINOS 38
2.6 The oscillation probability for $\nu_\mu \rightarrow \nu_e$ in MINOS 39
2.7 A summary of the best known values of neutrino oscillation parameters . . 41

3.1 The Fermilab accelerator complex 44
3.2 The NuMI beam line - tunnel schematic 45
3.3 The NuMI beam line - horn and decay pipe illustration 46
3.4 Accumulated protons on target at NuMI 47
3.5 Neutrino energy spectrum from different horn configurations 49
3.6 Assembling the scintillator strips 52
3.7 The PMT detectors 53
3.8 The coordinate systems of the MINOS detectors 54
3.9 Stopping power for muons 64
3.10 Flux ratio (far/near) from FLUKA before and after near data tuning 69

4.1 Preselection cuts 85

5.1 A simple artificial neural network (ANN) 91

6.1 Event display for a ν_e QE event - hits and clusters 111
6.2 Event display for a ν_e QE event - clusters and chains 112
6.3 Event display for a DIS ν_μ CC event - clusters and chains 113
6.4 Event display for a NC event - clusters and chains 114
6.5 Correlation between the 14 ANN input variables 116
6.6 ParticlePID ANN input variables 119
6.7 The 14:16:9:1 ParticlePID ANN 120
6.8 The potential FOM for various PID cut levels 121
6.9 ParticlePID selected signal efficiency and purity 121
6.10 ANN11 selected signal efficiency and purity 122

6.11 Selected signal efficiency and purity for the ParticlePID and ANN11 123
6.12 Reconstructed energy by event type for ParticlePID 125
6.13 ParticlePID value by event type 126
6.14 ANN11 value by event type 126
6.15 Reconstructed event energy for events selected by the ParticlePID 127
6.16 Reconstructed event energy for events selected by the ANN11 127
6.17 ParticlePID value for signal events by type 128
6.18 ParticlePID in the Near Detector by component 130
6.19 Reconstructed energy in the Near Detector for the ParticlePID by component 131
6.20 ParticlePID variables - group 1 132
6.21 ParticlePID variables - group 2 133
6.22 ParticlePID variables - group 3 134
6.23 ParticlePID variables - group 4 135
6.24 Comparing values of ParticlePID and ANN11 in Far Detector Monte Carlo 137
6.25 Comparing values of ANN11 and ANN14 in Far Detector Monte Carlo . . . 138
6.26 Comparing values of ParticlePID and ANN14 in Far Detector Monte Carlo 139
6.27 Reconstructed (1 - electromagnetic shower fraction) vs true y 141
6.28 Fits on Reconstructed (1 - electromagnetic shower fraction) vs true y 142
6.29 Vertex resolution - Far Detector - ν_e events 145
6.30 Vertex resolution - Far Detector - all events 146
6.31 Vertex resolution - Near Detector - all events 147

7.1 The muon removal from ν_μ CC event (MRCC) method 151

8.1 HOOHE Near Detector decomposition - ParticlePID 163
8.2 HOOHE Near Detector decomposition - ANN11 164
8.3 Far Detector prediction for ParticlePID 167
8.4 Far Detector prediction for ANN11 167
8.5 Far Detector prediction for ANN14 168

10.1 MRCC sideband after preselection without ν_μ CC correction 217
10.2 MRCC sideband after ParticlePID cut without ν_μ CC correction 218
10.3 MRCC sideband after ANN11 cut without ν_μ CC correction 219
10.4 MRCC sideband after ANN14 cut without ν_μ CC correction 220
10.5 MRCC sideband after preselection with ν_μ CC shower events correction . . 221
10.6 MRCC sideband after ParticlePID cut with ν_μ CC shower events correction 222
10.7 MRCC sideband after ANN11 cut with ν_μ CC shower events correction . . 223
10.8 MRCC sideband after ANN14 cut with ν_μ CC shower events correction . . 224
10.9 MRCC sideband for each PID after CC shower events correction 225
10.10 MRCC sideband expressed as a background rejection 226
10.11 MRCC sideband - data and Monte Carlo near to far efficiencies 229

11.1 ParticlePID sensitivity 237
11.2 ParticlePID sensitivity 238
11.3 ANN11 sensitivity 238

11.4 ANN11 sensitivity 239
11.5 Far data events per POT 240
11.6 The location of far data events in the detector 241
11.7 The ParticlePID and ANN11 values of the data 242
11.8 The limit on $\sin^2 2\theta_{13}$ (ParticlePID) 243
11.9 The limit on $\sin^2 2\theta_{13}$ (ANN11) 244

List of Tables

2.1 The bosons in the Standard Model 10
2.2 Oscillation parameters used in this analysis 42

3.1 NuMI beam configurations 48

4.1 The fiducial volumes of each detector 82
4.2 Number of events after preselection cuts in the Monte Carlo 86

6.1 Identification of reconstructed particles 110
6.2 Signal and background for the PIDs 124
6.3 Signal and background for the PIDs by resonance code and event type . . . 129

8.1 Near Detector data and Monte Carlo comparison 156
8.2 HOOHE Near Detector decomposition 163
8.3 MRCC Near Detector decomposition 166
8.4 Far Detector prediction - ParticlePID 168
8.5 Far Detector prediction - ANN11 169
8.6 Far Detector prediction - ANN14 169

9.1 Systematics for the ParticlePID in the Near Detector with HOOHE 187
9.2 Systematics for the ANN11 in the Near Detector with HOOHE 188
9.3 Systematics for the ANN14 in the Near Detector with HOOHE 189
9.4 Systematics for the ParticlePID in the Far Detector 190
9.5 Systematics for the ANN11 in the Far Detector 191
9.6 Systematics for the ANN14 in the Far Detector 192
9.7 Extrapolation systematics for ParticlePID/HOOHE (NC, ν_μ, and beam ν_e) 193
9.8 Extrapolation systematics for ANN11/HOOHE (NC, ν_μ, and beam ν_e) . . . 194
9.9 Extrapolation systematics for ANN14/HOOHE (NC, ν_μ, and beam ν_e) . . . 195
9.10 Far detector prediction systematics for ParticlePID (ν_τ) 196
9.11 Far detector prediction systematics for ANN11 (ν_τ) 197
9.12 Far detector prediction systematics for ANN14 (ν_τ) 197
9.13 Far detector prediction systematics for ParticlePID (signal ν_e) 198
9.14 Far detector prediction systematics for ANN11 (signal ν_e) 199

9.15 Far detector prediction systematics for ANN14 (signal ν_e) 200
9.16 Summary of background systematics - ParticlePID with HOOHE 203
9.17 Summary of background systematics - ANN11 with HOOHE 203
9.18 Summary of background systematics - ANN14 with HOOHE 203

10.1 Anti-ParticlePID (<0.5) 205
10.2 Anti-ANN11 (<0.5) 206
10.3 Anti-ANN14 (<0.5) 206
10.4 The sequential cuts applied to create the MRCC sample 209
10.5 The sequential cuts applied to create the ν_μ CC sample 209
10.6 MRCC sideband without ν_μ CC event correction 213
10.7 MRCC sideband with ν_μ CC shower event correction 213
10.8 MRCC sideband without ν_μ CC event correction 213
10.9 MRCC sideband with ν_μ CC shower event correction 214
10.10 MRCC sideband without ν_μ CC event correction 215
10.11 MRCC sideband without ν_μ CC event correction as efficiency 215
10.12 MRCC sideband with ν_μ CC shower event correction 216
10.13 MRCC sideband with ν_μ CC shower event correction as efficiency 216
10.14 MRCC sideband expressed as a background rejection 227
10.15 MRCC sideband - near to far efficiencies 230
10.16 MRCC sideband - near to far efficiencies - binomial error 231
10.17 The MRE Sideband 232

11.1 Far data event counts by run period 240

Acknowledgments

The MINOS Collaboration

P. Adamson, C. Andreopoulos, K. E. Arms, R. Armstrong, D. J. Auty, S. Avvakumov, D. S. Ayres, C. Backhouse, B. Baller, B. Barish, P. D. Barnes Jr., G. Barr, W. L. Barrett, E. Beall, B. R. Becker, A. Belias, R. H. Bernstein, M. Betancourt, D. Bhattacharya, M. Bishai, A. Blake, B. Bock, G. J. Bock, J. Boehm, D. J. Boehnlein, D. Bogert, P. M. Border, C. Bower, E. Buckley-Geer, S. Cavanaugh, J. D. Chapman, D. Cherdack, S. Childress, B. C. Choudhary, J. H. Cobb, J. A. B. Coelho, S. J. Coleman, L. Corwin, J. P. Cravens, D. Cronin-Hennessy, A. J. Culling, I. Z. Danko, J. K. de Jong, N. E. Devenish, M. Dierckxsens, M. V. Diwan, M. Dorman, D. Drakoulakos, T. Durkin, S. A. Dytman, A. R. Erwin, C. O. Escobar, J. J. Evans, E. Falk, G. J. Feldman, T. H. Fields, R. Ford, M. V. Frohne, H. R. Gallagher, A. Godley, J. Gogos, M. C. Goodman, P. Gouffon, R. Gran, E. W. Grashorn, N. Grossman, K. Grzelak, A. Habig, D. Harris, P. G. Harris, J. Hartnell, E. P. Hartouni, R. Hatcher, K. Heller, A. Himmel, A. Holin, C. Howcroft, L. Hsu, X. Huang, J. Hylen, D. Indurthy, G. M. Irwin, M. Ishitsuka, Z. Isvan, D. E. Jaffe, C. James, D. Jensen, T. Kafka, H. J. Kang, S. M. S. Kasahara, J. J. Kim, M. S. Kim, G. Koizumi, S. Kopp, M. Kordosky, K. Korman, D. J. Koskinen, S. K. Kotelnikov, Z. Krahn, A. Kreymer, S. Kumaratunga, K. Lang, R. Lee, G. Lefeuvre, J. Ling, P. J. Litchfield, R. P. Litchfield, L. Loiacono, P. Lucas, J. Ma, W. A. Mann, A. Marchionni, M. L. Marshak, J. S. Marshall, N. Mayer, A. M. McGowan, R. Mehdiyev, J. R. Meier, G. I. Merzon, M. D. Messier, C. J. Metelko, D. G. Michael, R. H. Milburn, J. L. Miller, W. H. Miller, S. R. Mishra, A. Mislivec, J. Mitchell, C. D. Moore, J. Morfín, L. Mualem, S. Mufson, S. Murgia, J. Musser, D. Naples, J. K. Nelson, H. B. Newman, R. J. Nichol, T. C. Nicholls, J. P. Ochoa-Ricoux, W. P. Oliver, M. Orchanian, T. Osiecki, R. Ospanov, J. Paley, V. Paolone, A. Para, R. B. Patterson, T. Patzak, Ž. Pavlović, G. Pawloski, G. F. Pearce, C. W. Peck, E. A. Peterson, D. A. Petyt, H. Ping, R. Pittam, R. K. Plunkett, D. Rahman, A. Rahaman, R. A. Rameika, T. M. Raufer, B. Rebel, J. Reichenbacher, D. E. Reyna, P. A. Rodrigues, C. Rosenfeld, H. A. Rubin, K. Ruddick, V. A. Ryabov, R. Saakyan, M. C. Sanchez, N. Saoulidou, J. Schneps, P. Schreiner, V. K. Semenov, S.-M. Seun, P. Shanahan, W. Smart, V. Smirnitsky, C. Smith, A. Sousa, B. Speakman, P. Stamoulis, M. Strait, P. Symes, N. Tagg, R. L. Talaga, E. Tetteh-Lartey, M. A. Tavera, J. Thomas, J. Thompson, M. A. Thomson, J. L. Thron, G. Tinti, R. Toner, I. Trostin, V. A. Tsarev, G. Tzanakos, J. Urheim, P. Vahle, V. Verebryusov, B. Viren, C. P. Ward, D. R. Ward, M. Watabe, A. Weber, R. C. Webb, A. Wehmann, N. West, C. White, L. Whitehead, S. G. Wojcicki, D. M. Wright, T. Yang, K. Zhang, H. Zheng, M. Zois, R. Zwaska

Thanks to the MINOS ν_e Appearance Analysis Group, without whom this paper would not be possible. Special thanks to Mayly, Josh, Anna, Lisa, Ruth, Greg, Tricia, Ryan, Joao, Masaki, Tingjun, Xiaobo, and Jia Jie. Thanks to Niki who instructed me in various neural network techniques.

Many thanks to Jason Brodsky who worked with our lab as an undergraduate. He was most helpful in scanning event displays to find issues with the ParticlePID algorithm and in developing and testing various potential event classification variables.

Thanks to Gary for providing me with the opportunity to explore potential improvements to the MINOS reconstruction software.

Thanks to Alex for providing comments on my thesis talk.

Thanks to the many people who have read and provided comments on this document, including Mom, Dad, Brian, Diana, and Jen.

My parents, brothers, and Diana have provided much needed support for which I am grateful.

This work is dedicated to Diana, my parents Linda Ann and John, and my brothers Mark and Matt.

The author in front of the MINOS Far Detector in Tower, Minnesota during the 2009 Ely Collaboration Meeting[1].

Chapter 1

Introduction and Summary

The neutrino has long been elusive. As one of the first particles to be hypothesized beyond the everyday proton, neutron, and electron, the neutrino remains one of the least studied and least understood particles in the Standard Model to this day.

This thesis represents a collection of work done by the author over a period of four years for the MINOS experiment. The main work of this thesis is a measurement of $\nu_\mu \rightarrow \nu_e$ neutrino oscillations in the MINOS detectors. This work would not have been possible without the assistance and efforts of the other collaborators on this analysis and on the MINOS experiment as a whole.

The document will begin with a brief history of neutrino experiments in section 2.1. The theory of neutrinos as currently accepted today will then be discussed in section 2.2, followed by a summary of the current experimental knowledge of the field in section 2.3. In an effort to present a coherent reference to the user, the theory is not presented chronologically within the historical summary of the field. While this provides two separate references to a reader experienced in the field, it may be less clear to the reader who is unfamiliar with neutrinos. It is therefore recommended that a reader not experienced in

the field only briefly read the history chapter prior to reading about the current knowledge of the theory. After surveying the theory, it is then recommended that the reader return to the history section where some of the topics discussed will be better received.

Once the theoretical foundations necessary for understanding a $\nu_\mu \rightarrow \nu_e$ analysis are set, the experiment will then be introduced in chapter 3. The steps necessary to carry out the analysis are presented in detail in chapter 4. The tools necessary to identify the candidate oscillated ν_e events in the detector are given in chapter 5, and these tools are employed by the standard event identification software, as discussed in sections 5.4 and 5.5. An alternate event reconstruction and event identification software, which is the main focus of this thesis, is then given in chapter 6.

Once the steps necessary for the analysis and the means of identifying the candidate oscillated ν_e events are presented, it is necessary to discuss the steps of verifying the quality of the data prior to making a measurement of ν_e appearance. A tool to provide a sample of data based hadronic showers independent of signal events is introduced in chapter 7. The process of predicting data in the Far Detector is explained in chapter 8, followed by the calculation of the systematics involved in the analysis in chapter 9. These mechanisms provide the means for three-step verification of the quality of the data in chapter 10. Only then can a look at the actual data be made, and a measurement or limit can then be set on $\nu_\mu \rightarrow \nu_e$ oscillations based on the observed data, as described in chapter 11. The thesis concludes in chapter 12 with a brief synopsis of future steps for this experiment and the field of neutrino oscillations in general.

Chapter 2

The Theory of Neutrino Oscillations

This chapter will first present a brief history of neutrinos, followed by the theoretical foundation for their existence and for the oscillations of neutrinos. The chapter will conclude with a review of the current world knowledge of neutrinos and their properties.

2.1 A Brief History

Early experiments with nuclear β decay involved the observation of an atomic nucleus emitting an electron while simultaneously having one of the contained neutrons converted into a proton. At the time, this was understood to be the disintegration of a nuclear neutron into a proton and an electron ($n \rightarrow p^+ + e^-$). This perceived two-body decay must occur while conserving the total energy of the system. Since the neutron and proton are both much more massive than the electron, the electron should carry almost the entirety of the energy from the decay, resulting in a monatomic energy spectrum of the emitted electron. However, an experiment that actually measured the energy spectrum of

the emitted electron found that the energy of the particle was distributed over a considerably substantial range[2]. Further studies showed that the emitted electrons carried all of the measurable emitted energy from decays, excluding the possibility that the large range of the energy spectrum could be due to the loss of energy by the emitted monoenergetic electron before it was measured[3].

The neutrino was first postulated[4] by Wolfgang Pauli in 1930 as a neutral and weakly interacting particle which participated in a 3-body decay of the neutron ($n \rightarrow p^+ + e^- + \overline{\nu}_e$). The addition of this third particle would carry off the appropriate amount of energy needed to compliment the energy of the emitted electron. Thus, the total energy of the system was conserved, effectively solving the problem of the energy spectrum of the electron emitted in nuclear β decay.

Enrico Fermi's work in 1933 first introduced the notion that the neutrino and electron in nuclear β decay were actually created at the time of the decay and were not simply released by the decay[5]. His application of the Dirac-Jordan-Klein method of the "amplitude of quantized probability" both predicted the half-life of various β decaying nuclei and constrained the mass of the neutrino to be much less than the mass of the electron. However, agreement between his theory and experimental results was only realized when the mass of the neutrino was taken to be zero[1].

Later confirmation that the neutrino could both be emitted from a process as well as be the cause of a nuclear disintegration process[6] provided the foundation necessary to establish the neutrino as a fundamental particle in nature and confirmed Fermi's theory that the neutrino could be created and destroyed via processes described by field equations. Neutrinos, generated by a nuclear reactor at Savannah River, were observed in the reverse β decay process, $\overline{\nu}_e + p^+ \rightarrow e^+ + n$. A neutrino from the reactor combined with a proton

[1]The apparent massless particle was named "neutrino" by Fermi, Italian for "small, neutral one".

in the target to produce a neutron and a positron. The target was composed of water containing dissolved $CdCl_2$. Two tanks of this water solution were sandwiched between three scintillator layers. The annihilation of the positron with an electron produced two back-to-back photons which were detected. The neutron also produced a number of gamma rays which were detected some time after the photons from the positron annihilation. The coincidence of a signal from both of the photons from the positron annihilation followed by the delayed signal from the neutron was the signature of a neutrino interaction in the experiment.

An experiment in 1957 by C. S. Wu[7] gave initial indications that parity was not conserved in the β decay of polarized ^{60}Co. A year later, M. Goldhaber performed an experiment[8] specifically designed to measure the helicity of the neutrino. The polarization of a photon emitted from the excited nucleus following the inverse β decay of a ^{152}Eu source was measured as an indication of the helicity of the neutrino. The neutrino was found to have negative helicity, or a spin anti-parallel to the direction of motion. This helicity is often referred to as "left-handed" (as opposed to "right-handed" for a particle with a spin parallel to the direction of motion, as is the case for anti-neutrinos).

In 1962, an experiment[9] at Brookhaven provided evidence that there were at least two different types of neutrinos, and that neutrinos retained and conserved the flavor information of the lepton associated with their production. This experiment created a beam of muons via charged π decay. These muons decayed and produced ν_μ which were then allowed to interact in a spark chamber where they produced muons but no electrons.

Even though the ν_τ had been theorized for some time (since the τ was discovered in 1975[10]), it was not directly detected until 2000 in the DONuT (Direct Observation of NuTau) experiment[11]. Here, all flavors of neutrinos were generated in a beam at Fermilab where 800 GeV protons struck a tungsten alloy beam dump. The decays of charmed particles

formed in the interaction of the proton beam with the beam dump provided a source for the ν_τ. A high resolution emulsion detector was used to distinguish the electron from a ν_e interaction from the electron resulting from the τ decay in a ν_τ interaction by measuring the displaced electron vertex. In the most recent result from the DONuT experiment[12], a total of 9 ν_τ charged current interaction events were observed.

An experimental measurement of the number of light neutrinos[13] was published in 2004 using Z decays from the LEP colliders, finding 2.9840 ± 0.0082 light neutrino flavors, as illustrated in figure 2.1. If any other neutrinos exist, they need to be either sterile (meaning that they do not couple to the Z boson), or they need to be substantially heavier than half of the Z boson mass[2].

Experiments observing neutrinos from natural distant sources began as a field around 1970, with the Homestake Solar Neutrino Detector[14]. Located in the Homestake Gold Mine, at Lead, South Dakota at a depth of 1478 meters below the surface, this detector collected data about solar neutrinos produced from $^8\mathrm{B} \rightarrow {}^8\mathrm{B}^* + e^+ + \nu_e$ for over 25 years beginning in 1970. Filled with 615 metric tons of tetrachloroethylene (C_2Cl_4), the detector measured ν_e from the sun by collecting and counting the Argon atoms produced by the interaction $\nu_e + {}^{37}\mathrm{Cl} \rightarrow {}^{37}\mathrm{Ar} + e^-$. Indications that something remained to be learned about the properties of neutrinos started to emerge with the measurement of $2.56 \pm 0.16(stat) \pm 0.16(sys)$ SNU[3], compared to the predicted[15] $9.3^{+1.3}_{-1.4}$ SNU. The disagreement with the prediction seen in the Homestake Solar Neutrino Detector was confirmed with other experiments utilizing different detector technologies.

[2]LEP operations were originally dedicated to Z boson production and reached a maximum center-of-mass energy of 209 GeV to study the production of $e^+e^- \rightarrow W^+W^-$ prior to shutdown in 2000. The LEP accelerator was located at CERN, and the tunnel that housed the machine is now being reused for the LHC.

[3]1 SNU = 1 solar neutrino interactions per 10^{36} target atoms per second

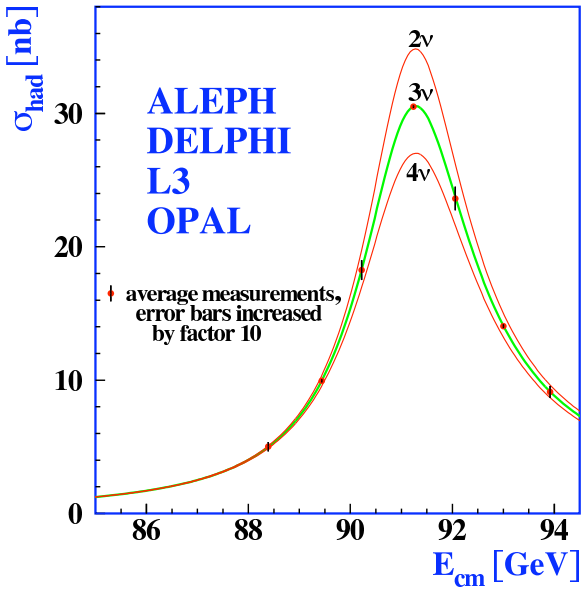

Figure 2.1: The measurement of the number of neutrino flavors from the detectors at LEP is presented. The calculated hadron production cross section around the Z resonance is shown for the hypothesized cases of 2, 3, and 4 flavors of neutrinos. The data is shown, and agrees with the 3 neutrino flavor hypothesis, finding 2.9840 ± 0.0082 light neutrino flavors. Image from[13].

SAGE[16] utilized ^{71}Ga→^{71}Ge neutrino capture[4] to measure neutrinos mostly from proton-proton fusion and found 69.7 SNU as compared to a predicted 128^{+9}_{-7} SNU. GALLEX [17] utilized a similar chemistry as SAGE and confirmed the discrepancy, measuring 77.5 ± 7.7 SNU compared to a predicted 130 SNU.

The Kamiokande II experiment[18] (Kamioka Nucleon Decay Experiment in its second version), again looked at solar neutrinos from ^{8}B, but unlike the previous experiments, it used an imaging water Čerenkov detector. This technology allowed for the observation of neutrino scattering ($\nu_e e \rightarrow \nu_e e$) from which the recoiling electron position and momentum vector could be measured and from which the direction of the incoming neutrino could be obtained. Again, the number of observed solar neutrinos was lower than expected, finding

[4]Neutrino capture is $\nu_e + n \rightarrow e^- + p$

a ratio of measured to expected events of about 46%.

These experimental confirmations of missing solar neutrinos combined with the fact that no current solar models could explain the measurements gave strong support to the possibility that the missing neutrinos were a manifestation of some property of the neutrino itself.

The possibility of neutrino oscillations was given as an explanation, where a neutrino formed as a ν_e in the sun may have been converted to a ν_μ or ν_τ by the time that it reached a terrestrial experiment. A ν_μ or ν_τ would have had no interaction with a detector because the energy of these neutrinos would have been below the threshold necessary for a charged current interaction. This oscillation behavior would be dependent on both the energy of the neutrino and the distance traveled by the neutrino, as will be explained in detail in section 2.2.6. The drawback to this explanation was the requirement that at least two of the neutrinos must have mass, a situation which at the time seemed unlikely due to Fermi's work.

To look for neutrino flavor changes, the Super-Kamiokande detector[19] was designed to measure interactions from both ν_e and ν_μ. It was a 50 kiloton water Čherekov detector capable of distinguishing between the electron or muon formed from the charged current interaction of ν_e or ν_μ. It was also capable of measuring the zenith angle of the incoming neutrino as a function of the direction of the produced lepton. In addition to measuring neutrinos from the sun, this experiment sought to measure neutrinos produced in the upper atmosphere where cosmic rays collided with nuclei producing $\pi^\pm$ which decayed producing about two muon neutrinos for every one electron neutrino[5]. Since both the energy and direction of the incoming neutrino could be determined, it was possible to

[5]The interaction with cosmic rays with nuclei in the upper atmosphere produce $\pi^\pm$ which decay to $\pi^+ \to \mu^+ + \nu_\mu$. The resulting muon also decays $\mu^+ \to e^+ + \overline{\nu}_\mu + \nu_e$

measure both the distance from the detector to the atmosphere where the neutrino was created and the energy relationship of neutrino oscillations. The experiment found that the measured number of neutrinos was dependent on the neutrino energy and the zenith angle (and thus the distance traveled), and the results favored maximal mixing between $\nu_\mu \leftrightarrow \nu_\tau$. This means that there was no measurable amount of $\nu_\mu \rightarrow \nu_e$ oscillations. The Sudbury Neutrino Observatory[20][21] was similar in design and function to the Super-Kamiokande detector, and produced similar results. This atmospheric neutrino ratio anomaly was also seen in experiments such as Soudan-2 [22]. All of these atmospheric neutrino experiments produced results consistent with neutrino oscillations.

The CHOOZ [23] reactor experiment measured the flux of $\overline{\nu}_e$ from a nuclear power reactor in Chooz, France. The results are consistent with Super-Kamiokande in the sense that the rate of ν_e disappearance was very small. The ν_e dissappearance is interpreted as oscillations of $\nu_e \rightarrow \nu_X$, where ν_X is some other flavor of neutrino.

Other experiments have looked directly for ν_τ interactions as a result of ν_μ oscillations, such as NOMAD[24]. These experiments have not observed $\nu_\mu \rightarrow \nu_\tau$ oscillations, but have been able to set limits on the parameters describing such oscillations.

2.2 Neutrinos and The Standard Model

The Standard Model represents the most accepted and most complete picture of particle physics knowledge today. As a $SU(3) \times SU(2) \times U(1)$ gauge theory, it describes the strong, weak, and electromagnetic fundamental forces. It does not include gravity, which is substantially weaker than these three forces and is of trivial consequence to experimental particle physics in the context of this document. The forces described by the theory are mediated by bosons listed in table 2.1. The eight gluons mediate the strong force by carrying

Boson	Charge	Spin	Mass(GeV)	Interaction
γ	0	1	0	Electromagnetic
$W^{\pm}$	± 1	1	80	Weak
Z^0	0	1	91	Weak
Gluon	0	1	0	Strong
Higgs	0	0	Unknown	-

Table 2.1: The properties of the bosons in the Standard Model. Note that there are 8 gluons which only differ by a color charge.

color and facilitate the binding of quarks into meson and baryons. Without this force, there would be no binding of quarks into protons and neutrons and thus no matter as we know it. The photon carries the electromagnetic force, perhaps the force which is most often used in everyday life and which is essential to technologies such as refrigerator magnets, radios and televisions, computers, and microwave ovens. An interplay between the strong and electromagnetic forces is responsible for nuclear α decay. The phenomenon of α decay is commonly used in household smoke detectors which sense smoke particles that interrupt the current of the α particles emitted from the nuclear α decay of ^{241}Am. The $W^{\pm}$ and Z bosons mediate the weak force and are responsible for nuclear β decay ($n \rightarrow p + \overline{\nu}_e + e^-$). Modern medicine utilizes this decay in the inverse form ($p \rightarrow n + \nu_e + e^+$) in positron electron tomography (PET scans). The Higgs particle has been theorized but has not been directly measured. It is believed to have a role in giving masses to the other particles and is currently one of the main research topics being pursued in the collider experiments at the LHC at CERN.

This research is focused on the $SU(2) \times U(1)$ portion of the Standard Model which describes the electro-weak interactions.

In all sections, the convention of $\hbar = c = 1$ will be followed for simplicity unless otherwise stated. These constants are responsible for converting between units of energy, time, and length, and can be put back into an equation at the end of manipulation through

the use of dimensional analysis.

2.2.1 Review of Field Theories

A brief review of field theories and the required math will be presented for reference. The steps necessary to explain the Standard Model will be given, carefully following from both [25] and [26].

Groups

The Standard Model is conveniently described by the symmetry of groups[6]. The general linear group of degree n is the set of all $n \times n$ invertible matrices. U(n) is the subset of this group consisting of all unitary matrices. SU(n), or special unitary group, is the subset of U(n) restricted to matrices having a determinant of 1. Each of these groups also defines the multiplication operator.

A group, $\mathbb{G}$, has an identity operator and rotational operators. These operators need not be commutative, but they are associative, such that $AB \neq BA$ or $AB = BA$ but $(AB)C = A(BC)$ always for $A, B, C \in \mathbb{G}$. Every member of the set can be accessed by starting with any other member of the set and applying the necessary rotations and scalar multiplications.

Additionally, the groups used in particle physics are classified as Lie groups. They possess the specific property that any rotation can be represented as an sum of infinitesimal rotations. For the group $SU(2)$ which is of interest here, the rotation of θ about the z axis, which is represented by J_3, can be simply expressed as an exponential (equation 2.1).

$$R(\theta) = \sum_{j=0}^{n} = \left(1 - j\frac{\theta}{n}J_3\right)^n \xrightarrow[n \to \infty]{} e^{-\mathrm{i}\theta J_3} \tag{2.1}$$

[6]The study of groups is of wide interest to mathematics and other fields, and is the basis for many computation technologies, including encryption

The generators of $SU(2)$ follow an algebra defined by equation 2.2

$$\frac{1}{2}\left[\tau_a, \tau_b\right] = \mathrm{i}\epsilon_{abc}\tau_c \tag{2.2}$$

Using equation 2.2 and two known generators of $SU(2)$, the other generator can be determined. An example of a set of generators frequently used in physics for the SU(2) group are the Pauli spin matrices, as given in equation 2.3.

$$\sigma_1 = \begin{bmatrix} 0 & 1 \\ 1 & 0 \end{bmatrix} \sigma_2 = \begin{bmatrix} 0 & -\mathrm{i} \\ \mathrm{i} & 0 \end{bmatrix} \sigma_3 = \begin{bmatrix} 1 & 0 \\ 0 & -1 \end{bmatrix} \tag{2.3}$$

Quantum Mechanics

The Schrödinger equation for a free particle of mass m operating on a complex wavefunction $\psi(\mathbf{x}, t)$ is shown in equation 2.4. The equation is obtained by the application of the differential operators, given in equation 2.5, on the equation for the classic energy momentum relation (equation 2.6).

$$\mathrm{i}\frac{\partial_\psi}{\partial_t} + \frac{1}{2m}\nabla^2\psi = 0 \tag{2.4}$$

$$E \rightarrow \mathrm{i}\hbar\frac{\partial}{\partial_t} \;\; \mathbf{p} \rightarrow -\mathrm{i}\hbar\nabla \tag{2.5}$$

$$E = \frac{p^2}{2m} \tag{2.6}$$

Two important features of this equation will be discussed for later use. Since $\rho = |\psi|^2$ is the probability density, and since probability is conserved, Gauss's theorem can be applied yielding equation 2.7.

$$-\frac{\partial}{\partial_t}\int_V \rho dV = \int_S \mathbf{j}\cdot\hat{\mathbf{n}}dS = \int_V \nabla\cdot\mathbf{j}dV \tag{2.7}$$

This equation describes how the total probability contained within a region varies when a change is made in either the probability density, in the surface of the region, or in the volume of the region over which the total probability is to be computed.

From the first and third parts of equation 2.7, the continuity equation (2.8) emerges.

$$\frac{\partial \rho}{\partial t} + \nabla \cdot \mathbf{j} = 0 \tag{2.8}$$

The continuity relation is responsible for the conservation of probability - essentially saying that if the probability density within some region changes over time, then some probability must be either entering or exiting the region, giving rise to a probability current, j.

The subtraction of the complex conjugate of equation 2.4 from itself yields equation 2.9. By comparing equation 2.4 to equation 2.8, it is evident that a current can be defined as given in equation 2.10.

$$\frac{\partial \rho}{\partial t} - \frac{\mathrm{i}}{2m}(\psi^* \nabla^2 \psi - \psi \nabla^2 \psi^*) = 0 \tag{2.9}$$

$$\mathbf{j} = -\frac{\mathrm{i}}{2m}(\psi^* \nabla \psi - \psi \nabla \psi^*) \tag{2.10}$$

The Klein-Gordon Equation

The Schrödinger equation is not capable of describing high energy particles in the relativistic realm which makes it unsuitable for forming a basis for high energy particle physics. A relativistic version of the Schrödinger equation, known as the Klein-Gordon equation, is found by following the previous steps, but beginning with the relativistic energy-momentum relationship, given in equation 2.11, instead of using the non relativistic form as used in equation 2.6.

$$E^2 = \mathbf{p}^2 + m^2 \tag{2.11}$$

Substituting the operators yields the Klein-Gordon equation (2.12).

$$-\frac{\partial^2\phi}{\partial t^2} + \nabla^2\phi = m^2\phi \tag{2.12}$$

From this, the relativistic version of the continuity equation can be obtained (2.13)[7].

$$\frac{\partial}{\partial_t}\underbrace{\left[\mathrm{i}\left(\phi^*\frac{\partial\phi}{\partial t} - \phi\frac{\partial\phi^*}{\partial t}\right)\right]}_{\rho} + \nabla\cdot\underbrace{\left[-\mathrm{i}(\phi^*\nabla\phi - \phi\nabla\phi^*)\right]}_{\mathbf{j}} = 0 \tag{2.13}$$

This result is analogous to the continuity equation (2.8).

Using four-vector notation, the Klein-Gordon equation can be rewritten as

$$(\partial_\mu\partial^\mu + m^2) = 0$$

and the probability and flux densities can be combined

$$j^\mu = (\rho, \mathbf{j}) = \mathrm{i}(\phi^*\partial^\mu\phi - \phi\partial^\mu\phi^*)$$

The continuity relation is satisfied

$$\partial_\mu j^\mu = 0$$

The free particle solution to the Klein-Gordon equation can then be written as

$$\phi = Ne^{-\mathrm{i}\,p\cdot x}$$

which has corresponding energy eigen values of

$$E = \pm(\mathbf{p}^2 + m^2)^{1/2}$$

There are two important observations about particles described by the Klein-Gordon equation. First, it can only describe spinless particles and so it is not of much

[7]The convention is to use ψ to represent a non-relativistic wave and ϕ to represent a relativistic field.

use for describing protons, neutrons, electrons, and neutrinos - all of which are spin $\frac{1}{2}$. Secondly, the eigenstates of the Klein-Gordon equation are both positive and negative. Although negative energy states are modernly interpreted as anti-particles, this historically posed a dilemma and motivated the work of Dirac.

The Dirac Equation

In a search for a solution to the relativistic Schrödinger equation which would be restricted to non negative energy states, Paul Dirac discovered a solution which simultaneously provided a mechanism for describing particles with spin. The equation (2.14) was linear in both time and spacial dependence.

$$H\phi = (\boldsymbol{\alpha} \cdot \mathbf{P} + \beta m)\phi \tag{2.14}$$

The coefficients α and β are determined by requiring a free particle to satisfy the relativistic energy-momentum relation 2.15, yielding 2.16, from which the following observations are made:

- α_i, β anticommute with each other
- $\alpha_i^2 = \beta^2 = 1$

$$H^2\phi = (\mathbf{P}^2 + m^2)\phi \tag{2.15}$$

$$\begin{aligned} H^2\phi &= (\alpha_i P_i + \beta m)(\alpha_j P_j + \beta m)\phi \\ &= (\alpha_i^2 P_i^2 + (\alpha_i\alpha_j + \alpha_j\alpha_i)P_iP_j + (\alpha_i\beta + \beta\alpha_i)P_i m + \beta^2 m^2) \end{aligned} \tag{2.16}$$

The Dirac-Pauli representation of 4×4 matrices (equation 2.17) are the most frequently used matrices which satisfy these requirements. Here, $\boldsymbol{\sigma}$ are the Pauli matrices previously described in equation 2.3 and $\mathbb{I}$ is the identity matrix.

$$\boldsymbol{\alpha} = \begin{pmatrix} 0 & \boldsymbol{\sigma} \\ \boldsymbol{\sigma} & 0 \end{pmatrix}, \quad \beta = \begin{pmatrix} \mathbb{I} & 0 \\ 0 & -\mathbb{I} \end{pmatrix} \tag{2.17}$$

Multiplying equation 2.14 on the left by β yields equation 2.18.

$$\mathrm{i}\beta\frac{\partial\phi}{\partial t} = -\mathrm{i}\beta\boldsymbol{\alpha}\cdot\nabla\phi + m\phi \tag{2.18}$$

The four Dirac matrices are introduced in equation 2.19 and are explicitly written in equation 2.20, where $\gamma^5 \equiv \mathrm{i}\gamma^0\gamma^1\gamma^2\gamma^3$

$$\gamma^\mu \equiv (\beta, \beta\boldsymbol{\alpha}) \tag{2.19}$$

$$\gamma^0 = \begin{bmatrix} \mathbb{I} & 0 \\ 0 & -\mathbb{I} \end{bmatrix} \gamma^i_{(i=1,2,3)} = \begin{bmatrix} 0 & \sigma_i \\ -\sigma_i & 0 \end{bmatrix} \gamma^5 = \begin{bmatrix} 0 & \mathbb{I} \\ \mathbb{I} & 0 \end{bmatrix} \tag{2.20}$$

The use of the gamma matrix notation yields another convenient form of the Dirac equation (2.21).

$$(\mathrm{i}\gamma^\mu\partial_\mu - m)\phi = 0 \tag{2.21}$$

However, it is possible to use any basis for the gamma matrices. Another convenient basis is the Weyl (or chiral) representation, given in equation2.22.

$$\gamma^0 = \begin{bmatrix} 0 & \mathbb{I} \\ \mathbb{I} & 0 \end{bmatrix} \gamma^i_{(i=1,2,3)} = \begin{bmatrix} 0 & \sigma_i \\ -\sigma_i & 0 \end{bmatrix} \gamma^5 = \begin{bmatrix} -\mathbb{I} & 0 \\ 0 & \mathbb{I} \end{bmatrix} \tag{2.22}$$

Because these representations are both in block form, it is possible to express the field as two separate components which are referred to as Weyl spinors (2.23).

$$\phi = \begin{pmatrix} \phi_L \\ \phi_R \end{pmatrix} \tag{2.23}$$

Applying this form to the Dirac equation (2.21) yields equation 2.24.

$$(\mathrm{i}\gamma^{\mu}\partial_{\mu} - m)\phi = \begin{pmatrix} -m & \mathrm{i}(\partial_0 + \boldsymbol{\sigma}\cdot\boldsymbol{\nabla}) \\ \mathrm{i}(\partial_0 - \boldsymbol{\sigma}\cdot\boldsymbol{\nabla}) & -m \end{pmatrix} \begin{pmatrix} \phi_L \\ \phi_R \end{pmatrix} = 0 \tag{2.24}$$

It is clear that in cases of zero mass[8] the left and right-handed parts of the equation completely decouple to give equation 2.25.

$$\mathrm{i}(\partial_0 - \boldsymbol{\sigma}\cdot\boldsymbol{\nabla})\phi_L = 0 \qquad \mathrm{i}(\partial_0 + \boldsymbol{\sigma}\cdot\boldsymbol{\nabla})\phi_R = 0 \tag{2.25}$$

2.2.2 The Weak Force

The Standard Model for the weak interactions was introduced by Sheldon Glashow in 1963 and was later improved by Steven Weinberg and Abdus Salam independently. This model is referred to as GWS. In addition to describing the weak interactions, this model also includes the electromagnetic interactions and so in its entirety it is sometimes referred to as the electro-weak theory of the Standard Model.

The model is structured as a $SU(2) \times U(1)$ gauge theory with the $SU(2)$ part giving rise to the massive weak bosons and the $U(1)$ part being responsible for the photon and thus the electromagnetic interactions.

A gauge transformation of a field, ϕ, in the $SU(2) \times U(1)$ symmetry is given by equation 2.26, where A^a_μ and B_μ are the $SU(2)$ and $U(1)$ gauge bosons. The different coupling constants associate with each part are called g and g'.

$$\phi \Longrightarrow e^{\frac{\mathrm{i}}{2}g\sigma^a A^a_\mu + \frac{\mathrm{i}}{2}g' B_\mu}\phi \tag{2.26}$$

[8]For very low mass and highly relativistic particles, where the mass contribution can be neglected, the zero mass approximation may be used.

The covariant derivative of ϕ is given by equation 2.27.

$$D_\mu \phi = (\partial_\mu - \frac{\mathrm{i}}{2} g \sigma^a A^a_\mu - \frac{\mathrm{i}}{2} g' B_\mu)\phi \tag{2.27}$$

Assuming that the field, ϕ, acquires a vacuum expectation value (equation 2.28), it is possible to determine the gauge boson mass terms in the theory by evaluating the Lagrangian at the scalar field expectation value, as shown in equation 2.29.

$$H = \frac{1}{\sqrt{2}} \begin{pmatrix} 0 \\ \nu \end{pmatrix} \tag{2.28}$$

$$\begin{aligned} \Delta\mathcal{L} &= \tfrac{1}{8}(0\ \nu)(g A^\alpha_\mu \sigma^\alpha + g' B_\mu)(g A^{\beta\mu}\sigma^\beta + g' B^\mu) \begin{pmatrix} 0 \\ \nu \end{pmatrix} \\ &= \tfrac{1}{8}(0\ \nu) \left| \begin{bmatrix} g A^3_\mu + g' B_\mu & g(A^1_\mu - \mathrm{i} A^2_\mu) \\ g(A^1_\mu - \mathrm{i} A^2_\mu) & -g A^3_\mu + g' B_\mu \end{bmatrix} \right|^2 \begin{pmatrix} 0 \\ \nu \end{pmatrix} \end{aligned} \tag{2.29}$$

The simplification of this expression yields[9] equation 2.30.

$$\Delta\mathcal{L} = \frac{1}{2}\frac{\nu^2}{4}(g^2 (A^1_\mu)^2 + g^2 (A^2_\mu)^2 + (-g A^3_\mu + g' B_\mu)^2) \tag{2.30}$$

From this expansion, there are three massive vector bosons that emerge. The $W^\pm$ are given by equation 2.31 and the Z^0 is given by equation 2.32.

$$W^\pm_\mu = \frac{1}{\sqrt{2}}(A^1_\mu \mp i A^2_\mu) \tag{2.31}$$

$$Z^0_\mu = \frac{1}{\sqrt{g^2 + g'^2}}(g A^3_\mu - g' B_\mu) \tag{2.32}$$

The mass of the $W^\pm$ is $m_W = \frac{\nu}{2} g$ and the mass of the Z^0 is $m_Z = \frac{\nu}{2}\sqrt{g^2 + g'^2}$. The massless vector field does not appear in this expansion (since the mass is zero). However, in order

[9] The handling of the numeric constants is done according to historical convention.

to be a vector field of this theory, it must be orthogonal to the other fields already defined. Therefore, the massless vector field A_μ, which is responsible for the electromagnetic vector potential, is simply defined as orthogonal to the Z^0 (2.32) , yielding 2.33.

$$\mathrm{A}_\mu = \frac{1}{\sqrt{g^2 + g'^2}}(gA^3_\mu + g'B_\mu) \tag{2.33}$$

The covariant derivative of a fermion field belonging to a general $SU(2)$ representation with a $U(1)$ charge of Y can be written as equation 2.34.

$$D_\mu = \partial_\mu - igA^a_\mu\sigma^a - ig'YB_\mu \tag{2.34}$$

In terms of the mass eigenstate fields, and making use of $T^\pm = \sigma^\pm \equiv \frac{1}{2}(\sigma^1 \pm \mathrm{i}\sigma^2)$, equation 2.34 can be rewritten as equation 2.35.

$$D_\mu = \partial_\mu - \mathrm{i}\frac{g}{\sqrt{2}}(W^+_\mu T^+ + W^-_\mu T^-) - \mathrm{i}\frac{1}{\sqrt{g^2 + g'^2}}Z_\mu(g^2T^3 - g'^2Y) - \mathrm{i}\frac{gg'}{\sqrt{g^2 + g'^2}}\mathrm{A}_\mu(T^3 + Y) \tag{2.35}$$

If the electron charge is expressed as equation 2.36 and the electric charge quantum number is expressed as equation 2.37, then the term of equation 2.35 responsible for the electromagnetic interaction takes on a more familiar form which is given in equation 2.38.

$$e = \frac{gg'}{\sqrt{g^2 + g'^2}} \tag{2.36}$$

$$Q = T^3 + Y \tag{2.37}$$

$$D^{EM}_\mu = \mathrm{i}e\mathrm{A}_\mu \tag{2.38}$$

Additionally, a weak mixing angle θ_ω can be defined such that

$$\cos\theta_\omega = \frac{g}{\sqrt{g^2 + g'^2}} \qquad \sin\theta_\omega = \frac{g'}{\sqrt{g^2 + g'^2}} \tag{2.39}$$

This provides for a change in basis

$$\begin{pmatrix} Z^0 \\ \mathrm{A} \end{pmatrix} = \begin{pmatrix} \cos\theta_\omega & -\sin\theta_\omega \\ \sin\theta_\omega & \cos\theta_\omega \end{pmatrix} \begin{pmatrix} A^3 \\ B \end{pmatrix} \tag{2.40}$$

which gives a more convenient form of equation 2.35, as shown in equation 2.41. All of the parameters describing the weak bosons are represented by the electron charge, e, the weak mixing angle, θ_ω, and the mass of one of the bosons.

$$D_\mu = \partial_\mu - \frac{\mathrm{i}}{\sqrt{2}}\frac{e}{\sin\theta_\omega}(W_\mu^+ T^+ + W_\mu^- T^-) - \mathrm{i}\frac{e}{\cos\theta_\omega \sin\theta_\omega} Z_\mu (T^3 - \sin^2\theta_\omega Q) - \mathrm{i}e\mathrm{A}_\mu Q \tag{2.41}$$

The weak mixing angle relates the masses of the bosons, according to 2.42.

$$m_W = m_Z \cos\theta_\omega \tag{2.42}$$

2.2.3 Leptons and the Weak Force

Thus far, there have been no experimental observations of right-handed neutrinos. It is assumed that they either do not exist, or that they are too massive to be created by and/or detected in current experiments. In order to describe a theory ensuring that only left-handed neutrinos couple to the weak bosons, it is possible to write all of the left-handed fermion fields (leptons and quarks) as $SU(2)$ doublets (equations 2.43 and 2.45), while writing the right-handed fermion fields as $SU(2)$ singlets (equations 2.44 and 2.46).

$$L_e = \begin{bmatrix} \nu_e \\ e^- \end{bmatrix}_L, \quad L_\mu = \begin{bmatrix} \nu_\mu \\ \mu^- \end{bmatrix}_L, \quad L_\tau = \begin{bmatrix} \nu_\tau \\ \tau^- \end{bmatrix}_L \tag{2.43}$$

$$l_e = e_R^-, \nu_{eR} \quad l_\mu = \mu_R^-, \nu_{\mu R} \quad l_\tau = \tau_R^-, \nu_{\tau R} \tag{2.44}$$

$$Q_u = \begin{bmatrix} u \\ d \end{bmatrix}_L, \quad Q_c = \begin{bmatrix} c \\ s \end{bmatrix}_L, \quad Q_t = \begin{bmatrix} t \\ b \end{bmatrix}_L \tag{2.45}$$

$$q_u = u_R, d_R \;\; q_c = c_R, s_R \;\; q_t = t_R, b_R \tag{2.46}$$

For the right-handed leptons, $T^3 = 0$ and Y is equal to the charge of the particle. For the left-handed leptons, $T^3 = \pm\frac{1}{2}$ and Y is chosen such that the charge of the particle equals $T^3 + Y$.

By design, $Y = T = 0$ for the right-handed neutrino. This ensures that the right-handed neutrino has no interaction with the bosons of the GWS electroweak theory, as can be seen with the parameterization in 2.35.

The Lagrangian can then be written for the first generation[10] as (ignoring the term for right-handed neutrinos which have no contribution)

$$\mathcal{L} = \overline{L}_e(i\not{D})L_e + \overline{e}_R(\mathrm{i}\not{D})e_R + \overline{Q}_u(\mathrm{i}\not{D})Q_u + \overline{u}_R(\mathrm{i}\not{D})u_R + \overline{d}_R(\mathrm{i}\not{D})d_R \tag{2.47}$$

Applying equation 2.41 to equation 2.47 yields

$$\begin{aligned} \mathcal{L} \;=\; & \overline{L}_e(\mathrm{i}\not{\partial})L_e + \overline{e}_R(\mathrm{i}\not{\partial})e_R + \overline{Q}_u(\mathrm{i}\not{\partial})Q_u + \overline{u}_R(\mathrm{i}\not{\partial})u_R + \overline{d}_R(\mathrm{i}\not{\partial})d_R \\ & + g(W^+_\mu J^{\mu+}_W + W^-_\mu J^{\mu-}_W + Z^0_\mu J^\mu_Z) + eA_\mu J^\mu_{EM} \end{aligned} \tag{2.48}$$

with

$$\begin{aligned} J^{\mu+}_W &= \tfrac{1}{\sqrt{2}}(\overline{\nu}_L\gamma^\mu e_L + \overline{u}_L\gamma^\mu d_L) \\ J^{\mu-}_W &= \tfrac{1}{\sqrt{2}}(\overline{e}_L\gamma^\mu \nu_L + \overline{d}_L\gamma^\mu u_L) \\ J^\mu_Z &= \tfrac{1}{\cos\theta_\omega}[\nu_L\gamma^\mu(\tfrac{1}{2})\nu_L + \overline{e}_L\gamma^\mu(-\tfrac{1}{2} + \sin^2\theta_\omega)e_L + \overline{e}_R\gamma^\mu(\sin^2\theta_\omega)e_R \\ &\quad + \overline{u}_L\gamma^\mu(\tfrac{1}{2} - \tfrac{2}{3}\sin^2\theta_\omega)u_L + \overline{u}_R\gamma^\mu(-\tfrac{2}{3}\sin^2\theta_\omega)u_R \\ &\quad + \overline{d}_L\gamma^\mu(-\tfrac{1}{2} + \tfrac{1}{3}\sin^2\theta_\omega)d_L + \overline{d}_R\gamma^\mu(\tfrac{1}{3}\sin^2\theta_\omega)d_R] \\ J^\mu_{EM} &= \overline{e}\gamma^\mu(-1)e + \overline{u}\gamma^\mu(+\tfrac{2}{3})u + \overline{d}\gamma^\mu(-\tfrac{1}{3})d \end{aligned} \tag{2.49}$$

where the various J's represent the currents associated with each electro-weak boson. Note that the currents listed in equation 2.49 only contain non-zero terms. Each one of the terms

[10] The first generation comprises u, d, e, and ν_e. The same equations are repeated for the second (s, c, μ, and ν_μ) and third (t, b, τ, and ν_τ) generations.

in the current represents a different particle interaction. For instance, in figure 2.2, the CC diagram $\nu_e \rightarrow e^- + W^+$ corresponds to the term $\overline{\nu}_L \gamma^\mu e_L$ in $J_W^{\mu+}$. For the NC diagram, $\nu_e \rightarrow \nu_e + Z^0$ corresponds to the term $\nu_L \gamma^\mu (\frac{1}{2}) \nu_L$ in J_Z^μ.

The weak interactions gives rise to two interaction vertices with neutrinos. One is for the neutral current (Z^0) and the other is for the charged current ($W^\pm$) interactions, as illustrated in figure 2.2.

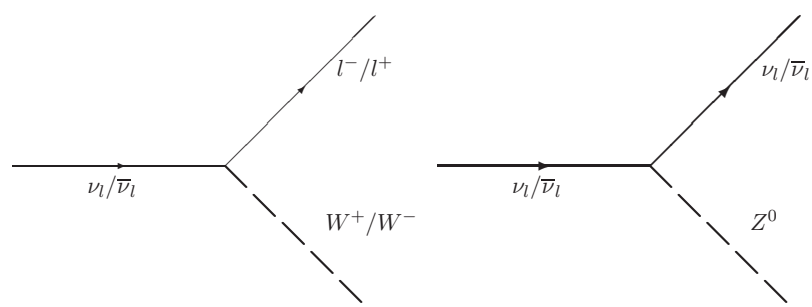

Figure 2.2: The two weak interactions of the neutrino. The charged current (CC) interaction is on the left and the neutral current (NC) interaction is on the right. In the CC interaction, an incoming neutrino produces a charged lepton of the same flavor of the neutrino and a W boson with a charge opposite that of the lepton. In the NC interaction the outgoing neutrino is the same flavor as in the incoming neutrino, and a neutral Z boson is produced.

2.2.4 Cabibbo, Kobayashi, and Maskawa

The weak interactions as just described do not tell the entire story for the weak interactions of quarks. The weak decay rates of a number of particles can only be correctly predicted under the assumption that the quarks involved in a weak interaction have undergone a basis rotation from the quarks present in the nucleons. This solution was first proposed by Nicola Cabibbo in 1963[27] when there were only three known quarks (u, d, and s). The work was extended by Makoto Kobayashi and Toshihide Maskawa[28] to handle six quarks, prior to the actual discovery of the t and b.

This change of basis is given in equation 2.50, and is performed by the CKM matrix, which is given in the standard parameterization as equation 2.51.

$$\begin{pmatrix} d' \\ s' \\ b' \end{pmatrix} = U_{CKM} \times \begin{pmatrix} d \\ s \\ b \end{pmatrix} \tag{2.50}$$

$$U_{CKM} = \begin{pmatrix} c_{12}s_{13} & s_{12}c_{13} & s_{13}e^{-\mathrm{i}\delta_{CP}} \\ -s_{12}c_{23} - c_{12}s_{23}s_{13}e^{-\mathrm{i}\delta_{CP}} & c_{12}c_{23} - s_{12}s_{23}s_{13}e^{-\mathrm{i}\delta_{CP}} & s_{23}c_{13} \\ s_{12}s_{23} - c_{12}c_{23}s_{13}e^{-\mathrm{i}\delta_{CP}} & -c_{12}s_{23} - s_{12}c_{23}s_{13}e^{-\mathrm{i}\delta_{CP}} & c_{23}c_{13} \end{pmatrix} \tag{2.51}$$

Here, c_{ij} and s_{ij} are the angles $\cos(\theta_{ij})$ and $\sin(\theta_{ij})$ describing the basis rotation, and δ_{CP} is a CP violation term. The weak interaction of an incoming quark, q, actually appears to the interaction vertex as q', thus allowing for the possibility for the generation of the outgoing quark to change.

This concept is only presented as a prerequisite to neutrino oscillations. In light of the fact that quarks appear in different bases based on their interaction, it is not unrealistic to expect neutrinos to do the same. However, such a situation is not guaranteed, as no observations have been made of neutrino to lepton (via $W^{\pm}$) or lepton to lepton (via Z) generation changes.

2.2.5 Neutrino Interaction Variables

A description will be given of a general neutrino interaction and the corresponding kinematic variables. The general neutrino interaction is given in figure 2.3. The incoming neutrino with energy E_ν produces a boson ($W^{\pm}$ or Z^0) and an outgoing leptonic component (either (e, μ, or τ) for $W^{\pm}$ or (ν_e, ν_μ, or ν_τ) for Z^0). The outgoing leptonic component has mass m, energy E_l and a longitudinal momentum p_l. The energy transferred to a quark

of mass M in the target nucleus (p, or n) is given by $\mathbf{Q}$ and is equal in magnitude to the energy lost by the incoming neutrino, given by $\mathbf{q}$.

$$Q^2 \equiv -q^2 = 2E_\nu(E_l - p_l) - m^2$$

The invariant hadronic mass of all of the hadronic shower particles is given by W, where

$$W^2 = M^2 + 2M(E_\nu - E_l) - Q^2$$

The Bjorken scale variable, x is defined as

$$x = Q^2/2M(E_\nu - E_l)$$

Finally, the fraction of incoming neutrino energy transfered to the hadronic component of the interaction, y, is given as

$$y = (E_\nu - E_l)/E_\nu$$

The hadronic y is also directly related to the electromagnetic fraction of a charged current ν_e event, which describes the fraction of the incoming neutrino energy that is present in the outgoing electron. The electromagnetic fraction thus is simply $1 - y$.

In general, the kinematic variables presented are not directly measurable in the MINOS experiment. The energy of the hadronic shower and lepton is often measured as a single quantity of total reconstructed event energy, a value which is closely related to the actual incident neutrino energy for CC interactions. A measurement of the transverse energy profile of the interaction may give some insight into the relative energies of each of the leptonic and hadronic components of the interaction. The event reconstruction software presented in chapter 6 will attempt to make a better measurement of the individual parts of the lepton and hadronic shower, and will be able to provide a limited measurement of Y for certain classes of ν_e charged current interactions.

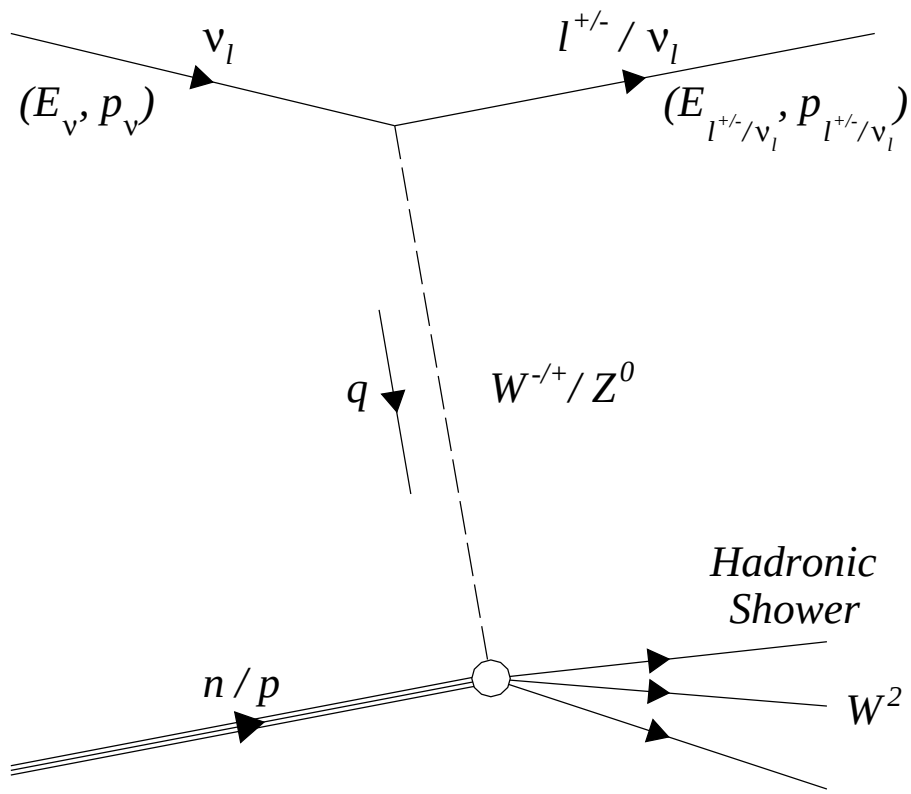

Figure 2.3: The kinematics of the general neutrino interaction are shown. An incoming neutrino produces either a lepton (by exchanging a $W^{\pm}$ in a charged current interaction) or neutrino (by exchanging a Z^0 in a neutral current interaction). The boson interacts with the target nucleus and produces a hadronic shower.

2.2.6 Oscillations

The flavors of neutrinos are matched to their lepton partners and thus appear as eigenstates of the weak interaction. The idea that the flavor eigenstates of the neutrinos are not identical to the mass eigenstates, originally put forth by Pontecorvo [29], leads to the relationship given in equation 2.52, where $|\nu_{\alpha=e,\mu,\tau}\rangle$ are the flavor eigenstates and $|\nu_i\rangle$ are the mass eigenstates in the case of n different neutrinos.

$$|\nu_\alpha\rangle = \sum_{i=1}^{n} U^*_{\alpha i}|\nu_i\rangle \tag{2.52}$$

Applying the Schrödinger equation to the ν_i component of ν_α in the rest frame of ν_i yields the time evolution of a neutrino state after time T_i (2.53), where m_i is the mass of that component.

$$|\nu_i(T_i)\rangle = e^{-\mathrm{i}m_i T_i}|\nu_i(0)\rangle \tag{2.53}$$

The phase factor in 2.53 is rewritten using the Lorentz-invariant phase factor in terms of time t and position L in the laboratory frame 2.54.

$$e^{-\mathrm{i}m_i T_i} = e^{-\mathrm{i}(E_i t - p_i L)} \tag{2.54}$$

Under the assumption that ν_α was produced with all mass eigenstate components sharing the momentum p and for $p \gg m_i$, the energy of a given component $E_i = \sqrt{p^2 + m_i^2} \approx p + m_i^2/2p$. Since neutrinos have a small mass, they are considered relativistic, and so $t \approx L$. This reduces equation 2.54 to equation 2.55

$$e^{-\mathrm{i}(E_i t - p_i L)} \rightarrow e^{-\mathrm{i}(m_i^2/2p)L} \tag{2.55}$$

The evolution of state ν_α after propagating a distance of L (and taking $E \simeq p$ as the average energy of the mass eigenstate components of the neutrino) is given in equation 2.56.

$$|\nu_\alpha(L)\rangle \approx \sum_{i=1}^{n} U^*_{\alpha i} e^{-\mathrm{i}(m_i^2/2E)L} |\nu_i\rangle \tag{2.56}$$

Combining equation 2.56 with equation 2.52 illustrates in equation 2.57 how a neutrino, ν_α, after traveling a distance of L, can become a superposition of all of the flavor eigenstates.

$$|\nu_\alpha(L)\rangle \approx \sum_{\beta=1}^{n} \left[\sum_{i=1}^{n} U^*_{\alpha i} e^{-\mathrm{i}(m_i^2/2E)L} U_{\beta i} \right] |\nu_\beta\rangle \tag{2.57}$$

The probability of measuring ν_α as ν_β, or a $\nu_\alpha \to \nu_\beta$ oscillation, is given in equation 2.58, where $\Delta m^2_{ij} = m_i^2 - m_j^2$ and δ_{ij} is the Kronecker delta.

$$\begin{aligned} P(\nu_\alpha \to \nu_\beta) &= |\langle \nu_\beta | \nu_\alpha(L)\rangle|^2 \\ &= \textstyle\sum_{i,j} U^*_{\alpha i} U_{\beta i} U_{\alpha j} U^*_{\beta j} e^{-\mathrm{i}\Delta m^2_{ij} L/2E} \\ &= -4 \textstyle\sum_{i>j} \Re(U^*_{\alpha i} U_{\beta i} U_{\alpha j} U^*_{\beta j}) \sin^2\left(\frac{\Delta m^2_{ij} L}{4E}\right) \\ &\quad +2 \textstyle\sum_{i>j} \Im(U^*_{\alpha i} U_{\beta i} U_{\alpha j} U^*_{\beta j}) \sin\left(\frac{\Delta m^2_{ij} L}{2E}\right) + \quad \delta_{\alpha\beta} \end{aligned} \tag{2.58}$$

As previously illustrated in figure 2.1, the current experimental evidence points towards the existence of three neutrinos. Thus, the matrix U, given in equation 2.59, is of dimension 3. It is usually parameterized in terms of three mixing angles, θ_{12}, θ_{13}, and θ_{23}, and one CP violating phase, δ_{CP}. In recognition of the work done on neutrino oscillations by Pontecorvo[29], and later by Maki, Nakagawa, and Sakata[30], the matrix U is usually

referred to as the PMNS matrix or U_{PMNS}.

$$
\begin{aligned}
U_{PMNS} &= \begin{pmatrix} U_{e1} & U_{e2} & U_{e3} \\ U_{\mu 1} & U_{\mu 2} & U_{\mu 3} \\ U_{\tau 1} & U_{\tau 2} & U_{\tau 3} \end{pmatrix} \\
&= \underbrace{\begin{pmatrix} 1 & 0 & 0 \\ 0 & c_{23} & s_{23} \\ 0 & -s_{23} & c_{23} \end{pmatrix}}_{atmospheric} \underbrace{\begin{pmatrix} c_{13} & 0 & s_{13}e^{-i\delta_{CP}} \\ 0 & 1 & 0 \\ -s_{13}e^{i\delta_{CP}} & 0 & c_{13} \end{pmatrix}}_{cross-mixing} \underbrace{\begin{pmatrix} c_{12} & s_{12} & 0 \\ -s_{12} & c_{12} & 0 \\ 0 & 0 & 1 \end{pmatrix}}_{solar}
\end{aligned}
\tag{2.59}
$$

Here, c_{ij} and s_{ij} denote $\cos(\theta_{ij})$ and $\sin(\theta_{ij})$ and are the terms which describe neutrino oscillations. The terms have been separated into different sectors which have historically been probed independently based on the experiment and system being studied. A nonzero phase δ_{CP} indicates CP violation.

The combined effect of different values of Δm^2_{12} and Δm^2_{23} with different values of L/E for solar and atmospheric experiments has the effect of suppressing all but one neutrino mass eigenstate pair term from equation 2.58. For solar experiments, the dominating terms are θ_{12} and Δm^2_{12} and for atmospheric experiments, the dominating terms are θ_{23} and Δm^2_{23}. The cross-mixing terms, θ_{13} and Δm^2_{13}, do not appear alone as a dominate term in nature, and are probed with the use of accelerator and reactor based experiments.

The matrix U_{PMNS} can also be written in the same form as U_{CKM} (equation 2.51) as given in equation 2.60.

$$
U_{PMNS} = \begin{pmatrix} c_{12}s_{13} & s_{12}c_{13} & s_{13}e^{-\mathrm{i}\delta_{CP}} \\ -s_{12}c_{23} - c_{12}s_{23}s_{13}e^{-\mathrm{i}\delta_{CP}} & c_{12}c_{23} - s_{12}s_{23}s_{13}e^{-\mathrm{i}\delta_{CP}} & s_{23}c_{13} \\ s_{12}s_{23} - c_{12}c_{23}s_{13}e^{-\mathrm{i}\delta_{CP}} & -c_{12}s_{23} - s_{12}c_{23}s_{13}e^{-\mathrm{i}\delta_{CP}} & c_{23}c_{13} \end{pmatrix} \tag{2.60}
$$

The probability of a neutrino oscillation as used in this analysis has been discussed in detail in [31][32]. The probability of $\nu_\mu \to \nu_e$, which is the oscillation mode that is being measured in this analysis, is given for a vacuum in equation 2.61. The dominating term of $P(\nu_\mu \to \nu_e)$ is $\sin^2\theta_{23}\sin^2 2\theta_{13}\sin^2\frac{\Delta m^2_{31}L}{4E}$. However, in the final measurement made with this analysis, all terms must be considered as they have nontrivial contributions.

$$\begin{aligned} P(\nu_\mu \to \nu_e) \;=\; & s^2_{23}\sin^2 2\theta_{13}\sin^2\frac{\Delta m^2_{31}L}{4E} + c^2_{13}c^2_{23}\sin^2 2\theta_{12}\sin^2\frac{\Delta m^2_{21}L}{4E} \\ & +8c^2_{13}s_{13}c_{12}s_{12}s_{23}c_{23}\sin\frac{\Delta m^2_{21}L}{4E}\sin\frac{\Delta m^2_{31}L}{4E}\cos\left(\frac{\Delta m^2_{32}L}{4E}+\delta_{CP}\right) \\ & -2s^2_{12}s^2_{23}\sin^2 2\theta_{13}\sin\frac{\Delta m^2_{21}L}{4E}\sin\frac{\Delta m^2_{31}L}{4E}\cos\frac{\Delta m^2_{32}L}{4E} \\ & +4c^2_{13}s^3_{12}s_{13}s_{23}(s_{23}s_{13}s_{12}-2c_{12}c_{23}\cos\delta_{CP})\sin^2\frac{\Delta m^2_{31}L}{4E} \end{aligned} \tag{2.61}$$

In all of the equations presented describing neutrino oscillations, the mass of a single neutrino never appears alone, but rather always as a mass squared difference between two neutrinos. This feature of neutrino oscillations makes it impossible to determine the actual masses of neutrinos from oscillation experiments alone. Additionally, the relative ordering of the masses of the neutrinos are not known from these experiments, as illustrated in figure 2.4. While Δm^2_{32} is known to be about two orders of magnitude larger than Δm^2_{12}, the sign of Δm^2_{32} is not known. Following other orderings in physics, it is assumed that the larger mass splitting is above the smaller mass splitting ($m_3 > m_2$). This ordering is termed "normal hierarchy". However, there is no physical reason preventing the case of "inverted hierarchy", where $m_3 < m_2$.

2.2.7 CP Violation

Gauge theories, such as the Standard Model, are required to simultaneously satisfy Charge, Parity, and Time (CPT) conservation. As already mentioned, neutrinos were experimentally found to be left-handed. Applying the charge operator to a neutrino results

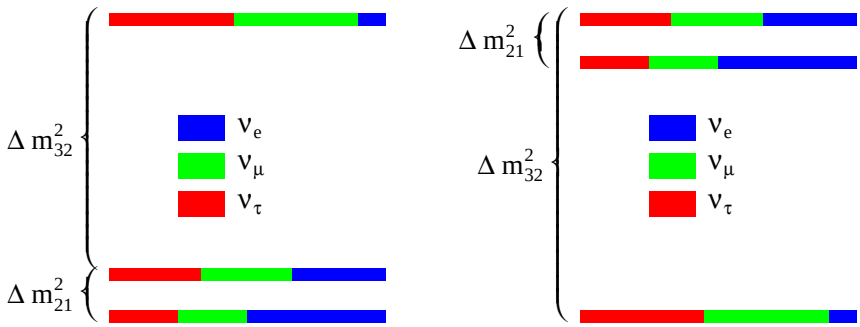

(a) Normal Hierarchy (b) Inverted Hierarchy

Figure 2.4: The two possible neutrino mass hierarchies are presented. The normal mass hierarchy is shown in (a) and the inverted mass hierarchy is shown in (b).

in an anti-neutrino with left-handed spin which is a condition that has never been observed. Thus, the neutrino violates the charge symmetry. However, simultaneously changing the charge and flipping the parity results in an anti-neutrino with right-handed spin, which is in agreement with observations. Neutrinos therefore are expected to observe a CP symmetry. It is assumed that they also observe time reversal symmetry, since overall CPT conservation is required.

The application of the CPT transformation to a neutrino oscillation[33] reverses the transition process and converts the neutrinos to anti-neutrinos, as described in equation 2.62.

$$CPT \;\; \nu_\alpha \rightarrow \nu_\beta = \overline{\nu}_\beta \rightarrow \overline{\nu}_\alpha \tag{2.62}$$

In the context of the oscillation probabilities as given in equation 2.58, the interchange of $U \leftrightarrow U^*$ has the effect of reversing the oscillation process, as recorded in equation 2.63

$$P_{rob}(\nu_\alpha \rightarrow \nu_\beta; U) = P_{rob}(\nu_\beta \rightarrow \nu_\alpha; U^*) \tag{2.63}$$

Assuming that CPT holds, the substitution of equation 2.62 into equation 2.63 yields equation 2.64.

$$P_{rob}(\overline{\nu}_\beta \rightarrow \overline{\nu}_\alpha; U) = P_{rob}(\nu_\beta \rightarrow \nu_\alpha; U^*) \tag{2.64}$$

It remains a possibility that neutrinos do not completely follow CP symmetry. However, any deviation in CP must be countered by T to give the overall CPT conservation. The effects of CP and T violation in three flavor neutrino mixing is described in [34] and is summarized here.

The CP transformation of neutrino oscillations results in the exchange of the neutrino with the anti-neutrino. This has the same effect as taking the complex conjugate of U, which results in a sign change on the CP violating phase, δ_{CP}. The interchange $\nu_{\alpha,\beta} \leftrightarrow \overline{\nu}_{\alpha,\beta}$ is the same as $U^*_{\alpha i} \rightarrow U_{\alpha i}$ resulting in $\delta_{CP} \rightarrow -\delta_{CP}$. The application of the time reversal on the oscillation probability has the effect of switching the sign in the exponent of the time dependent form of the oscillation probability, given in equation 2.65.

$$P_{rob}(\nu_\alpha, t_0 \rightarrow \nu_\beta, t) = \left| \sum_i U_{\beta i} e^{\mathrm{i}E_i(t-t_0)} U^*_{\alpha i} \right|^2 \tag{2.65}$$

Since the probability only depends on the modulus of the amplitude, the exchange of the sign in the exponent can be countered by the complex conjugation of U. The interchange $t_0 \leftrightarrow t$ is the same as $\nu_\alpha \leftrightarrow \nu_\beta$ which has the same effect as $U^*_{\alpha i} \rightarrow U_{\alpha i}$ and $U_{\beta i} \rightarrow U^*_{\beta i}$ resulting in $\delta_{CP} \rightarrow -\delta_{CP}$. The combined effect of CPT transformations then yields $\nu_{\alpha,\beta} \leftrightarrow \overline{\nu}_{\alpha,\beta}$ and $t_0 \leftrightarrow t$ (or $\nu_\alpha \leftrightarrow \nu_\beta$). Thus, $P_{rob}(\nu_\alpha \rightarrow \nu_\beta) \rightarrow P_{rob}(\overline{\nu}_\beta \rightarrow \overline{\nu}_\alpha)$. For CP transformations, any violation can be parameterized as

$$\Delta P^{CP}_{rob,\,\alpha\beta} = P_{rob}(\nu_\alpha \rightarrow \nu_\beta) - P_{rob}(\overline{\nu}_\alpha \rightarrow \overline{\nu}_\beta)$$

and for T transformations, the violation can be parameterized as

$$\Delta P^{T}_{rob,\,\alpha\beta} = P_{rob}(\nu_\alpha \rightarrow \nu_\beta) - P_{rob}(\nu_\beta \rightarrow \nu_\alpha)$$

Assuming that CPT invariance holds, the violation observed in CP transformations must be exactly offset by the violation observed in T transformations such that

$$\Delta P^{CP}_{rob,\,\alpha\beta} = -\Delta P^{T}_{rob,\,\alpha\beta} \tag{2.66}$$

The neutrino survival probabilities will therefore not display any CP asymmetry

$$\Delta P^{CP}_{rob,\,\alpha\alpha} = \Delta P^{T}_{rob,\,\alpha\alpha} = 0 \rightarrow P_{rob}(\nu_\alpha \rightarrow \nu_\alpha) = P_{rob}(\overline{\nu}_\alpha \rightarrow \overline{\nu}_\alpha) \tag{2.67}$$

All measurements of CP violation must then be made in neutrino appearance experiments. In the case of three flavor neutrino mixing, there is one CP violating phase, δ_{CP}, and so there is a single difference between the oscillation probabilities.

$$\Delta P^{CP}_{rob,\,e\mu} = \Delta P^{CP}_{rob,\,\mu\tau} = \Delta P^{CP}_{rob,\,\tau e} \equiv \Delta P_{rob} \tag{2.68}$$

where

$$\begin{aligned} \Delta P_{rob} = \quad & -4 s_{12} c_{12} s_{13} c_{13}^2 s_{23} c_{23} \sin\delta_{CP} \\ & \times \left[\sin\left(\frac{\Delta m^2_{12}}{2E} L\right) + \sin\left(\frac{\Delta m^2_{23}}{2E} L\right) + \sin\left(\frac{\Delta m^2_{31}}{2E} L\right) \right] \end{aligned} \tag{2.69}$$

The term ΔP_{rob} vanishes when any of the following conditions is true:

- One of the $\Delta m^2_{ij} = 0$
- One of the $\theta_{ij} = 0^\circ$ or 90°
- $\delta_{CP} = 0^\circ$ or 180°

Experiment evidence from the CHOOZ experiment[35] indicates that θ_{13} is small, making the measurement of δ_{CP} a very difficult task. However, knowledge of whether CP violation actually occurs in the leptonic sector has far reaching consequences for physics, as it may help to explain the matter/antimatter asymmetry seen in the universe[36].

The MINOS experiment is sensitive to the amount of CP violation as parameterized by δ_{CP}. Any measurement of $\nu_\mu \rightarrow \nu_e$ made in this analysis must then be reported in terms of a given value of δ_{CP}.

2.2.8 Lepton Mass

The lepton mass terms that appear in GWS use the same scalar field that was used to give a mass to the weak bosons. This gives terms like (for the electron)

$$\Delta\mathcal{L}_e = -\lambda_e \overline{E}_L^{\mu} \phi_\mu e_R + h.c. \tag{2.70}$$

where λ_e is a dimensionless coupling constant. Replacing ϕ by the vacuum expectation value, $\nu/\sqrt{2}$, and denoting the Hermitian Conjugate as "h.c." gives

$$\Delta\mathcal{L}_e = -\frac{\lambda_e \nu}{\sqrt{2}} \overline{e}_L e_R + h.c. \tag{2.71}$$

with the mass of the electron given by

$$m_e = \frac{\lambda_e \nu}{\sqrt{2}} \tag{2.72}$$

A similar procedure is followed for the quarks, except with

$$\begin{aligned} \Delta\mathcal{L}_q &= -\lambda_d \overline{Q}_L^{\mu} \phi_\mu d_R - \lambda_u \epsilon^{\mu\rho} \overline{Q}_L^{\mu} \phi_\rho u_R + h.c. \\ &= -\tfrac{\lambda_d \nu}{\sqrt{2}} \overline{d}_L d_R - \tfrac{\lambda_u \nu}{\sqrt{2}} \overline{u}_L u_R + h.c. \end{aligned} \tag{2.73}$$

It is most important to note that this formulation under the GWS theory does not allow for massive neutrinos, as no such mass terms can be constructed since the decision was already made to not have a ν_R term in the theory. However, at least two neutrinos must have mass for neutrino oscillations to occur. To achieve this feat, the Standard Model must be extended to allow massive neutrinos.

Giving Mass to Neutrinos

There are two possible ways for a particle to obtain a mass in the Standard Model. However, both the Dirac mass term (equation 2.74) and the Majorana mass terms (equation 2.75) require the right-handed $SU(2)$ singlet, and the model, by construction, does not

include a ν_R term. The Standard Model must then be extended to accommodate these additional particles.

$$-\mathcal{L}_D = m_D \overline{\nu}_L \nu_R + h.c. \tag{2.74}$$

$$\begin{aligned} -\mathcal{L}_{ML} &= -\tfrac{m_L}{2}(\overline{\nu}_L)^C \nu_L + h.c. \\ -\mathcal{L}_{MR} &= -\tfrac{m_R}{2}(\overline{\nu}_R)^C \nu_R + h.c. \end{aligned} \tag{2.75}$$

It is possible that ν_R do exist, but they are either "sterile", so that they do not have weak interactions, or that they are extremely massive. Therefore, they are either not generated by or detectable in the current terrestrial experiments. The possibility that the right-handed neutrinos are massive to counter the almost massless left-handed neutrinos gives rise to the so called "see-saw" mechanism[37].

If the Majorana mass terms are correct, then lepton number is not conserved and then there is no quantum number left to distinguish between ν and $\overline{\nu}$. Thus, the neutrino is its own anti particle and double neutrino-less β decays can occur[38].

Both of these explanations remain as viable possibilities with the knowledge obtains so far through experiments.

2.2.9 Matter Effects

Special considerations need to be taken into account in an experiment that measures neutrinos which pass through the earth or other matter. Mikheyev, Smirnov, and Wolfenstein formulated the inclusion of matter effects, referred to as the MSW effect[39]. All flavors of neutrinos will interact with the electrons in the earth via the neutral weak current, but only ν_e will interact with the electrons in the earth via the charged weak current. This interaction is due to forward scattering and it has a potential of the form given

in equation 2.76 for the charged current interaction with the electron neutrino. Here, G_F is the Fermi constant and n_e the local density of electrons in the earth.

$$V_m^e = \sqrt{2} G_F n_e \tag{2.76}$$

A demonstration of the effect of this flavor asymmetry in earth interactions is illustrated in the case of two flavor oscillations. The 2x2 version of the PMNS matrix, U_2, is defined in equation 2.77.

$$U_2(\theta) = \begin{pmatrix} \cos\theta & \sin\theta \\ -\sin\theta & \cos\theta \end{pmatrix} \tag{2.77}$$

The original interaction Hamiltonian gains an additional term to include the matter interaction, as shown in equation 2.78.

$$\begin{aligned} H &= U_2(\theta) \begin{pmatrix} 0 & 0 \\ 0 & \frac{\Delta m^2}{2E} \end{pmatrix} U_2^\dagger(\theta) + \begin{pmatrix} V_m^e & 0 \\ 0 & 0 \end{pmatrix} \\ &= \frac{\Delta m^2}{2E} \begin{pmatrix} \sin^2\theta + \frac{2E}{\Delta m^2} V_m^e & -\sin\theta\cos\theta \\ -\sin\theta\cos\theta & \cos^2\theta \end{pmatrix} \end{aligned}$$

The Hamiltonian is then diagonalized with the addition of another mixing angle, θ_m

$$H = \frac{\Delta m^2}{2E} U_2(\theta_m) \begin{pmatrix} \lambda_1 & 0 \\ 0 & \lambda_2 \end{pmatrix} U_2^\dagger(\theta_m) \rightarrow \frac{\Delta m^2}{2E} U_2(\theta_m) \begin{pmatrix} 0 & 0 \\ 0 & \lambda_2 - \lambda_1 \end{pmatrix} U_2^\dagger(\theta_m) \tag{2.78}$$

The following parameters are then defined

$$\begin{aligned} C_2 &= \sqrt{\sin^2 2\theta + (\cos 2\theta - A_2)^2} \\ \cos 2\theta_m &= \tfrac{\cos 2\theta - A_2}{C_2} \\ \sin 2\theta_m &= \tfrac{\sin 2\theta}{C_2} \\ \lambda_1 &= \tfrac{1}{2}(1 + A_2 + C_2) \\ \lambda_2 &= \tfrac{1}{2}(1 + A_2 - C_2) \end{aligned} \tag{2.79}$$

where $A_2 \equiv \frac{2E}{\Delta m^2} V_m^e$ describes the potential. The parameters in the case of oscillations in a vacuum are thus related to the same parameters including matter effects by the transformation

$$\begin{aligned} \sin 2\theta &\rightarrow \frac{\sin 2\theta}{\sqrt{\sin^2 2\theta + (\cos 2\theta - A_2)^2}} \\ \Delta m^2 &\rightarrow \Delta m^2 \sqrt{\sin^2 2\theta + (\cos 2\theta - A_2)^2} \end{aligned} \tag{2.80}$$

The matter effects are responsible for both shifting the oscillation peak in the energy spectrum and for changing the relative size of the mass squared difference between the neutrinos. Since the magnitude in the shift of Δm^2 is different for neutrinos and antineutrinos, a properly designed experiment should be able to determine the correct ordering of the neutrino masses.

The oscillation probability equations with matter effects for three neutrino flavors are used in this experiment. They follow the example above, but are more complicated and will only be summarized here. The complete definition of the equations used can be found in [31]. Additionally, two new parameters must be defined to describe the matter effects for the three neutrinos. The parameters used are

$$\begin{aligned} \alpha &= \frac{\Delta m_{21}^2}{\Delta m_{31}^2} \\ \Delta &= \frac{\Delta m_{31}^2 L}{4E} \\ A &= \frac{2EV_m^e}{\Delta m_{31}^2} = \frac{V_m^e L}{2\Delta} \\ C_{13} &= \sqrt{\sin^2 \theta_{13} + (A - \cos 2\theta_{13})^2} \\ C_{12} &= \sqrt{\sin^2 2\theta_{12} + \left(\cos 2\theta_{12} - \frac{A}{\alpha}\right)^2} \end{aligned} \tag{2.81}$$

The oscillation probability equations are formed from an expansion to first order in α that is accurate to all orders in s_{13} with an expansion to first order in s_{13} that is accurate to all

orders in α. An example for $P(\nu_\mu \to \nu_e)$ with matter effects is given in equation 2.82.

$$
\begin{aligned}
P(\nu_\mu \to \nu_e) \;=\;& s_{23}^2 \tfrac{\sin^2 2\theta_{13}}{C_{13}^2} \sin^2 C_{13}\Delta \\
& -2\alpha s_{12}^2 s_{23}^2 \tfrac{\sin^2 2\theta_{13}}{C_{13}^2} \sin C_{13}\Delta \\
& \quad \times \left[\Delta \tfrac{\cos C_{13}\Delta}{C_{13}}(1 - A\cos 2\theta_{13}) - A \tfrac{\sin C_{13}\Delta}{C_{13}} \tfrac{\cos 2\theta_{13} - A}{C_{13}}\right] \\
& +\alpha s_{13} \sin 2\theta_{12} \sin 2\theta_{23} \tfrac{\sin C_{13}\Delta}{AC_{13}^2} \\
& \quad \times\{\cos\delta_{CP}[C_{13}\sin(1+A)\Delta \\
& \qquad -(1 - A\cos 2\theta_{13})\sin C_{13}\Delta] \\
& \qquad -C_{13}\sin\delta_{CP}[\cos C_{13}\Delta - \cos(1+A)\Delta]\} \\
& +c_{23}^2 \tfrac{\sin^2 2\theta_{12}}{C_{12}^2} \sin^2 \alpha C_{12}\Delta \\
& -s_{13} \tfrac{\sin 2\theta_{12}}{C_{12}} \sin 2\theta_{23} \tfrac{(1-\alpha)\sin\alpha C_{12}\Delta}{1+A-\alpha+A\alpha c_{12}^2} \\
& \quad \times\{\sin\delta_{CP}[\cos\alpha C_{12}\Delta - \cos(A+\alpha-2)\Delta] \\
& \qquad +\cos\delta_{CP}[\sin(A+\alpha-2)\Delta \\
& \qquad -\sin\alpha C_{12}\Delta(\tfrac{\cos 2\theta_{12} - \frac{A}{\alpha}}{C_{12}} - \tfrac{\alpha A C_{12}}{2(1-\alpha)} \tfrac{\sin^2 2\theta_{12}}{C_{12}^2})]\} \\
& -2\alpha s_{13} \sin 2\theta_{12} \sin 2\theta_{23} \cos(\Delta + \delta_{CP}) \tfrac{\sin A\Delta}{A} \tfrac{\sin(A-1)\Delta}{(A-1)}
\end{aligned}
\tag{2.82}
$$

The enhancement of the neutrino oscillations and the suppression of antineutrino oscillations by matter effects provides an artificial CP bias which further complicates the determination of δ_{CP} in all neutrino experiments. One possible way to isolate the CP violation from the matter induced asymmetry is to measure the oscillated neutrino energy spectrum at multiple baselines[34]. Any change in the oscillation probability as measured at different baselines is due entirely to matter effects, as δ_{CP} is a constant.

Some examples of the energy dependence of neutrino oscillations are illustrated using the oscillation parameters adopted by the MINOS experiment which are summarized in table 2.2. Here, $\sin^2 2\theta_{13} = 0.15$, $\sin^2 2\theta_{12} = 0.86$, $\sin^2 2\theta_{23} = 1$, $\Delta m_{21}^2 = 8 \times 10^{-5}$ eV^2, $|\Delta m_{32}^2| = 2.43 \times 10^{-3}$ eV^2, and L = 735 km. The probability for $\nu_\mu \to \nu_\mu$ is visually

illustrated for the MINOS experiment (with L = 735 km) in figure 2.5 for the normal hierarchy case. The oscillation probability minimum is 0.2% and corresponds to neutrinos with energy of approximately 1.46 GeV. The probability of $\nu_\mu \rightarrow \nu_e$ is given in figure 2.6. Here, the maximum probability of ν_e appearance depends on both the mass hierarchy used and the inclusion of matter effects. For the case of vacuum oscillations the maximum oscillation probability is about same for both hierarchies (7.7%), but it is centered on neutrino energies of about 1.57 GeV for the normal compared to 1.27 GeV for the inverted hierarchies. The inclusion of the matter effects enhances the peak oscillation probability to 9.4% and decreases the peak of the oscillation to about 1.46 GeV for the normal hierarchy. For the inverted hierarchy, the oscillation peak is suppressed to 6.0% and the center of the peak is increased to about 1.38 GeV.

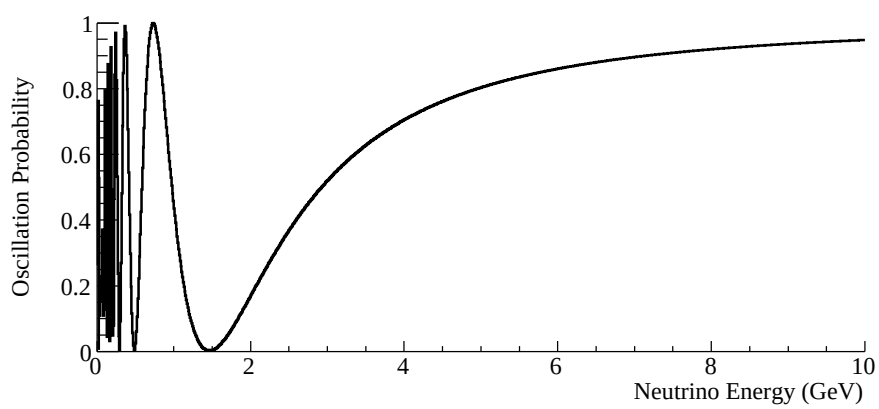

Figure 2.5: The oscillation probability for $\nu_\mu \rightarrow \nu_\mu$ at the Far Detector in the MINOS experiment is shown as a function of neutrino energy for the normal hierarchy. The oscillation probability minimum of 0.2% is approximately at 1.46 GeV. This is computed with $\sin^2 2\theta_{13} = 0.15$, $\sin^2 2\theta_{12} = 0.86$, $\sin^2 2\theta_{23} = 1$, $\Delta m^2_{21} = 8 \times 10^{-5}$ eV^2, $|\Delta m^2_{32}| = 2.43 \times 10^{-3}$ eV^2, and L = 735 km.

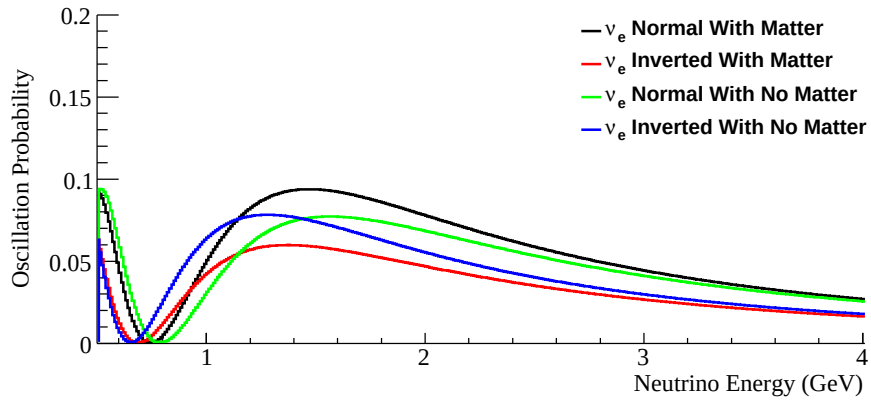

Figure 2.6: The probability for $\nu_\mu \rightarrow \nu_e$ oscillations at the Far Detector in the MINOS experiment (with L = 735 km) is shown as a function of neutrino energy. The probabilities calculated for the normal and inverted hierarchies both with and without matter effects are shown. The oscillation probability maximum of about 7.7% is approximately at 1.57 GeV for the normal and 1.27 GeV for the inverted hierarchies, which corresponds to the oscillation probability minimum seen for ν_μ disappearance. The different locations of the oscillation maximum between the normal and inverted hierarchy can be clearly distinguished for the case calculated without matter effects. The inclusion of matter effects results in the shifting of the peaks of the oscillation maximums for the normal and inverted hierarchies towards each other. Additionally, matter effects enhance the oscillations for the normal hierarchy and suppress the oscillations for the inverted hierarchy. With matter effects included, the oscillation probability maximum is enhanced to 9.4% and is centered at 1.46 GeV for the normal hierarchy. For the inverted hierarchy, the oscillation probability maximum is suppressed to 6.0% and is centered at 1.38 GeV. This is computed with $\sin^2 2\theta_{13} = 0.15$, $\sin^2 2\theta_{12} = 0.86$, $\sin^2 2\theta_{23} = 1$, $\Delta m^2_{21} = 8 \times 10^{-5}$ eV^2, $|\Delta m^2_{32}| = 2.43 \times 10^{-3}$ eV^2, and L = 735 km.

2.3 Experimentally Measured Properties of Neutrinos

Historical experiments have contributed to the design and implementation of later experiments, thereby slowly improving the cumulative world knowledge of neutrino physics. This section will only summarize the current best measurements of the properties of neutrinos. The measurements set by individual experiments is readily available in [33].

2.3.1 Neutrino Mass

Upper limits have been set on the masses of the neutrinos from experiments measuring the missing energy from decays of the form $l \rightarrow \nu_l + X$, where X is any combination of measurable particles. The current best measurements for the neutrino masses are given[33] as $m_{\nu_e} < 2$ eV, $m_{\nu_\mu} < 0.19$ MeV, and $m_{\nu_\tau} < 18.2$ MeV.

Astrophysical observations have also set limits on the neutrino masses. These limits[33] are much more restrictive. A recent result using CMB and SOSS LRG power spectrum data limits the sum of the neutrino masses to be < 0.28 eV.

2.3.2 Oscillation Parameters

The current best measured values describing neutrino oscillations[33] come from a number of different sources. A summary of all known parameters describing the neutrino oscillations are presented together in figure 2.7 to illustrate the amount of knowledge this field has amassed to date.

A combination of results from KamLAND, Borexino, and Super-Kamiokande-I provides a measurement of $\sin^2 2\theta_{12} = 0.87 \pm 0.03$. The MINOS experiment measured $\sin^2 2\theta_{23} > 0.85$ in 2008, although the best measurement to date was made in 2005 by Super-Kamiokande, finding $\sin^2 2\theta_{23} > 0.92$.

A measurement of the mass splitting Δm^2_{21}, combining results from KamLAND, Borexino, and Super-Kamiokande-I, finds that $\Delta m^2_{21} = 7.59^{+0.19}_{-0.21} \times 10^{-5}$ eV^2. The measurement of $|\Delta m^2_{32}|$ by MINOS using a ν_μ accelerator beam is found to be almost two orders of magnitude larger than Δm^2_{21}, with $|\Delta m^2_{32}| = 2.43 \pm 0.13 \times 10^{-3}$ eV^2.

A limit on $\sin^2 2\theta_{13}$ is obtained from the CHOOZ reactor experiment by measuring $\overline{\nu}_e$ disappearance. The limit given is dependent on the value of Δm^2_{32}[35]. At the measured value of $|\Delta m^2_{32}| = 2.43 \pm 0.13 \times 10^{-3}$ eV^2 from MINOS, the limit obtained from the CHOOZ

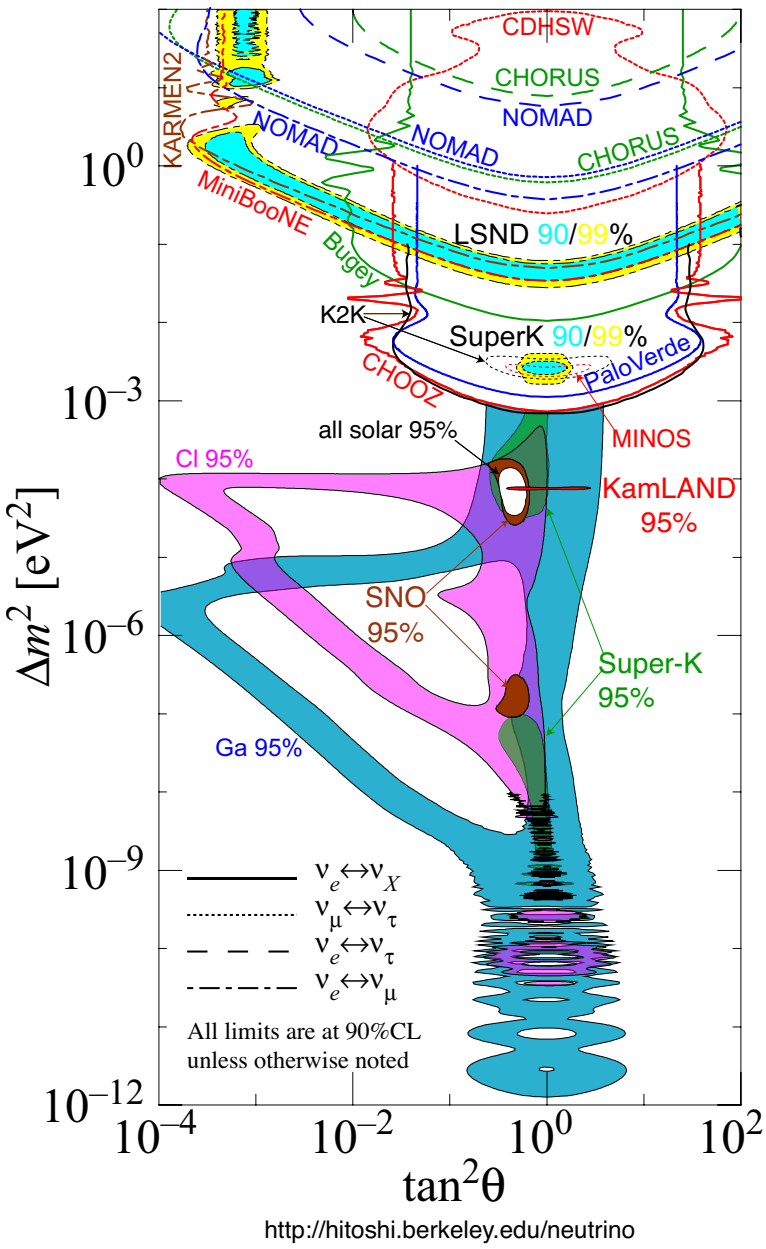

Figure 2.7: This figure presents the various oscillation parameters, as measured by different experiments, in an illustration of the amount of information amassed by the field to date[40].

Parameter	Value
θ_{13}	$\sin^2 2\theta_{13} < 0.15$
θ_{12}	$\sin^2 2\theta_{12} = 0.86 \pm 0.04$
θ_{23}	$\sin^2 2\theta_{23} = 1.00_{-0.08}$
Δm^2_{21}	$\Delta m^2_{21} = 8.0 \pm 0.3 \times 10^{-5}$ eV^2
$\lvert\Delta m^2_{32}\rvert$	$\lvert\Delta m^2_{32}\rvert = 2.43 \pm 0.13 \times 10^{-3}$ eV^2
Density	2.75 ± 0.25 g/cm^3
Baseline (L)	735 km

Table 2.2: The summary of the known parameters used in calculating the neutrino oscillations with matter effects in this analysis are presented. Both the hierarchy and δ_{CP} are unknown. Therefore, results of this analysis will be presented in terms of these two unknown parameters.

experiment is $\sin^2 2\theta_{13} < 0.15$. The goal of this thesis is to provide a measurement of $\sin^2 2\theta_{13}$ which improves the result obtained by the CHOOZ experiment.

The sign of Δm^2_{32} (the mass hierarchy) and the CP violating phase, δ_{CP}, are not known. The measurement of these two parameters will be the goal of future experiments.

The parameters describing the oscillations, including matter effects, as used in this analysis are summarized in table 2.2.

Chapter 3

The MINOS Experiment

The Main Injector Neutrino Oscillation Search (MINOS) experiment was designed to measure neutrino oscillations using a neutrino beam generated from protons extracted from the Fermilab Main Injector. The experiment is simply described as consisting of three parts. A neutrino source provides the particles necessary for the experiment. A detector close to the source measures the particle flux and provides a means to calibrate the measurement. A detector located far from the source measures neutrinos after some number of them may have oscillated.

The neutrino source and Near Detector are location at Fermilab, in Batavia, Illinois. The Far Detector is located in the Soudan mine in Tower, Minnesota. Figure 3.1 illustrates the relative positions of the Fermilab complex and Main Injector, target hall, Near Detector, and Far Detector.

3.1 The NuMI Beamline

The NuMI (Neutrinos at the Main Injector) beamline at Fermilab began providing neutrinos to the MINOS detectors in January 2005. This device was constructed for the

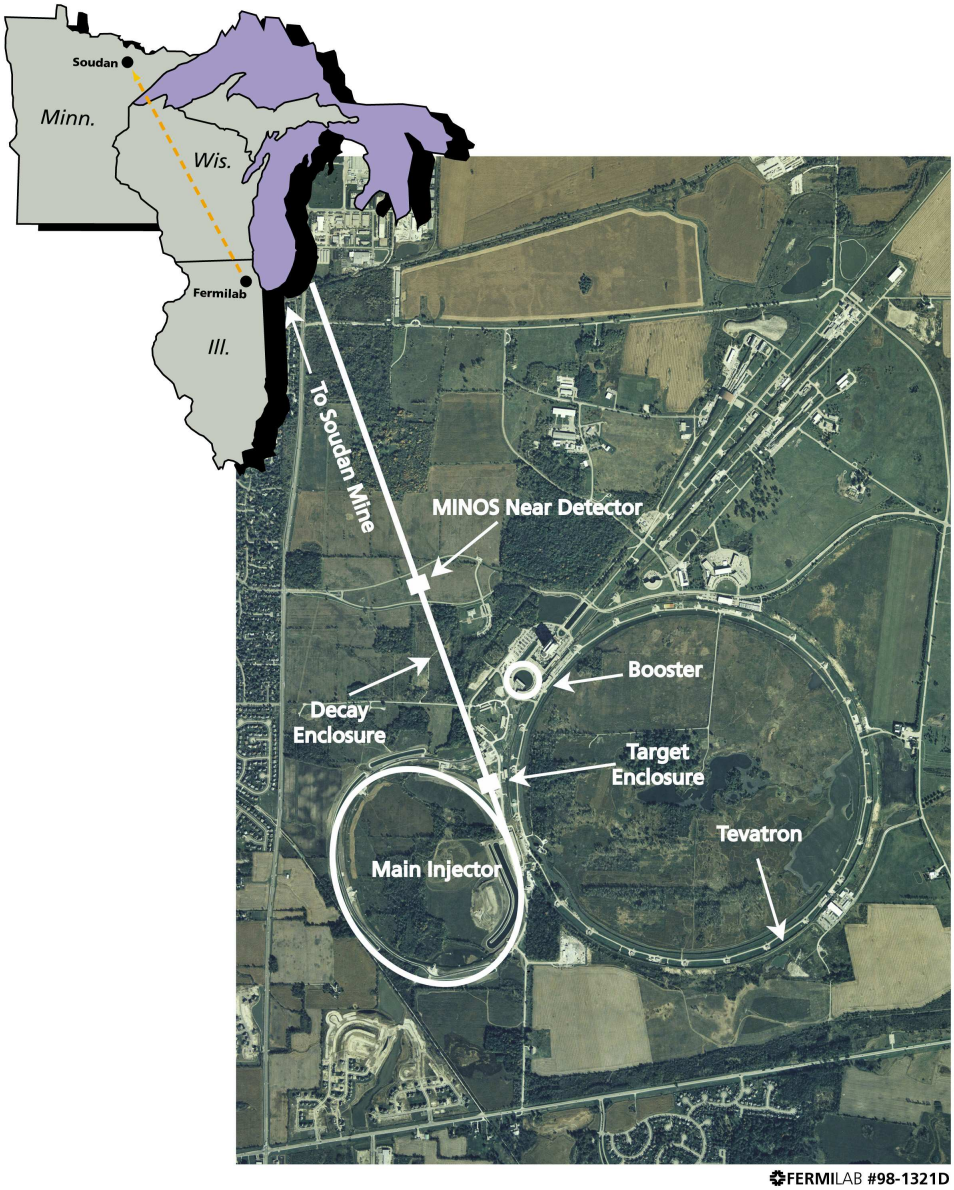

Figure 3.1: An illustration of the Fermilab accelerator complex[41]. The Main Injector, NuMI target hall, Near Detector, and Far Detector are indicated.

MINOS experiment with the ability to also be used in other future experiments. Figure 3.2 shows a schematic of the beam line, illustrating the extraction point of the Main Injector up to and including the Near Detector hall. The details of the target hall, decay volume, and muon monitors can be seen in the cartoon of the NuMI beam line that is presented in figure 3.3.

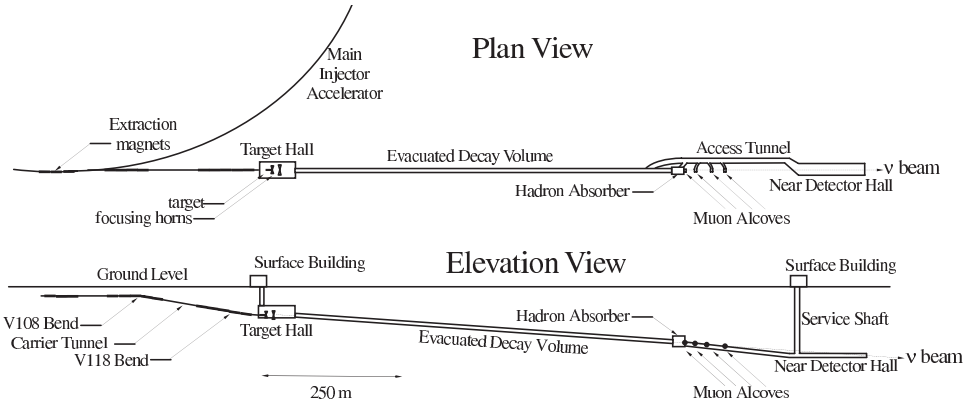

Figure 3.2: The schematic of the NuMI beam line[42]. The 120 GeV protons are extracted from the Main Injector and transported to the target hall, where they interact with a graphite target, produce pions and kaons, which are then focused and allowed to decay in the decay volume. Remaining hadrons are stopped by a beam dump, and muons are stopped by the rock, both of which are located after the decay volume. The resulting neutrino beam enters the Near Detector hall pointed 3° down from horizontal so that it will pass through the Far Detector hall 3° up from horizontal at a distance of 735 kilometers away.

Protons of 120 GeV are extracted from the Main Injector in up to a 9.6 μs spill containing six batches at most every 1.87 seconds utilizing a specially designed three magnet proton kicker system[44]. Normal running conditions only extract five batches in a 8.0 μs spill, allowing one batch to be used for anti-proton production for use in other experiments. Typical conditions in the first year of running saw average NuMI extractions containing 2.1×10^{13} protons every 2.2 - 2.4 seconds[42].

Once deflected from the Main Injector ring, this beam is positioned such that it enters the Near Detector pointing down by 3° from horizontal and enters the Far Detector

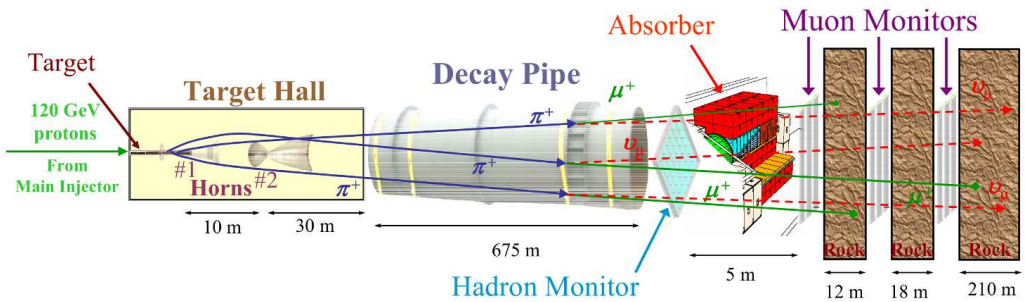

Figure 3.3: An illustration of the NuMI beamline[43]. The 120 GeV protons from the Main Injector collide with a graphite target, producing pions and kaons. Those charged particles are then focused by two electromagnetic horns. The pions and kaons are then allowed to decay in an evacuated decay pipe, producing neutrinos and other particles. A beam dump then stops any hadrons that reach the end of the decay pipe. Muons formed in the decays travel further through the rock, being measured by three muon monitors to obtain information about the energy, spectrum, and size of the beam. The 210 meters of rock after the final muon monitor prevent all but neutrinos from reaching the Near Detector hall.

pointing up 3° from horizontal. The beam travels a distance of 350 meters from the Main Injector, at which point it collides with the NuMI production target which is made of 47 segments of graphite. The number of protons colliding with the target is the unit of measure of exposure for the experiment and is abbreviated as POT (protons on target). The integrated exposure for the experiment is shown in figure 3.4. The total data used in this analysis is 7.0×10^{20} POT. Divisions in this figure due to experiment or facility shutdowns for maintenance or due to other issues are easily identifiable. Large shutdown periods provide boundaries dividing the total data sample into three separate run periods.

Interactions between the protons and the graphite target produce pions and kaons which are focused by two parabolic toroidal electromagnets, also called "horns". The water cooled horns are pulsed with an electrical current in time with the target collisions. The relative position of the horns to each other and to the target, as well as the magnitude of the electrical current used to energize the horns are variable, allowing for the generation

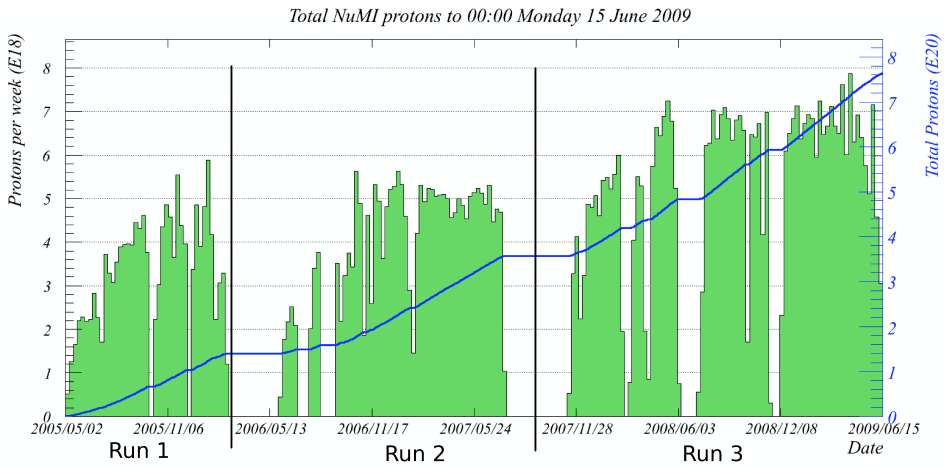

Figure 3.4: The total number of protons on target (POT) after four years of running the NuMI beam. The three run periods, indicating accelerator shutdowns, are labeled and are separated by vertical lines. This analysis will use a total of 7.0×10^{20} POT.

of different neutrino energy spectra. These configurations are summarized in table 3.1. The horns can be positioned via a remote control rail drive for a maximum distance of longitudinal travel of 2.5 meters. The field generated by these horns selects particles of a single charge (depending on the sign of the horn current) and also focuses particles of a particular momentum range towards the detectors. Configurations used in this analysis all use "normal" horn current, which focuses π^+/K^+ and results in neutrinos. Also possible, but not used in the data collected for this analysis is "reverse" horn current, which produces π^-/K^- and results in antineutrinos. The most commonly used configuration has been the L010185 which is optimized for focusing pions and provides the best spectrum for an oscillation search. The remaining configurations are useful in understanding the beam spectra and are used to tune the data simulation.

The particles produced in the target collision, which are primarily pions and kaons, then enter a decay pipe evacuated to 0.5 Torr. This decay pipe is 2 meters in diameter and 675 meters long. The length of the pipe was chosen to accommodate the decay length of a

Beam Configuration	Target Position(cm)	Horn Current(kA)	Peak $E_\nu \pm$ RMS (GeV)
L010000	10	0	7.4 ± 4.1
L010170	10	170	3.1 ± 1.1
L010185	10	185	3.3 ± 1.1
L010200	10	200	3.5 ± 1.1
L100200	100	200	5.6 ± 1.5
L250200	250	200	8.6 ± 2.7

Table 3.1: The various beam configurations of the NuMI beam. The target position is the distance between the target and the first focusing horn (10 cm is the smallest allowed distance due to physical size constraints). A larger target position moves the target upstream in the beam. The peak neutrino energy spectrum is shown. The case of 0 kA horn current is also called "horn off" mode and results in a wide range of neutrino energies.

10 GeV pion. However, the diameter of the decay pipe is not ideal for low energy particles which may collide with the walls of the pipe before decaying, thus reducing the low energy portion of the resulting neutrino spectrum. This decay pipe was filled with helium during run 3 due to concerns about the integrity of the vacuum, as the beam pipe had suffered an undetermined amount of radiation damage over the previous running.

The neutrinos generated from the π/K$\rightarrow \mu + \nu$ decays have an energy, E_ν, directly related to the energy of the parent particle

$$E_\nu \approx \frac{(1 - \frac{m_\mu^2}{M^2})E}{1 + \gamma^2 \tan^2 \theta_\nu}$$

where m_μ and M are the muon and parent hadron masses, E is the parent hadron energy, $\gamma = E/M$ is the parent's Lorentz boost, and θ_ν is the angle in the lab between the neutrino and the parent hadron[45].

The energy spectrum of the beam in the Near Detector is presented in figure 3.5 for the three configurations used in this analysis. The horn off (L010000) configuration does not focus any of the particles after the target collisions and thus there is no peak in the energy spectrum. The normal running condition (L010185) focuses particles providing

a neutrino energy peak of about 3.3 GeV which corresponds closely to where the $\nu_\mu \rightarrow \nu_\mu$ oscillation minimum is located. The high energy configuration (L250200) is used for beam studies. This configuration focuses more particles, resulting in more neutrino interactions in the detector. It also has a higher energy peak, centered at about 8.6 GeV. The resulting neutrino beam composition is approximately 91.8% ν_μ, 7.0% $\overline{\nu}_\mu$, 1.04% ν_e, and 0.1% $\overline{\nu}_e$.

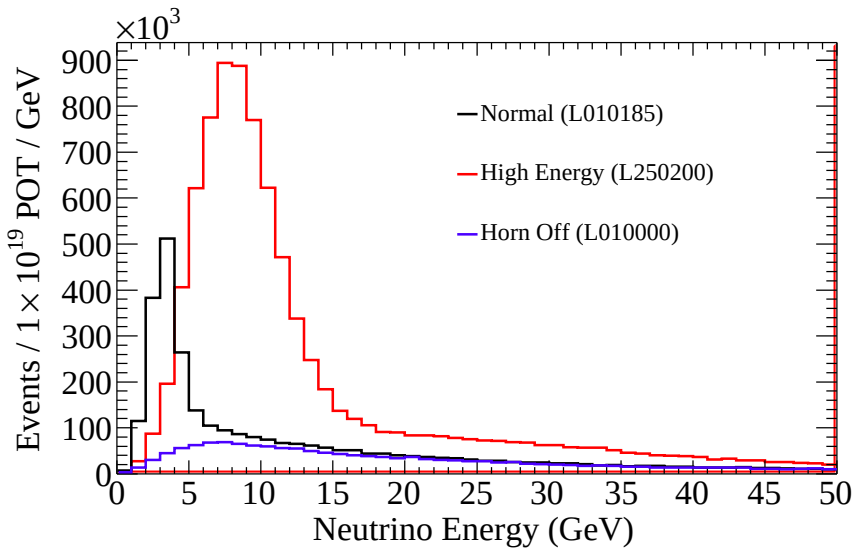

Figure 3.5: The neutrino energy spectrum in the Near Detector for different horn configurations is shown. The peak that is apparent in the normal running conditions vanishes when the horn is shut off. The high energy configuration both increases the the distance between the target and the first horn and also increases the strength of the magnetic field generated by the horns. These two conditions work together in order to focus the more energetic pions and kaons and result in a higher energy peak.

At the end of the decay pipe a beam dump stops any remaining hadrons. The beam dump is comprised of a water cooled aluminum and steel segment, a second volume of steel that is not cooled, and then concrete blocks. Past the beam dump is a large volume of rock 240 meters long which stops the remaining muons from reaching the detector hall.

The intensity of the beam is measured by two toroidal beam current transformers

with an uncertainty determined to be $\pm 1\%$ [46]. Three muon monitoring detectors are placed at intervals in the rock and are used to monitor beam conditions, including beam energy and spot size, and placement.

The position of the Far Detector is known to 1 cm in the horizontal and 76 cm in the vertical positions [47][48]. This translates to a 15 μ rad beam angle with respect to the ideal line drawn to connect the near and Far Detectors. Due to geometry effects, the spectrum seen by the Near Detector is that of a line source and the spectrum seen at the Far Detector is that of a point source. These geometry effects are well understood and are taken into account in the simulated data.

3.2 The MINOS Detectors

The near and far MINOS detectors were designed to be functionally identical. While they do posses different characteristics in location, size, and data acquisition electronics, the technology used to gather energy from the neutrino interactions and the particles generated in these interactions are the same in both detectors. The close similarities between the detectors aid in reducing any systematic differences between the events measured in either detector. Additionally, a third detector[49] was made using the same technology and was tested for detector response to known particles utilizing a test beam at CERN.

3.2.1 Detector Technology

Description

The MINOS detectors were primarily designed to detect $\nu_\mu \rightarrow \nu_\mu$ oscillations (or ν_μ disappearance). Charged current ν_μ interactions characteristically result in a muon containing most of the event energy. It was desirable to measure the energy of this muon,

from which the original neutrino energy could be estimated. Due to the low probability of a neutrino interaction in matter, it was desirable to build as massive of a detector as possible. With these two considerations in mind, the detectors were chosen to have a magnetic field and alternating layers of active detector and iron. The iron layers provided substantial mass for the neutrinos to interact with, and provided a path for the magnetic field which would cause muons to bend from which a momentum measurement could be made. The detectors are sufficiently long such that a muon range measurement can be made for all but the most energetic muons. The ability to measure the sign of the muon momentum based on the direction of curvature in the magnetic field also allows for the discrimination between ν_μ and $\overline{\nu}_\mu$ interactions. This general detector plan provided the necessary mass to gather sufficient data and also provided for two simultaneous measurements of the momentum of the muon generated by ν_μ interactions. The detectors can also identify ν_e interactions which produce an electron, although the resulting electromagnetic shower is coarsely sampled, as a 1 GeV electron only traverses about 6 planes.

Alternating planes of scintillator material and iron were constructed. The iron planes were 2.54 cm in thickness in both the near and Far Detectors, and 2.5 cm thick in the calibration detector[1]. The scintillator planes are comprised of strips of extruded polystyrene scintillator measuring 1 cm thick by 4.1 cm wide. These strips are surrounded by a TiO_2 doped polystyrene coating which reflects light that is then captured by a wavelength shifting fiber for delivery to a multisegmented photo multiplier tube (PMT)[50]. The construction of the scintillator strip is show in figure 3.6. The assembly of the strips and the connection of the wavelength shifting fibers to the PMT is shown in figure 3.7. The strips are arranged side by side into either a 20 or 28 strip module which is made light tight by covering the

[1]This standard/metric difference was due the sourcing of the industrially available sheet iron in the USA (Fermilab) and Europe (CERN), and is taken into account when comparing events between the Calibration Detector and the Near and Far Detectors.

module with an aluminum foil. Each of the strip modules also includes a light injection system for calibration studies. An LED situated above the fiber bundle of each module is able to inject a specific amount of light into the fibers in order to measure the response in the readout electronics system. A PIN diode is also present, and provides a precise measurement of the intensity of the light from the light injection system which illuminates the fibers.

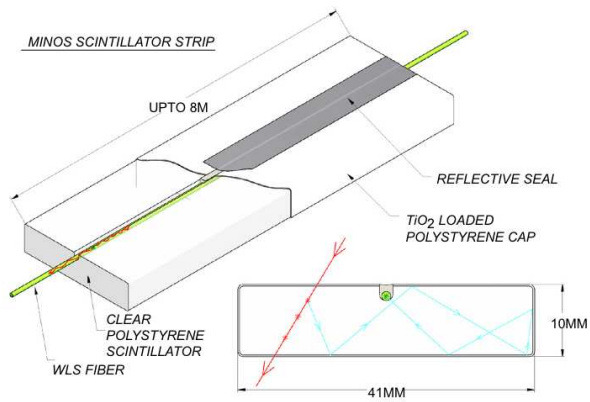

Figure 3.6: An illustration of the assembly of the scintillator strips in the MINOS detectors[51]. The extruded clear polystyrene scintillator is clad with a reflective white TiO_2 polystyrene to minimize light loss. The light is gathered and trapped in a wavelength shifting fiber which is laid in a recess in the extruded piece and secured with reflective metallic tape.

The scintillator strips are rotated between adjacent planes, such that the strips in a given plane are orthogonal to the strips in the previous and next planes. This scheme allows for the event topology to be measured in two different two dimensional views (Z vs U or Z vs V). This orientation of the planes allows for a limited three dimensional event reconstruction.

A diagram of the coordinate systems of the near, far, and calibration detectors is given in figure 3.8. The U and V axis are aligned with the scintillator strips, arranged in such a way as to avoid the potential access difficulty of the electronic readout being located

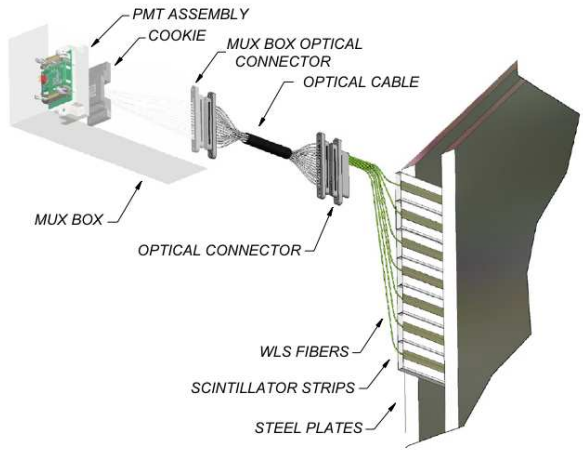

Figure 3.7: An illustration of the PMT detectors in the MINOS detectors[51]. The wavelength shifting fibers are gathered from the strips and are held against a PMT. In the Near Detector, the M64 style PMT is used, where a single fiber is placed on each pixel. In the Far Detector, the M16 style PMT is used which places eight fibers on each pixel. The pattern of the fiber placement into each pixel on the Far Detector differs between each side of the detector so that simultaneous activation of a pixel from multiple fibers can be detected.

under the detector. The origin of the coordinate system in both the near and Far Detectors is centered on the electromagnetic coil hole.

A GPS receiver at each detector provides a time stamp used for synchronizing the detectors with the beam pulse.

Near Detector

The Near Detector measures 980 metric tons and is located 104 meters underground at a distance of 1040 meters from the NuMI beam target. This detector has a unique shape. The coil is offset from the center of the detector, with a fully instrumented region being on the side with the most space from the coil. There is a partially instrumented region on the side that is closest to the coil. This portion of the detector is not used in the analysis and serves primarily as a return for the magnetic field. Carrying 40 kA, the coil induces an average field of 1.17 Tesla when measured at the neutrino beam

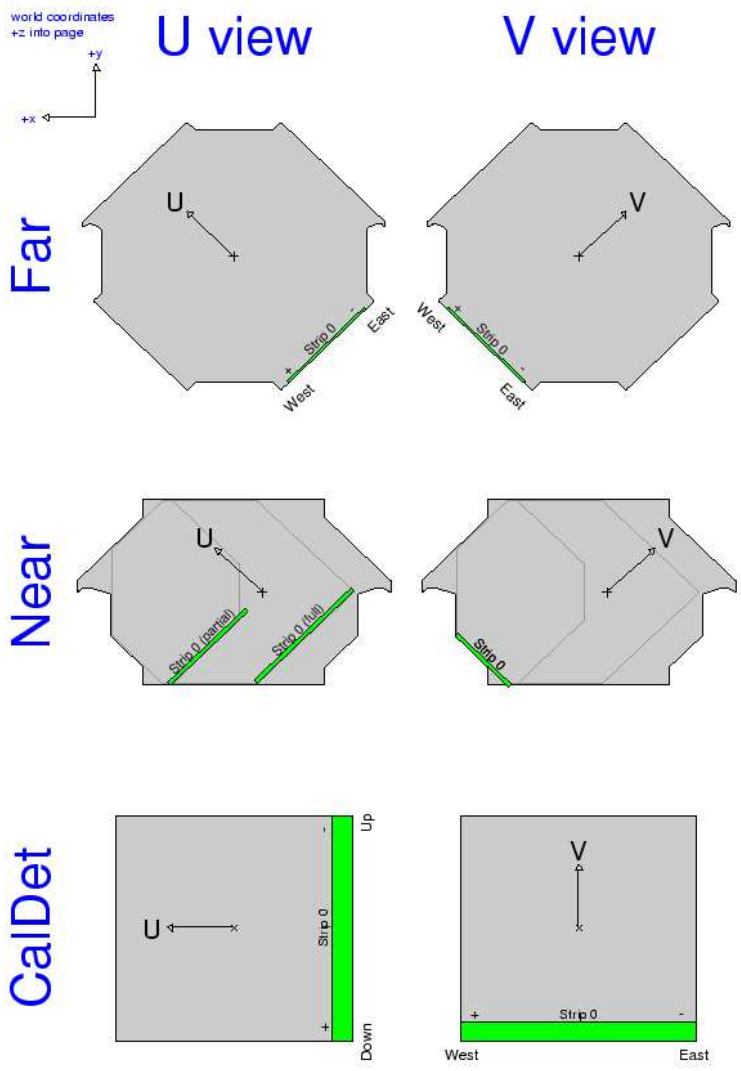

Figure 3.8: The Coordinate Systems of the MINOS Detectors[52]. The U and V axis are aligned with the strips and form the two dimensional views (Z vs U or Z vs V). The origin of the coordinate system in both the near and Far Detectors is centered on the electromagnetic coil hole. The direction of the neutrino beam is into the page.

center, located 1.49 meters to the left of the coil (when looking at the upstream face of the detector). The upstream section of the detector contains a fully instrumented spectrometer, analogous to the Far Detector design. The downstream portion of the detector contains a partially instrumented calorimeter, made of the same material, but only having active detector material for one plane in every four iron planes. This portion of the detector is not used for the ν_e appearance analysis. Each fiber from a scintillator strip is connected to its own PMT pixel on a 64 anode Hamamatsu photomultiplier tube (PMT).

The front end electronics digitize the PMT signal with 16 bits of precision in contiguous 18.8 ns time intervals (corresponding to the 53 MHz RF of the main injector) with zero dead time. A spill trigger mode records the output for every photomultiplier pixel over a 13 μs time period starting about 1.5 μs before the arrival of the neutrinos at the detector. A dynode trigger mode is used for out-of-spill recording of cosmic ray events, resulting in a continuous digitation for a period of 150 ns, independent for each PMT, based on a dynode signal threshold.

Far Detector

The Far Detector measures 5.4 metric kilotons. It is located in the Soudan Mine in Tower, Minnesota at a distance of 705 meters underground and 735.3 kilometers from the NuMI beam target. It is comprised of two modules separated by a 1.15 meter gap. The first module is comprised of 249 planes for a total length of 14.78 meters. The second module has 237 planes for a total length of 14.10 meters. Each module has an independently operated coil carrying about 15.2 kA and inducing an average field of 1.27 Tesla in the steel. The benefits to having two separate modules included less requirements for the coil in addition to the ability to have half of the detector in a operational state while the remainder of the second module was still under construction. The face of each plane is octagonally shaped,

measuring 8 meters across.

Due to the scale of the Far Detector compared to the Near Detector, combined with the much lower event rate in the Far Detector than in the Near Detector, it was both financially desirable and technically feasible to have multiple strips read out on the same electronics channel. Each plane consists of 192 strips. Eight wavelength shifting fibers from eight individual strips were delivered to each pixel of a 16 anode Hamamatsu photomultiplier tube (PMT) in such a way that it was unlikely for a pixel to be simultaneously activated by two different strips. Each strip assigned to the same pixel is separated by at least approximately 1 meter from the other strips on that pixel. The strips are read out by a PMT on both sides of the detector, and the strips sharing a pixel on one side of the detector do not share the same pixel of the other side of the detector. This minimization of electronics by collecting data from multiple strips on a single electrons channel is called multiplexing. This sharing of electronics requires an additional reconstruction step unique to the Far Detector which disambiguates the data and presents it in a form directly comparable to the Near Detector, such that a single measurement of collected photoelectrons on a PMT pixel corresponds to a single and unique strip within the detector.

The front end electronics digitizes signals from each PMT with a 14 bit ADC when the common dynode signal exceeds 0.25 photoelectrons. Each digitalized signal is time stamped with a resolution of 1.5624 ns. Coincidence between at least two PMTs above the threshold on one side of the detector within a contiguous group of 20 or 24 planes is required in order to digitize the hits. Collections of data passing these requirements are sent to a computer farm where the data is futher processed based on software triggers.

The data acquisition system (DAQ) buffers the data while awaiting a spill trigger from the Near Detector. The GPS time stamp of this trigger is used to select at least a 100 μs event window around the time of the spill, requiring at least a 156 ns activity free

period on either side of the window. All hits 30 μs prior to the trigger are also recorded in the event so that channels that were active prior to the beam trigger are not mistaken as coming from any beam induced event.

Fake spill triggers are also recorded. These triggers appear identical to an actual spill trigger to the Far Detector, except there is no beam activity. The data collected from these triggers provides a valuable tool for understanding non-beam induced background events in the Far Detector, such as cosmic events.

When spill triggers are not available either due to network errors, or because there are actually no spills, all sequential blocks of hits bounded by at least 156 ns of inactivity are recorded. These out-of-spill triggers are primarily cosmic events. The integrated trigger rate in the Far Detector is about 4 Hz and is dominated by cosmic rays and single photoelectron noise, as the detector only sees an actual beam induced neutrino interaction at a rate of about 1.9 per day.

3.2.2 Physics of the Detector Technology

When a neutrino interacts within the detector, it can produce multiple charged particles. As a charged particle travels through the scintillator strip, it can excite or ionize the scintillator which then produces light. Some of this light is captured into a wavelength shifting fiber which transports this light to the PMT. The amount of light produced by a charged particle in a scintillator strip is proportional to the amount of energy lost by that particle as it traversed the strip.

3.2.3 Calibration

Since neutrino oscillations are in part described by the energy of the incident neutrino, it is necessary to have an accurate measurement of the energy deposited in the

detector by an neutrino interaction event. There are a number of steps in order to convert the number of photons incident on the surface of the PMT, as measured by the front end electrons, to a calibrated amount of energy in units such as GeV. Each of these steps must be carefully understood and calibrated. The methods used and the calibrations obtained are discussed in detail in [53][54] and are summarized here.

There are two tools available to calibrate the detector. The first tool is the light injection system. This consists of an ultra-violet LED situated above the wavelength shifting fibers at the end of the strip. This LED can be pulsed for a programmable duration and intensity, creating a well understood quantity of light which is then transmitted via the fibers to the PMT. The second tool is to look at cosmic muons which pass through the detector or which stop in the detector.

When energy is deposited in a scintillator strip by an ionizing particle, light is generated and is collected by the wavelength shifting fiber. This light is transmitted to the PMT, which generates a signal that is digitalized by a ADC, thus converting it into a piece of information that provides the starting point of the calibration chain.

Before describing the calibration chain in detail, a summary will be given. The number of ADC units can be directly correlated to photoelectrons through a calibration made with the light injection system. The number of photoelectrons, as a measured quantity, is used for various detector studies but is not transformed further to higher level calibrated quantities. Instead, the ADC value is again used and is first adjusted to account for the nonlinear response of the PMT. This step again uses the light injection system to correlate raw ADC values with values corresponding to known light levels. Cosmic muons are also used in this step to monitor and adjust for the drifting of this linearity calibration over time. The value measured at this step which is the linearity corrected signal is named “SigLin”. The next step attempts to ensure consistent behavior between adjacent

strips. This calibration of strip to strip correlation is termed "SigCor", and is again obtained through the use of cosmic muons. The signal must then be adjusted based on where the interaction occurred within the detector to account for attenuation and readout effects. The signal calibration based on the mapping of the event to a specific position within the detector is termed "SigMap", and relies on the cosmic muons in the Near Detector and a special set of mapping data in the Far Detector. Finally, the values are converted to units of energy with a calibration that makes use of cosmic stopping muons. Since the energy deposited by a stopping muon is well understood, these units are termed Muon Energy Units (MEU). An additional calibration is then finally applied to convert MEU units to GeV.

A Calibrated Conversion of ADC to Photoelectrons

The light injection system is used to measure the gains of each ADC value in order to associate a given ADC value with a number of photoelectrons incident on the PMT. The strip ends are pulsed with light corresponding to about 50 photoelectrons per pulse at a rate of 300/hour in the Far Detector and 1000/hour in the Near Detector. The amount of signal actually measured for a given PMT pixel can be as much as two times more or less than the 50 photoelectrons, due to differences in the injection fibers, the readout fibers, and the PMT efficiencies.

The gains can change over time. Seasonal variations are less than 3% per year, and shorter term variations are even less due to the environmental controls of the detector halls. The variations are measured using the light injection data and photon statistics [49][50].

The number of photoelectrons incident on the PMT is related to the number of ADC counts measured by the electronics and can be calculated using Poisson statistics. If λ is the number of photoelectrons incident on the photocathode of the PMT and μ is the

number of measured ADC counts, then the gain of the system is

$$G = \frac{\mu}{\lambda} \tag{3.1}$$

The number of measured ADC counts for a given amount of light injected will form a spectrum due to the Poisson statistics, with an RMS of

$$\begin{aligned} \sigma_{tot}^2 &= \sigma_{PE}^2 + \sigma_{1PE}^2 + \sigma_{ped}^2 \\ &= \left(\sqrt{\lambda}G\right)^2 + \left(\sqrt{\lambda}Gw\right)^2 + \sigma_{ped}^2 \end{aligned} \tag{3.2}$$

where contributions are taken for the RMS of the creation of the photoelectrons on the photocathode (PE), for the width of the single photoelectron peak (1PE), and for the electronics noise and resolution, or pedestal (ped). The single photoelectron peak is an easily identifiable feature of the PMT and electronics system and corresponds to a single photoelectron incident on the photocathode. This peak is isolated in the ADC count distribution and the width of the peak, w, is easily measured. This width can be attributed to the fact that the PMT response to an incident photoelectron is actually the sum of the responses in the cascade of photoelectrons from the photocathode to each following dinode.

Combining equations 3.1 and 3.2, it is possible to obtain an expression (equation 3.3) for the gain and the number of photoelectrons for a given light injection sample as a function of the measurable parameters (ADC spectrum RMS (σ), pedistal RMS (σ_{ped}), single photoelectron RMS (w), and mean ADC value (μ).

$$\begin{aligned} \sigma_{tot}^2 - \sigma_{ped}^2 &= \tfrac{\mu^2}{\lambda} + \tfrac{\mu^2 w^2}{\lambda} = \tfrac{\mu^2}{\lambda}(1 + w^2) \\ \lambda &= \tfrac{\mu^2}{\sigma^2 - \sigma_{ped}^2}(1 + w^2) \\ G &= \tfrac{\mu(\sigma^2 - \sigma_{ped}^2)}{(1+w^2)} \end{aligned} \tag{3.3}$$

Linearity Adjustment (ADC to SigLin)

In both detectors, the PMT and front end electronics displayed non-linear response to signals over approximately 100 photoelectrons. In order to remove this non-linear behavior, it is necessary to convert the raw ADC values to linearity correctly ADC values (called "SigLin"). Once a month, light injection data is taken over a range of injected light intensity (with 1000 pulses at each light level) in order to gather a sample for this correction.

The non-linear response is different in each detector due to the specific PMT type and the differences of single verses doubled ended readout. The Near Detector uses a quadratic fit to model the correction. The Far Detector makes use of the fact that the fibers illuminated from the light injection on the side of the LED all go to the same PMT pixels whereas the same fibers each map to a different PMT pixel on the other side of the detector. The non-linear response of the pixel near the LED receiving light contributions from multiple fibers is then corrected to the average linear response of the activated pixels of the corresponding fibers on the other side of the detector.

A correction for detector response drift over time is also applied at this stage of the calibration. A sample of cosmic muons collected over a period of 24 hours is used to form a set of data specifying the median pulse height per plane over the time period, m_t. The cosmic events used must have a reconstructed track, must not be recorded during beam spills or light injections, must be less than 70° off of the beam axis, and must have been triggered by hits in 4 of 5 consecutive planes. The energy recorded in each hit along the track is scaled based on the angle off of the beam axis because a muon traveling at a greater angle to the beam axis traverses a longer distance in a scintillator strip and thus deposits more energy. The first and last hits of the track are not used as to eliminate reconstruction discrepancies. Only hits directly associated with a track are considered in order to avoid the effects of sporadically placed delta rays. Additional constraints are placed on the cosmic

events, requiring them to be of sufficient distance from the edge of the detector and coil hole. All hits are then adjusted to an arbitrarily chosen reference time period, which has been set at about six months after data taking began ($m_{t=0}$ is 00:00:00 on December 1st, 2005). The uncalibrated pulse height p_{unc} is then adjusted to obtain the calibrated pulse height, p_{cal} by

$$p_{cal} = p_{unc}\frac{m_{t=0}}{m_t} \tag{3.4}$$

Strip to Strip Calibration (SigLin to SigCor)

The linearity adjusted signal (SigLin) is then adjusted to account for the strip to strip response to obtain the strip correlation adjusted signal (SigCor). The difference between strip responses arises from scintillator light output (due to construction, assembly, and composition) and the electronics between the PMTs up to and including the data acquisition units (from differences in the lengths of wires and the tolerances of the components used in the electronics assemblies, and the PMT and electronics response).

This adjustment starts with SigLin calibrated data from the cosmic muon sample for a specific time period. To that sample, an attenuation and path length correction is applied. This is used to calculate the average response of a strip to a muon passing through the center of the strip and perpendicular to the surface of the strip. The strips are then assigned an adjustment factor which will adjust the response of a given strip to match that of the calculated average strip.

The adjustment for Near Detector strips is calculated every month and varies by 30% within the calorimeter and by 33% in the spectrometer. The difference between two time periods is about 3.6% in the calorimeter and 7.2% in the spectrometer. The Far Detector adjustment is calculated every three months. As an example, the adjustment for a particular three month period has a range of 27.3% in that data set and an average

difference from the previous three month period of about 4.4%.

Attenuation Calibration (SigCor to SigMap)

The amount of light transmitted to the PMT by the wavelength shifting fiber will depend on the location along the strip where the interaction occurred because of the attenuation effects of the fiber. In both detectors, this correction is calculated from comic muons. The longitudinal position of the track along the strip is plotted relative to the energy deposited in the strip. A fit to a double exponential is used to make the correction. The attenuation is give by

$$A(x) = A_1 e^{-x/L_1} + A_2 e^{-x/L_2}$$

where L_1 and L_2 are attenuation lengths and A_1 and A_2 are the fitted parameters.

This correction also makes use of a data set which used a radioactive source to map the strip response along the length of each strip prior to the assembly of the planes.

Muon Energy Unit Calibration (SigMap to MEU)

This final step in the formal calibration chain is used to calibrate the three detectors (calibration detector, near, and far) so that the same particle (energy and momentum) traveling through each of the detectors will produce the same response. Steps to perform this calibration are explained in detail in [55] and will be summarized here. This step relies on a sample of stopping muons. Muons lose energy in the detector according to the Bethe-Bloch equation[33]. They typically deposit about 30 MeV per plane with the exception of the last few planes where the slow moving muon experiences rapidly increasing ionization. The energy deposited as a function of muon momentum is illustrated in 3.9.

It is not possible to accurately measure the momentum of the muon via a range measurement, which is only accurate to within 2% between the detectors. Instead, a track

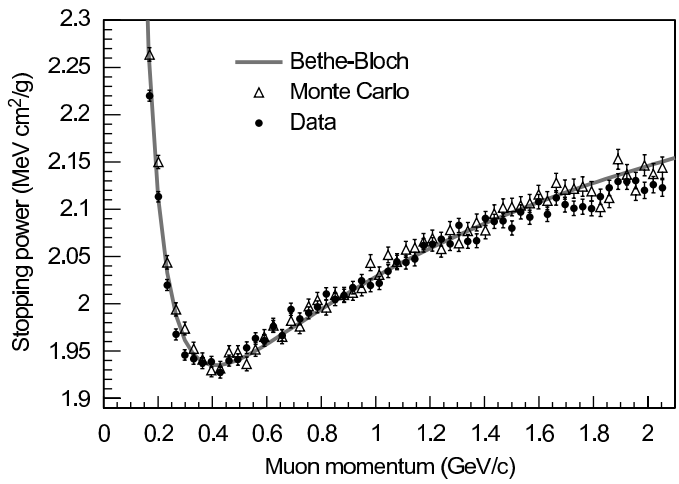

Figure 3.9: The stopping power for muons is shown as predicted according to the Bethe-Bloch equation along with the measured response from data and the simulated response from the GEANT3 Monte Carlo simulations. It is clear that the Bethe-Bloch equation nicely describes the actual physical behavior. The image is from [56]. The stopping muon calibration makes use of the linear region of energy deposition for muons with momentum between approximately 0.5 and 1.1 GeV/c.

window technique is used, where the section of the track corresponding to muon momentum between 0.0 and 0.5 GeV/c is discarded and only the section between 0.5 and 1.1 GeV/c is used. The small variation in dE/dx over this energy range corresponds to a total error of 0.2% in the measured energy deposition when the position of where the muon stopped is known to within 2%. The window used is 14 planes (83 cm) wide and is positioned to start 16 planes (95cm) from the position where the muon stopped.

The average energy, as measured in SigMap, deposited over the strips in the window is measured. The measurement includes a path length correction for muon tracks which are not perpendicular to the face of the plane. A sample of these muons is collected and the median of that value is taken as a MEU to SigMap calibration factor, where the MEU (Muon Energy Unit) is the average amount of energy deposited by a muon in a plane traveling perpendicular to the plane.

Absolute Energy Calibration

At this point, the detectors have been calibrated so that a unit of measured energy has the same meaning between the detectors and so that the unit of measured energy is proportional to commonly used units of measure (such as GeV). An adjustment factor is calculated from the calibration detector test beam data which converts MEUs to GeVs. This factor is later used in the decalibration steps of data simulation. It is not used to determine the energy of a reconstructed event in this analysis.

3.2.4 Cross Talk

As previously mentioned, the Near and Far Detectors each use different PMT devices with different numbers of pixels. PMTs with multiple pixels can have cross talk, which is defined as an input signal on a given pixel resulting in an output signal corresponding to a different pixel. The Far Detector multiplexes the signals from eight different strips onto one single pixel. This configuration introduces a difference in the PMT cross talk between the Near and Far Detectors, as the Near Detector has each scintillator strip assigned to a unique PMT pixel. The cross talk can appear in two forms[50]. Optical cross talk occurs when light from a fiber shines on an adjacent pixel including (or instead of) the one that it is actually connected to. This can most often be caused by an improperly placed or misaligned fiber. There is also a certain amount of electrical cross talk present on all pixels caused by electrons leaking from one dynode chain to another.

A discrepancy in the optical cross talk between the data and the simulated events has previously been shown to introduce substantial errors[57]. Attempts to remove optical cross talk from the Far Detector data by making use of the double ended readout in a software based filter[58] were not substantially successful. However, optical cross talk can be measured with cosmic muon events. When properly modeled, the effects of this phenomenon

in the simulated data are drastically reduced[59].

3.2.5 Storing Data

Once data is read out of the detector, it is stored temporarily on computers located at the detector site. The data files are then moved over the internet to Fermilab, where they are stored in a PNFS tape robot archival system. The files are also made available for analysis on a high capacity disk storage system (dCache)[60]. In the event of a network outage, the local detector storage is able to cache the data files for a number of days, until the network again becomes available.

3.3 Simulated Data

For an experiment that is attempting to measure the effects of neutrino oscillations, which are based on a theoretical model, it is first important to understand what observation is expected both in absence of oscillations and in the presence of oscillations in the vicinity of the known parameters. These predictions can then be compared to the measured data and an agreement or discrepancy can be interpreted as an indicator of the underlying phenomena.

The expected event rate and spectrum in the Far Detector after oscillations is the end result of a multiple step simulation and prediction process, which is broken into distinct parts. This chapter will cover the first of the parts including the simulation of the neutrino beam, the neutrino interactions, and the detector response to these interactions.

All simulated data used in this analysis is in the form of Monte Carlo. This term is used to describe a method of generating a sample of events which have properties that are based on measured probability distributions from data of particular physics phenomenon as measured in other experiments. The general procedure to generate a simulated event

involves using a random number to extract a set of parameters describing an event from the allowed range of values, while simultaneously calculating the probability that an event with those chosen parameters could actually occur. Following such a procedure, a large sample of Monte Carlo generated events can be accumulated. When the events are weighted by the probability that they will actually occur, the resulting Monte Carlo sample closely resembles the parameter distributions which provided the inputs to the simulation.

3.3.1 Simulating the Neutrino Beam

The production of pions and kaons in the NuMI target is simulated using `FLUKA05` Monte Carlo[61]. This code is responsible for simulating the collision of the 120 GeV protons from the Main Injector on the carbon NuMI target. The output of this program is a list of particles produced during the simulated beam pulse, including the energy and momentum of these particles. Any particles exiting the target are recorded and then passed to a `GEANT3` [62][63] simulation of the NuMI beam line. This simulation takes into account the magnetic field of the focusing horns, the decay pipe, and the material of the beam line and horns including that surrounding the target hall and decay pipe. As the particles step through the `GEANT3` simulation, they are allowed to decay. Any decays resulting in a neutrino are recorded for further use. This combination of `FLUKA05` and `GEANT3` is often referred as a single step of Monte Carlo generation is and termed `GNuMI`.

The neutrinos from these decays are assigned an energy governed by the decay kinematics. For two-body relativistic decays of π/K$\rightarrow$ $\mu + \nu$, the neutrino energy, E_ν, is given by

$$E_\nu \approx \frac{(1 - \frac{m_\mu^2}{M^2})E}{1 + \gamma^2 \tan^2 \theta_\nu}$$

where m_μ and M are the muon and parent hadron masses, E is the parent hadron energy, $\gamma = E/M$ is the parent's Lorentz boost, and θ_ν is the angle in the lab between the neutrino

and the parent hadron[45]. These neutrinos are forced to pass through either the Near or Far Detector, depending on which detector the Monte Carlo is being generated for. The probability for such a decay to occur, resulting in a neutrino that passes through the chosen detector is

$$\frac{dP}{d\Omega_\nu} \approx \frac{1}{4\pi} \frac{4\gamma^2(1+\tan^2\theta_\nu)^{3/2}}{(1+\gamma^2\tan^2\theta_\nu)^2}$$

In both equations $\beta = \sqrt{1-(1/\gamma^2)} \approx 1$. The probability of the event to occur is recorded and is later used as a beam weight on the simulated events. The distribution of the beam weighted simulated events will closely resemble the spectrum of the actual data.

The dominant uncertainty in the flux in both detectors is caused by an uncertainty in the production of the hadrons off of the target. A method to minimize the uncertainty by tuning the Monte Carlo to data was created[64] and is referred to as SKZP tuning. This uncertainty can be parameterized in terms of p_t and p_z. This, and the other beam uncertainties have the same effect in both detectors. The events observed in the Near Detector are used as a way to constrain the uncertainty of the flux predicted in the Near Detector. This in turn provides a correction for and reduces the systematic uncertainty of the flux in the Far Detector. Using the different beam configurations, as listed in table 3.1, it is possible to probe various regions of (p_t, p_z), thus providing data that is used in the constraining fit. The constrained neutrino fluxes of both detectors are then used as inputs for generating the simulated neutrino interactions within the detectors. An illustration of the effect of this data based adjustment to the `FLUKA-GEANT` flux is shown in figure 3.10 as the predicted ratio of far to near ν_μ flux both before and after the tuning.

3.3.2 Simulating Interactions in the Detectors

Once the flux of different neutrino types at each detector is known, it is necessary to simulate the interaction of these neutrinos with the detector.

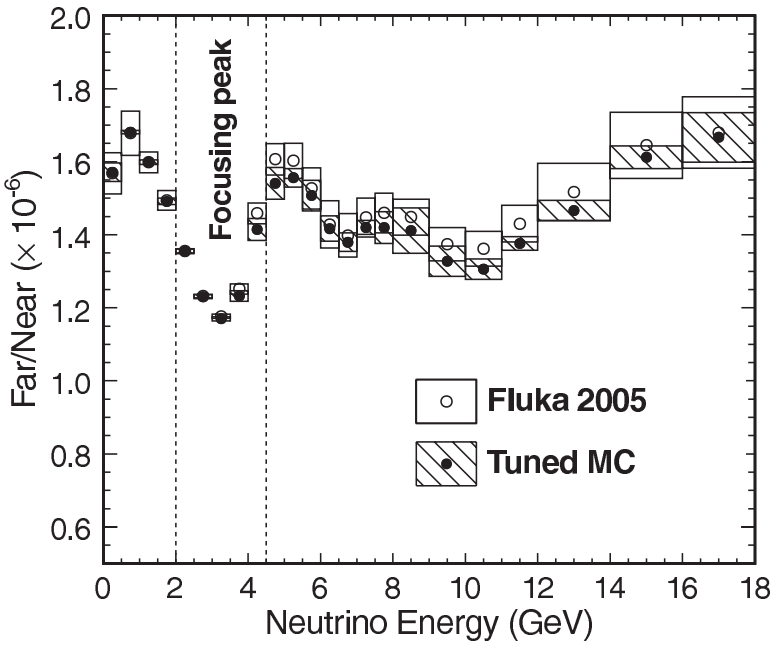

Figure 3.10: The flux ratio (far/near) from FLUKA before and after near data tuning. Image is from [42].

Every neutrino which has been generated by `GNuMI` which passes through the detector is made to interact at a randomly chosen location within the detector. The probability of the interaction actually occurring, based on the neutrino interaction cross section, is also recorded and is later used to give a weight to events so that any simulated measured quantities would be representative of actual data. Simulated events are then combined into files which contain the correct number of weighted events for some reported exposure (in POT). Neutrino interactions are also simulated in the rock of the cavern surrounding each detector. The muons generated in these interactions can reach the detector. However, such events do not generate a measurable background for this analysis, because the particles reaching the detector do not have a reconstruction event vertex located within the fiducial volume and are discarded.

There are a number of steps to simulate the data in the detectors. First, a neu-

trino with a given flavor, energy, and momentum is made to interact with an iron nucleus. The simulation determines how much energy is to be transfered to the outgoing lepton or neutrino, depending on if the event is chosen to simulate an CC or NC type interaction. Also determined is how much energy is transfered via the weak interaction boson ($W^{\pm}$ or Z^0) to the iron nucleus, and what resulting particles (and their momenta and energies) are generated as a result of the interaction. The particles generated by this interaction simulation must then be allowed to interact with the other particles of the nucleus where the interaction occurred. Finally, the particles which have exited the target nucleus are propagated through a simulation of the detector and the energy deposited by these particles in the detector is recorded. The energy deposited must then be interpreted as energy deposited in the scintillator strips along the paths of these particles.

Simulating the Interaction

An interaction in the detector is simulated as a function of incident neutrino energy and type. The energy of the outgoing lepton in a charged current interaction (or neutrino in a neutral current interaction) is randomly chosen and the probability of such an interaction is recorded. The more difficult part of the interaction to model is the hadronization model which simulates the interaction of the weak interaction boson ($W^{\pm}$ or Z^0) with the iron nucleus[2]. The hadronization model used in the MINOS experiment to simulate the neutrino interactions is based on `NEUGEN`[65] (Neutrino Event Generator). Originally designed for the Soudan 2 experiment, `NEUGEN` attempts to simulate the neutrino interactions at low energies using an extended version of the KNO[66] model. At higher energies, the simulation relies on `JETSET`[67] which uses the full perturbative quantum field theory treatment of

[2]The interaction is primarily modeled for neutrino interactions with iron, because most of the interactions (95% by detector weight) will occur in the iron. Interactions with scintillator strips also occur and are included proportionately.

parton interactions. For intermediate energies, events are weighted such that there is a linear transition from fully using the KNO model up to energies of 2 GeV to a full use of the `JETSET` simulation for energies above 3 GeV. The combined use of these two different simulation softwares, in addition to some some other improvements, is the basis for the AGKY interaction simulation used in the MINOS experiment[68].

The `NEUGEN` code is able to simulate different neutrino scattering processes. For low energy neutrinos (<1 GeV), quasi-elastic (QE) scattering is the dominant process, and the cross section of this process is expressed in terms of the weak form factors, using a dipole form for the axial form factor with $F_A(0) = -1.25$ GeV/c^2 and $M_A = 1.032$ GeV/c^2 and using a pseudo-scalor form factor which is negligible for all but ν_τ scattering[65]. Resonance production (RES) uses the Rein and Seghal model[69], dominated by the $\Delta(1232)$ at low energies. This model neglects the lepton mass, resulting in an extension of the model to accommodate for ν_τ interactions through a reduction in phase space for these events. Deep inelastic scattering (DIS) [70] is calculated in terms of five structure functions using parton distributions accessed through the `PDFLIB` libraries[71].

Coherent pion production (COH) is also simulated. Although the cross section is small, the production of a π^0 is an important background to the $\nu_\mu \rightarrow \nu_e$ appearance analysis, as the π^0 quickly decays into two photons which create and electron like electromagnetic shower. This type of scattering is also determined with the Rein and Seghal model [72]

Other interactions are also considered by this simulation, but will not be discussed here as they do not have a significant impact to this analysis.

The simulation of each of these scattering mechanism must be combined in the proper proportions to ensure that the overall simulation agrees with measured data. Bubble chamber data is used to constrain this simulation in order to gain good agreement between the code and the observed physics[68].

The hadronization in all scattering cases is based on KNO scaling. This relies on the fact that the final state multiplicity can be defined as a function of W. For a given interaction, the final state multiplicity is first determined. Then `NEUGEN` can assign particle types based on this chosen multiplicity. For example, for charge-neutral pairs, particles are assigned as $\pi^+\pi^-$ (60%), $\pi^0\pi^0$ (30%), K^+K^- (5%), and $K^0\bar{K^0}$ (5%)[65].

Recently, there has been a lot of work in the field to develop a multiple purpose and all model inclusive neutrino event simulation. Named `GENIE`[73], this software provides an interface to various existing simulators and algorithms. Each algorithm to be considered in the simulation is selected by the end user in a configuration file. The algorithm defines what type of events it is supposed to generate, the cross sections of such events, and other details. When simulating a single event, `GENIE` will randomly select the type of interaction and the algorithm to use based on the incident neutrino energy and known branching ratios. The use of this new technology streamlines neutrino event simulation and has recently been incorporated into MINOS, where it has proven to work well and has been shown to give equivalent results to the previous method used in directly interfacing with `NEUGEN`. While not used in this analysis, it is important to introduce `GENIE`, as this analysis is one of the last neutrino experiment analyses which will not be using this software.

3.3.3 Modeling the Detector Response

`GEANT3`[62] is used to simulate the passage of particles through the detector. A software model of the detector is first made which includes descriptions of the materials present, including the density of various atomic elements in a structure and the size and location of each of these structures. This description includes the detector (iron, scintillator, electronics racks, walkways, etc), the air around the detector, and the rock surrounding the experiment hall. In additional to material descriptions, the properties of the magnetic field

from the energized detector coil are also included in the description.

Obtained from the `NEUGEN` simulation software is a list of particles produced in a given neutrino interaction and the energy and momentum vector for each particle. Each of these particles is discretely stepped through the simulated environment, being allowed to interact with the material that it is passing through based on well known interactions[33]. These particles deposit energy until their energy has been exhausted, until they decay, until they are captured by the material, or until they exit a region defined around the detector where it is no longer necessary to record interactions because they are no longer able to effect the measured quantities in the detector. A summary of the energy (in GeV) deposited in each scintillator strip is recorded.

Decalibration

The simulation is not yet complete, as a measurement of energy deposited in a strip is not representative of actual data. The detector used in the simulation is an ideal detector. It is therefore necessary to modify this simulated data to add in the exact features that the calibration corrects for in the actual data. It is also necessary to convert the energy deposited in each strip (in GeV) to a number corresponding to a raw ADC signal so that the simulated data will resemble the actual data taken from the detector as to provide a means to check the calibration procedure. This step of decalibration is almost identical to the calibration steps, only applied in reverse. The combined application of decalibration and then calibration on simulated data will produce a sample which closely resembles the calibrated data set. Each simulated data file processed is assigned a random start time during which there are valid calibration constants recorded. Each of the events in a single file are spaced 1.9 seconds apart. This time assignment to the simulated data ensures that all measured time dependent calibration constants appear in the simulated data.

The energy in each strip is converted from GeV to MEU using the inverse of the calibration absolute energy scale step. The MEU are converted to photons generated by the interaction. These photons are propagated along the wavelength shifting fiber, accounting for attenuation, light level shifting, strip gain, and strip to strip correlation effects, resulting in a number of photons incident on the PMT. Poisson statistics are used to obtain the number of photoelectrons incident on the photocathode from the number of photons reaching the PMT. The number of photoelectrons is then converted to a raw ADC signal by compensating for the PMT gains and by putting in the non linear behavior of the PMT and readout electronics.

3.3.4 Oscillation Weights

In the Near Detector, the neutrino flavors available from the beam simulation ($\nu_\mu/\overline{\nu}_\mu$ and beam $\nu_e/\overline{\nu}_e$) represent the types of neutrinos that will be passing through the detector. However, an additional step is needed to adjust these neutrinos prior to simulating their interaction in the Far Detector in order to account for potential oscillations. Separate files are generated to include the neutrinos from the beam simulation which are either not oscillated, or which have been oscillated from ν_e or ν_μ to either ν_e, ν_μ, or ν_τ. In each of these files, information about the original and oscillated neutrino flavor, along with the neutrino energy for each of the simulated events is retained. This process allows for the reweighing of the events during the analysis so that a sample of Far Detector Monte Carlo can be generated without the need to simulate the events for each set of hypothetical oscillation parameters.

3.4 Batch Processing and Standard Data Reconstruction

Both data and Monte Carlo raw files need to be processed so that the information contained within them is available to the scientist in a convenient format. The files are processed in a batch system using a set of over 100 computers in the Fermilab General Purpose Farm[74].

The reconstruction of a file of either actual data or Monte Carlo events is achieved through the following steps. The data recorded in each electronics channel (or "digit") must be separated in time and associated with a beam spill trigger. The digits associated with a particular beam spill trigger are considered to be part of the same "snarl". The Far Detector also includes the additional step required to demultiplex the information recorded in the digits to the corresponding strips. The information about the nonzero energy deposited in each strip, and parameters describing these strips (including position, plane number, and view) is recorded into objects called "hits".

The data in each snarl must then be divided into separate events. The hits in each snarl are grouped based on their location within the detector and the time at which the energy deposition was recorded by the front end electronics. This separation of a snarl into a list of events is called "slicing". Each event is actually a group of hits in a four dimensional slice of the data. The slicing process is important in the Near Detector, where as many as twenty events may be present in a single spill. Slicing in the Far Detector is still important even though only about one neutrino interaction is expected per day since there is large amount of non beam induced activity from cosmogenic sources and from muons resulting from neutrino interactions in the rock surrounding the detector.

A track finding algorithm looks for isolated hits which fall on a line. A quadratic fit is used to expand that line to encompass as many hits between the front and back of the

event as possible. The information contained in these hits is used as a seed for a Kalman filter. The filter is used to fit the track and to determine the position and momentum of the muon. If a good fit on the track is obtained, a second pass looks for additional hits that should be associated with the track. The strips which remain after all tracks are identified are then grouped into shower objects, which are just spatially isolated regions of hits. The tracks and showers which are found for a given event are included in event data object. The event object also records other basic information, such as the time when the event was recorded, and the beam and detector conditions at that time. Summary event information is also stored, such as the total number of strips found in the event, the sum of the energy of the strips in the event, and the number of reconstructed track and shower objects. Monte Carlo files then undergo the additional step of matching the information used to simulate the interactions to the corresponding resulting reconstructed events. The resulting reconstructed Monte Carlo files conveniently contain both the reconstructed event information as well as the information describing the true interaction that was responsible for the generation of the reconstructed event.

3.5 Considerations for the Measurement

The measurement of $\nu_\mu \rightarrow \nu_e$ oscillations requires the identification of ν_e events. The charged current interactions of ν_e are generally characterized by a electron, and the identification of an electron in the event is the best way to identify a signal candidate.

In ideal QE ν_e events, the electron receives most of the incoming neutrino energy, and the recoiling proton is not visible in the detector. Such events have a single electromagnetic shower and are easy to identify. Sometimes, the recoiling proton will be energetic enough to deposit energy in a few strips within the detector. Depending on the location

of this energy deposition, the strips corresponding to the proton may be distinguishable from the strips corresponding to the electron. However, due to the coarse resolution of the detector, it is not possible to perform a kinematic measurement of these events.

The RES ν_e events will also produce an electron, in addition to multiple pions resulting from the Δ resonance decay. Charged pions may deposit energy in a muon-like track. Neutral pions will decay into two photons and will produce an electromagnetic shower. In cases where the electron does not carry most of the incoming neutrino energy,the additional pions may have the effect of making the event look either like a ν_μ CC event (due to charged pion tracks) or like an electromagnetic event which does not have a good electromagnetic fit (due to electromagnetic showers from multiple sources).

When a large amount of energy is transfered to the target nucleus, as is common in DIS events, the electron may carry only a fraction of the visible event energy. Again, multiple neutral or charged pions may be generated, although with greater energy than in the RES events.

Events classified as ν_e coherent pion production also occur, though infrequently. Such events are not used to make decisions about classifying events, and are only taken into account when actually predicting the observed data spectrum.

The selection of signal ν_e events as described must compete with background events.

The interaction of a ν_τ produces a τ which decays to an electron. The vertex displacement of the electron is not measurable due to the low resolution of the detector. The hadronic shower associated with the event is indistinguishable from the shower produced by a ν_e interaction. The ν_τ background is mostly irreducible. Fortunately, there are not many ν_τ events present in the data sample.

The charged current interaction of a ν_μ generally produces a long muon track

which is easily identified. However, it is possible for most of the neutrino energy to be transfered to the hadronic shower in a high-Y interaction. In such cases, the muon track is short enough to be comparable to that from a charged pion in a ν_e DIS hadronic shower. If the hadronic shower includes an energetic neutral pion, an electromagnetic shower may be generated creating another irreducible background.

Neutral current interactions only contain a hadronic shower. They are not dependent on the energy of the incoming neutrino and instead are dependent only on the energy transfered to the target nucleus. Again, if the hadronic shower contains a neutral pion decays and generates a electromagnetic shower, the event will be part of the irreducible background.

The previous analysis[75] used an event selector which was trained to select only QE ν_e events. Other events that were selected as ν_e candidates were done so by their similarities (low-Y) to QE ν_e events. The event classifiers described in chapter 5 are trained to select all types of ν_e events, although the variables used to do so are only intended to correctly describe QE ν_e events. The method presented in chapter 6 goes a step further and not only attempts to classify all types of ν_e events, but attempts to do so by identifying the various parts of the hadronic shower. This method allows for the proper treatment of all types of ν_e signal events.

Chapter 4

The Analysis

4.1 The Procedure

A summary of the analysis procedure will be given here, although the details of this procedure will be covered in a number of chapters. In order to measure $\nu_\mu \rightarrow \nu_e$ oscillations, it is necessary to

- Have data and Monte Carlo samples for both detectors.
- Be able to weight the Monte Carlo events so that they are representative of the neutrino beam spectrum of the actual data.
- Possess the ability to classify signal (ν_e) candidate events through the use of particle identification functions, described in chapters 5 and 6.
- Understand the event composition in the Near Detector, so that the components of the beam can be individual oscillated in order to provide a prediction for the Far Detector data, as described in chapter 8.

This analysis is carried out as a blind analysis. This means that the Far Detector data which contains the signal event region will not be looked at until the final measurement is to be made. The purpose of this procedure is to eliminate the possibility of prior knowledge of the content of the signal region leading to an unintentional biasing of the procedure used which would then produce potentially inaccurate results. Although the region of the

Far Detector data sample containing the signal is unavailable for study prior to the final measurement, there are regions of the Far Detector data that can be used as a confirmation of the method without the possibility of observing signal events. These "side-band" studies will be covered in chapter 10.

4.2 Preparing the Data

The first step in the analysis is to obtain samples of Monte Carlo and data for each of the detectors. The samples are restricted to ensure the quality of the events for a number of reasons which are briefly mentioned and will be discussed in detail later. The detectors must be operating in a normal data taking mode and must be functioning correctly at the time when the data is collected. These samples must be filtered as to remove all events but those originating from beam neutrino interactions. Those events are then required to be contained within the instrumented part of the detector. Finally, some simple cuts are made to eliminate as much background as possible without excluding any of the possible signal events.

All samples at this point in the discussion have already undergone the batch reconstruction, as described in section 3.4. The data taken from each spill have already been sliced into events prior to the reconstruction, and so further discussion for the rest of this document will be limited to the handling of each individual event.

4.2.1 Data Quality

A number of restrictions are applied to the raw data to ensure the quality and consistency of the sample. This step only effects the data samples, as the Monte Carlo is only generated assuming properly functioning detectors and beam.

The first requirement is that the event occurred during a period of good beam.

This means that the event can be associated with a particular spill for which there is information recorded in the database, such as the number of protons in the spill. The beam is only considered good if the horns are operating at the correct current for the beam configuration. The detector coil must be of sufficient voltage and current, and the field must be in the proper direction.

The Far Detector also requires that the event does not occur during a period of light injection and that the event occurs no more than 20 μs before and no more than 30 μs after the spill trigger.

4.2.2 Fiducial Volume Restriction

The physical location of the neutrino interaction vertex for each event within the detector needs to be determined. This calculation is simple if a track is found in the event, in which case, the event vertex is taken to be the track vertex. In the case where no track was reconstructed, the event vertex is, in z, the furthest upstream hit in the set of continuous hits in the event, and in the transverse plane, the energy weighted position of the hits in the event.

A restriction on the event vertex is made to ensure that the event is in a fully instrumented region of the detector and that the event is sufficiently far from the edge of the detector and the coil hole (in the Far Detector) and sufficiently far from the partially instrumented region (in the Near Detector). An event which is too close to one of these boundary regions has a chance of a substantial amount of event energy exiting the detector without being recorded. This would result in a partially reconstructed event from which no accurate information could be determined.

The fiducial volume region is defined as the space within the instrumented region of the detector which has a consistent response to events. A study designed to maximize

the fiducial volume[76] determined that the number of events per unit time per unit area in the detector was a constant within the fiducial volume region as defined in table 4.1. The study found that it was not possible to increase the size of the fiducial volume without suffering a partial loss of events on the edges of the volume.

Detector	Center of Fiducial Volume (x,y)	Inner Radius	Outer Radius	Z boundary
Near	(1.4885,0.1397)	0	0.8000	[1.01080, 4.99059]
Far	(0,0)	0	3.7417	[0.49080, 14.29300] or [16.27110, 27.98270]

Table 4.1: The specifications of the fiducial volume regions of each detector. The two regions of acceptable z position in the Far Detector correspond to the two supermodules. All units are in meters. The volumes are cylindrical, with the center axis of the cylinder parallel to the z axis of the detector.

4.3 ν_e Candidate Event Energy Calibration

As previously mentioned, the energy in each detector is calibrated to GeV units with the calibration detector data. The amount of energy deposited in each strip is then well known in terms of GeV. However, if the sum of the energy deposited in the strips from a ν_e candidate event is taken as the event energy, a good agreement with Monte Carlo is not achieved. This is due to the fact that most ν_e candidate events deposit a fraction of their energy into a recoiling proton or other low energy hadronic activity which is often not recorded in the scintillator strips, but which instead is deposited primarily in the iron planes.

A separate calibration is used for the ν_e candidate events in each of the detectors. A linear fit is made on reconstructed event energy in MEU to true neutrino energy using Monte Carlo ν_e QE CC events[77]. The constants obtained by this fit are then used to convert the total reconstructed energy of a ν_e candidate event in MEU to GeV. Any uncertainty

introduced by this additional energy calibration step is accounted for by the relative energy scale calibration systematic.

4.4 Signal Selection

The oscillated signal ν_e events need to be sufficiently isolated from the background so that a measurement of neutrino oscillations can be accurately made.

The first step in this process is to apply a number of cuts which are intended to remove background events that are easily differentiated from signal events. This process is called "preselection". These cuts aim to remove events which have an energy outside of the region of interest where oscillations could not occur. They also remove events which have a clearly identifiable muon track which indicates a ν_μ CC background event.

- The event is required to extend at least 5 planes, thereby removing the neutron background events.
- The event must not be a cosmic event. Cuts are applied in an attempt to remove any cosmic rays that might be present. There is a possibility for cosmic rays to traverse the detector in the same time window as the spill trigger. Any reconstructed event that has a track that travels more than 0.6 meters in y or that has a track having an angle off of y satisfying $\cos y < 0.6$ is rejected as a possible cosmic event because it is not parallel to the beam. Likewise, if the event has a shower and the slope of a line fit to the energy weighted hits of the shower has a slope relative to the z axis > 10, the event is also rejected as a possible cosmic. These cuts were chosen[78] to eliminate possible cosmic events in this analysis, so care has not been taken to ensure that they do not also remove beam ν_μ events.

- The event is required to have a reconstructed shower, as events with only a reconstructed track would signify a ν_μ CC interaction. The effect of the shower cut is shown in figure 4.1(a). In the Far Detector, the event is required to be the largest energy event in the spill, as it is highly improbable that two neutrino interactions could occur in the same spill[1]. This final cut serves to remove any remaining low energy background or other noise. If an event has a track that is sufficiently small, it is possible that the track is due to a muon from the hadronic shower of the event, rather than from the neutrino to lepton conversion. In this case, the event should not be classified as a ν_μ CC and should not be removed by the track cut. The track planes cut requires that an event with a track must have a track that is less than 25 planes long. The track like planes cut requires that no more than 15 of the planes in the track can fall within the energy range of a typical muon. These two cuts efficitively remove muons with energy greater than 2 GeV. An illustration of the effect of the track planes and track like planes cuts on Far Detector Monte Carlo is shown in figures 4.1(b) and 4.1(c).

- The energy of the reconstructed event is constrained to be between 1 and 8 GeV. No oscillated ν_e events are expected outside of this energy range. Also, below 1 GeV, events do not contain enough information for an accurate reconstruction and identification. The energy cut is illustrated in figure 4.1(d).

After application of these preselection cuts, a significant portion of the background has been removed while almost all of the signal has been retained, as illustrated in figure 4.2 for both the Near and Far Detector (assuming oscillations at the CHOOZ limit with $\sin^2(2\theta_{13}) = 0.15$ and $\delta_{CP} = 0$). Prior to the application of the preselection cuts, the signal

[1]Beam induced events occur at a rate of about 1.9 per day, and an oscillated ν_e is expected at a rate of about 1 every 32 days

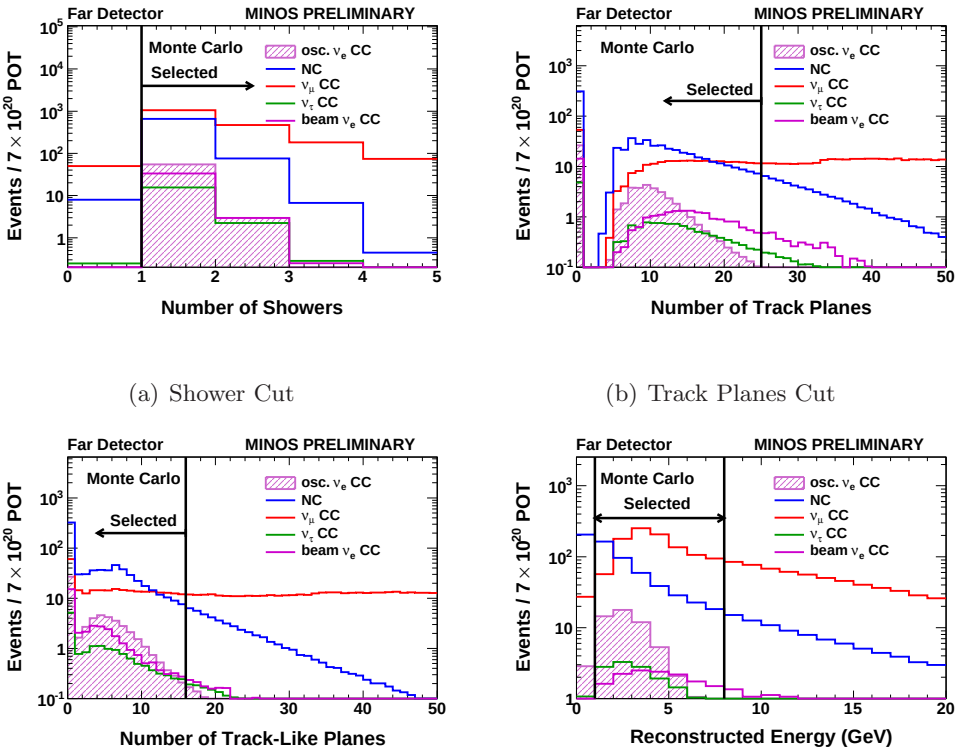

(a) Shower Cut

(b) Track Planes Cut

(c) Track Like Planes Cut

(d) Energy Cut

Figure 4.1: An illustration of the effect of the various preselection cuts on the signal ν_e events and the background components in the Far Detector MC. The events are required to have a reconstructed shower (a). Events with long muon tracks are eliminated with a track planes (b) and a track like planes cut (c). The events are required to have an energy in the region where oscillations are expected to occur (d).

to background ratio is 1:42 in the Far Detector. After the preselection cuts have been applied, the signal to background ratio has improved to 1:9 in the Far Detector.

Near Detector Monte Carlo						
Cut Level	Signal ν_e	Total Background	NC	ν_μ	ν_τ	Beam ν_e
In Fiducial Volume	-	256044.52	56463.60	195922.41	-	3658.51
Event has >5 planes	-	175797.61	33971.20	138504.37	-	3322.04
Passes Cosmic Cut	-	175797.61	33971.20	138504.37	-	3322.04
Has a shower	-	169664.77	33327.63	133052.28	-	3284.85
Track plane cut	-	60323.75	27498.45	29982.96	-	2842.34
Track like plane cut	-	53654.68	26266.10	24597.53	-	2791.05
$E > 1$ GeV	-	50278.72	24284.49	23220.00	-	2774.22
$E < 8$ GeV	-	42789.88	20125.42	21289.22	-	1375.23
Far Detector Monte Carlo						
In Fiducial Volume	63.61	2676.88	741.57	1881.38	18.86	35.08
Event has >5 planes	54.38	2035.65	472.28	1513.32	15.93	34.12
Passes Cosmic Cut	53.33	2025.60	465.07	1510.60	15.80	34.12
Has a shower	53.30	2003.09	462.01	1491.40	15.57	34.12
Track plane cut	52.74	662.83	394.67	224.92	12.83	30.40
Track like plane cut	52.27	610.94	380.31	188.20	12.26	30.16
$E > 1$ GeV	51.50	582.53	356.93	183.54	11.98	30.07
$E < 8$ GeV	49.65	459.93	286.88	150.72	9.96	12.37

Table 4.2: The number of events after each cut level for the raw Near and Far Detector Monte Carlo. The cuts are applied sequentially. The signal in the Far Detector assumes oscillations at the CHOOZ limit with $\sin^2(2\theta_{13}) = 0.15$ and $\delta_{CP} = 0$. The Near Detector Monte Carlo is normalized to 1×10^{19} POT and the Far Detector Monte Carlo is normalized to 7×10^{20} POT.

Chapter 5

Event Identification

Events which have passed the preselection cuts now need to be identified. It is necessary to distinguish the signal ν_e events from the background events. Algorithms capable of distinguishing between different event types are known as Particle Identifiers (PIDs).

Three different PIDs are used in the analysis. One is used to obtain the primary result, and the other two are used to cross check that result. The general description of PIDs, including how they are made and what they look at will be described first, followed by a description of each of the PIDs that are used.

5.1 Event Variables

A number of variables are used in the identification of ν_e interactions. General properties of these events are as follows. The CC interaction of the ν_e will always produce an electron. Depending on the type of CC interaction (QE, RES, DIS), there will also be a recoiling proton, π^0, or other hadronic activity. However, not all of these particles are always visible in the detector. Additionally, in order to be individually distinguishable,

they must be of sufficient energy to traverse multiple planes and they must deposit enough energy to cause multiple hits in these planes.

The electron generated by the ν_e interaction will cause an electromagnetic shower. This essentially means that the electron will produce two photons, each photon will produce an e^+/e^- pair, the e^+ and e^- will each emit more photons, and so on. Every one of these particles will deposit some energy in the detector. The energy deposition of this shower is characterized by the following formula[33]

$$\frac{dE}{dt} = E_0\, b\, \frac{(bt)^{a-1} e^{-bt}}{\Gamma(a)}$$

where $t = x/X_0$, E is the energy deposited over a distance of x, E_0 is the original energy of the incoming particle, and X_0 is the radiation length of the material which is dependent on the atomic mass and atomic number of the material. The parameters a and b describe the shape of the shower.

Electromagnetic showers tend to have a narrow transverse shower profile as compared to the hadronic shower. Since the energy deposited from an electromagnetic shower is coming from a single parent particle, the shower shape is often described as more compact than that of a hadronic shower, which is comprised of interactions from a number of different particles. A measurement of the compactness of the shower can be made. The Moliere Radius is the radius of an imaginary cylinder which contains 90% of the shower energy. Usually calculated from a transverse projection of the event about the event vertex, this quantity can also be calculated with the axis along the center of the cylinder aligned to the axis of the shower.

5.2 Identifying Signal Events with an Artificial Neural Network

Artificial Neural Networks (or ANNs) are a type of event classification algorithm. Such software attempts to duplicate an organic brain, which is capable of being trained to produce an output based on a given set of inputs.

The ANN is comprised of levels of nodes. The nodes mimic neurons, each of which has a connection to all other nodes on the previous and following levels. The node takes in a numerical input, performs a calculation on it, and then sends the output to the nodes on the next layer. The first level of nodes has one node for each input variable, and the value of each input variable is the input to it's corresponding node. The last layer of nodes are the output nodes, and the value of each output node is taken to be the output value of the ANN. In the ANNs that we are concerned with there is only one output node; the value of which is interpreted as the probability that the input event is an oscillated ν_e event[1]. The layers between the input and output nodes are called "hidden layers" because they are not visible to the user. The connections between the nodes in adjacent layers mimic dendrites and are called a "weight matrix". Each connection between nodes has an assigned weight. Even though a node is connected to all of the nodes in the previous layer, it may only actually use the information from a subset of the nodes in the previous layer in its calculation. An illustration of the components of a simple ANN structure is given in figure 5.2.

The input value to each inner layer or output neuron is the weighted sum of the input values plus a bias for that neuron. For neuron j, the input value, x_j, is the bias weight

[1] In more complicated ANNs, it is possible to not only separate signal and background, but also to classify types of signal and background through the use of additional output nodes.

of the neuron, w_j, plus the weighted sum of each of the neuron outputs in the previous level.

$$x_j = w_j + \sum_i w_{ij} y_j$$

The calculated value at this node is then adjusted. If it is an output layer neuron, the value is scaled by a weight. If it is a hidden layer node, the sigmoid function is applied to the input value x_j.

$$y_j = \frac{1}{1 + e^{-x_j}}$$

The use of one or more hidden layers leads to a network structure that includes a linear combination of one or more sigmoid functions. Two important properties of this structure are that a linear combination of sigmoid functions can approximate any continuous function of one or more variables[79] and that training the ANN with an answer of 1 for signal and 0 for background leads to an approximate function which gives the probability that the values of the input variables correspond to a signal event[80].

The network is trained through an iterative process[81] over a set of Far Detector Monte Carlo events. The weights are initially set to random values between -0.5 and 0.5. An error is calculated for the network, e_p, for each test event, p.

$$e_p = \frac{1}{2}(o_p - t_p)^2$$

where t_p is the expected answer that the ANN is being trained to give (usually set to 1 for signal and 0 for background) and o_p is the output of the network. The minimization of the total error for the training set $E = \sum_p e_p$ over multiple iterations of the training set (called "epochs") leads to a trained ANN.

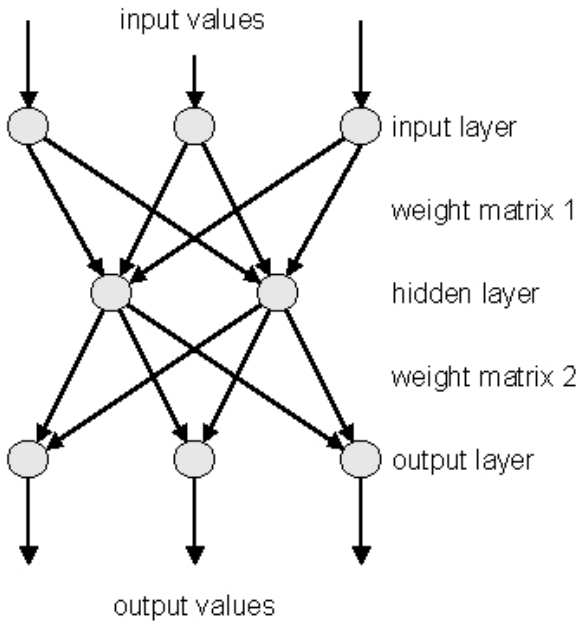

Figure 5.1: An illustration of a simple artificial neutral network (ANN)[82]. The values describing a given event provide the input values. One or more hidden layers are used. A weight matrix connects each of the layers of nodes. One or more output nodes provide the result of the ANN. This algorithm represents a linear combination of multiple sigmoid functions which is capable of approximating any multivariate continuous function.

5.3 Quantifying the ANN's Signal from Background Separation Ability

Every individual training of an ANN will give slightly different results due to the randomization of the weights and the different combinations of input variables and inner layer structure. In order to ensure that the best[2] ANN is chosen, a method is needed to quantify the quality of the results given or the ability of the ANN to distinguish between signal and background events.

The unit of measure is the Figure of Merit (or FOM). ANNs, once trained, are chosen so that this value is maximized. When the ANN is applied to a sample of events and a cut on the ANN value is applied, the number of signal ν_e events, s, and total background events, b, can be recorded. As a measure of statistical significance, the FOM is most similar to $s/\sqrt{b}$ which is correct in experiments where the statistical error is dominant. However, since this experiment expects a small signal to background ratio of about 1:2, it is important to take the systematic error on the background into account. Therefor, FOM is defined as

$$FOM = \frac{s}{\sqrt{\sigma_{stat}^{bg} + \sigma_{sys}^{bg}}} \equiv \frac{s}{\sqrt{b + \sigma_{sys}^{bg}{}^{2}}}$$

where s is the number of signal events, $b \equiv \sigma_{stat}^{bg}$ is the number of background events selected by the PID, and σ_{sys}^{bg} is the systematic uncertainty on the background.

When training an ANN, as it will be used in this analysis for all three PIDs that will be mentioned, each input variable is normalized (so that it goes from 0 to 1). A single output node is used and is set to 1 for signal and 0 for background events. The Far Detector Monte Carlo that will be used in training and selecting the ANN is divided into three equal parts. Each third of Monte Carlo is further adjusted to form a sample representative of

[2]Or rather, as close as we can get to a perfect ANN

actual data, by selecting events to include in the sample based on the oscillation probability of each event. The oscillation probability is calculated without matter effects and with $\sin^2(2\theta_{13}) = 0.15, |\Delta m^2_{31}| = 2.43 \times 10^{-3} eV^2, \sin^2(2\theta_{23}) = 1, |\Delta m^2_{12}| = 8.0 \times 10^{-5} eV^2$, and $\sin^2(2\theta_{12}) = 0.86$. Additionally, the samples each have the fiducial volume and preselection cuts applied. After training an ANN with the first sample of Monte Carlo for a number of epocs (usually between 100 and 200), the ANN is then applied to a second sample of Monte Carlo events. This sample is used to calculate the optimal cut on the ANN value which will maximize the FOM. The trained ANN is then applied to a third sample of Monte Carlo and the cut found using the second sample of Monte Carlo is applied to evaluate the FOM for the particular ANN.

It is useful to note the ideal iterative and time consuming process of fully evaluating an ANN. Once an ANN is trained and is chosen to be used as a PID, it must be used to create all of the necessary data and Monte Carlo samples of selected ν_e candidate events. From these samples, all of the systematic studies and the Near Detector decomposition must be carried out. Only after these studies are performed is the background systematic error known. The background systematic is then used in part to calculate the FOM. This process is clearly not feasible for each ANN that is considered, so an estimated background systematic error is assumed based on the previous analysis or other studies which are carried out prior to the evaluation of a potential ANN. This shortcut leads to a nearly optimally trained ANN. However, it does leave the possibility that a perfectly trained ANN will not be chosen because the systematic error used in the FOM calculation is too high compared to what that actual ANN would give if all of the studies were carried out. This estimation process is accepted because it is the only feasible method given the timeframe of an analysis. Additionally, a reasonably estimated systematic error will still produce a highly effective ANN.

5.4 ANN11 - The Primary PID

The method used in the first ν_e appearance analysis[75] will be reproduced for this analysis with minor adjustments[83]. Because this analysis uses a different version of software for the Monte Carlo and the reconstruction from the first analysis, the ANN must be retrained. With additional time to work on this method, it has been improved by optimizing the event variables used as inputs and by improving the procedure used to train the PID.

The ANN11 uses 11 input variables which are detailed here[3]

- The parameters a and b from the electromagnetic shower fit over the projection of all strips in the event onto the z axis.
- † The Moliere Radius of the event, which is the radius of an imaginary cylinder centered along the shower axis containing 90% of the shower energy.
- † The RMS of the transverse profile of the event.
- † The sum of the magnitude of the longitudinal projections of the vectors defined by each hit and the event vertex. Each vector is weighted by the energy deposited in the corresponding strip.
- A Minimal Spanning Tree is formed from hits having a pulse height that is larger than the average event pulse height. This variable is the sum of the distances between the hits in this tree.
- The fraction of maximum energy loss in each of a 2, 4, or 6 plane window.
- The shower axis is found by doing an energy weighted least squares fit to the position of the shower strips. This variable is the total energy in the strips which are located within a distance of 1.5 strips to the shower axis divided by the total event energy.

The variables used in this ANN are all calculated over the strips from the entire event. No attempt is made to find the shower component of the event or to extract information from the shower. This is done under the assumption that most desired signal

[3]Variables marked by a † are calculated in each detector view separately and then summed in quadrature to obtain the value of the variable.

events will have a single electron shower and thus all of the strips recorded for the event are directly a result of the electron shower.

This PID saw improvement in training over a number of distinct iterations. Originally inferior to the ParticlePID (see chapter 6), competition between the tuning of both of these PIDs lead to a final PID with an equal FOM to that of the ParticlePID, once the actual systematic errors and the extrapolation was taken into account. The details of this PID will be discussed throughout chapter 6.

5.5 ANN14 - A Cross Check PID

An additional PID was generated[83] with 14 input variables with the intended purpose of being a cross check of the ANN11. Additionally, this PID was designed to be more aggressive in its classification, resulting in both decreased amounts of accepted signal and background. This PID was found by first training an ANN with many variables (in excess of 20). Then a single variable was removed and the ANN was retrained 100 times (to account for the randomization of the training). If the removed variable did not significantly impact the FOM, then the procedure continued. However, a variable which impacted the FOM on removal was retained. This processes resulted in an ANN with 14 input variables.

Five of the input variables are the same as in the ANN11[4]:

- The parameters a and b from the electromagnetic shower fit over the projection of all strips in the event onto the z axis.
- † The RMS of the transverse profile of the event.
- † The sum of the magnitude of the longitudinal projections of the vectors defined by each hit and the event vertex. Each vector is weighted by the energy deposited in the corresponding strip.

[4]Variables marked by a † are calculated in each view separately and then summed in quadrature to obtain the value of the variable.

- The shower axis is found by doing an energy weighted least squares fit to the position of the shower strips. This variable is the total energy in the strips which are located within a distance of 1.5 strips to the shower axis divided by the total event energy.

Two of the variables that were added are energy dependent:

- The reconstructed event energy in GeV
- The length of the event as the number of planes traversed by the event

The seven remaining variables reflect topological features of the event:

- The distance between the event vertex and the strip with the largest pulse height
- The tangent of the shower angle with respect to the beam direction
- The distance between the two strips with the largest pulse heights
- The fraction of the maximum energy loss in a 1 plane and in a 5 plane window
- The fraction of the maximum energy loss in the 6th and 20th strips of the event

The ANN14 is mostly a harsher version of the ANN11, selecting both fewer signal ν_e and background events. The details of this PID will be discussed throughout chapter 6.

Chapter 6

An Alternative Event Reconstruction and Analysis

An alternative to the standard reconstruction software was produced in an attempt to improve the signal selection efficiency as well as to provide a cross check of the primary reconstruction method.

6.1 Motivation

The reconstruction used in the current analysis is extremely simple in nature. All variables are extracted from the list of strips produced by the event slicer, such as RMS, Molière radius, and electromagnetic shower profile. While correct for a low-Y electron neutrino interactions where only the resulting electron shower is visible, these variables can only provide a general measure of the event characteristics for other event types having substantial energy in the hadronic shower. For instance, a neutral current neutrino interaction may produce a number of π^0 which are spatially separated but have their combined energy deposition profile fitted to a single electromagnetic shower. Multiple distinct charged

pions may decay to muons which leave individual short tracks which are not separated by the standard reconstruction. These tracks are instead taken to be part of the event shower and are combined into a single variable. While a variable such as RMS or Molìere radius would have a dependence on the transverse distribution of these multiple particle paths, any information about these individual paths would not be collected.

An alternative reconstruction was designed with the intention of gathering as much information as possible from the individual components of the shower. A strong emphasis was placed on the ability to identify and isolate the electron shower in medium to high-Y electron neutrino interactions so that an electromagnetic fit could be calculated on the electron part of the shower alone. It was also desirable to be able to count the number of spatially distinct $\pi^{+/-}$ (and the resulting muon) tracks as a way to classify the hadronic shower contribution to the event topology. Lastly, the ability to distinguish between energy left by different particles in the shower in each view opened the possibility for a three dimensional reconstruction software.

6.2 The ParticlePID Algorithm

The new reconstruction algorithm was created with the intent of being able to identify the different individual particles resulting from a neutrino interaction. Thus, the algorithm and resulting ANN event classifier was named ParticlePID.

6.2.1 Data Input and Preparation

The ParticlePID algorithm uses the strip lists stored in the standard reconstruction data files. The algorithm is therefore able to act directly on the strip lists that are derived after the slicing and calibration stages from the standard reconstruction. This choice of data input also allows the ParticlePID reconstruction to be run at the same time as the standard

ν_e appearance analysis. Faster development cycles were realized as a result because the processing could be carried out independent of the batch processing system used for the standard reconstruction.

6.2.2 Objects Used in this Algorithm

The task of describing the algorithm is facilitated by first describing the data structures used by the algorithm.

Strip

A strip is the basic data quantity in the detector and corresponds to a single scintillator strip. It has a plane and strip number identification, view (U or V) specification, as well as a position along the beam, z, and a position relative to the length along the strip, t. It also records the calibrated energy in MEU units deposited in the strip.

Cluster

A cluster is an object containing one or more strips in a single plane. These strips are closely located in the transverse t position. The cluster is specified by the sum of the energy contained in its member strips, as well as an energy weighted position in z and t.

Chain

A chain is an ordered list of one or more clusters in a single view which are associated with a probable particle path. The chain has a defined starting and ending position and an energy which is the sum of the component clusters. A parent chain may also have one or more daughter chains attached to it at points past the first cluster in z. Thus a chain may also be able to represent paths of multiple particles which either resulted

from a particle disintegration along the parent chain or which were the result of multiple particle paths which overlapped for some length of the event but then were separated enough such that different particles passed through distinct scintillator strips for a portion of the event.

The chain keeps a record of the clusters that it contains. Some basic properties of these clusters, including slopes and offsets of linear fits for the first and last clusters in a chain of two or more clusters, are also stored. Up to 4 clusters are used for the linear fit on either end of the chain.

Particle3D

In order to make a three dimensional representation of a particle path, one or more chains from each view are combined. A Particle3D object records the chains which contained the clusters that were associated with the particle path. Sometimes, a chain in one view could be associated with multiple chains in the other view. This happens when multiple particle paths overlap in a single view. The Particle3D object also records the energy used from each cluster in each chain, as a given cluster could have energy shared between multiple Particle3D objects. Parameters of the object are calculated and stored in the object, including the starting and ending position, the total energy, the path length, the length in z, the parameters of an electromagnetic shower fit along the path of the object, and the fraction of clusters in the object containing muon-like energy. The Particle3D object also includes the necessary data space to record the possible identification of the actual particle which could have been responsible for this reconstructed Particle3D object.

6.2.3 Dynamic Clustering

Strips in a single view and plane can be combined into a cluster. The process of forming the clusters is described as dynamic, because the processes of clustering can be done many times for the same event.

Strips are arranged by sorting by plane (z position) and then by strip (t position). For each plane, strips are combined into clusters based on the following parameters

- Minimum cluster energy - the minimum energy of a cluster for the cluster to be used by the algorithm
- Minimum strip energy - the minimum energy in a strip for the strip to be included in a cluster
- Maximum t skip - the maximum distance between adjacent strips in transverse position, t, for the strips to be considered in the same cluster

This preliminary list of clusters is further refined with a search for clusters containing multiple energy peaks, where a peak is defined as a strip with some energy which is greater than the energy in either of the adjacent strips. A cluster with multiple peaks is assumed to contain overlapping gaussian distributions (one for each peak). The single cluster with multiple peaks is then split into multiple clusters, each with a single peak. The energy in each strip in the original cluster is shared among the final clusters proportionally to what is expected given the size of the peak strips and the distance from the peaks according to overlapping gaussian distributions.

When an amount of energy is assigned to a given cluster, that amount of energy is associated proportionally to the energy of the component strips. If a portion of the energy in a cluster is associated with a particle path and adopted by a Particle3D object, then that amount of energy is proportionally removed from the component strips and is no longer

available to be made into additional Particle3D objects. If an event is then reclustered, the new clusters are made based on the adjusted energy of the remaining strips. This ability to recluster the event allows for the early removal of particle paths following a clear structure (such as a long muon), which then can expose the detail of the paths of other particles originally obscured by the already identified paths.

6.2.4 Long Track Identification

The first step in the reconstruction is to find and isolate long chains. This step was originally designed with the intention of retaining the ability to discard the Particle3D object corresponding to a long muon (if any were found) in order to construct an MRCC event (see chapter 7). However, for the actual analysis, the standard MRCC process was used. The ParticlePID algorithm acted only on the shower remnant and effectively was used as a shower reconstruction rather than an event reconstruction. The separate step of muon removal was retained, as it still supplies a computational benefit to the overall algorithm.

This step intends to find a single long muon track in an event. Clusters are defined in this step as having single strips of at least 0.05 MEU of energy. It begins by looking for a chain in each view. The chain is built from the back of the detector to the front. The last 5 planes with clusters are fitted to a line and the chain starts to be assembled with the two clusters in the last two planes which are closest to the fitted line. This method takes advantage of the fact that long muon tracks are isolated in z from other particle tracks, but may have a smattering of hits at the end of the track. Once the chain is assigned two clusters with this method, the algorithm iteratively checks each of the clusters in a plane, moving from the back to the front of the detector, against the following criteria from which the best choice for a cluster in that plane is retained as a candidate for addition to the chain:

Punch Through This step uses the front slope and offset of the chain to predict a position in up to the next 4 planes from the plane of the last cluster added to the chain. The closest cluster to the predicted position which agrees with the predicted position to within 0.02 meters in t is retained as the candidate.

Linear Projection If no candidate cluster is yet chosen, the front slope and offset of the chain is used to predict the position of the cluster in this plane. The closest cluster to the predicted position which agrees with the predicted position to within the maximum allowed deviation is retained as the candidate.

Same Δt If no candidate cluster is yet chosen, the cluster whose distance in t to the previously added cluster in the chain which is within the maximum allowed deviation and which is less than the distance in t between the previous and penultimately added cluster in the chain is retained as the candidate.

Second-order Polynomial Projection If no candidate cluster is yet chosen and if the chain has more than two clusters, the last three clusters in the chain are used to predict the position of the cluster in this plane with a second-order polynomial projection. The closest cluster to the predicted position which agrees with the predicted position to within the maximum allowed deviation is retained as the candidate.

If a candidate cluster is chosen, it must also pass the maximum allowed deviation test which is defined as the maximum difference in t between the candidate cluster and the last cluster added to the chain as being less than 0.025 meters + (0.01 meters $\times$ # planes) between the candidate cluster and the last cluster added to the chain. In addition to being an inherit cosmic event filter, this requirement also ensures that the long muons are indeed energetic and truly long as it only reconstructs muons with minimal curvature.

The motivation for allowing the candidate cluster to come from as many as four planes away via the punch through mechanism is to avoid any showers from Bremsstrahlung or clusters caused by other interacting particles which cross the path of the muon. When the punch through mechanism is used, there are planes which will be skipped from the chain associated with this long muon. The clusters in these planes will be found and accounted for before the long muon finding is completed.

At this point, for a ν_μ CC event with a long muon track, a chain has been found in each view containing clusters which correspond to the long muon candidate. Each chain is checked for quality against the following requirements:

- the number of clusters in each chain must be greater than 3
- a muon fraction, f_μ, check, where the requirement is that $f_\mu > 0.5$, and

  $$f_\mu = \frac{N_\mu}{N_{tot}}$$

  where N_μ is the number of clusters in the chain with energy between 0.5 and 2.5 MEU and N_{tot} is the total number of clusters in the chain
- plane fraction, f_p, check, where the requirement is that $f_p > 0.8$, and

  $$f_p = \frac{N_p}{N_{tot}}$$

  where N_p is the sum of the total number of planes having a cluster from each view and N_{tot} is the total possible number of planes from both views (based on the starting and ending plane in each view)

The number of planes with a cluster from both views is taken as the number of planes from the chain found in each of the U and V views. The total possible planes from combining both views considers the first and last plane from each of the chains and picks the lowest

first plane and the greatest last plane to get the maximum number of planes that could be made from the combination of the views. Here a check is also done for the Near Detector to determine the number of clusters in both views which lie within the partially instrumented region of the near detector. By examining both chains concurrently and assuming that they belong to the same particle interaction, it is possible to get a good estimate of the number of planes which are in the partially instrument region. The number of planes with clusters from both views is then adjusted with the addition of eight times the number of these clusters within partially instrumented planes to account for the deficit due to sparse instrumentation in the partially instrumented planes.

If each of the chains passes these quality cuts, then an attempt can be made to combine them into a Particle3D object. The chains must overlap by at least one meter in z to ensure a three dimensional reconstruction. Next, an isolation point in z is determined. The isolation point is defined as the point forward of which includes interactions from other particles and beyond which only contains energy deposition from the long muon and subsequent interactions. This point is determined as the start of the forward most region in z where there are three adjacent planes in each view which each contain only one hit and where those hits are assigned to clusters in the chains found in the long muon finder. Forward of this point, an amount of energy consistent with a muon must be extracted from the clusters, as the clusters may also contain energy from other particle interactions. Beyond this point, all remaining clusters must be assigned to the muon chains.

Energy is removed from clusters forward of z to account for energy deposition by overlapping particle interactions. The average energy deposition of the muon track per cluster is calculated using the clusters beyond the isolation point. For all clusters forward of the isolation point, if the clusters energy is more than 1.2 times the average cluster energy then only the energy in the amount of the average cluster energy is retained in the long muon

chain for that cluster. Otherwise, the entire energy is retained for that cluster. Clusters beyond the isolation point are added to the chains corresponding to the long muon. Cluster not previously assigned are often from Brehmstralung, muon decays, and other interactions caused by energy loss from the muon.

These two chains are then combined to make a Particle3D object in a process described in section 6.2.6. This object is declared to be a muon-type Particle3D object because of the previously applied restriction on energy deposition from component clusters and because of the length requirement of the chains used in the object.

6.2.5 Shower Component Identification

Once the long track has been identified and isolated, if it is present, the remaining clusters are put through a step to identify other possible particle paths. Clusters are defined in this step as containing at least 0.2 MEU total energy, being comprised of strips each of at least 0.05 MEU with a maximum gap of 0.05 meters. In each view, a Hough Transform[84] is used to find clusters which fall along similar lines.

Originally designed to find tracks in bubble chamber experiments, the Hough Transform is capable of finding lines within any image. The algorithm starts with a reference point, (t_0, z_0), which is conveniently chosen as the event vertex. A possible line in the image is defined as the line perpendicular to and at the end of a vector beginning at (t_0, z_0) and extending a distance of r at some angle, θ. For each point in the image, all possible lines passing through that point are drawn by sweeping through values of θ and recording the corresponding r which is given by $r = z\cos\theta + t\sin\theta$. The information is stored in a histogram of θ versus r, so in reality, not all values of θ are considered, but only those corresponding to the center of a histogram bin. The resolution of the algorithm is therefor adjustable and is tuned to find a balance between increased precision at finding lines and

faster processing time. Multiple points in the image that make up a true line will fall along the same θ and r values and will form a peak in the histogram. The peaks in the histogram are then used to identify possible lines.

A step is performed to clean the possible lines found by removing all vertical lines except the lowest in z (the rest of which could not be from an interaction starting at the event vertex). Additionally, lines which connect clusters where the smallest distance in z between any two clusters on that line is greater than 0.2 meters are not used. For each unique line found in the Hough Transform, a list of clusters within 1.5 strip widths of that line is assigned to the line. These lines are then sorted by giving preference to the most forward lines having the most clusters (which is more representative of an EM shower). Iterating over the lines found in the Hough Transform, chains are created for the lines which either point towards the event vertex or towards an existing chain until clusters are exhausted. When pointing to an existing chain, it is required that the pointing is aimed towards the front of the chain, as would be expected for overlapping or decaying particles. If a long muon has been found in the previous step then that vertex is used as the event vertex, otherwise the event vertex is taken as the vertex of the first line found in the Hough Transform that is used (the most forward with the most clusters). The long track identification step could have actually be carried out in the Hough Transform step at a greater computational expense without any added benefit.

The list of chains is then searched for the maximum path chain. Each path along each chain and subsequent daughter chains is followed, measuring the energy along that path. In each view, the maximum path chain undergoes a process of muon removal which will determine if the chain contains a muon plus other energy. If the fraction of muon like energy clusters (<2.5 MEU) in the chain is greater than 0.2, and there are at least two consecutive clusters in the chain of muon like energy, a muon chain is created using the

clusters with energy within this muon like energy range. The remaining clusters are split, giving the muon chain up to the average muon like energy in the muon chain for each of the remaining clusters. This muon chain is retained for later use. The remaining clusters stay with the chain to be used for the rest of this step. The maximum path chain from each view, after muon removal, are then combined into a Particle3D object. This particular Particle3D object represents the primary shower, or shower core, of the event.

At this point, any existing long muon and/or primary shower components have been identified and converted into Particle3D objects. The event must have either a long muon or primary shower Particle3D for the reconstruction of the event to continue. With an event having either of these objects, an initial event vertex can be identified with preference given to the vertex of the long muon Particle3D over the primary shower Particle3D if it is present. The remaining chains found in the Hough Transform are then used to complete the reconstruction of the event.

An attempt is made to combine chains in a given view which fall along the same line but which have not yet been connected due to gaps in clusters between the chains. Then all chains are checked against the current vertex position to ensure that they do not exist on both sides of the vertex - if they do, they are split into two chains, each pointing to the vertex. Chains are then matched between views based on their position in z, the amount of overlap in z, and the closeness of the quantity of energy contained by each chain.

A chain in one view can be matched to one or more chains in another view. In either case, a Particle3D object is created for each of these sets of chains between views. The Particle3D objects then undergo a process of sharing energy from clusters which were in a chain in one view that matched to multiple chains in the other view. The amount of energy taken from a shared cluster is the average of the energy from unshared clusters around the shared cluster in the Particle3D object. This sharing continues from the greatest

to least energy Particle3D object until the energy in the shared cluster is exhausted.

All Particle3D objects then undergo final calculations of parameters and a final guess of the type of particle responsible for the creation of each Particle3D object.

Any remaining clusters which are not used in chains are isolated in space. Any of these isolated clusters with more than 3 MEU are identified as possible neutrons are are represented as a Particle3D object with only a z and t (u or v) position. These objects are only useful for event energy accounting, as they do not provide and three dimensional information.

6.2.6 Making a Particle3D Object

Constructing the Particle3D Object

A Particle3D object is made from a chain in each view. The 3D representation is achieved by first recording a list of z and t (u or v) positions for each cluster in each chain, stored in objects called 3D points. Then the missing number (v or u) is calculated to fall on the line connecting the points from the other view on either side of the point to be calculated. This works well for all points not at the end of either chain. For the end points of the chains which have the furthest extent in z, the missing number is calculated by an extrapolation of the two closest available points in the opposite view.

Guessing the original particle type

Once a Particle3D object is constructed, a number of tests are carried out to categorize the most probably particle interaction responsible for this reconstructed object. From these tests, a Particle3D is assigned one or more possible particle types along with a range of 3D points where that Particle3D object exhibits the particle type traits. From there, a final step makes a decision assigning a single particle type to the object. These

tests are detailed in table 6.1.

Particle3D Object Particle Type	Possible Actual Particle	Test	Template
muon	μ, π^-, π^+	The energy of each 3D point is > 0.2 and < 3 MEU allowing for one point to be out of range if it is surrounded on each side by a hit in range	
proton	p, n	The 3D points from the end to the front of the Particle3D object are decreasing in energy	
electron	e, π^0	There is a peak in the 3D points with energy decreasing on either side of the peak	
other	π^0, e	There are two or more distinct peaks, each passing the criteria for an electron	
neutron	n, e	Starting from the first 3D point, the energy rapidly decreases	

Table 6.1: A list of possible particle types that can be assigned to a Particle3D object and the tests applied the the 3D points of the Particle3D object used to identify the regions of the object exhibiting the traits of these particle types

Examples

To illustrate the algorithm previously detailed, a number of events are shown. A well formed quasi-elastic oscillated ν_e event demonstrates the process of clustering hits in figure 6.1. The same event then shows how the clusters relate to the chains (shown as red lines), and how those chains combine to make a Particle3D object in figure 6.2. A DIS ν_μ event is shown in figure 6.3 and a NC event is shown in figure 6.4.

Electromagnetic Fitting

For reference, the procedure used to calculate the electromagnetic fit is described here. The algorithm will not attempt to fit a shower between super modules in the Far Detector. The 3D points from a Particle3D object are converted into energy depositions along radiation length and are fitted to the electromagnetic shower function for variables a (bounded between 1.5 and 5), b (bounded between 0.01 and 1.5), and E_0 (unbounded)

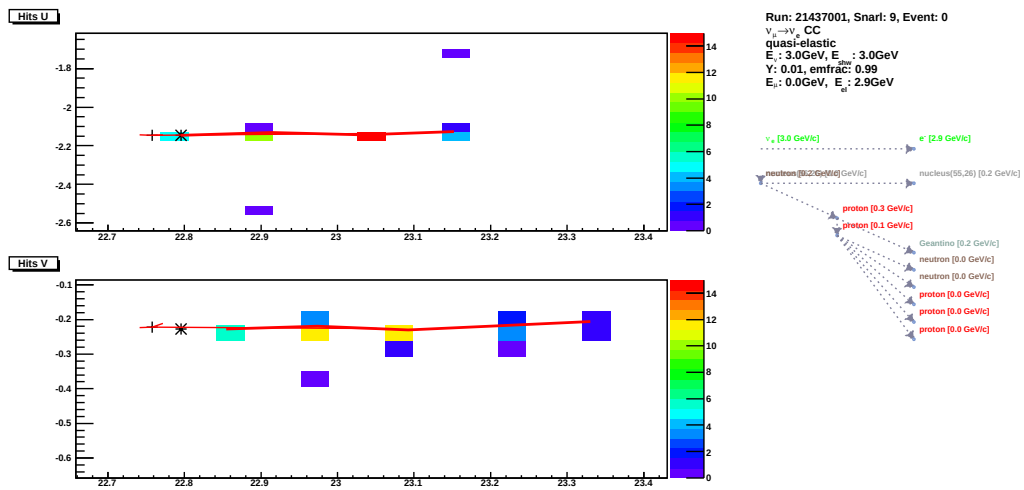

(a) Hits shown for a ν_e QE event

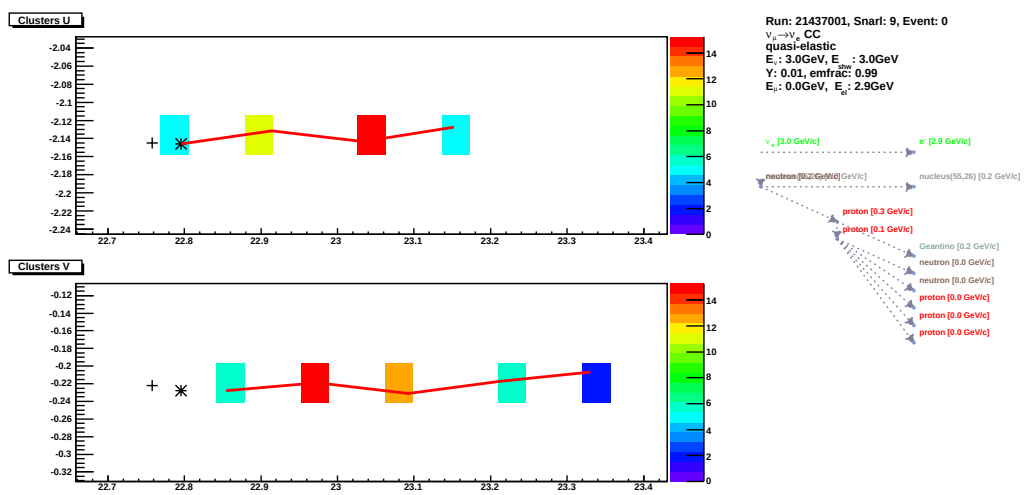

(b) Clusters shown for a ν_e QE event

Figure 6.1: Visualization of the hits (top) which are combined into clusters (bottom). The chains found are plotted in both steps for this oscillated quasi-elastic ν_e event.

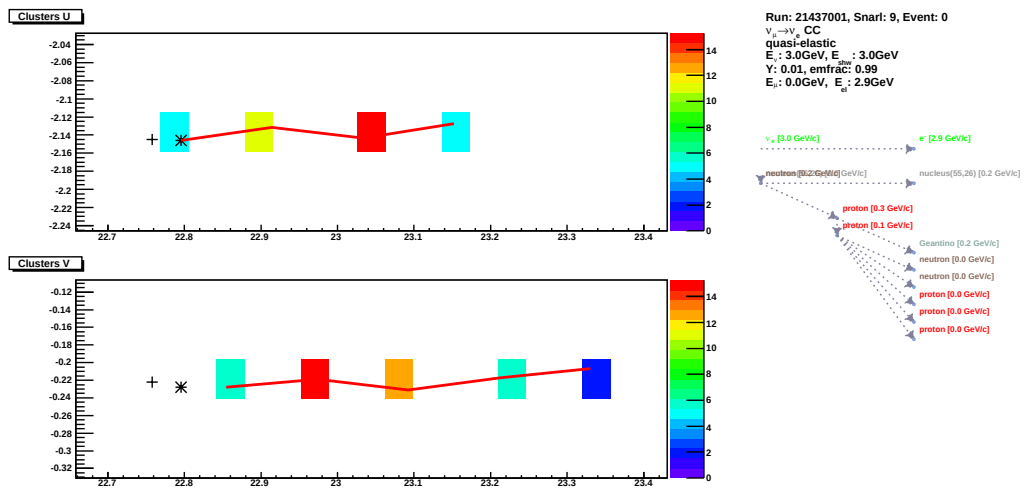

(a) Clusters and chains for a ν_e QE event

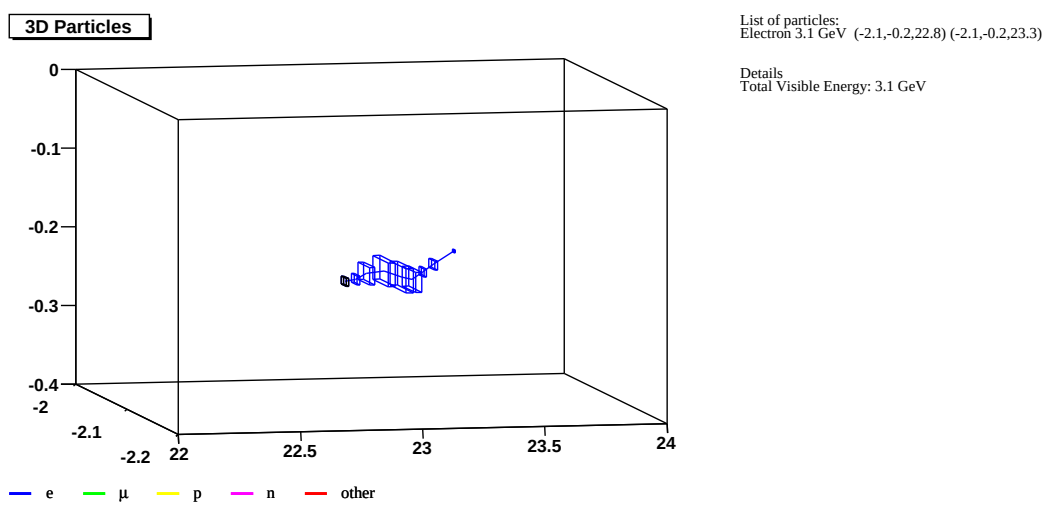

(b) 3D representation of reconstructed particles found by combining chains in each view

Figure 6.2: Visualization of the clusters and resulting chains (top) which form the Particle3D object (bottom) for this oscillated quasi-elastic ν_e event.

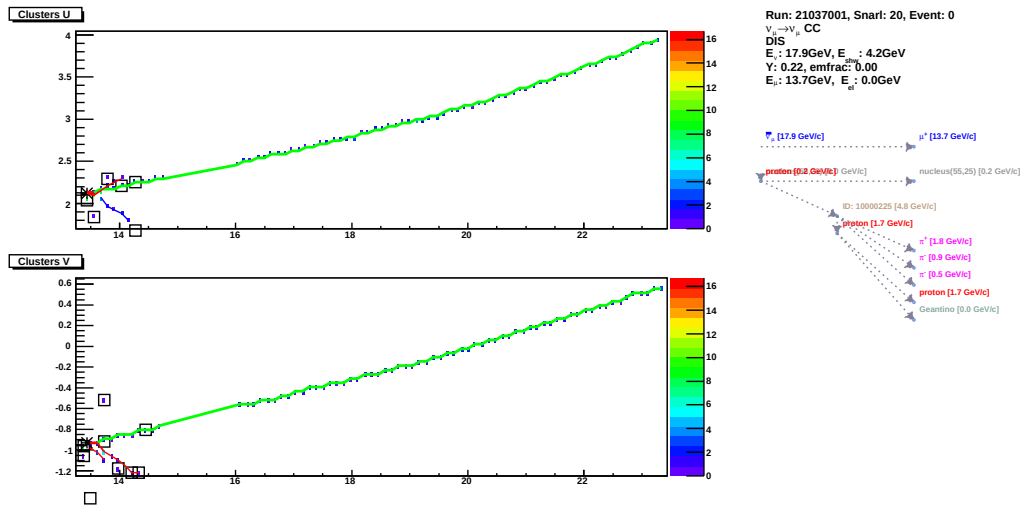

(a) Clusters and chains for a DIS CC event

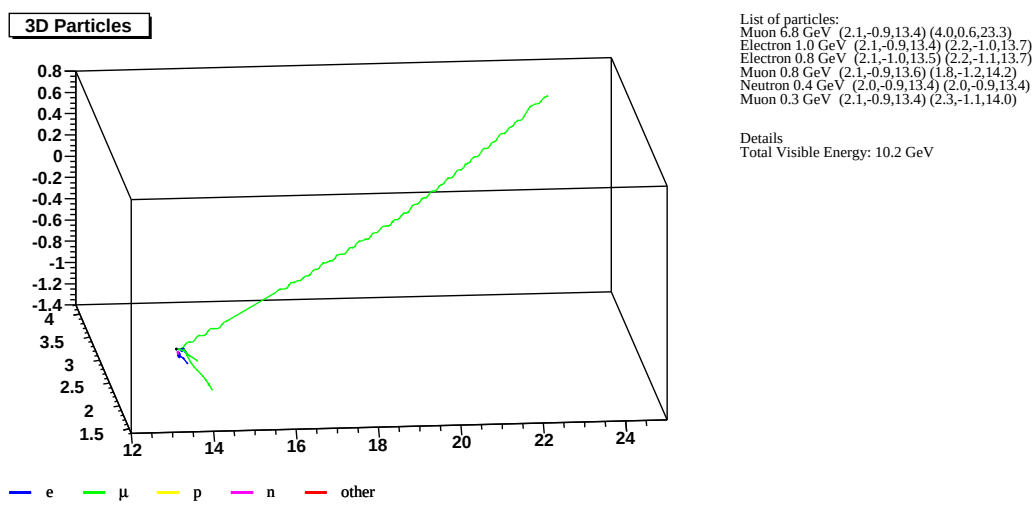

(b) 3D representation of reconstructed particles found by combining chains in each view

Figure 6.3: Visualization of the clusters and resulting chains (top) which form the Particle3D object (bottom) for this DIS ν_μ event. Components of the hadronic shower are found, although limited in accuracy. The π^+ is reconstructed as two electrons, the proton is misidentified as a neutron, and the two π^- are called muons. The primary muon in the interaction is properly reconstructed.

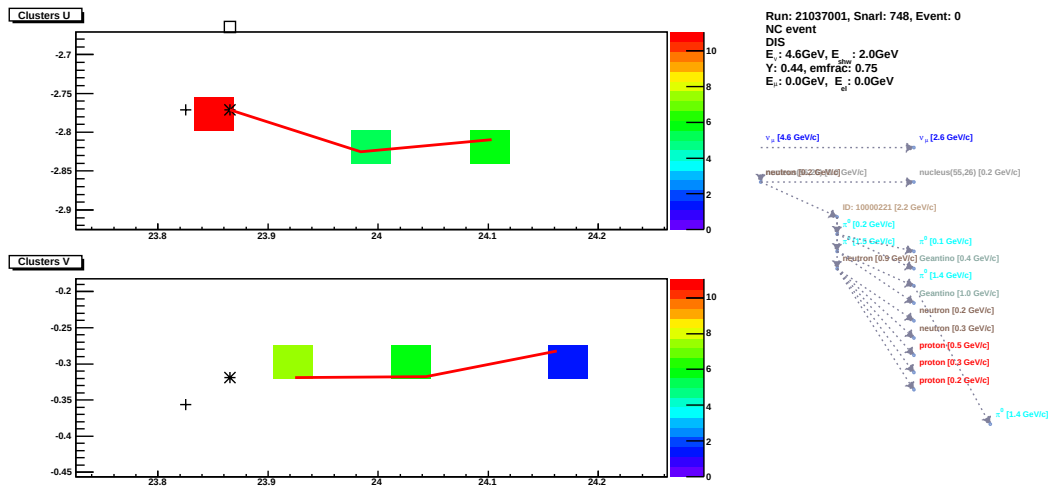

(a) Clusters and chains for a NC event

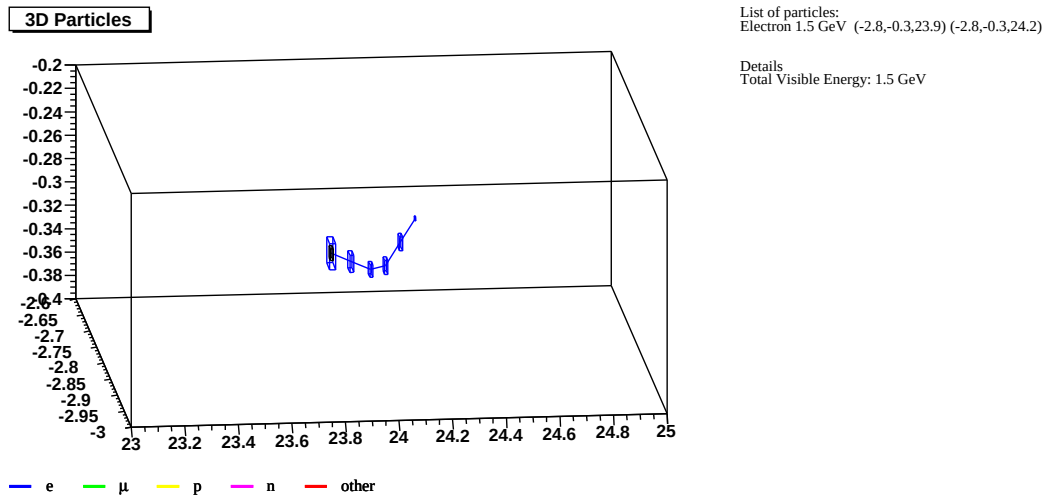

(b) 3D representation of reconstructed particles found by combining chains in each view

Figure 6.4: Visualization of the clusters and resulting chains (top) which form the Particle3D object (bottom) for this NC event. This NC event is primarily composed of an energetic π^0, which is indistinguishable from an electron due to the resolution of the detector.

using the equation for electromagnetic shower development [33]

$$\frac{dE}{dt} = E_0\, b\, \frac{(bt)^{a-1} e^{-bt}}{\Gamma(a)}$$

A "perfect" shower profile is then generated using the parameters found in the fit. This shower profile is compared to the actual shower profile in the reconstructed Particle3D object giving rise to a number of variables describing the quality of the shower, including χ^2/NDF, energy difference before and after the shower maximum, and energy difference in the three planes centered at the shower maximum. An attempt was made to determine if the shower was a result of an electron or a photon electromagnetic shower by looking at the position of the shower maximum, t_{max}.

$$t_{max} = (1-a)/b = 1.0 \times (\ln y + C_j), \qquad j = e, \gamma$$

Here, $y = E/E_c$, E is the energy of the incident particle and E_c is the critical energy of the material. The critical energy (approximately 1.5 MeV) is the threshold below which electrons and photons will no longer cascade, but instead will dissipate energy by ionization and excitation. Since $C_e = -0.5$ for electron induced showers and $C_\gamma = +0.5$ for photon induced showers, a shift in the shower profile peak can be used as an indicator of the parent particle type. For each shower profile being fit, an ideal shower profile was constructed for both the electron and photon induced shower hypothesis by using the measured fit values of the parameters a and E_0 with the assumption that $b = 0.5$. The two ideal profiles were then compared to the measured profile and a χ^2 difference was calculated to determine which hypothesis best fit the measured shower profile. While this technique proved useful for electron showers with energy of at least 5 GeV, there was not enough separation power in this method for events of energies typically found in this analysis.

6.3 Oscillated ν_e Event Selection

Prior to training an ANN, it was first necessary to determine which variables would be used as inputs to the ANN. Potential variables were generated using outputs of the ParticlePID reconstruction with a focus on variables sensitive to electromagnetic shower properties. These variables were screened for correlations between each other, and a set of variables which were not highly correlated with each other was chosen. Studies were performed by creating simple ANNs with 25 or more input variables. The effectiveness each of these large ANNs was measured, and the input variables were systematically removed and the ANN was retrained without the removed variable in order to measure the separation power of each variable. Variables with the lowest event identification power were removed until 14 variables remained. No more variables could be removed without noticeably effecting the FOM of the ANN. The correlations between the selected variables are shown in figure 6.5.

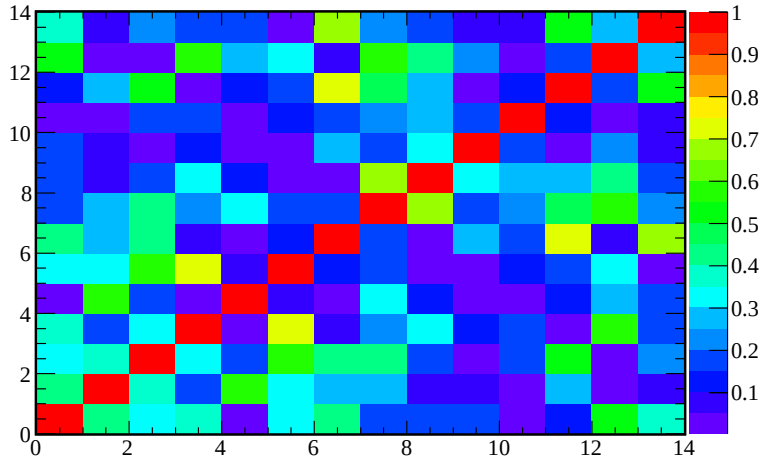

Figure 6.5: The correlations between the ParticlePID ANN input variables are shown. In general, the 14 variables used in the ParticlePID ANN are not highly correlated.

6.3.1 Useful Variables for Event Identification

A number of variables have been generated and explored as possible inputs to an ANN for the purpose of distinguishing oscillated ν_e signal from background events. The variables which have been selected for use in the final ANN are presented here.

- Path length of longest particle
- Moliére Radius calculated from the 3D points of all found Particle3D objects about the event vertex
- Reconstructed electromagnetic shower fraction calculated as the sum of energy of all Particle3D objects reconstructed as electrons divided by the total event energy
- Total number of reconstructed Particle3D objects in the event
- The energy weighted angle off of z from 3D points of all found Particle3D objects
- The fraction of energy of largest Particle3D to total energy
- For the largest energy Particle3D, the electromagnetic fit parameters b, a, E_0 and the χ^2 of the fit. Also a/E_0 is used as a separate parameter, as it is related to the position of the shower maximum in units of radiation length from the start of the shower.
- For the largest energy Particle3D, the difference in energy in the largest three planes of the shower profile of the largest energy Particle3D in the event and the "perfect" EM shower profile formed with the EM showers parameters (a,b,E_0) found in the EM shower fit of this Particle3D object
- For the largest energy Particle3D, the χ^2/NDF arising from the comparison of the shower profile of the largest energy Particle3D in the event and the "perfect" EM shower profile formed with the EM showers parameters (a,b,E_0) found in the EM shower fit of this Particle3D object
- The total number of plane clusters in the event

The differences in the behavior of these variables for oscillated ν_e events and background events will provide the basis for event identification. These variables are shown in figure 6.6 after the application of preselection cuts for both signal and background.

6.3.2 Training the Neural Network

The power of an ANN is dependent on both the structure of the ANN and the specific training which the ANN has undergone. Since each iteration of the training involves a random adjustment to the previous iteration, it is necessary to train multiple ANNs and pick the superior one. The number of nodes in the hidden layers also effects the power of the ANN. In order to find the best ANN, a batch processing computer system was employed to train sets of 10 ANN, each with 200 training epochs, with each set representing a different combination of inner layers with the first inner layer having between 15 and 25 nodes and the second inner layer having between 5 and 12 nodes. After training, the resulting ANN was applied to a test sample from which a cut on the resulting PID was determined which maximized the FOM of that test sample. A third sample combined the trained ANN and the PID cut found from the previous two samples and was used to evaluate the FOM of the ANN. The ANNs with the maximum possible FOMs, assuming $\epsilon_{syst} = 7\%$ were retained for comparison. Of the six best ANNs which had different internal structures and identical performance (within 1%), one was arbitrarily chosen as the singular ANN to use for this analysis. The structure and relative weights of the chosen ANN with 14 input variables and inner layers with 16 and 9 nodes is displayed visually in figure 6.7. This ANN has the optimal cut at 0.7 assuming a 5% systematic error on the background. The FOM is plotted for systematic errors of 3.5, 5, and 7% over the range of the PID in figure 6.8.

This ANN selects signal events over the entire preselection energy range (1-8 GeV) with the highest efficiency and purity in the region of interest (2-5 GeV), as shown in figure

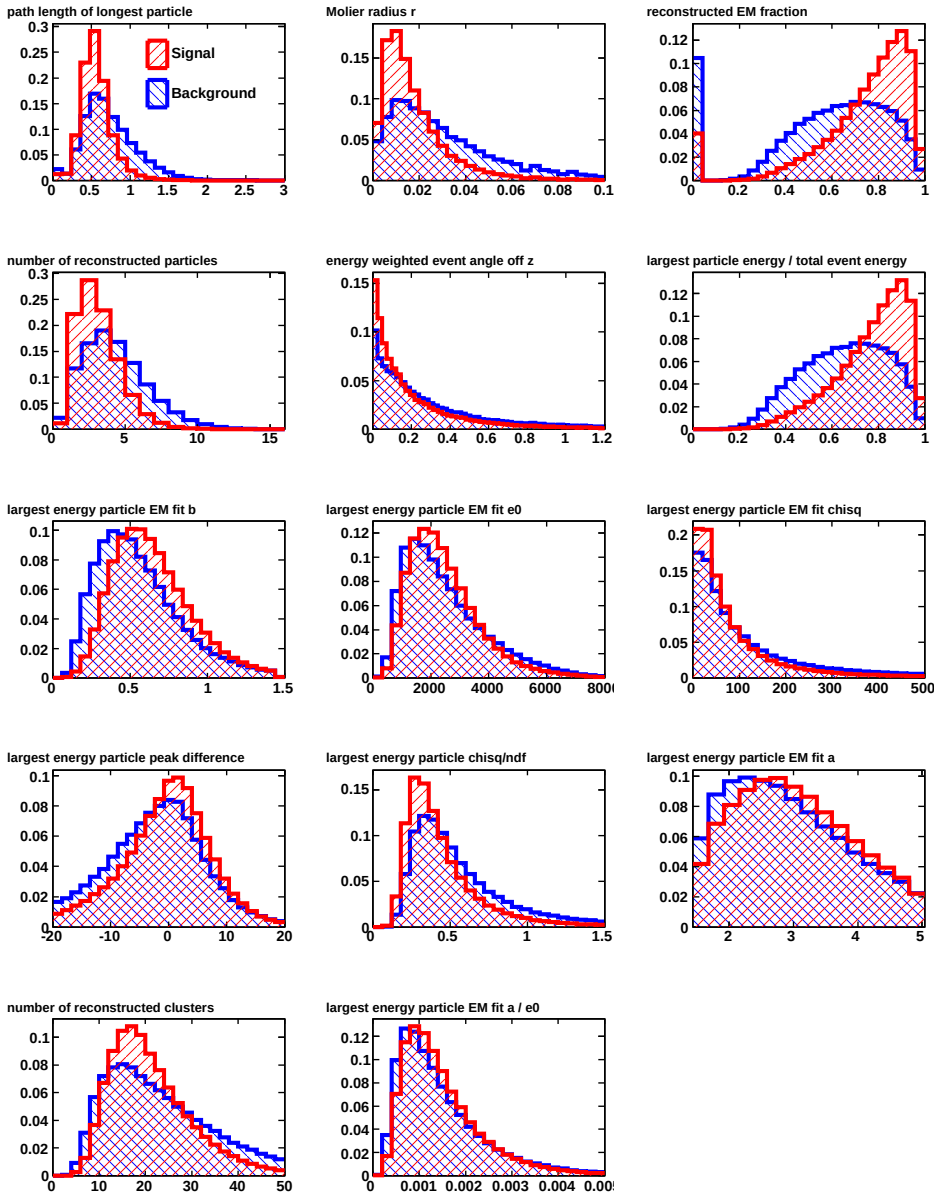

Figure 6.6: The signal and background distributions of the input variables used in the ParticlePID ANN, normalized to unity, after the fiducial volume and preselection cuts have been applied.

6.9. This is to be compared to the efficiency and purity for the ANN11, shown in figure 6.10. For convenience, the efficiency and purity for both the ParticlePID and ANN11 are shown in figure 6.11. The ParticlePID has a greater efficiency than the ANN11 in all but the 7-8 GeV bin, as it selects more signal ν_e events overall. The efficiency in the peak (3-4 GeV) is greater by 7% and the largest difference in the efficiency is 13% in the 4-5 GeV bin. The purity for the ParticlePID is lower everywhere compared to the ANN11, as the ParticlePID also selects more background events. The largest difference is in the 7-8 GeV bin, where the purity for the ParticlePID is 36% lower than for the ANN11. The purity is the same in the 1-2 GeV bin, and is lower by 4% in the 2-3 GeV bin, 9% in the 3-4 GeV bin, 14% in the 4-5 GeV bin, 22% in the 5-6 GeV bin, and 21% in the 6-7 GeV bin. This trend of decreasing purity with increased energy is consistent with the ParticlePID selecting more DIS background events which have on average larger event energy compared to the other background event types.

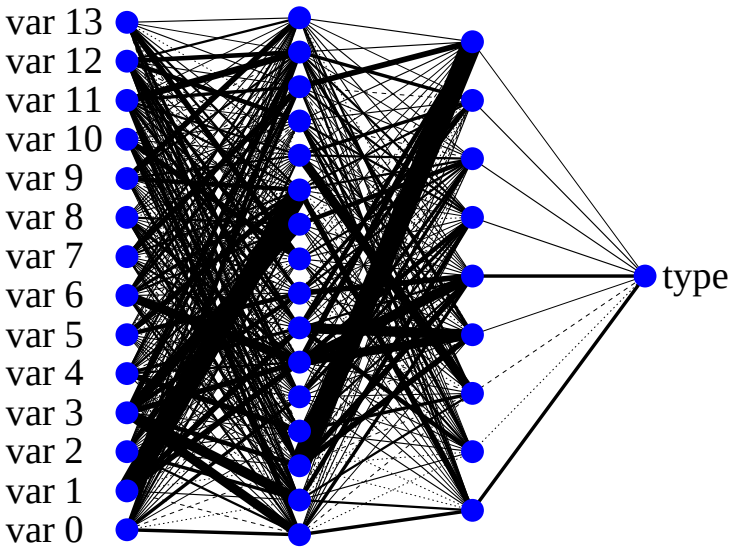

Figure 6.7: The ParticlePID ANN used in this analysis is shown. The relative weights between the 14 input nodes, the 16 and 9 node hidden layers, and the output node, are indicated by line width.

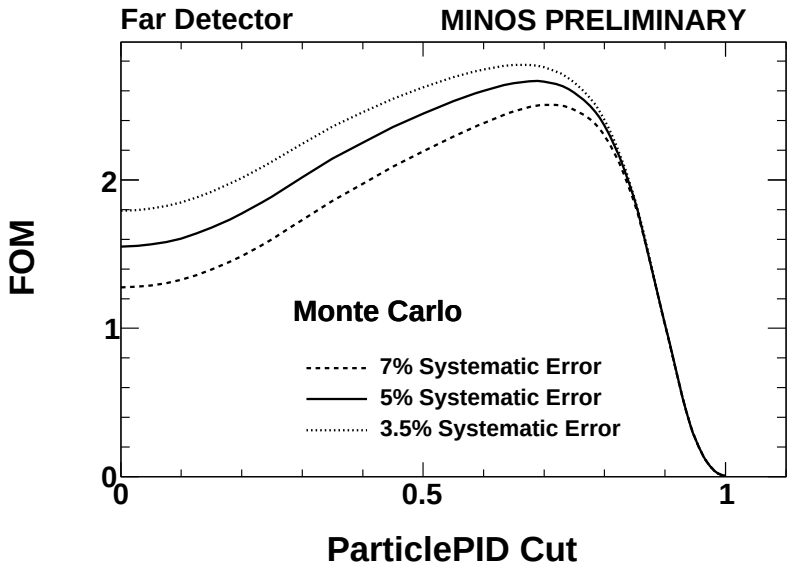

Figure 6.8: The potential FOM for various ParticlePID ANN cut levels is shown. The optimal cut assuming a 5% systematic error on the background is at 0.7.

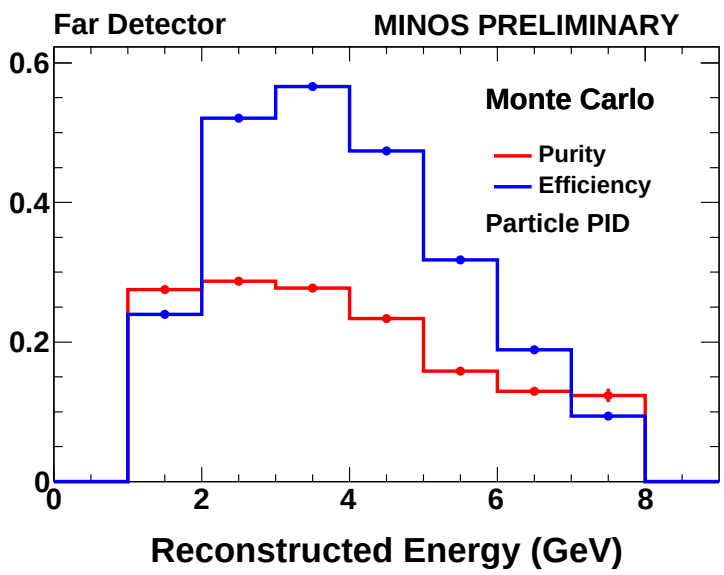

Figure 6.9: The efficiency and purity of the ν_e signal as a function of reconstructed energy after the ParticlePID cut in the Far Detector Monte Carlo is presented. The efficiency is the ratio of signal ν_e events remaining after the ParticlePID cut to the events present after the fiducial volume cut. The purity is the ratio of the signal ν_e events to the total events present after the ParticlePID cut.

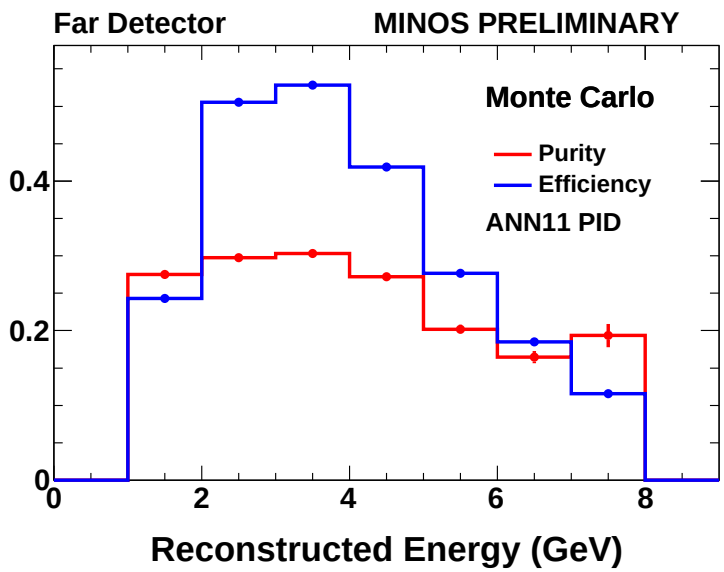

Figure 6.10: The efficiency and purity of the ν_e signal as a function of reconstructed energy after the ANN11 cut in the Far Detector Monte Carlo is presented. The efficiency is the ratio of signal ν_e events remaining after the ANN11 cut to the events present after the fiducial volume cut. The purity is the ratio of the signal ν_e events to the total events present after the ANN11 cut.

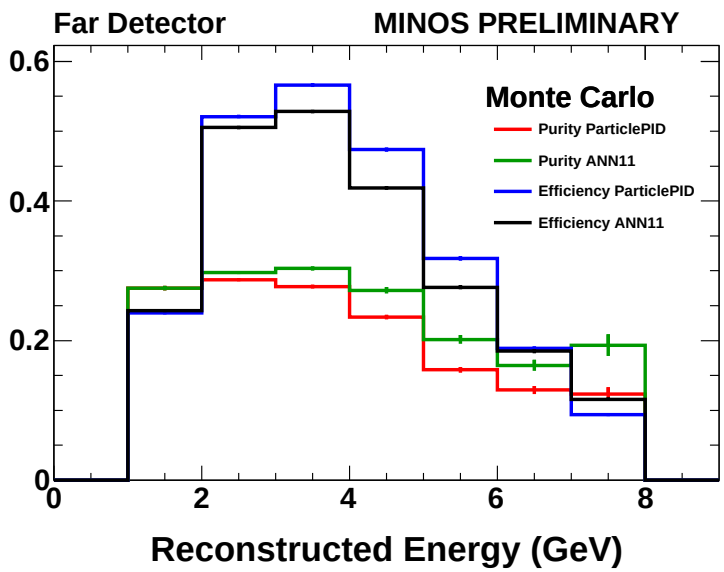

Figure 6.11: The efficiency and purity of the ν_e signal as a function of reconstructed energy after each of the ParticlePID and ANN11 cuts in the Far Detector Monte Carlo are presented. The efficiency is the ratio of signal ν_e events remaining after the PID cut to the events present after the fiducial volume cut. The purity is the ratio of the signal ν_e events to the total events present after the PID cut.

6.3.3 Examining the Selected Sample

The ParticlePID ANN is applied to the Far Detector Monte Carlo with a cut at 0.7. The resulting selected sample is presented in table 6.2. The FOM presented for each of the 3 PIDs in this table assumes a systematic error of 5%. While this is a good start for comparison, this number is not too important, as each PID has its own actual systematic. Also, the numbers presented are from Far Detector Monte Carlo only and do not take into account any effects of extrapolation in a prediction of Far Detector events. Each of the signal and background components is shown as a function of reconstructed energy after fiducial, preselection, and ParticlePID cut in figure 6.12. The selected signal (scaled by 10× for clarity) along with the background components is presented in figure 6.13 as a function of the ParticlePID value. The shape of the background distributions is similar to that of ANN11, shown in figure 6.14, although the distribution for the signal events has a more pronounced peak. This same set of events is shown as a function of reconstructed energy in figure 6.15. This distribution looks identical to that produces by the ANN11, shown in figure 6.16.

	Signal	Background	NC	ν_μCC	ν_e^{beam}CC	ν_τCC	FOM
Fid. Vol. Cuts	57.53	2653.99	740.07	1859.82	36.05	18.05	0.40
Pre-selection Cuts	45.00	463.18	286.84	154.08	12.52	9.75	1.42
ParticlePID > 0.7	22.64	62.55	44.63	10.79	4.97	2.16	2.66
ANN11 > 0.7	21.61	53.82	40.31	7.23	4.45	1.84	2.76
ANN14 > 0.75	18.29	38.13	28.20	4.92	3.61	1.40	2.83

Table 6.2: The signal and background is presented at different cut levels using only Far Detector Monte Carlo. The FOM is presented for the three PIDs with all PIDs assuming a 5% systematic error.

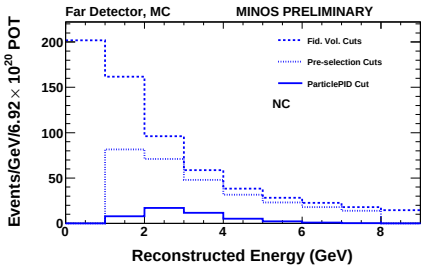

(a) NC

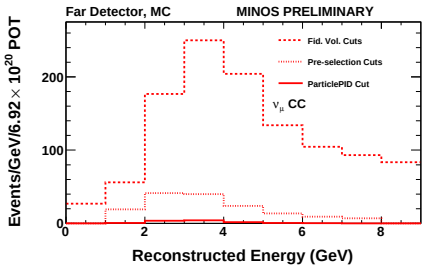

(b) $\nu_\mu CC$

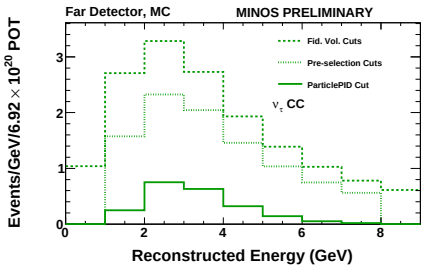

(c) ν_τCC

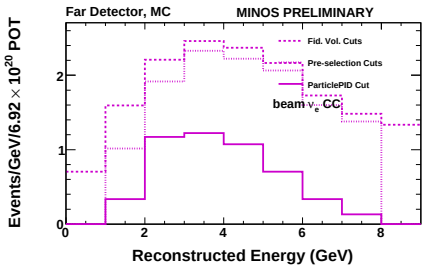

(d) ν_e^{Beam}

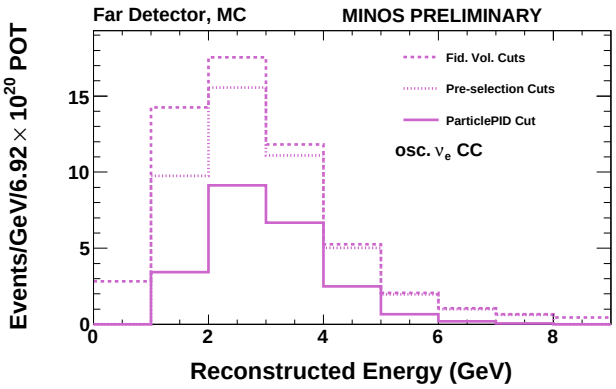

(e) Signal ν_eCC

Figure 6.12: The reconstructed energy for each event class at the fiducial, preselection, and ParticlePID Cut levels is shown. Note how the distribution changes shape between the cut levels for all background type events, but not for signal events. Also, after the ParticlePID cut is applied, the distributions of all components have similar shapes. This is because the ParticlePID selects ν_e-like events - the different components of the ParticlePID selected sample are indistinguishable from each other.

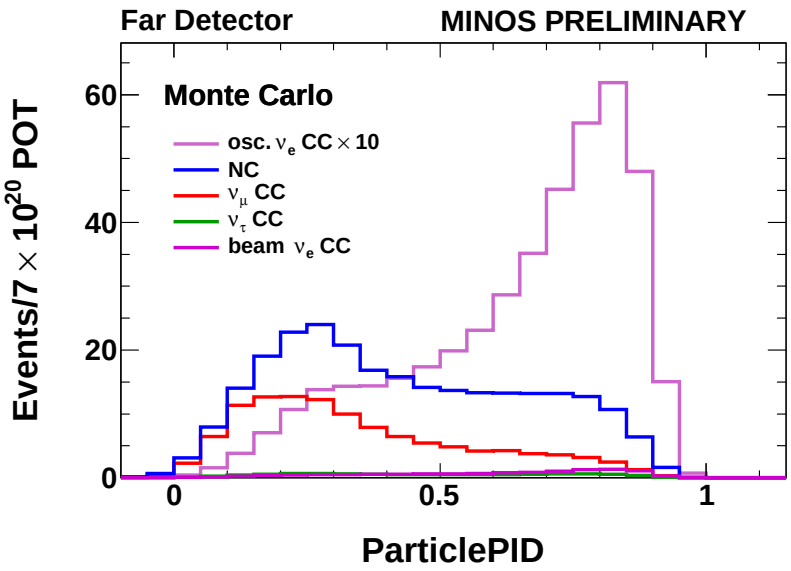

Figure 6.13: The computed ParticlePID value for the signal and background components of the Far Detector Monte Carlo sample. The signal is scaled by a factor of 10 for clarity. The events are scaled to represent 7×10^{20} POT.

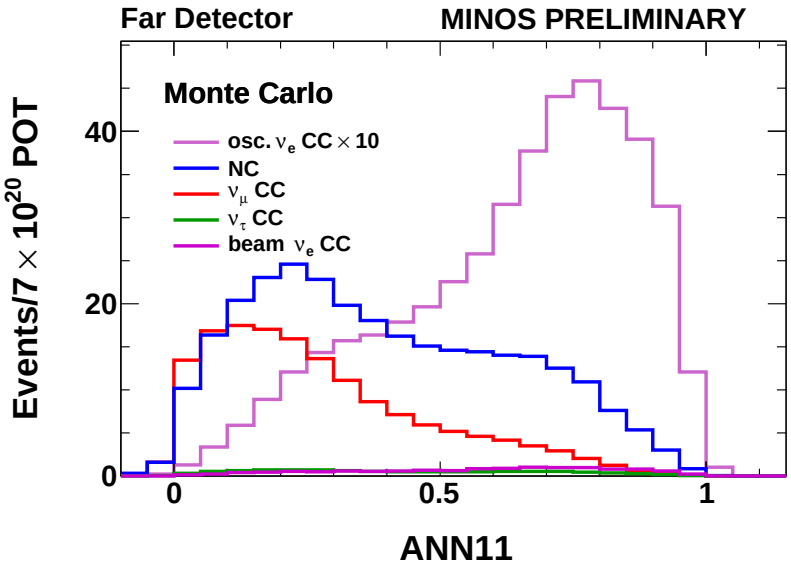

Figure 6.14: The computed ANN11 value for the signal and background components of the Far Detector Monte Carlo sample. The signal is scaled by a factor of 10 for clarity. The events are scaled to represent 7×10^{20} POT.

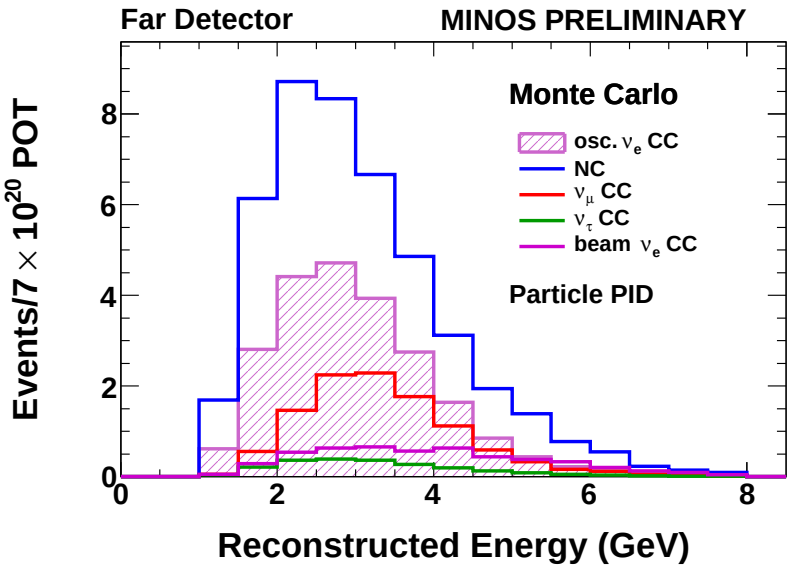

Figure 6.15: The reconstructed event energy for events selected by the ParticlePID from Far Detector Monte Carlo. The events are scaled to represent 7×10^{20} POT.

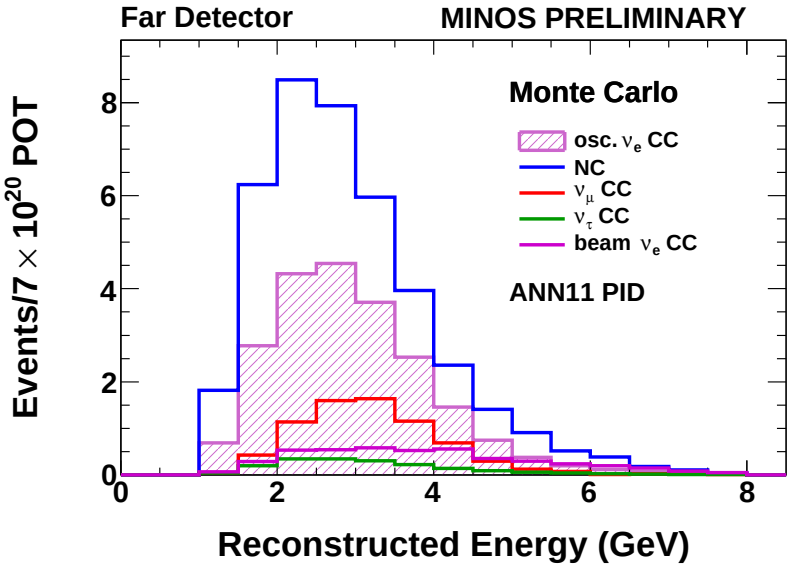

Figure 6.16: The reconstructed event energy for events selected by the ANN11 from Far Detector Monte Carlo. The events are scaled to represent 7×10^{20} POT.

A detailed examination of the events selected by each PID is presented in table 6.3. Here, Far Detector Monte Carlo events are listed by type and resonance code. The ParticlePID selects more DIS ν_e events than the ANN11. This reflects the reconstruction algorithm of the ParticlePID which attempts to isolate components of the hadronic shower. The number of QE and RES types events are the same for both the ParticlePID and the ANN11. The differences between these selected events will be discussed further in section 6.4.1. The value of the ParticlePID for the selected signal is shown in figure 6.17 for each resonance code. The QE and RES signal events are strongly peaked at high values of the ParticlePID. Many of the DIS events are assigned lower values of the ParticlePID, indicative of the inability to identify certain ν_e DIS events because too much of the incoming neutrino energy has been transfered to the hadronic shower resulting in little to no energy being given to the electron.

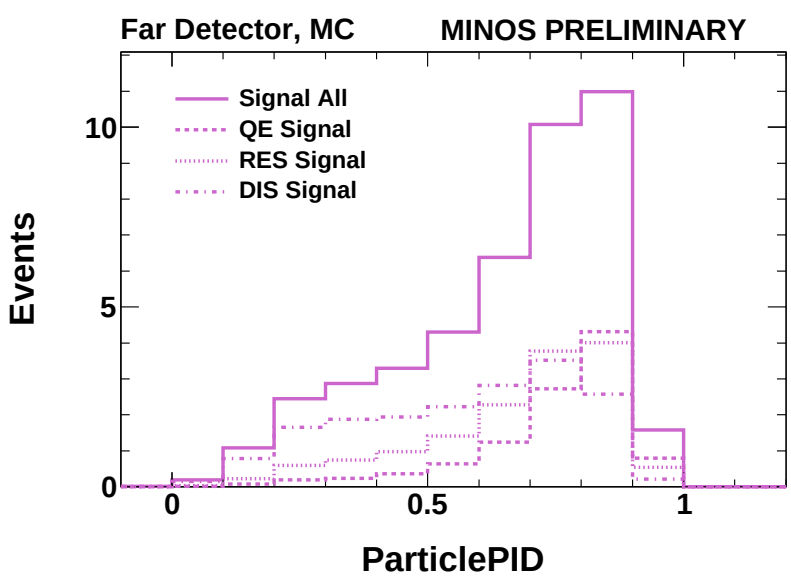

Figure 6.17: The distribution of the ParticlePID value in the Far Detector Monte Carlo for various signal event types

Selection	Type	QE	RES	DIS	Coh
Presel	All	22.65 (4.46%)	57.78 (11.37%)	424.34 (83.50%)	3.41 (0.67%)
	NC	1.99 (0.69%)	23.90 (8.33%)	258.05 (89.97%)	2.90 (1.01%)
	CC	3.05 (1.98%)	12.83 (8.33%)	138.06 (89.61%)	0.13 (0.08%)
	ν_e	10.83 (24.06%)	15.06 (33.47%)	18.81 (41.81%)	0.30 (0.66%)
	ν_τ	4.57 (46.91%)	2.91 (29.80%)	2.27 (23.28%)	0.00 (0.00%)
	ν_e^{beam}	2.21 (17.63%)	3.08 (24.61%)	7.14 (57.01%)	0.09 (0.75%)
ParticlePID	All	10.72 (12.59%)	12.54 (14.73%)	59.66 (70.03%)	2.27 (2.66%)
	NC	0.02 (0.04%)	1.68 (3.76%)	40.90 (91.65%)	2.03 (4.55%)
	CC	0.02 (0.16%)	0.32 (2.96%)	10.44 (96.84%)	0.00 (0.04%)
	ν_e	7.84 (34.61%)	8.32 (36.73%)	6.32 (27.89%)	0.18 (0.77%)
	ν_τ	1.26 (58.19%)	0.61 (28.24%)	0.29 (13.57%)	0.00 (0.00%)
	ν_e^{beam}	1.59 (32.06%)	1.62 (32.59%)	1.70 (34.19%)	0.06 (1.16%)
ANN11	All	10.73 (14.22%)	12.32 (16.33%)	50.05 (66.35%)	2.34 (3.10%)
	NC	0.05 (0.13%)	2.00 (4.96%)	36.15 (89.66%)	2.11 (5.24%)
	CC	0.01 (0.15%)	0.22 (2.99%)	7.00 (96.84%)	0.00 (0.02%)
	ν_e	7.95 (36.82%)	8.06 (37.30%)	5.42 (25.09%)	0.17 (0.79%)
	ν_τ	1.12 (60.99%)	0.51 (27.60%)	0.21 (11.41%)	0.00 (0.00%)
	ν_e^{beam}	1.59 (35.72%)	1.54 (34.54%)	1.27 (28.55%)	0.05 (1.20%)
ANN14	All	9.50 (16.84%)	9.60 (17.02%)	35.31 (62.58%)	2.01 (3.56%)
	NC	0.02 (0.08%)	1.06 (3.76%)	25.30 (89.73%)	1.81 (6.44%)
	CC	0.00 (0.07%)	0.11 (2.17%)	4.81 (97.76%)	0.00 (0.00%)
	ν_e	7.21 (39.41%)	6.81 (37.25%)	4.13 (22.58%)	0.14 (0.77%)
	ν_τ	0.87 (62.25%)	0.38 (26.98%)	0.15 (10.76%)	0.00 (0.00%)
	ν_e^{beam}	1.39 (38.67%)	1.25 (34.53%)	0.92 (25.40%)	0.05 (1.40%)

Table 6.3: For each of the PIDs, a breakdown of the selected events in Far Detector Monte Carlo by resonance code and event type. Note that ParticlePID selects about one more DIS signal ν_e and about 8.5 more DIS background events then the ANN PIDs. This is because of the reconstruction which is attempting to isolate components of the hadronic shower. The ParticlePID selects the same number of QE and RES type events as the ANN11. However, the two algorithms are not selecting the same events - a detail which is not apparent from the numbers presented here.

6.3.4 Variable Stability

It is important that the variables used in the ParticlePID ANN have similar behavior in both data and Monte Carlo. The first of many checks involves a data to Monte Carlo comparison in the Near Detector for each ANN input variable at preselection. Each variable is presented, scaled to 1×10^{20} POT, in figures 6.20 through 6.23. In general, the data to Monte Carlo agreement is within 20% - a level which is acceptable and comparable to that seen in the ANN11 and ANN14.

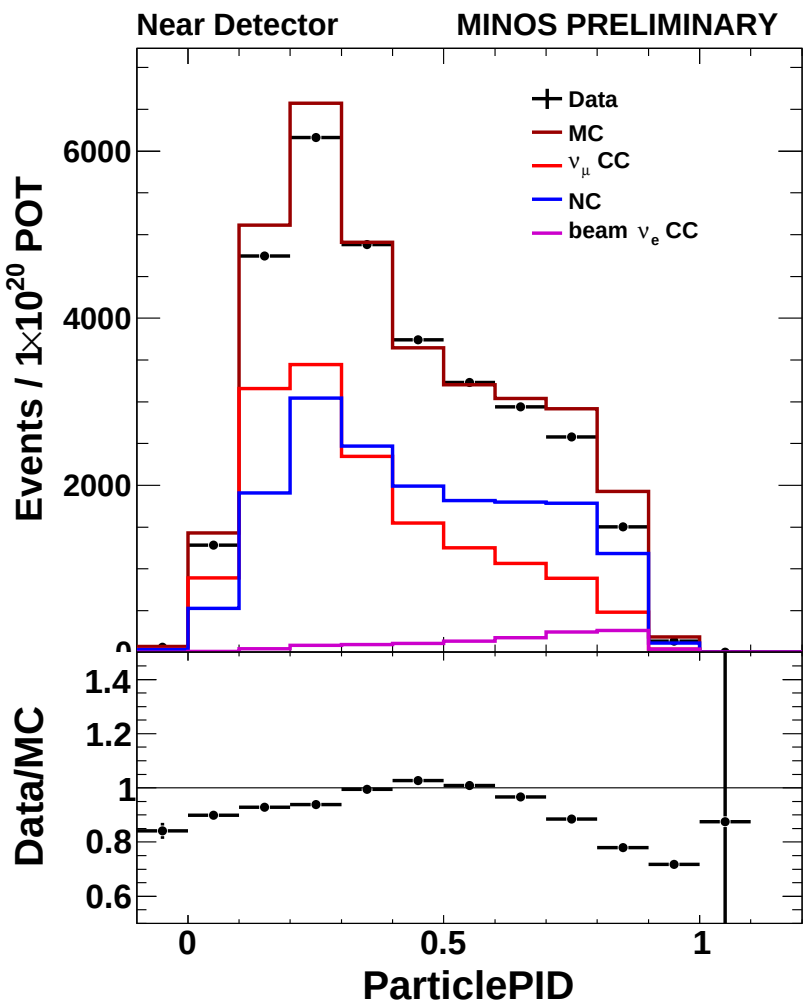

Figure 6.18: Top: Distribution of the ParticlePID in the Near Detector after the preselection cut for Monte Carlo and Data scaled to 1.00×10^{19}POT.

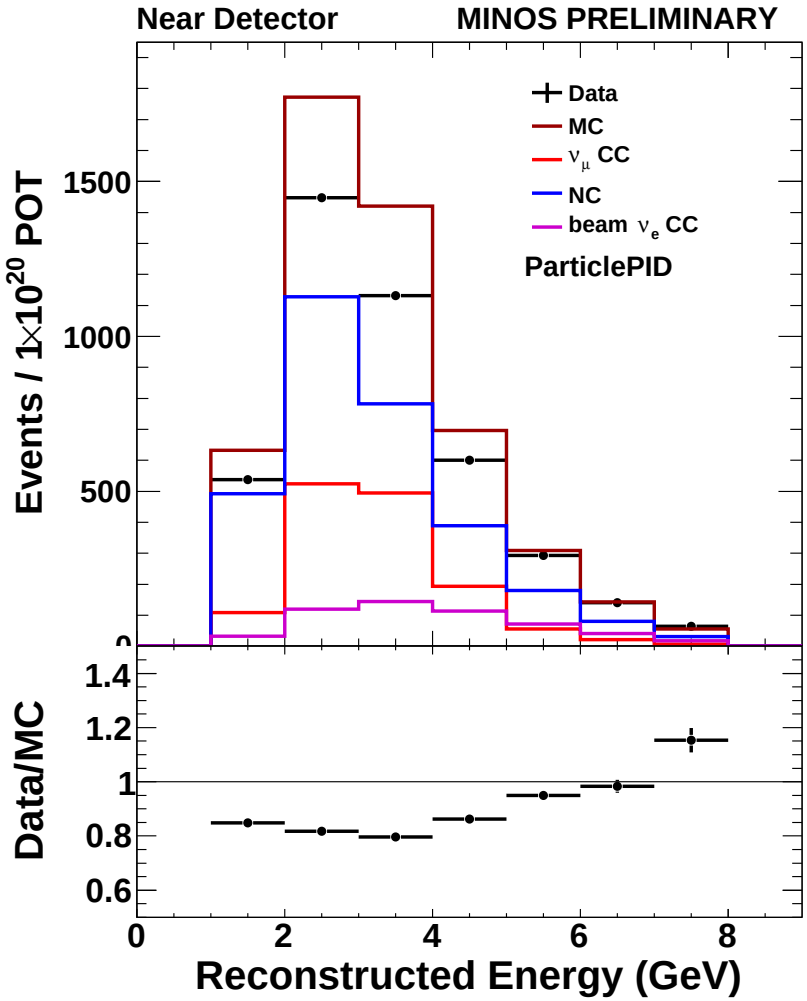

Figure 6.19: Top: Distribution of the reconstructed energy after the ParticlePID cut in the Near Detector for Monte Carlo and Data scaled to 1.00×10^{19}POT. Bottom: Data/Monte Carlo ratio

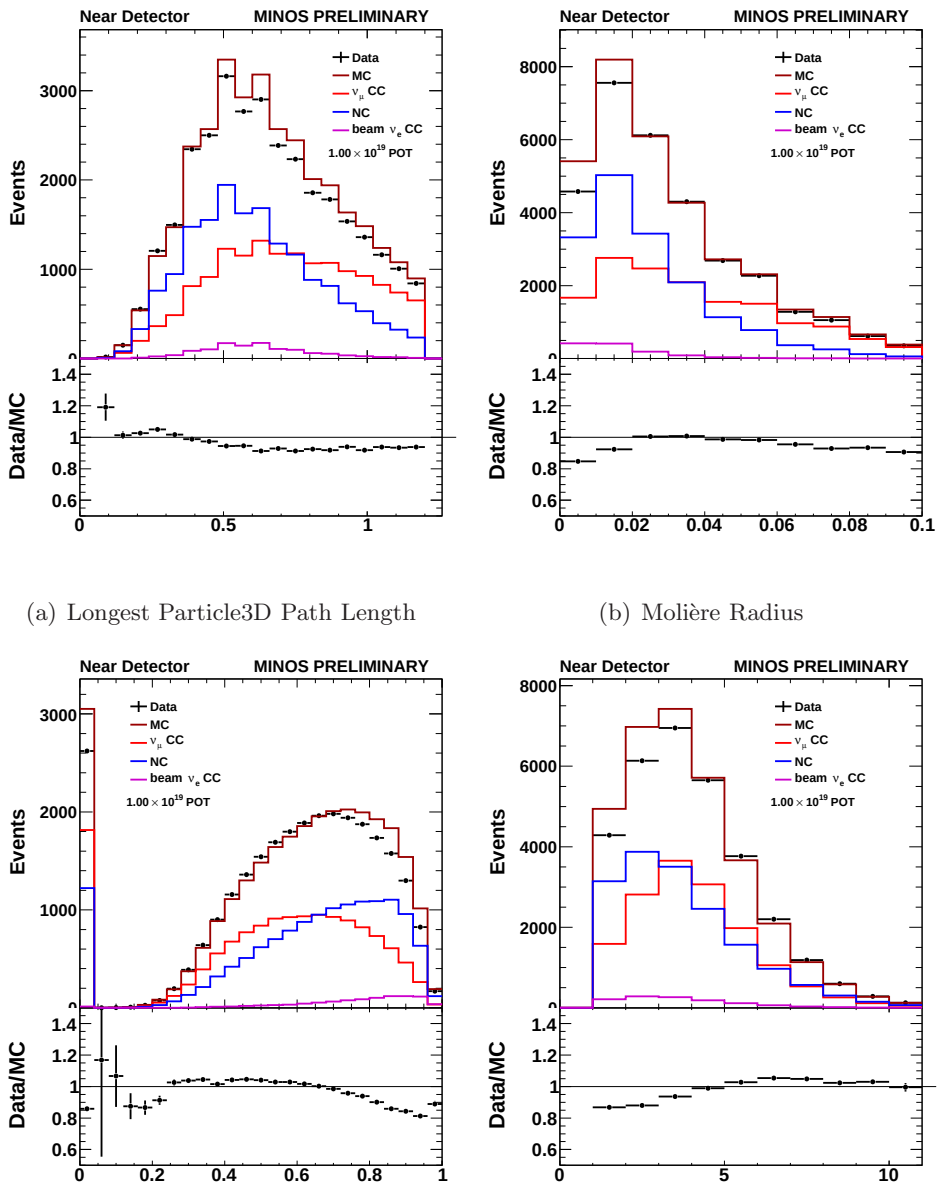

(a) Longest Particle3D Path Length

(b) Molière Radius

(c) Reconstructed EM Fraction

(d) Total Reconstructed Particles

Figure 6.20: Four of the variables used as inputs to the ParticlePID ANN are presented. The path length of the longest reconstructed particle is shown in (a). The Molière Radius of the event (in units of radial distance from z) computed using the 3D points of the reconstructed particles is shown in (b). The reconstructed electromagnetic shower fraction of energy in the event is shown in (c). The total number of reconstructed particles in the event is shown in (d).

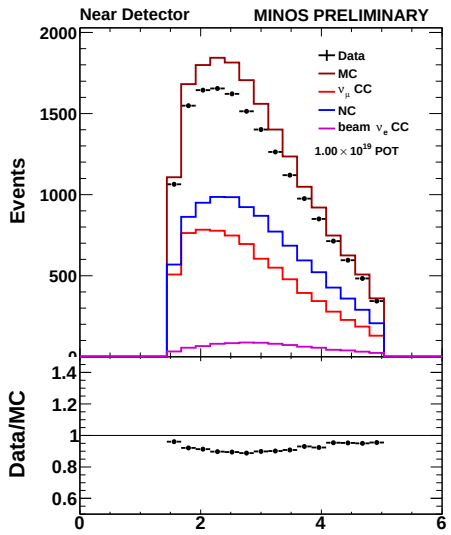

(a) EM Fit Parameter a

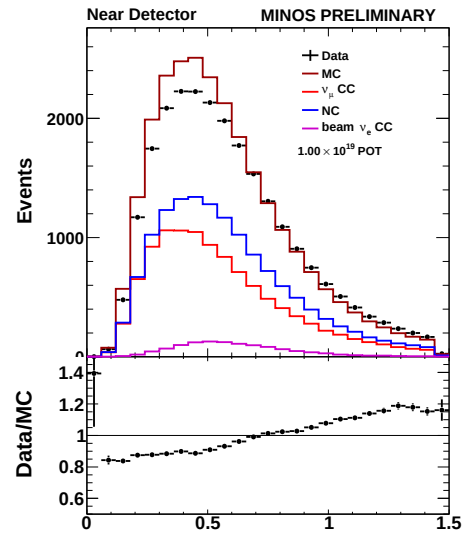

(b) EM Fit Parameter b

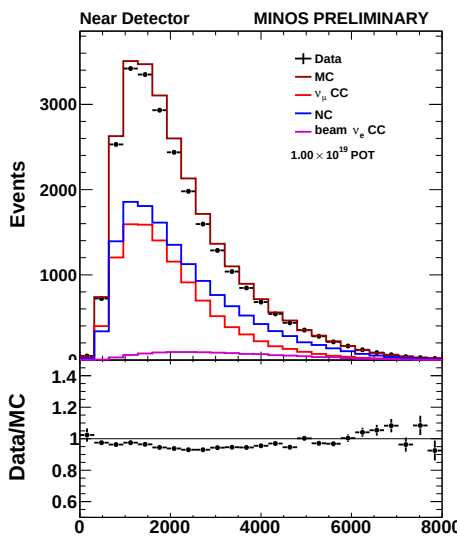

(c) EM Fit Parameter E_0

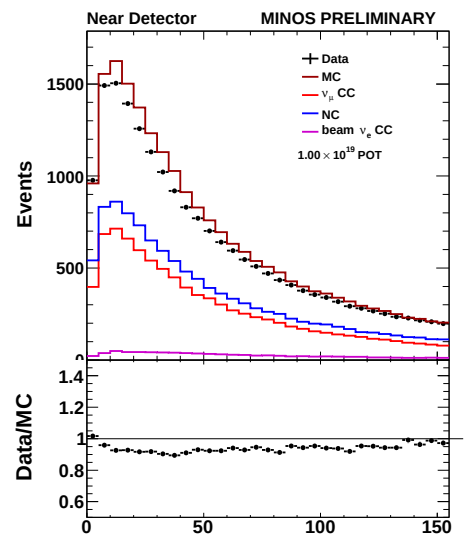

(d) EM Fit χ^2

Figure 6.21: Four of the variables used as inputs to the ParticlePID ANN are presented. The parameters of the electromagnetic shower fit to the largest energy reconstructed particle in the event are given for a, b, and E_0 in figures (a), (b), and (c). The χ^2 of the fit is given in figure (d).

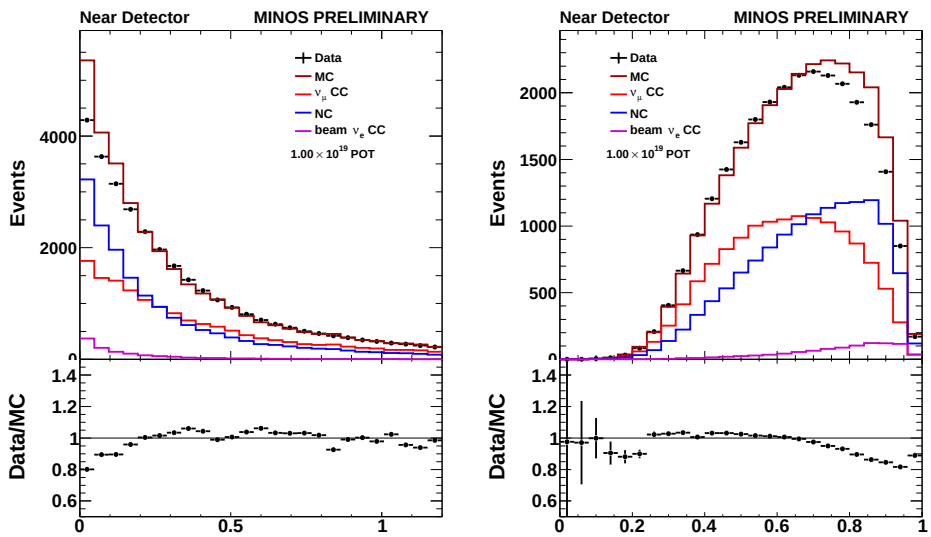

(a) Angle off of z axis

(b) Primary Particle3D Energy Fraction

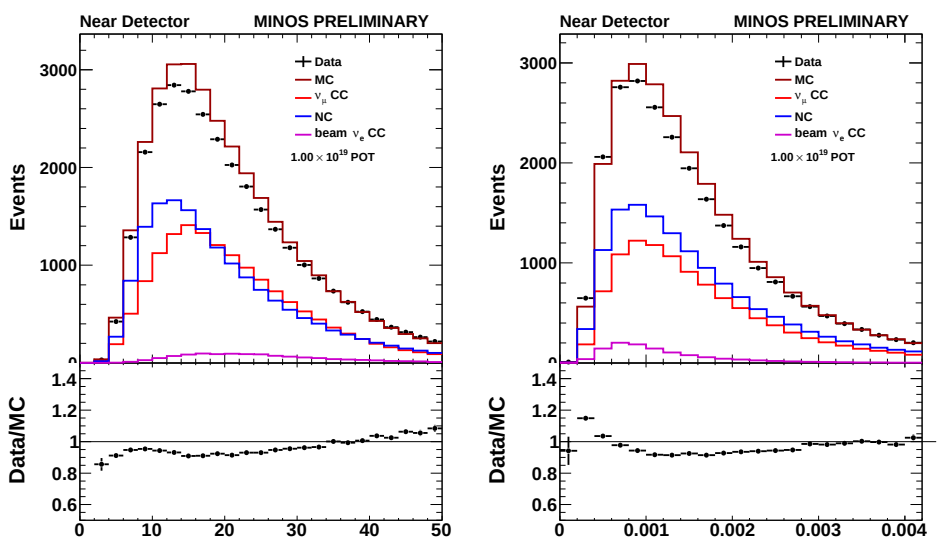

(c) The number of clusters in the event

(d) EM Fit Paramters a/E_0

Figure 6.22: Four of the variables used as inputs to the ParticlePID ANN are presented. The energy weighted angle from the z axis computed with the 3D points of the reconstructed particles is given in (a). The ratio of the energy of the largest reconstructed particle to the total event energy is given in (b). The number of clusters found in the event is shown in (c). The electromagnetic shower fit parameters to the largest energy reconstructed particle in the event provide the variable in (d), which is a/E_0 and is a measure of the distance to the shower maximum from the start of the shower in units of radiation length.

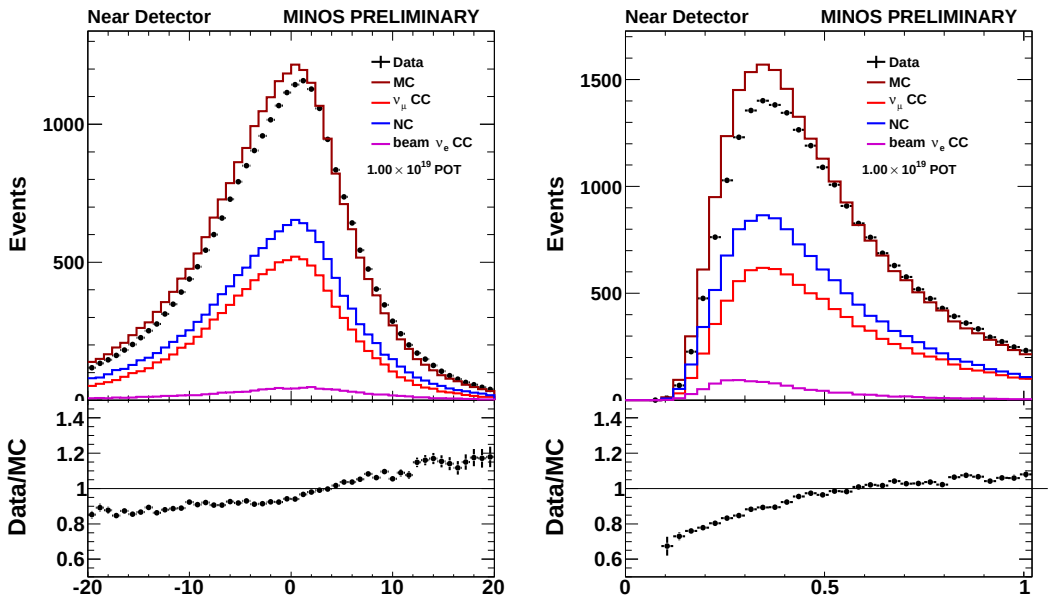

(a) Electromagnetic Profile Difference From Ideal - Largest Three Planes

(b) Electromagnetic Profile Difference From Ideal - χ^2

Figure 6.23: Two of the variables used as inputs to the ParticlePID ANN are presented. A "perfect" electromagnetic shower profile formed with the electromagnetic showers parameters (a,b,E_0) found in the electromagnetic shower fit of this Particle3D object is generated. The difference in the energy between the three most energetic planes at the peak of the profile form the variable shown in (a), and the χ^2 comparison between the actual and ideal shower profiles is shown in (b).

6.4 Other Details

Some additional details of the ParticlePID reconstruction and event identification algorithm will be presented here.

6.4.1 PID Overlap

The breakdown of events by resonance code type as presented in table 6.3 suggest that the ParticlePID is selecting the same number of QE, RES, and COH type events as the ANN11. The difference between the number of events selected between the two PIDs is entirely contained in DIS events, where the ParticlePID selects about one more signal and about 8.5 more background DIS events than the ANN11. This information might tend to suggest that the ParticlePID is simply the ANN11 with a higher acceptance on DIS type events. However, this is not the case.

The ParticlePID selects events of different topologies from the ANN11. This is evident in the comparison of the values of the two PIDs for a single event. Qualitatively, in comparing the ParticlePID to the ANN11 (as shown in figure 6.24), it can be seen by the shape of the distribution that these event selectors are less correlated than the ANN11 and the ANN14 (as shown in figure 6.25). The comparison of the ParticlePID to ANN14 is included for completeness in figure 6.26. The width of these distributions, as measured perpendicular to a diagonal line with a slope of one, gives a measure of how different the PIDs actually are.

Quantitatively, 39% of the events selected by the ParticlePID are not selected by the ANN11. By event type, 14% of RES, 30% of QE, and 46% of DIS events that are selected by the ParticlePID are not selected by the ANN11. If the only difference between the two PIDs was the additional selection of 10 more DIS events (with the assumption that the RES and QE events which are selected with the same quantity are actually the same

events) as presented in table 6.3, then it should be expected that only about 12% of the events selected by the ParticlePID would not selected by the ANN11. This large difference is explained by the fact that the ParticlePID and the ANN11 event selectors are actually selecting events with different topological characteristics.

This should be compared to the ANN14, for which only 12% of the events selected by the ANN14 are not selected by the ANN11. By event type, 5% of RES, 10% of QE, and 15% of DIS events selected by the ANN14 are not selected by the ANN11.

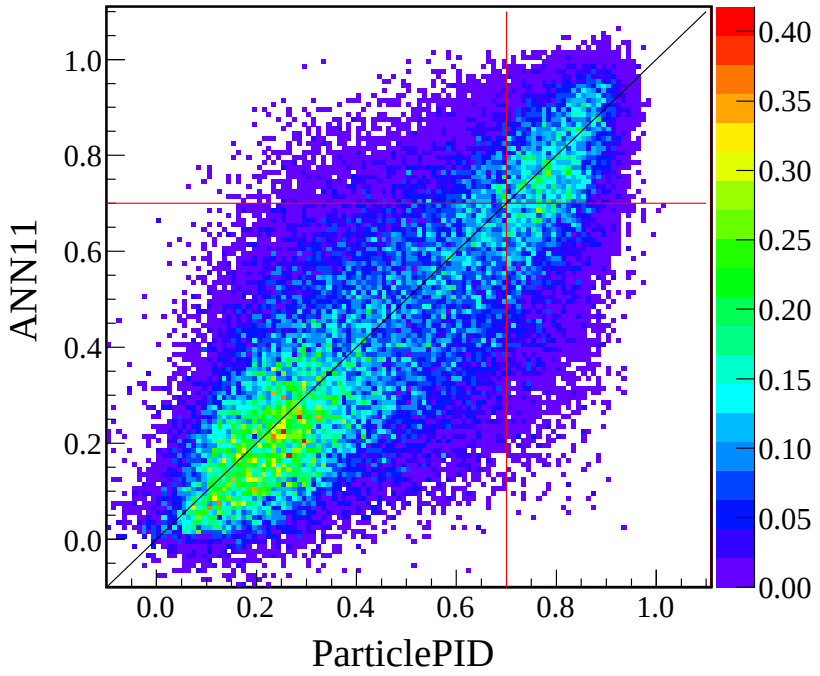

Figure 6.24: The ParticlePID and ANN11 values for each Far Detector Monte Carlo Event in a sample is shown.

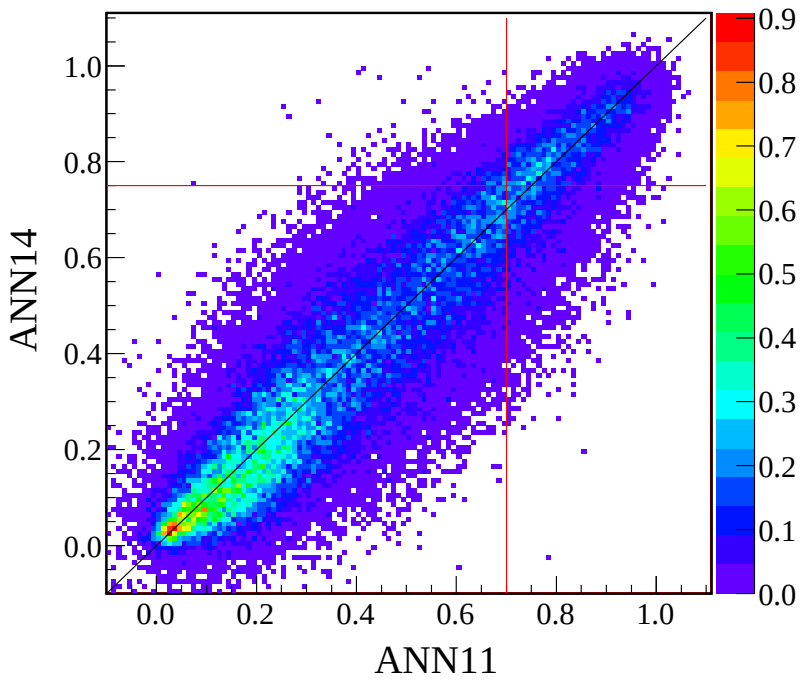

Figure 6.25: The ANN11 and ANN14 values for each Far Detector Monte Carlo Event in a sample is shown.

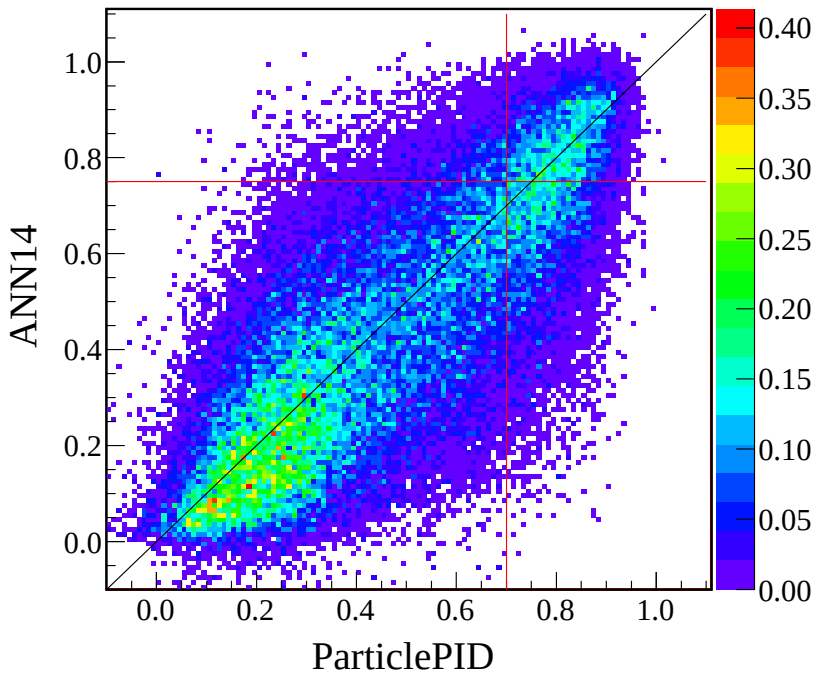

Figure 6.26: The ParticlePID and ANN14 values for each Far Detector Monte Carlo Event in a sample is shown.

6.4.2 Reconstruction of the Electromagnetic Shower Fraction

Since the ParticlePID reconstruction can identify the electromagnetic component of the shower, it is possible to reconstruct the electromagnetic shower fraction for ν_e CC type events. The electromagnetic shower fraction is closely related to the kinematic variable hadronic y, as shown in figure 6.27. This reconstructed electromagnetic shower fraction variable is used in the ParticlePID ANN and is the only reconstructed variable present which directly corresponds to a kinematic variable intrinsic to the interaction.

The value $\Upsilon \equiv$(1 - reconstructed electromagnetic shower fraction) as a function of the Monte Carlo true hadronic y value for ν_e CC events after preselection is shown in figure 6.27(d). A fit can be performed to this distribution, from which it can be seen that the Υ agrees with y (the fit has a slope of 1) for events with $\Upsilon < 0.4$ (see figure 6.28(a)). There is a transition for larger values of y where an increased production of π^0 begins to cause a decrease in Υ. The ParticlePID algorithm is looking for the largest electromagnetic shower component and using that to calculate the value of the electromagnetic shower fraction. A π^0 in an event absent of an electron appears identical to an event with an electron and no π^0. The fit is offset from zero because events where the algorithm only finds a single electron still have a non zero y. In such cases, the energy transferred to the target nucleus is not sufficient to cause a distinguishable energy deposition in the detector. If the fit is instead performed on Υ for y, there is a correlation to values of $y < 0.7$ (see figure 6.28(b)). The fit of this distribution has a slope of about 0.3 and is a good indicator that the electromagnetic fraction is including energy from hadronic π^0 showers in the calculation, as expected

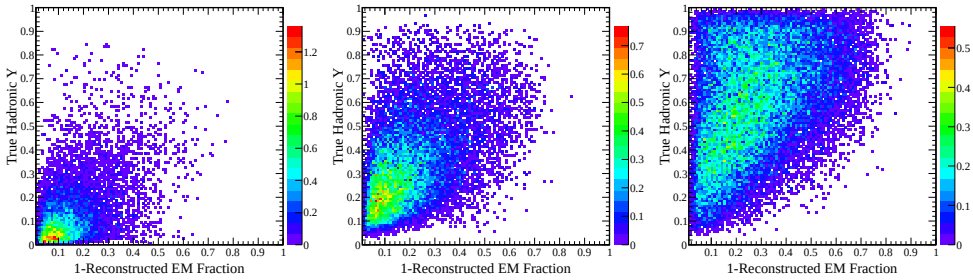

(a) ν_e QE CC (b) ν_e RES CC (c) ν_e DIS CC

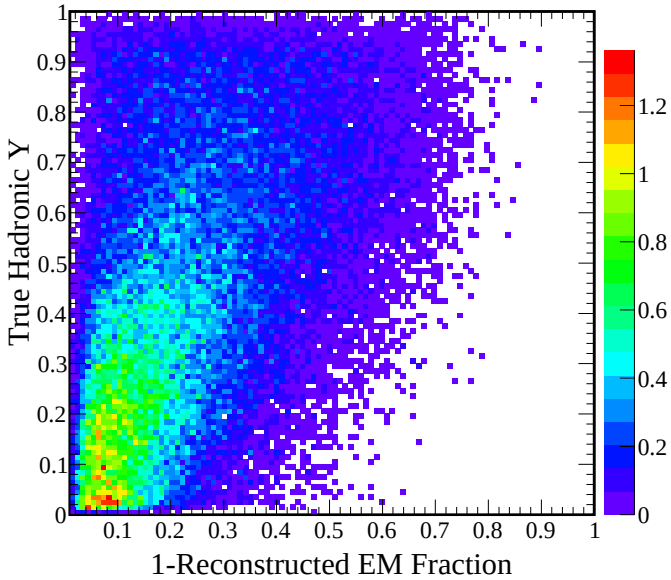

(d) All ν_e CC

Figure 6.27: Figures (a), (b), and (c) illustrate the different regions of hadronic y from which QE, RES, and DIS type charged current events are generated and the corresponding value of Υ =1 - reconstructed shower energy. Figure (d) includes all ν_e in the preselection sample. All plots are obtained for ν_e Far Detector Monte Carlo events after the preselection cut.

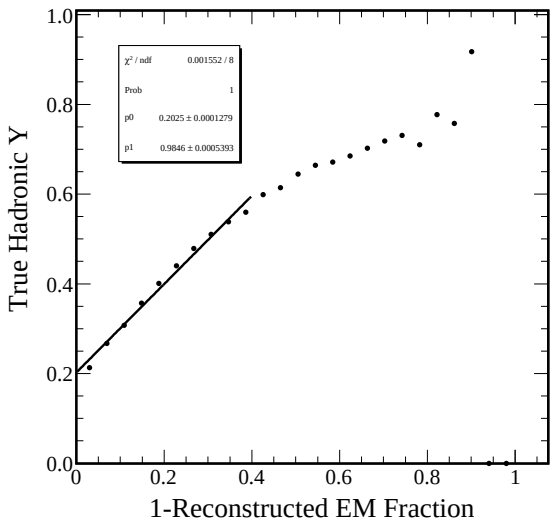

(a) A fit on all ν_e

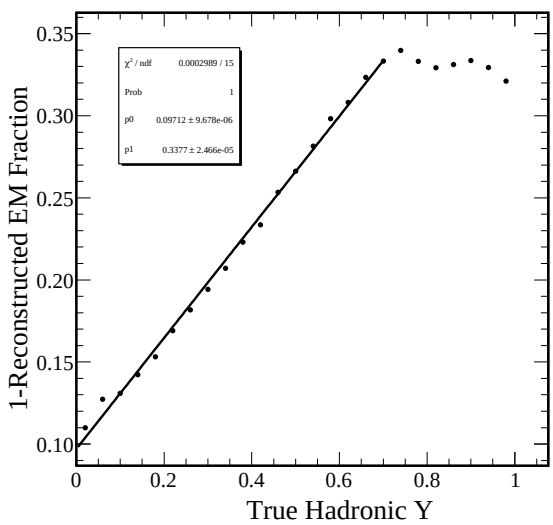

(b) A fit on all ν_e

Figure 6.28: A linear fit on y for Υ in the all ν_e sample in figure (a) shows a good correlation between y and Υ for $\Upsilon < 0.4$. A linear fit on Υ for y in figure (b) shows a good correlation for $y < 0.7$. The true hadronic y is closely related to Υ for low y. At higher y, there is a greater chance of π^0 production, which will cause an decreased Υ as more electromagnetic shower activity is found by the reconstruction software. All plots are obtained for ν_e Far Detector Monte Carlo events after the preselection cut.

6.4.3 Vertex Resolution

The ParticlePID algorithm and the standard reconstruction both attempt to measure the location of the neutrino interaction within the detector. The vertex found by the standard reconstruction is currently used in the determination of which events are contained within the fiducial volume of the detector for both the ANN11 and ParticlePID analyses for simplicity in processing. The vertex calculated by the ParticlePID is otherwise used as the only vertex position within the algorithm for the calculation of Particle3D positions, electromagnetic shower fits, and the other variables produced for use in the ParticlePID ANN. A comparison between the vertex positions measured by the ParticlePID and standard reconstruction algorithms for ν_e events in the Far Detector Monte Carlo after preselection cuts is presented in figure 6.29. Improved measurements are seen in the position of x and y, with resolutions that are about 10% better for the ParticlePID. The spacing between the scintillator planes is evident in the measurement of the vertex position in z. Here, the ParticlePID too often places the position of the event in z one plane beyond where the actually interaction occurred. This is due to an improperly calculated z axis offset used in the code and is something that could be improved in future use of the software. The transverse position is about 12% better for the ParticlePID and the overall distance between the measured and true vertex is about the same for the two methods, but the resolution on that measurement for the ParticlePID is better by about 18%. Also interesting is the shape of the distribution for the total distance between the measured and true vertex, which contains a single peak for the ParticlePID and which has an irregular and possibly multiple peak distribution for the standard reconstruction.

The same comparisons for all events after preselection cuts are shown for the Far Detector in figure 6.30 and the Near Detector in figure 6.31. Similar features are evident. The transverse vertex position is 11% better for the ParticlePID in the far and 17% better

in the near with an improvement in resolution of 19% in the far and 31% in the near. The total difference in vertex position is 12% better for the ParticlePID in the far and 18% better in the near with an improvement in resolution of 25% in the far and 40% in the near.

The ParticlePID shows better near to far agreement in both the mean and the RMS of the distributions than those obtained with the standard reconstruction for all vertex measurements compared to true positions. The far to near ratio of the difference between the measured and actual transverse vertex position is 96% for the ParticlePID compared to 89% for the standard reconstruction. The same comparison for the RMS of the distribution yields a ratio within 97% for the ParticlePID compared to 83% for the standard reconstruction. The far to near ratio of the difference between the measured and actual total vertex position is 99% for the ParticlePID compared to 93% for the standard reconstruction. The same comparison for the RMS of the distribution yields a ratio of 101% for the ParticlePID and 81% for the standard reconstruction.

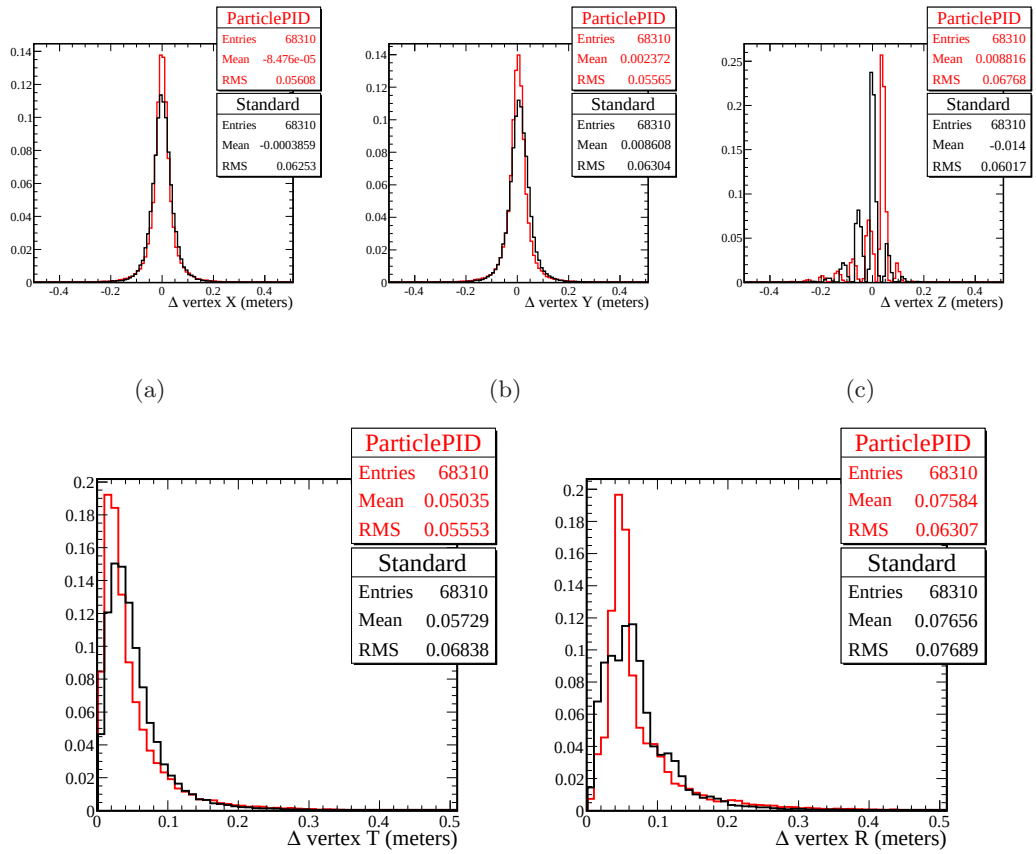

(a) (b) (c)

(d) (e)

Figure 6.29: The vertex resolution in the Far Detector Monte Carlo for ν_e events after the preselection cut. The events are included in proportions to what is expected in the actual Far Detector data. Comparisons between the true interaction location and the vertex found with the standard reconstruction and the ParticlePID algorithm are both shown. Comparisons between the true and measured event vertex in x, y, and z are presented in (a), (b) and (c). The difference in the transverse plane is presented in (d) and the total distance between the true and measured vertex is presented in (e). In general, the ParticlePID algorithm produces a vertex measurement that has better agreement with the true interaction position than that measured by the standard reconstruction. Grouping can be seen in the measurement of z which corresponds to the distance between scintillator planes. There is a systematic shift in the ParticlePID measurement of the vertex in z, which corresponds to a position in the next plane downstream from the actual interaction.

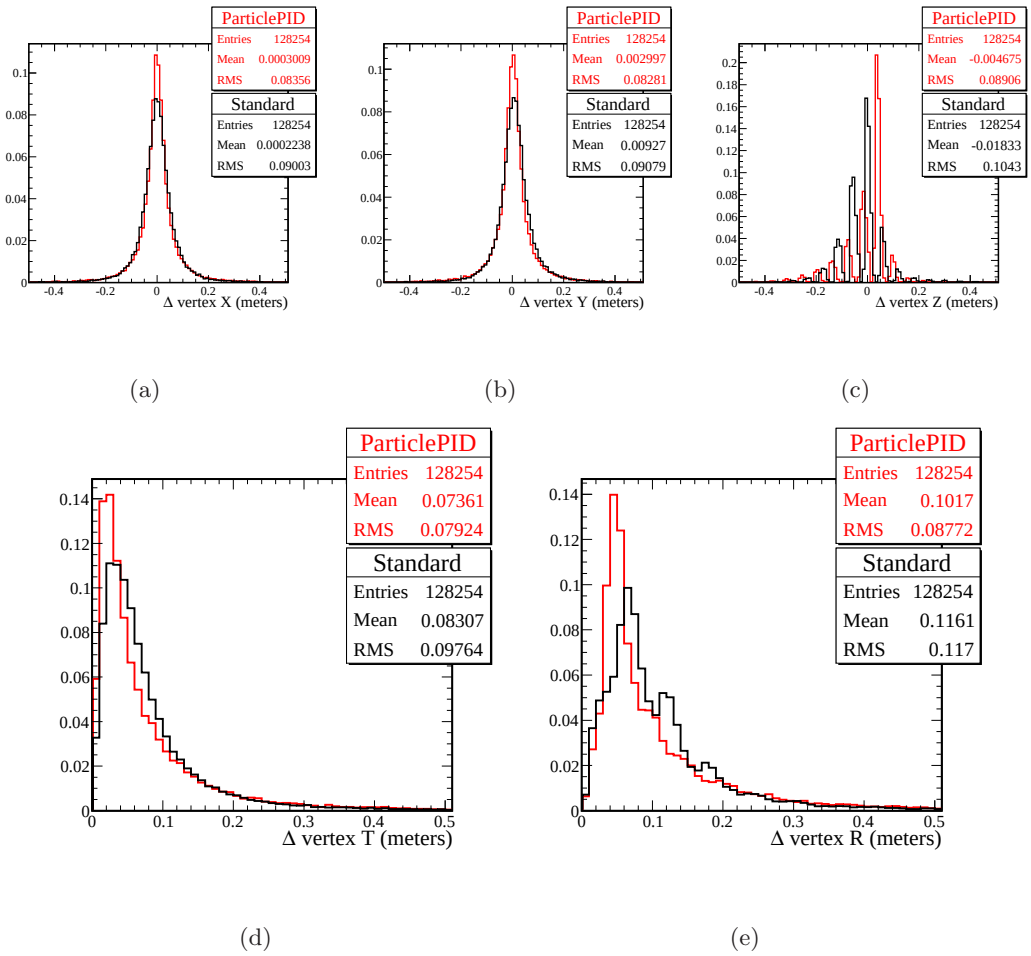

Figure 6.30: The vertex resolution in the Far Detector Monte Carlo for all event types after the preselection cut. The events are included in proportions to what is expected in the actual Far Detector data. Comparisons between the true interaction location and the vertex found with the standard reconstruction and the ParticlePID algorithm are both shown. Comparisons between the true and measured event vertex in x, y, and z are presented in (a), (b) and (c). The difference in the transverse plane is presented in (d) and the total distance between the true and measured vertex is presented in (e). In general, the ParticlePID algorithm produces a vertex measurement that has better agreement with the true interaction position than that measured by the standard reconstruction. Grouping can be seen in the measurement of z which corresponds to the distance between scintillator planes. There is a systematic shift in the ParticlePID measurement of the vertex in z, which corresponds to a position in the next plane downstream from the actual interaction.

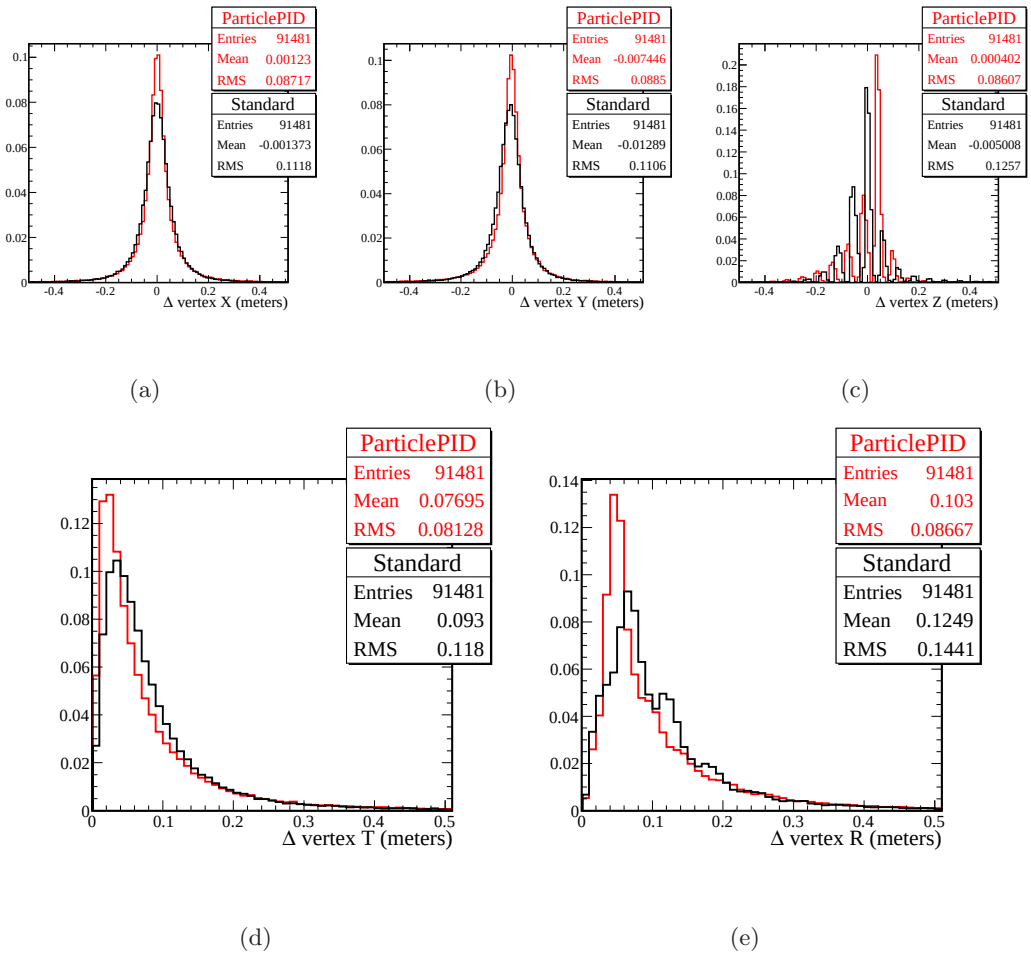

Figure 6.31: The vertex resolution in the Near Detector Monte Carlo for all event types after the preselection cut. The events are included in proportions to what is expected in the actual Far Detector data. Comparisons between the true interaction location and the vertex found with the standard reconstruction and the ParticlePID algorithm are both shown. Comparisons between the true and measured event vertex in x, y, and z are presented in (a), (b) and (c). The difference in the transverse plane is presented in (d) and the total distance between the true and measured vertex is presented in (e). In general, the ParticlePID algorithm produces a vertex measurement that has better agreement with the true interaction position than that measured by the standard reconstruction. Grouping can be seen in the measurement of z which corresponds to the distance between scintillator planes. There is a systematic shift in the ParticlePID measurement of the vertex in z, which corresponds to a position in the next plane downstream from the actual interaction.

6.4.4 Other Attempts

A brief mention will be made of the other explored uses of the reconstruction information generated by the ParticlePID algorithm.

An attempt was made to reconstruct the kinematic quantities describing QE ν_e interactions. In Monte Carlo events, where both the proton and electron were reconstructed as individual Particle3D objects, such a calculation is possible. However, there are a substantial number of events which do not have a useable proton reconstructed as a Particle3D object. While it was possible to perform the calculation for selected Monte Carlo events, it does not provide a useful tool to analyze the entire event sample.

An attempt was made to measure the average charge of a shower through a measurement of the curvature of the Particle3D object. While a charge dependent bias was seen in the distribution of the shower curvature, it was only on the order of a few percent and thus was not useful as a distinguishing variable.

Chapter 7

An Additional Tool - Muon Removal

It is desirable to check the quality of the reconstruction software on actual data events containing showers. However, doing so could easily unblind the analysis. There is a method that has been developed[85] which uses ν_μ CC events to provide a sample of data based shower events which are completely independent of the NC and ν_e events, thereby preventing the possibility of unblinding the analysis. This procedure is described here as a prerequisite to the following chapters, which will make reference to this method.

7.1 Muon Removed ν_μ CC (MRCC) Events

The process of a ν_μ CC interaction is identical to the NC interaction with the exception that in the CC interaction a $W^\pm$ is exchanged whereas in the NC interaction a Z is exchanged, as illustrated in figure 2.2. The hadronic interaction in both events is

identical in nature [1].

7.1.1 Method

The MRCC processing occurs as a second reconstruction pass during the standard reconstruction. After the event has been reconstructed, a check is performed to see if it has a reconstructed track. If it does, the hits associated with that track are marked for removal. Hits which are shared between the track and other objects, such as showers, have their energy adjusted accordingly to subtract out the energy deposited by a typical muon. Attributes of the removed track are saved for later use, so that a sample of MRCC events can be chosen with the requirement that they all originally had a well defined track that was removed. The list of hits, less those associated with the removed muon, are then reprocessed through the remaining steps of reconstruction to form the MRCC event.

The MRCC event is then processed through the ν_e analysis code as if it were a normal event. Events chosen for the MRCC sample are those which in the original event had a track with a good track fit and which pass the ν_μ CC analysis PID[86] in order to ensure that the sample does not contain any non ν_μ CC events. The information about the removed muon track (energy, position, etc) is retained for use elsewhere. The procedure is illustrated in figure 7.1.1. The original ν_μ CC event, the hits remaining after the muon removal, and a close up of the final hadronic shower remnant are detailed.

7.1.2 Uses

This method will be used in three different places in the analysis. In the first case, as described in section 8.2.2, MRCC events will be used in the Near Detector beam

[1] Actually, only nearly identical - a quark in the target nucleus changes in the CC and not in the NC interaction.

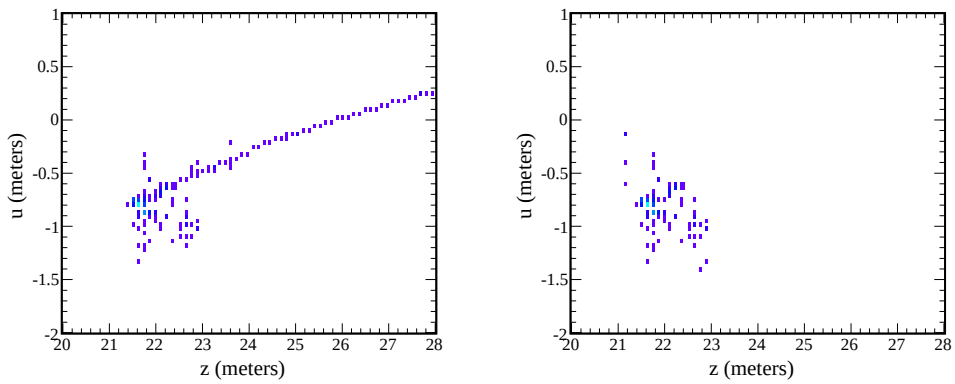

(a) Standard Event (b) Muon Removed Event

Figure 7.1: An illustration of the Muon Removal from ν_μ CC Event (MRCC) method. The original ν_μ CC DIS event is shown in figure (a). After the strips assigned to a muon track are identified and removed, the remaining information is reprocessed to form the muon-removed event, shown in figure (b). The muon removed events only contain information about the hadronic showers and they are used to form an independent data based sample of NC-like events.

decomposition. Secondly, MRCC events are used in the MRE process described in section 7.1.3. Here, a Monte Carlo electron is added to the data based hadronic shower from the MRCC event. Since electrons are well modeled by Monte Carlo, but the hadronic showers are not, this provides a data based correction to ν_e event selection efficiencies. Finally, the MRCC events are used as a cross check of the extrapolation method, as described in section 10.2. A prediction is made for the Far Detector data MRCC events and is compared to the actual Far Detector data MRCC event sample to confirm that the extrapolation method is functioning as expected.

7.1.3 Muon Removed ν_μ CC with Monte Carlo Electron Events (MRE)

A technique was developed to use data based hadronic showers from MRCC events along with a Monte Carlo electron in order to provide a data based sample of ν_e events

independent of the actual Far Detector signal events[87]. This sample is called MRE (Muon Removed Electron added). The information about the removed muon (energy and direction) is used to obtain a single Monte Carlo electron from a sample already made for this purpose. The strip energy information from this bare electron is merged with the strip energy information from the hadronic shower produced by the MRCC process to produce a data-Monte Carlo hybrid event. This event is then reprocessed through the reconstruction software.

The MRE sample is useful both as a sideband check of the Far Detector data, as described in section 10.3, and also as a independent measurement of signal ν_e selection efficiency in the Far Detector, as explained in section 9.5.2.

Chapter 8

Predicting the Far Detector Data

In order to make a measurement of any oscillated ν_e signal in excess of the expected background, it is vital to understand how much background is expected. The PIDs used to select the ν_e events from the Far Detector data sample will also select ν_e-like events which are actually NC, ν_μ CC, ν_τ CC, or beam ν_e CC events. Each of these background types must be accounted for separately in the prediction, as the extrapolation of each from the Near Detector occurs by different mechanisms.

8.1 Overview of the Extrapolation Method

The extrapolation method used in the analysis is discussed in detail in [88] and is summarized here. For each of the components that are present in the Near Detector, $\alpha =$ (NC, ν_μ CC, or beam ν_e), a prediction, F_i^α can be made for the expected number of events in the Far Detector for that component in 1 GeV bins of energy, i,

$$F_i^\alpha = \left(\frac{f_i^\alpha}{n_i^\alpha}\right) N_i^{\alpha,data} \tag{8.1}$$

where f_i^α and n_i^α are the number of type α selected events in energy bin i in the Far

and Near Detector Monte Carlo after the PID is applied. The Far to Near Detector Monte Carlo ratio accounts for differences in the flux between the two detectors including $1/R^2$ effects, and differences in beamline geometry, focusing, and decay kinematics, the mass of each detector, and any differences in selection efficiency for the background component. The ratio also includes the effects of oscillations for a given set of oscillation parameters for these components. This Near to Far Detector ratio is applied to the Near Detector data, $N_i^{\alpha,data}$, to give the Far Detector prediction.

The prediction of the oscillated ν_e and ν_τ components of the Far Detector data must be carried out differently, as neither of these event types are present in the Near Detector. The components arise from the oscillations of the ν_μ events, and so their prediction begins with the prediction for the ν_μ CC events in the Far Detector using the method described previously. However, now the prediction is made using ν_μ CC selected samples created in a way similar to the selection used in the creation of MRCC events. Since oscillations are dependent on the true energy of the neutrino and not the energy of the resulting interaction event, it is necessary to convert the predicted reconstructed energy for ν_μ CC events to true energy before making the ν_e and ν_τ predictions.

The predicted number of ν_μ CC events in the Far Detector in bins of true energy takes the predicted number in terms of reconstructed energy and converts it to true energy with the use of a reconstructed to true energy matrix, RT_{kj}^{CClike}, which is generated using Far Detector Monte Carlo. This number is then scaled by the efficiency, E_j, and purity, P_j, of the ν_μ CC like sample at the Far Detector. The resulting prediction for the ν_μ CC event energy spectrum in bins of true energy, j, is given as

$$F_j^{\nu_\mu CC} = \left[\sum_k \frac{f_k^{CClike}}{n_k^{CClike}} N_k^{CClike,data} RT_{kj}^{CClike} \right] \frac{P_j}{E_j} \tag{8.2}$$

The predictions for the ν_e and ν_τ components are then calculated. The Far De-

tector predicted ν_μ spectrum in bins of true energy is oscillated, where the probibility of a transition from $\nu_\mu \rightarrow \nu_{e/\tau}$ at true energy, j, is given by $P_j^{\nu_\mu \rightarrow \nu_{e/\tau}}$. A correction is made to account for the differences between the cross section of the ν_μ ($\sigma_j^{\nu_\mu}$) and the $\nu_{e/\tau}$ ($\sigma_j^{\nu_{e/\tau}}$). The energy spectrum is then transformed from true to reconstructed energy using $TR_{ij}^{\nu_{e/\tau}}$. This matrix is calculated using the Far Detector Monte Carlo, but this time for the particular neutrino type being predicted (ν_e or ν_τ). Finally, the spectrum takes into account the selection efficiency for the component, $\epsilon_i^{\nu_{e/\tau}}$, which is taken from the Far Detector Monte Carlo. The final predicted reconstructed energy spectrum for the Far Detector data components ν_e and ν_τ is given by

$$F_i^{\nu_{e/\tau}CC} = \sum_j F_j^{\nu_\mu CC} \left(\frac{\sigma_j^{\nu_{e/\tau}}}{\sigma_j^{\nu_\mu}} \right) P_j^{\nu_\mu \rightarrow \nu_{e/\tau}} TR_{ij}^{\nu_{e/\tau}} \epsilon_i^{\nu_{e/\tau}} \tag{8.3}$$

An adjustment is applied to the predicted ν_e efficiency, $\epsilon_i^{\nu_e}$, using the sample of Near Detector MRE events in the form

$$\epsilon_{i,adj}^{\nu_e} = \epsilon_i^{\nu_e} \times \frac{N_{MRE}^{Data}}{N_{MRE}^{MC}}$$

This adjusted efficiency is used to eliminate errors arising from an improperly modeled hadronic shower, since the hadronic shower used in MRE is from data events. The total effect[89] of this adjustment lowers the expected signal in the ParticlePID by 3% and increases the expected signal in the ANN11 by 1%. There is a negligible effect on the ANN14.

8.2 Near Detector Decomposition

As can be clearly seen by the extrapolation method mentioned previously, it is necessary to know how many events in the Near Detector data fall into each of the event categories (NC, ν_μ CC, and beam ν_e). The decomposition cannot be simply determined

from the Near Detector Monte Carlo because a comparison of data to Monte Carlo quickly demonstrates that there are some large differences, as illustrated by the data/Monte Carlo ratio in table 8.1. The discrepancy after the preselection cuts is 8%, and the largest discrepancy seen after a PID cut is 18% for the ParticlePID.

Cut	NC	$\nu_\mu CC$	beam ν_e	Total MC	Data	Data/MC
Preselection	19604.31	20773.69	1344.50	41722.50	38208.63	0.916
ParticlePID	3014.11	1381.16	531.46	4926.73	4037.81	0.820
ANN11	3262.31	1177.66	536.75	4976.72	4348.18	0.874
ANN14	2381.50	868.48	473.36	3723.33	3118.62	0.838

Table 8.1: Each component of the Near Detector Monte Carlo is shown for each PID. The total number of Monte Carlo and data events is also shown for each selection method. The Data/Monte Carlo ratio illustrates a disagreement which needs to be corrected by a Near Detector data decomposition utilizing either the Horn On-Horn Off or MRCC decomposition methods. These numbers are normalized to 1×10^{19} POT and include data and Monte Carlo from Run 3 only for this example.

Two techniques have been developed to perform the decomposition on the Near Detector data. The Horn On-Horn Off with High Energy Beam method (HOOHE) makes use of the differences in the beam energy spectrum with different horn configurations to perform the decomposition. The MRCC method uses the MRCC samples as an independent measure of NC event modeling to extract the Near Detector data NC component, from which the other components can be calculated. The HOOHE method is the primary method used in the analysis and the MRCC method provides a means to cross check the primary method.

8.2.1 Horn On-Off Method

The Horn On-Off Method (HOO) method was originally developed[90] to estimate the component contributions to the Near Detector data spectrum using samples from the horn off (L010000) and the horn on (L010185) configurations, and was used in this manner[91] in the previous analysis.

For this analysis, the method has been extended[92] to use an arbitrary number of beam configurations. This method, its application to the analysis, and the resulting decomposition, will be summarized here.

Method

Each beam configuration, BC, satisfies the following linear equation which requires the total observed Near Detector data spectrum at a given beam condition to equal the sum of the components of that beam condition measured by the decomposition method. The number of data events, N, in each beam component (NC, ν_μ CC, or beam ν_e in a given beam configuration, BC, is related to the number of events in the normal horn on data (L010185) configuration by a ratio between the special beam configuration to the normal beam configuration for the Monte Carlo for that component.

$$\frac{N_{NC}^{BCMC}}{N_{NC}^{ONMC}} N_{NC}^{ONdata} + \frac{N_{CC}^{BCMC}}{N_{CC}^{ONMC}} N_{CC}^{ONdata} + \frac{N_{beam\nu_e}^{BCMC}}{N_{beam\nu_e}^{ONMC}} N_{beam\nu_e}^{ONdata} = N_{Total}^{BCdata} \tag{8.4}$$

This assumes that the Monte Carlo correctly describes the differences in the spectrum of each component between the different beam configurations. It does not require the Monte Carlo to actually match the data for any given beam configuration. Any uncertainties in the Monte Carlo beam modeling will therefore be second order effects.

A system of these linear equations can be constructed such that

$$\underbrace{\begin{pmatrix} r_{NC}^{BC1} & r_{CC}^{BC1} & r_{beam\nu_e}^{BC1} \\ r_{NC}^{BC2} & r_{CC}^{BC2} & r_{beam\nu_e}^{BC2} \\ r_{NC}^{BC3} & r_{CC}^{BC3} & r_{beam\nu_e}^{BC3} \\ \dots & \dots & \dots \end{pmatrix}}_{R} \underbrace{\begin{pmatrix} X_{NC} \\ X_{CC} \\ X_{beam\nu_e} \end{pmatrix}}_{X} = \underbrace{\begin{pmatrix} N_{BC1} \\ N_{BC2} \\ N_{BC3} \\ \dots \end{pmatrix}}_{N} \tag{8.5}$$

where $r_{NC}^{BC1} = \frac{N_{NC}^{BC1\ MC}}{N_{NC}^{ON\ MC}}$, $X_{NC} = N_{NC}^{ON\ data}$, and $N_{BC1} = N_{Total}^{BC1\ data}$. The vector, X is the

decomposition of the Near Detector data that needs to be determined. This system of linear equations can be solved for X using the method of least squares minimization.

The least squares method solves a system of linear equations, $Ax = b$, by minimizing the 2-norm of the weighted residual vector, $W(Ax-b)$. This equivalently means that the solution can be found by the minimization of $\chi^2 = (Ax-b)^T W^T W(Ax-b)$. If the diagonal weight matrix, $W_{ij} = \frac{\delta_{ij}}{\sigma_i}$, is used, then the equation reduces to $\chi^2 = \sum_i \frac{(\sum_j A_{ij}x_j - b_i)^2}{\sigma_i^2}$. The covariance matrix of the data points, V, is defined as $W = V^{-1/2}$.

The solution to $RX = N$ can be found by minimizing $\chi^2 = (RX-N)^T V^{-1}(RX-N)$, which is accomplished by taking the derivative and setting it to 0. In the case where R and N are independent, this yields

$$\begin{aligned} V &= \partial_N(RX-N)cov(N)\partial_N(RX-N)^T + \partial_R(RX-N)cov(R)\partial_R(RX-N)^T \\ &= cov(N) + (X^T \otimes I_m)cov(R)(I_m \otimes X) \end{aligned} \tag{8.6}$$

where $\otimes$ is a direct product between matrices and I_m is the $m \times m$ identity matrix. In the general case, V can be solved numerically. In the method to be used in this analysis, there are exactly three beam configurations used which results in a unique solution. The minimum χ^2 is then simply achieved for $X = R^{-1}N$ which results in the following propagation of errors:

$$\begin{aligned} cov(X) &= \partial_N(R^{-1}N)cov(N)\partial_N(R^{-1}N)^T + \partial_R(R^{-1}N)cov(R)\partial_R(R^{-1}N)^T \\ &= R^{-1}cov(N)R^T + (N^T R^{-T} \otimes R^{-1})cov(R)(R^{-T} \otimes R^{-1}N) \end{aligned} \tag{8.7}$$

Application to the Analysis

This method has been presented with the assumption that each component is measured as a single quantity. However, the actually decomposition will be done in bins of energy. Each bin will therefore contribute its own system of equations, $R_i X_i = N_i$. The

$RX = N$ equation then becomes

$$\begin{pmatrix} R_1 & 0 & 0 & \dots \\ 0 & R_1 & 0 & \dots \\ 0 & 0 & R_2 & \dots \\ \vdots & \vdots & \vdots & \end{pmatrix} \begin{pmatrix} X_1 \\ X_2 \\ X_3 \\ \vdots \end{pmatrix} = \begin{pmatrix} N_1 \\ N_2 \\ N_3 \\ \vdots \end{pmatrix} \tag{8.8}$$

where each term in equation 8.8 is a block matrix.

This analysis will use three different beam configurations: the Horn-Off (OFF) configuration (L010000), the Horn-On (ON) normal configuration (L010185), and the Horn-On pseudo high energy (pHE) configuration (L250200). The use of three different samples will provide a fully constrained set of linear equations from which the beam components can be determined. This decomposition is termed HOOHE for each of the three beam components (Horn On - Horn Off - High Energy). The decomposition will be done separately for each of the three runs, and will use 1 GeV energy bins (from 1 to 8 GeV). Only the horn on data will be taken from individual run periods. Due to limited data in the other beam configurations, the same pseudo high energy and horn off data will be used in all three run periods, introducing a cross run correlation into the covariance matrix for these beam configurations. Each of the energy bins and runs will have its own set of equations:

$$\begin{pmatrix} 1 & 1 & 1 \\ r_{NC}^{OFF} & r_{CC}^{OFF} & r_{beam\ \nu_e}^{OFF} \\ r_{NC}^{pHE} & r_{CC}^{pHE} & r_{beam\ \nu_e}^{pHE} \end{pmatrix} \begin{pmatrix} X_{NC} \\ X_{CC} \\ X_{beam\ \nu_e} \end{pmatrix} = \begin{pmatrix} N_{ON} \\ N_{OFF} \\ N_{pHE} \end{pmatrix} \tag{8.9}$$

The systematic uncertainty on the r parameters is computed[91] by comparing the value obtained after fiducial (fid), preselection (pre), and PID (pid) selections to see if the differences are consistent within the Monte Carlo statistics.

A χ^2 test is used to measure the variation between cut levels.

$$\chi^2 = \chi^2_{fid} + \chi^2_{pre} = \frac{\Delta r^2_{fid}}{\delta \Delta r_{fid}{}^2} + \Delta r^T_{pre} V^{-1} \Delta r_{pre} \tag{8.10}$$

where $\Delta r_{fid} = r_{fid} - r_{pre}$ and $(\Delta r_{pre})_i = r_{pre} - (r_{pid})_i$ and $(r_{pre})_i$ is the ratio in the ith PID bin. V_{pre} is the covariance matrix of Δr_{pre}. An additional systematic error is added to each r value to ensure that $\chi^2 \leq 1$.

Because the computed χ^2 includes ratios between two samples, where one sample is really a subset of the other sample, errors must be computed on the χ^2 to take these correlations into account. These errors are then included in the definitions of $\delta \Delta r_{fid}$ and V_{pre}, as shown in equations 8.11 and 8.12.

$$\delta \Delta r_{fid} = \delta \Delta r^{stat}_{fid} + \beta^2 (r^2_{fid} + r^2_{pre}) \tag{8.11}$$

$$V_{pre} = V^{stat}_{pre} + \beta^2 \sum_{ij} \sqrt{r^2_{pre} + (r_{pid})^2_i} \frac{(V^{stat}_{pre})_{ij}}{\sqrt{(V^{stat}_{pre})_{ij} (V^{stat}_{pre})_{jj}}} \sqrt{r^2_{pre} + (r_{pid})^2_j} \tag{8.12}$$

where the value of β is the minimum value that satisfies $\chi^2_{fid} \leq 1$ and $\chi^2_{pre} \leq N$ where N is the number of PID bins with nonzero events.

The r_{CC} ratio is highly sensitive to differences in the flux prediction. Since the horn off and pseudo high energy configurations produce more high energy ν_μ CC events (resulting in longer muon tracks), and since the preselection and PID cuts applied to the event sample are designed to remove long muon CC events, it is necessary that the energy flux of ν_μ CC events be correctly modeled. A data-based correction is made to the ν_μ CC Monte Carlo energy spectrum to account for any mismodeling of the energy flux in the Monte Carlo. A sample is prepared of ν_μ CC selected events for both data and Monte Carlo and a weight, w, as a function of reconstructed energy, $recoE$, is constructed.

$$w_r(recoE) = N^{\nu_\mu}_{data}(recoE) / N^{\nu_\mu}_{MC}(recoE) \tag{8.13}$$

The Monte Carlo is then used to map the reconstructed energy to true neutrino energy, $trueE$, in the Monte Carlo, giving a flux correction weight, $w_t(trueE)$ that can then be applied to the true energy of the ν_e selected ν_μ CC Monte Carlo events.

$$w_t(trueE) = \sum_{recoE} w_r(recoE) N_{MC}^{\nu_\mu}(recoE, trueE) \tag{8.14}$$

An additional systematic is calculated for data/Monte Carlo differences and is calculated using data and Monte Carlo at the fiducial volume level cut. The ν_μ CC components of the data are easily identified with a ν_μ CC selection. The NC components are taken to be the total data minus the ν_μ CC component, which results in $\approx 6\%$ beam ν_e contamination in the NC component. These data ratios are compared to the Monte Carlo ratios, resulting in a 36% systematic uncertainty on the beam ν_e (a 30% estimate based on flux, cross-section, and selection efficiency, and a 20% from `FLUGG` to `FLUKA` discrepancies). This systematic due to data / Monte Carlo differences is summarized as

$$\sigma^2 = (r_{data} - r_{MC})^2 + \delta r_{data}^2 + \delta r_{MC}^2 \tag{8.15}$$

where r_{data} and r_{MC} are the ratios computed from data and Monte Carlo, and δr_{data} and δr_{MC} are the statistical errors on each of the ratios.

A regularization term is applied for each bin of energy and run period in order to ensure that the decomposed spectrum will have nonnegative values in each energy bin. The expected value of the solution is based on the Monte Carlo with an adjustment taken for the actual number of observed data events. The regularization term that is added is

$$X_{MC}^T = (\rho N_{NC}^{ON\ MC},\ \ \rho N_{CC}^{ON\ MC},\ \ \rho N_{beam\ \nu_e}^{ON\ MC}) \tag{8.16}$$

where $\rho = \frac{N_{Total}^{ON\ data} - N_{beam\ \nu_e}^{ON\ MC}}{N_{Total}^{ON\ MC} - N_{beam\ \nu_e}^{ON\ MC}}$. A 100% error is taken on the beam ν_e component in addition to the statistical errors taken on all of the components. This large error is taken because

there is a small number of beam ν_e and the main purpose of the inclusion of the beam ν_e events is to avoid bins with negative events.

Finally, a constraint is included requiring each component to have a nonnegative number of events and requiring the sum of the components to equal the total number of observed data events. These requirements are achieved by first requiring that the total horn on data exactly matches the decomposition total in all of the bins. Negative bins are eliminated by setting their contents to zero.

Results

The Near Detector decompositions for the ParticlePID in terms of reconstructed energy are presented in Figures 8.1 for runs 1, 2, and 3. These decompositions show how the method adjusts the raw Monte Carlo event energy spectrum for each background type. The adjustment made on the ν_μ CC events for the ParticlePID spectrum is much more consistent over the three run periods compared to that for ANN11, which is presented in figure 8.2. However, this is not an issue, as any run period dependent ANN11 acceptance is adjusted for in this decomposition step.

The number of events and associated errors for each beam component are presented for Runs 1, 2, and 3 in table 8.2. A comparison between ParticlePID and the ANN11 shows that the predominate difference between the two methods is entirely in the selected NC events. The ParticlePID selects 10% less NC, 2% less ν_μ CC, and the same number of beam ν_e. The difference between the ANN14 and the ANN11 is mostly the same for all even types, with the ANN14 selecting 30% less NC, 36% less ν_μ CC, and 14% less beam ν_e. However, these differences are not too informative, as all of the components agree within the errors between the ParticlePID and ANN11.

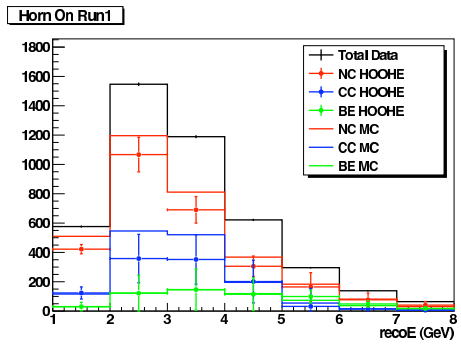

(a) Run 1

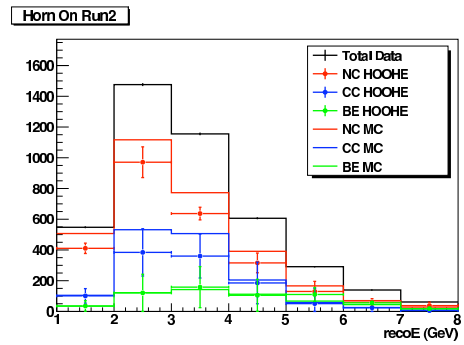

(b) Run 2

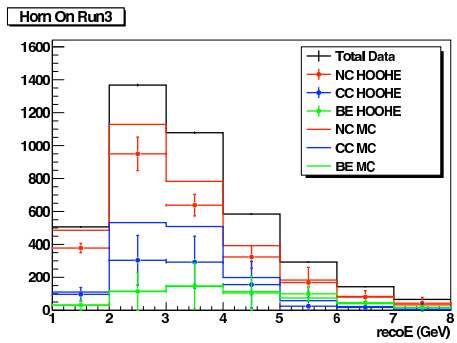

(c) Run 3

Figure 8.1: The Near Detector decomposition obtained using the HOOHE decomposition method for the ParticlePID for Runs 1, 2, and 3. Figures are from [92].

		Total	NC	ν_μ CC	beam ν_e
ParticlePID	Run 1	4433 ± 20	2767 ± 228	1086 ± 327	579 ± 225
	Run 2	4277 ± 16	2562 ± 164	1111 ± 281	604 ± 216
	Run 3	4038 ± 14	2580 ± 198	896 ± 306	561 ± 216
ANN11	Run 1	4698 ± 20	3029 ± 240	1075 ± 320	594 ± 228
	Run 2	4599 ± 17	2860 ± 216	1164 ± 307	575 ± 229
	Run 3	4348 ± 15	2854 ± 254	920 ± 329	574 ± 226
ANN14	Run 1	3290 ± 17	2088 ± 164	709 ± 259	493 ± 198
	Run 2	3269 ± 14	2013 ± 156	755 ± 241	501 ± 195
	Run 3	3119 ± 13	2045 ± 181	573 ± 259	501 ± 201

Table 8.2: The HOOHE Near Detector decomposition for each PID and run period, normalized to 1×10^{19} POT.

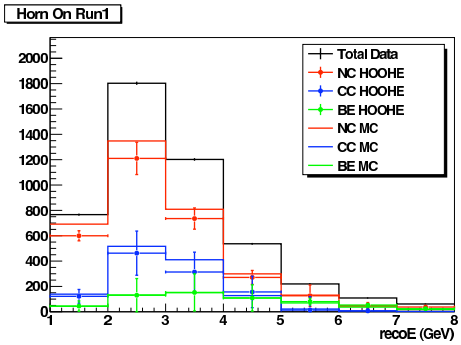

(a) Run 1

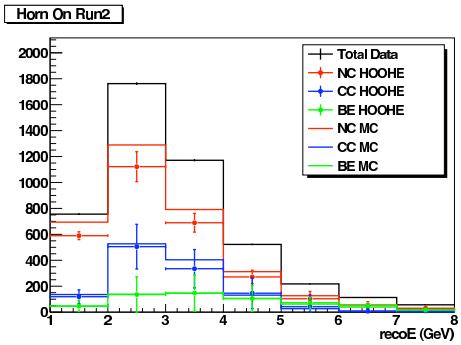

(b) Run 2

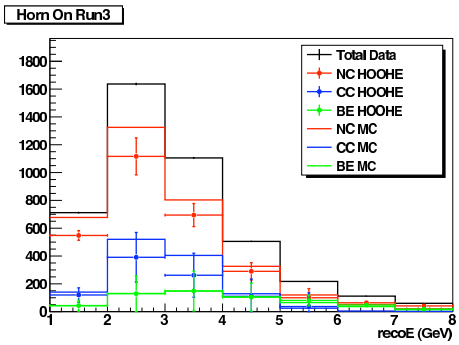

(c) Run 3

Figure 8.2: The Near Detector decomposition obtained using the HOOHE decomposition method for the ANN11 for Runs 1, 2, and 3. Figures are from [92].

8.2.2 MRCC Method

The MRCC method[85] of Near Detector decomposition is an alternate to the previously described HOOHE method and serves as a cross check of that method. The assumption is made that the difference between the Near Detector data and Monte Carlo is due to the mismodeling of hadronic showers, and that events with little or no hadronic showers (such as beam ν_e) are modeled well. This assumption is supported by the calibration detector data[49], which indicates a good modeling of electrons and muons within the detector.

As with the HOOHE method, all components are predicted in 1 GeV bins of reconstructed energy. A correction is made to the Monte Carlo NC events, which are comprised entirely of hadronic showers by definition, with the use of the independent sample of data based hadronic showers from the MRCC data. The NC events in the Near Detector Monte Carlo are corrected to obtain the Near Detector data NC component, given by

$$NC_{data} = NC_{MC} \times \frac{MRCC_{data}}{MRCC_{MC}} \tag{8.17}$$

The beam ν_e predicted by the Near Detector Monte Carlo are assumed to be correct and the Near Detector data beam ν_e component is simply taken to equal the predicted beam ν_e from the Monte Carlo.

The Near Detector data ν_μ CC events are taken as remaining Near Detector data events after the data NC and beam ν_e components are assigned.

The results of the MRCC decomposition are presented in table 8.3.

8.2.3 Near Data Decomposition Method Summary

Both the HOOHE and MRCC Near Detector data decompositions agree with each other within errors. The HOOHE method is chosen for use in the extrapolation because it

		Total	NC	ν_μ CC	beam ν_e
ParticlePID	Run 1	4433 ± 20	2912 ± 237	979 ± 288	542 ± 163
	Run 2	4277 ± 16	2728 ± 225	1010 ± 252	540 ± 162
	Run 3	4038 ± 14	2727 ± 221	771 ± 237	540 ± 162
ANN11	Run 1	4698 ± 20	3304 ± 217	835 ± 270	559 ± 168
	Run 2	4599 ± 17	3153 ± 228	891 ± 248	555 ± 166
	Run 3	4348 ± 15	3080 ± 218	721 ± 234	547 ± 164
ANN14	Run 1	3290 ± 17	2241 ± 241	581 ± 225	468 ± 140
	Run 2	3269 ± 14	2172 ± 201	630 ± 199	467 ± 140
	Run 3	3119 ± 13	2128 ± 196	508 ± 211	482 ± 145

Table 8.3: The MRCC Near Detector decomposition for each PID and run period.

results in slightly smaller systematic errors (see chapter 9) in the number of predicted Far Detector background events. It also has the aesthetic advantage of calculating all of the components based on Near Detector data, unlike the MRCC method which must assume that the Monte Carlo beam ν_e spectrum is correct.

8.3 Far Detector Prediction

Now that the Near Detector data components are known, it is possible to use the Near Detector data and Monte Carlo, and the Far Detector Monte Carlo, to make a prediction for the Far Detector data as described previously in 8.1. Predictions are given for both the assumption of no $\nu_\mu \rightarrow \nu_e$ oscillations (with $\sin^2 2\theta_{13} = 0$) and for oscillations at the CHOOZ limit (with $\sin^2 2\theta_{13} = 0.15$ and $\delta_{CP} = 0$).

The predicted Far Detector energy spectrum calculated with the HOOHE decomposition method in terms of reconstructed energy is presented for ParticlePID, ANN11, and ANN14 in figures 8.3, 8.4, and 8.5, assuming oscillations at the CHOOZ limit.

The prediction number of events for each event type by run period for ParticlePID, ANN11, and ANN14 are listed in tables 8.4, 8.5, and 8.6, both assuming no oscillations and

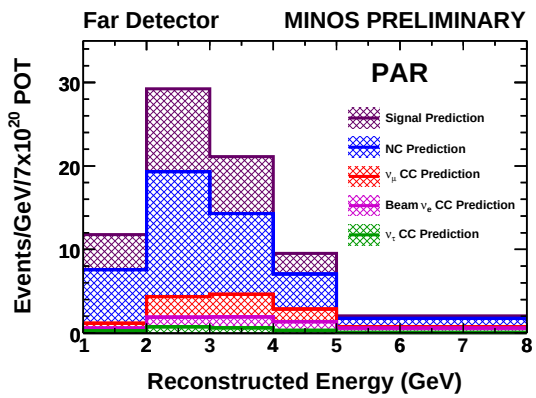

Figure 8.3: The Far Detector predicted reconstructed energy spectrum for the ParticlePID for the signal and background components using the HOOHE decomposition method. Oscillations are calculated at the CHOOZ limit ($\sin^2 2\theta_{13} = 0.15$ and $\delta_{CP} = 0$).

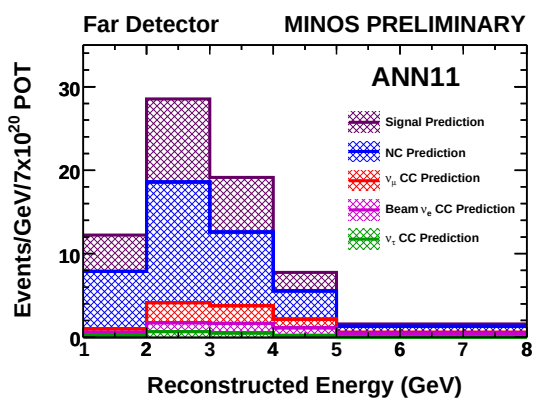

Figure 8.4: The Far Detector predicted reconstructed energy spectrum for ANN11 for the signal and background components using the HOOHE decomposition method. Oscillations are calculated at the CHOOZ limit ($\sin^2 2\theta_{13} = 0.15$ and $\delta_{CP} = 0$).

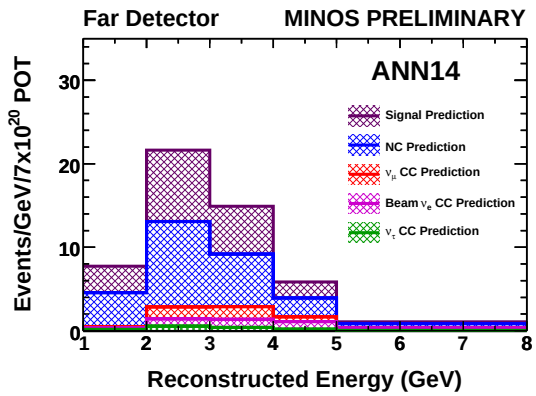

Figure 8.5: The Far Detector predicted reconstructed energy spectrum for ANN14 for the signal and background components using the HOOHE decomposition method. Oscillations are calculated at the CHOOZ limit ($\sin^2 2\theta_{13} = 0.15$ and $\delta_{CP} = 0$).

assuming oscillations at the CHOOZ limit.

	$\sin^2 2\theta_{13} = 0.15 \quad \delta_{CP} = 0$				$\sin^2 2\theta_{13} = 0$			
	Run 1	Run 2	Run 3	Total	Run 1	Run 2	Run 3	Total
NC	6.89	10.38	20.97	38.24	6.89	10.38	20.97	38.24
ν_μ CC	1.46	2.45	3.84	7.75	1.47	2.46	3.86	7.79
beam ν_e CC	0.89	1.59	2.87	5.35	0.95	1.69	3.05	5.69
ν_τ CC	0.39	0.60	1.15	2.14	0.43	0.65	1.25	2.33
Total Background	9.64	15.02	28.84	53.50	9.73	15.18	29.14	54.05
Signal ν_e	4.39	6.95	12.86	24.20	0.03	0.05	0.09	0.17

Table 8.4: The number of predicted Far Detector events by event type for ParticlePID. The numbers on the left are given at the CHOOZ limit, with $\sin^2 2\theta_{13} = 0.15$, and the numbers on the right are given for no oscillations, with $\sin^2 2\theta_{13} = 0.$; both are with $\delta_{CP} = 0$ and for normal hierarchy.

	$sin^2 2\theta_{13} = 0.15 \quad \delta_{CP} = 0$				$\sin^2 2\theta_{13} = 0$			
	Run 1	Run 2	Run 3	Total	Run 1	Run 2	Run 3	Total
NC	6.29	9.76	19.67	35.75	6.29	9.79	19.67	35.75
ν_μ CC	1.10	2.02	3.14	6.26	1.11	2.04	3.16	6.31
beam ν_e CC	0.84	1.35	2.54	4.73	0.90	1.43	2.71	5.04
ν_τ CC	0.33	0.51	0.98	1.82	0.36	0.55	1.07	1.98
Total Background	8.57	13.67	26.34	48.58	8.66	13.81	26.61	49.08
Signal ν_e	4.19	6.63	12.35	23.17	0.03	0.05	0.09	0.17

Table 8.5: The number of predicted Far Detector events by event type for ANN11. The numbers on the left are given at the CHOOZ limit, with $\sin^2 2\theta_{13} = 0.15$, and the numbers on the right are given for no oscillations, with $\sin^2 2\theta_{13} = 0.$; both are with $\delta_{CP} = 0$ and for normal hierarchy.

	$sin^2 2\theta_{13} = 0.15 \quad \delta_{CP} = 0$				$\sin^2 2\theta_{13} = 0$			
	Run 1	Run 2	Run 3	Total	Run 1	Run 2	Run 3	Total
NC	4.12	6.59	13.62	24.33	4.12	6.59	13.62	24.33
ν_μ CC	0.68	1.25	1.87	3.80	0.68	1.26	1.88	3.82
beam ν_e CC	0.69	1.13	2.05	3.87	0.74	1.20	2.18	4.12
ν_τ CC	0.25	0.39	0.76	1.40	0.27	0.42	0.83	1.52
Total Background	5.74	9.35	18.30	33.39	5.81	9.46	18.51	33.78
Signal ν_e	3.51	5.60	10.44	19.55	0.02	0.04	0.07	0.13

Table 8.6: The number of predicted Far Detector events by event type for ANN14. The numbers on the left are given at the CHOOZ limit, with $\sin^2 2\theta_{13} = 0.15$, and the numbers on the right are given for no oscillations, with $\sin^2 2\theta_{13} = 0.$; both are with $\delta_{CP} = 0$ and for normal hierarchy.

Chapter 9

Understanding Systematics

The predicted Far Detector spectrum, as described in 8.3, is not yet complete. It is necessary to understand the uncertainties in each of the terms of the extrapolations and how the the error on these terms will give rise to an overall uncertainty on the final prediction.

Uncertainties can be calculated on the predicted NC + ν_μ CC + beam ν_e background with equation 9.1 by adjusting the Near and Far Detector Monte Carlo for a given systematic which results in the overall effect on the extrapolated number, δF,

$$\delta F^{NC+\nu_\mu CC+beam\ \nu_e CC} = \sum_i \sum_\alpha \delta R_i^\alpha N_i^{\alpha,data} \tag{9.1}$$

where R_i^α is the ratio of far to near Monte Carlo (f_i^α / n_i^α) for background component α=(NC,ν_μ CC, beam ν_e).

The uncertainties in the ν_e and ν_τ background arise from either systematic uncertainties on the ν_μ CC-like spectrum (equation 9.2) or from effects relating the selection

efficiency of each component (equation 9.3).

$$\delta F^{\nu_{e/\tau}} = \sum_{ij} \delta F_j^{\nu_\mu} \times \left(\frac{\sigma_j^{\nu_{e/\tau}}}{\sigma_j^{\nu_\mu}} \right) P^{\nu_\mu \to \nu_{e/\tau}} TR_{ij}^{\nu_{e/\tau}} \epsilon_i^{\nu_{e/\tau}} \tag{9.2}$$

$$\delta F^{\nu_{e/\tau}} = \sum_{ij} F_j^{\nu_\mu} \times \delta \left(\left(\frac{\sigma_j^{\nu_{e/\tau}}}{\sigma_j^{\nu_\mu}} \right) P^{\nu_\mu \to \nu_{e/\tau}} TR_{ij}^{\nu_{e/\tau}} \epsilon_i^{\nu_{e/\tau}} \right) \tag{9.3}$$

The uncertainties are calculated for each source of systematic and then added in quadrature to get the overall uncertainty on the components. All systematic uncertainties are evaluated over the three run periods combined with the exception of systematic uncertainties which are due to time dependent features, such as target degradation. For these cases, the systemic uncertainty is evaluated for each run period separately.

The list of these systematics follow from [93][94], and are elaborated upon as appropriate.

9.1 Systematics of the Beam Simulation

An uncertainty arising in the beam simulation will be observed by both detectors and will result in a net effect which is smaller than the effect in a single detector due to the partial cancelation of the effect in the extrapolation in the δR_i^α term.

9.1.1 Uncertainty on the Data Based Adjustment to the Simulated Flux

The flux was generated with `FLUKA` and was then tuned to the MINOS ν_μ CC data to obtain the data based flux weights using the SKZP method. These weights are then applied to the Monte Carlo events. A one sigma error band is provided by the tuning process of the weights which includes uncertainties in hadronic production at the target as well as in the beam and target parameters. A sample of Monte Carlo events is weighted at

both extremes of the error band in order to evaluate this error. This data based simulation tuning error yields a 6% total background error for both the Near and Far Detectors for all three PIDs. Since an error in the weights would effect the Near and Far Detectors in the same way, the overall extrapolation error is less than 0.2% for the main background components.

9.1.2 Flux Simulation

The `FLUKA` generator was used to simulate the hadronic production at the NuMI target. Recent improvements in modeling have yielded the `FLUGG` model[95] which has been shown to better describe the beam[96]. This new model showed a change on beam ν_e events on the order of 20% in the Near and 10% in the Far Detector. It is this discrepancy that this systematic is intended to cover.

This systematic is calculated by comparing the spectrums of either ν_e or ν_μ for both `FLUKA` and `FLUGG` models. Although there is a large error on the beam ν_e events on the order of 14% in the Near and 9% in the Far Detectors, the overall extrapolation error is about 0.5% since the beam ν_e comprise such a small part of the background.

9.1.3 Target Degredation

Studies of event rate over time showed a decreasing event rate which was attributed to target degradation. The beam systematics group found that a model with two missing target fins (fins 7 and 8) fit nicely to the observed data[97]. `FLUGG` files were produced including this adjustment, and a weighting function was generated[98] that merged the good target and degraded target fluxes.

No systematic is taken for run 1 (when the target appeared normal), a systematic of 1.2 missing fins was used for run 2 and a systematic of 2 missing fins was used for run 3.

These choices were based on the advice of the beam systematics group. The effect of this systematic is less than 0.15% in the extrapolation.

9.2 Uncertainties of the Physics Simulation in the Detectors

9.2.1 Cross Section

This systematic evaluates the effect of the uncertainty of the parameters feeding the `NEUGEN` simulation. As explained in section 3.3.2, `NEUGEN` is responsible for simulating the interaction of the neutrinos in the detector.

The ν_e and ν_μ CC interactions have a cross section uncertainty of M_A(QE) ($\pm$15%), M_A(RES) ($\pm$15%), KNO ($\pm$50%) [99]. For the ν_τ, an overall scaling is applied on the order of $\pm$15% for the QE and RES ν_τ and $\pm$50% for the DIS ν_τ [100]. This results in approximately a $\pm$45% uncertainty for the ν_τ in the region of interest for this analysis. Other sources of systematics were considered for the ν_τ[101][102], including statistical effects from the τ decay branching ratios, and uncertainties in the oscillation parameters. The effect of these additional sources of uncertainty in the ν_τ are dwarfed by the uncertainty in the cross section and are not included in the analysis.

The systematic is recalculated by measuring the effect of rescaling the Monte Carlo events by the appropriate uncertainty based on the neutrino type and resonance code. The uncertainty in the KNO parameter causes as much as a 9% discrepancy in the Near Detector and the Far Detector background components, but the effect cancels in the extrapolation to less than 1% for all components.

9.2.2 Hadronization Model

The hadronization model is tuned to bubble chamber data. However, not all of the parameters are well constrained by this data in the areas of interest to this analysis. The parameters which were cause for concern were identified by the physics simulation group and are detailed below[103]. The largest uncertainty is introduced by the baryon x_f selection in AGKY, which is as high as 22%. However, all of the hadronization model systematics cancel in the extrapolation with none larger than 2% for the ParticlePID or ANN11. In general, the uncertainties for each parameter are higher in the ParticlePID than in the ANN11. This is because the ParticlePID is sensitive to the individual components of a shower. However, this increased shower measurement leads to a better near/far agreement, with the total extrapolation error of $^{+1.4\%}_{-1.1\%}$ for ParticlePID and ± 2.3 for ANN11.

Baryon x_f selection in AGKY

In the AGKY model, the selection of the baryon 4-momentum is preferentially chosen in the backward hemisphere where the di-quark is located. The error on the selection of the 4-momentum is conservatively made with the assumption that the current model is wrong and instead the 4-momentum is generated in the center of mass from a phase space decay.

Probability of a π^0

The probability of a hadronic shower producing one or more π^0 is of substantial interest to this analysis, as the shower from a π^0 decay is an irreducible background of the oscillated ν_e signal sample. The probability of producing a π^0 is taken to be 30% and is based on data from numerous experiments. A 20% variation on the π^0 creation probability is used (varying the probability from 21% to 39%) in the calculation of this systematic.

Ambiguity in x_f vs p_T correlation

This systematic measures the effect of different implementations of the AGKY model between `NEUGEN` v3.5.0 and `GENIE` v2.0.0, specifically with regard to what happens after an event is rejected during the p_T squeezing step of the algorithm. The difference in p_T obtained using `GENIE` instead of `NEUGEN` is taken as the systematic.

Average p_T in AGKY

The parameter responsible for the p_T squeezing in the remnant system decay is changed from the default of -3.5 to -1.5. This results in broader showers and this difference is taken as the systematic.

Isotropic two-body decays in AGKY

The assumption that all two body decays in the AGKY model are isotropic is tested by measuring the effect of having all two-body decays occur at an angle of 90° with respect to the momentum transfer direction.

Average particle multiplicity and dispersion

The AGKY model will generate interactions resulting in one baryon (p or n) and any number of charged or neutral π and K mesons which are kinematically possible and which satisfy charge conservation[68].

The average charged hadron multiplicity is computed from

$$< n_{ch} >= a + b \log W^2$$

where a and b are determined by bubble chamber experiments. The total hadron multiplicity

is then determined by

$$< n_{tot} >= 1.5 < n_{ch} >$$

The actual hadron multiplicity is then calculated from the KNO scaling law

$$< n > \times P(n) = f(n/ < n >)$$

where $P(n)$ is the probability of generating n hadrons and f is the Levy function

$$Levy(z, c) = 2e^{-c}c^{cz+1}/\Gamma(cz + 1)$$

evaluated with $z = n/ < n >$.

The parameter c is found from a fit to data from the Fermilab deuterium-filled 15-foot bubble chamber[104], resulting in $c = 7.93 \pm 0.34$ for νp interactions and $c = 5.22 \pm 0.15$ for νn interactions.

The tuning of the model to bubble chamber experiments is not exact, and different values of a and b are found for different experiments. This systematic is calculated by varying a and b within the range obtained for each bubble chamber experiment. Additionally, the KNO scaling is adjusted by the error on the fit of parameter c in the evaluation of the systematic.

Charged-neutral pion multiplicity correlations

As explained in the previous section, the neutral and charged particle multiplicities are related. However, measurements at a few GeV indicate that the charged and neutral pion multiplicities are actually independent. The AGKY model was improved[105] to selected the neutral and charged particle multiplicities independently. The difference between the improved model and the AGKY model actually used is taken as this systematic.

9.2.3 INTRANUKE

Since most of the neutrino interactions in MINOS occur within the steel planes, it is most likely that hadrons resulting from the neutrino interaction within an iron atom will interact with other nucleons in that atom before escaping. The modeling of these intranuclear interactions is handled by the `INTRANUKE` program.

There are ten parameters which each contribute a systematic error. Events are weighted based on $\pm 1\sigma$ shifts in each parameter in order to obtain the errors. A total `INTRANUKE` error is calculated as the sum in quadrature of the errors from varying each of these parameters.

A process to speed the evaluation of this systematic was developed[106] to avoid the need to compute every neutrino interaction for each set of varied parameters. Monte Carlo events are generated once and then weighted based on the probability that the event in the Monte Carlo could have appeared with the same final state, but starting with a different set of the ten parameters that feed the `INTRANUKE` program.

This systematic was not evaluated for ν_τ events due to a problem with the information stored for these events. However, any such `INTRANUKE` error for ν_τ events would be insignificant to the already established 45% error on the ν_τ events due to the cross section systematic.

The systematics introduced by varying the `INTRANUKE` parameters are slightly larger in the ParticlePID than the ANN11 because the ParticlePID is designed to measure the different parts of a shower. However, this increased shower measurement leads to a better near/far agreement, with the total extrapolation error of $^{+0.7\%}_{-1.1\%}$ for ParticlePID and $^{+0.9\%}_{-1.0\%}$ for ANN11.

9.3 Uncertainties in Detector Response

9.3.1 Absolute Energy Scale

This systematic measures the effect of the 5.7% uncertainty on the absolute energy calibration of the calibration detector[107]. Monte Carlo samples are made where the strip energy is shifted by the calibration uncertainty in the reconstruction (but not in the simulation). This uncertainty can effect events moving into or out of the 1-8 GeV preselected energy region, can effect the energy binned extrapolation, and can cause shifts in the calculated PID values. However, this uncertainty is small, measuring 1% for ParticlePID and ANN11, and 2% for ANN14.

9.3.2 Hadronic versus EM Energy Scale

The hadron and electromagnetic energy deposition within the detector is simulated by different methods in the Monte Carlo. The calibration detector studies indicated that the energy deposited by the hadronic part of an event could be off by as much as ±5%. To calculate this systematic, Monte Carlo events are weighted based on the hadronic energy component and are shifted in total energy by adjusting the hadronic contribution to the event energy by ±5%. The weighting allows for a recalculation of the selection efficiency, while the energy shifting allows for events to move in and out of the event energy selection window. The effect on all PIDs is less than 1% in the extrapolation.

9.4 Extrapolation Effects

When a comparison is made between the Near and Far Detectors in order to obtain the predicted number of events in the Far Detector, there are some differences between the two detectors that need to be accounted for. These are effects where δR_i^α is not necessarily

small.

9.4.1 Normalization

The normalization error for the NC, ν_μ CC and beam ν_e CC is due to uncertainties of 1% in the measurement of POT, 0.2% in each of the steel and scintillator thickness, and 2.1% in the measurement of the fiducial mass of each detector as obtained from data/MC discrepancies[108]. The signal ν_e and ν_τ have a 4% error based on the previously mentioned sources, in addition to the fact that these samples take an error from the ν_μ CC events, from which these predictions are calculated. The overall effect on the extrapolation for all components is 2.4%.

9.4.2 Calibration

The uncertainty in the calibration is comprised of a combination of individual uncertainties for each step in the calibration chain. The total effect on the background prediction is less than 1.8% for the ParticlePID and less than 2.8% for the ANN11.

Relative Energy Calibration

The relative energy calibration converts units of SigCor to MEU. Comparison between Monte Carlo and Data yields a 0.9% discrepancy in the Far Detector and 1.9% discrepancy in the Near Detector[107]. These uncertainties added in quadrature give a 2.1% near to far energy scale uncertainty.

Gains

The gains are measured by pulsing each strip end with light that is accurately measured by a PIN diode. The raw ADC values are converted to photo electrons and this

measurement is used to track the aging of the detector response for Monte Carlo simulations. The measurement of the gains are known to within a systematic shift of 5% with a channel-to-channel variation of 7%[109]. To calculate the systematic, two sets of Monte Carlo are generated for the + and the - 5% systematic shift. For each of these samples, the energy in each channel is adjusted via a 7% random variation according to a Gaussian distribution.

This introduces an error on the prediction of less than 3%.

Attenuation

The attenuation of the signal from a strip is adjusted based on the position along the strip where the energy deposition occurred. This adjustment is calibrated using the stopping muon calibration, which leaves a residual difference of about 1%[110].

Strip-to-strip

The response of each strip is calibrated to be equal. The uncertainty on this calibration is less than 0.5%[111].

This systematic is calculated as the difference between standard Monte Carlo and Monte Carlo in which the quantity SigCor is varied for each strip according to a Gaussian distribution with a 0.5% width.

Linearity

The systematic uncertainty on the linearity of each strip response is calculated by varying the quantity SigLin for each strip according to a gaussian with the width set to the uncertainty of the SigLin parameters determined by the linearity calibration code.

This results in less than a 1% effect for the all components.

9.4.3 Preselection

A method to measure the systematic uncertainty introduced by the preselection cuts[112] was used. This uncertainty[113] was calculated with a sample of events which passed the fiducial volume and data quality cuts, as well as a given PID cut, but to which no preselection cuts were applied. Then the efficiency was measured to this sample after either the preselection cut for the number of contiguous planes or the number of showers was applied. The difference in the efficiencies between the Near and Far Detector Monte Carlo is taken as the systematic for the particular preselection cut. The same procedure is followed to evaluate the effect of the track planes and track-like planes cut, except the sample used prior to the cut is as described above but with the additional contiguous planes and number of shower cuts both applied.

Care must be taken when evaluating the track planes and track-like planes cut for the ParticlePID in order to avoid misleading results. These two track quantity cuts are applied to standard reconstruction values, not to the track length as defined by the ParticlePID algorithm. The ParticlePID algorithm will not attempt to reconstruct an event which is partially or entirely outside of the fully instrumented region of the Near Detector as a computational time saver. The standard reconstruction does reconstruct events in this region which are not used in this analysis. This difference between the two algorithms introduces an artificial near/far difference (since the Far Detector is completely fully instrumented). This difference has no relevance to this analysis, since the events responsible typically contain long muon tracks which exit out the side of the partially instrumented region in the Near Detector.

The ParticlePID was designed to set a status bit indicating if an event was not reconstructed because it was not contained within the fully instrumented region. While this procedure showed merit, it was decided that this feature would not be used, as a large

number of events were removed from the Near Detector samples. The application of the preselection cuts effictively removed all events that were not fully contained, eliminating the need to rely on this status bit.

Thus, the track quantity preselection cuts play a role not only to remove the ν_μ CC events, but also act as a data quality cut for the ParticlePID by removing events which have long tracks, but which were not completely reconstructed, presumably because those tracks exited the fully instrumented region. Therefore, in order to properly evaluate the track quantity preselection systematics for the ParticlePID, it is necessary first apply an additional cut to remove the events which are not reconstructed by the ParticlePID because they exit the detector. This cut, which is a subset of the normal track planes preselection cut, removes all events having a track at least 25 planes in length while simultaneously requiring the track length in planes found by the standard reconstruction to be at least three times the length of the track found by the ParticlePID.

The preselection systematic is 1% for all PIDs.

9.4.4 Cross Talk Modeling

The PMT cross talk has two sources. The charge cross talk is due to the leaking of secondary electrons in the PMT to neighboring pixels corresponding to a 0.3 photoelectron effect in the strip pulse height distribution. Optical cross talk occurs when light leaks to an adjacent pixel and corresponds to a 1 photoelectron effect in the strip pulse height distribution. This crosstalk has a different behavior between the detectors because the detectors use different PMT pixel array configurations and because the Far Detector is multiplexed. The reconstruction does not use strips with energy less than 2 photoelectrons in an attempt to minimize the effects of crosstalk. Therefore, crosstalk only has a small effect in the region where it exceeds 2 photoelectrons.

The charge cross talk is evaluated by comparing the standard Monte Carlo which includes a simulation for cross talk to a Monte Carlo absent of any cross talk effect modeling. This systematic has negligible differences and is not included in the list of systematics. The optical cross talk produces a larger effect which is evaluated by comparing the standard Monte Carlo to one with a more accurate cross talk map[57]. The total effect of crosstalk is 4% for both the ParticlePID and ANN11.

9.4.5 Near Detector Event Intensity

While the Far Detector sees no more than one event per spill due to the distance from the target, the number of events per spill seen in the Near Detector can vary greatly depending on the intensity of the beam. Therefore, this systematic is calculated for the Near Detector only.

This systematic measures the effect of the change in beam intensity on the Near Detector events. Specifically of concern is whether the Near Detector events suffer a reduction in reconstruction quality when there are more events in the detector during a single spill. It is important to note that steps were taken to ensure that the Near Detector Monte Carlo correctly matched the Near Detector data in snarl intensity at the correct moment in time[114].

A special sample of "first events" was made, by selecting the first events in each run, but only using the first event when it was separated from the second event by more than 100 ns. This sample was used as the low intensity sample, because there was not enough statistics available from actual low intensity running.

The PID selection efficiency (PID/fiducial) histogram was calculated for the "first events" and for the standard samples in both data and MC. Each of these histograms was area normalized. The ratios of the "first events" to the standard samples were calculated

for both data and MC. The final systematic is taken as the double ratio of these data/MC ratios. The statistical errors of these correction factors are taken as the Near Detector event intensity uncertainty.

9.5 Far Detector Systematics for ν_τ and Signal ν_e Events

Both the ν_τ and signal ν_e events are unique to the Far Detector - they do not appear at all in the Near Detector. These events are predicted in the Far Detector based on ν_τ and signal ν_e efficiencies obtained from the Far Detector Monte Carlo, along with the predicted ν_μ CC flux, as explained in section 8.1. The use of the predicted ν_μ CC flux requires the inclusion of the systematic effects found in the ν_μ disappearance analysis[115].

9.5.1 ν_μ CC Systematics

Since the method of predicting the ν_μ, NC, and beam ν_e components in this analysis is equivalent to the method used in the ν_μ disappearance analysis[115], the systematics found in that analysis are adopted here. This includes a 4% normalization uncertainty, a 50% NC scale uncertainty, and a 10% error on the ν_μ CC energy scale. The systematic error is determined by applying these shifts to the Monte Carlo and measuring the effect on the predicted number of events.

9.5.2 Signal Efficiency

Electron Component

The PIDs are applied to the calibration detector data from the electron test beam and efficiencies (PID/fiducial) are calculated for data and MC[116]. The difference between the data and Monte Carlo efficiencies as a function of electron momentum is parameterized

by fitting a 4th degree polynomial to the data/Monte Carlo ratio. This function is used to reweight the Far Detector signal ν_e Monte Carlo as a function of true electron momentum. The difference in the number of selected Far Detector Monte Carlo ν_e events before and after the weighting is taken as the systematic.

Hadronic Component

The hadronic uncertainty on the signal comes from the fact that hadronic showers are expected to be modeled less accurately than bare electrons, for which the properties and simulations are well understood.

Using the MRCC events previously processed as a source of data based hadronic showers, a bare Monte Carlo electron is put in place of the removed muon, matching the energy and momentum of the original muon to form MRE events. This data-Monte Carlo hybrid event is then processed through reconstruction and filtered by the preselection and PID selectors. This method provides an independent sample of ν_e CC like events with a hadronic shower that is representative of the data without looking at actual signal events.

The adjustment made to the predicted signal ν_e includes the systematic uncertainty in that calculation.

9.6 Systematics - Detailed Tables

The systematics are presented in a number of tables using the HOOHE near detected data decomposition method[117]. The systematics for the ParticlePID, ANN11, and ANN14 in the Near Detector are presented in tables 9.1, 9.2, and 9.3. The Far Detector systematics (including only the NC, ν_μ CC, and beam ν_e CC) are presented in tables 9.4, 9.5, and 9.6. The extrapolation systematics for the prediction appear in tables 9.7, 9.8, and 9.9. It is important to note that the systematics that appeared large in the near and far

tables are now significantly reduced in the prediction because systematic shifts in the same direction between the detectors will tend to cancel in the R_i^α ratio. Finally, the systematics for the predicted ν_τ are in tables 9.10, 9.11, and 9.12 the systematics for the predicted signal ν_e appear in tables 9.13, 9.14, and 9.15.

9.6.1 Near Detector

Syst.	NC		ν_μ CC		beam ν_e CC		Total	
Abs Escale	-0.60%	-0.38%	-0.07%	-0.12%	1.04%	-0.14%	-0.28%	-0.28%
Attenuation	-0.51%	-	0.07%	-	0.52%	-	-0.24%	-
EMvsHad	-1.59%	2.04%	-1.57%	1.84%	-2.41%	2.53%	-1.67%	2.03%
FLUGG	0.20%	-	0.00%	-	13.43%	-	1.56%	-
Gain (N $\pm 1\sigma$)	0.28%	-1.02%	0.95%	-0.97%	2.19%	-0.85%	0.67%	-0.99%
Had1 (Baryon x_f)	-21.96%	-	-27.05%	-	-2.02%	-	-21.25%	-
Had2 (π^0 sel.)	8.89%	-8.68%	9.17%	-9.02%	0.71%	-0.70%	8.09%	-7.92%
Had3 (mult. corr.)	-15.44%	-	-10.76%	-	-1.15%	-	-12.60%	-
Had4 (imp. amb.)	-7.01%	-	-9.02%	-	-0.82%	-	-6.91%	-
Had5 (p_T squz)	-5.86%	-	-7.67%	-	-0.57%	-	-5.80%	-
Had6 (iso. 2-body dec.)	-6.69%	-	-8.61%	-	-0.59%	-	-6.57%	-
Hadron Mult.	-1.13%	0.41%	-1.61%	-2.78%	-1.45%	-1.05%	-1.30%	-0.64%
INUKE0 (q-exchange)	-0.05%	0.06%	-0.10%	0.11%	-0.17%	0.17%	-0.07%	0.09%
INUKE1 (π elastic)	0.66%	-0.65%	0.74%	-0.74%	-0.11%	0.11%	0.60%	-0.59%
INUKE2 (π inel.)	-0.98%	0.89%	-1.08%	1.14%	0.15%	-0.07%	-0.89%	0.86%
INUKE3 (π abs.)	-1.36%	1.36%	-1.53%	1.49%	0.45%	-0.41%	-1.21%	1.21%
INUKE4 ($\pi \rightarrow 2\pi$)	-0.22%	0.21%	-0.17%	0.18%	-0.21%	0.21%	-0.20%	0.20%
INUKE5 (N-knockout)	0.91%	-0.91%	1.01%	-1.01%	2.23%	-2.23%	1.08%	-1.08%
INUKE6 ($N \rightarrow (2)\pi$)	-0.45%	0.45%	-0.51%	0.51%	-0.61%	0.61%	-0.49%	0.49%
INUKE7 (form. time)	8.43%	-14.50%	8.83%	-14.02%	0.04%	-0.79%	7.65%	-12.90%
INUKE8 (π xsec)	-1.08%	1.20%	-1.10%	1.22%	-0.01%	0.00%	-0.97%	1.08%
INUKE9 (N xsec)	-0.06%	0.10%	-0.10%	0.18%	-1.26%	1.31%	-0.20%	0.25%
KNO	5.81%	-8.05%	5.97%	-8.35%	7.02%	-7.52%	5.98%	-8.08%
Linearity	-0.22%	-	-0.22%	-	0.10%	-	-0.18%	-
MAQE	0.04%	-0.02%	0.05%	-0.03%	4.34%	-4.13%	0.50%	-0.46%
MARES	1.99%	-1.33%	1.58%	-1.15%	5.97%	-5.75%	2.30%	-1.75%
OptXTalk	0.18%	-	1.34%	-	2.52%	-	0.75%	-
Rel Escale (N $\pm 1\sigma$)	-0.56%	-0.35%	-0.03%	-0.03%	0.93%	0.05%	-0.25%	-0.22%
SKZP	4.00%	-4.00%	3.94%	-3.94%	5.39%	-5.39%	4.13%	-4.13%
Strip2strip	-0.46%	-	0.08%	-	-0.03%	-	-0.26%	-
TargetDeg	-0.19%	-	-1.53%	-	-1.37%	-	-0.69%	-
Total Extrap	32.62	-35.05	36.06	-38.05	18.74	-18.68	30.54%	-32.62%

Table 9.1: The Near Detector systematics for the ParticlePID using the HOOHE decomposition method are shown.

Syst.	NC		ν_μ CC		beam ν_e CC		Total	
Abs Escale	-3.72%	3.29%	-4.46%	3.35%	2.53%	-1.32%	-3.21%	2.80%
Attenuation	-0.05%	-	-0.21%	-	0.14%	-	-0.07%	-
EMvsHad	-1.81%	1.93%	-1.25%	1.57%	-2.70%	2.87%	-1.77%	1.95%
FLUGG	0.20%	-	0.00%	-	14.20%	-	1.68%	-
Gain (N $\pm 1\sigma$)	1.29%	-1.17%	1.51%	-2.33%	1.97%	-1.12%	1.42%	-1.44%
Had1 (Baryon x_f)	-23.06%	-	-24.11%	-	-1.41%	-	-20.94%	-
Had2 (π^0 sel.)	8.77%	-8.56%	8.28%	-8.15%	0.53%	-0.52%	7.75%	-7.58%
Had3 (mult. corr.)	-15.50%	-	-9.84%	-	-1.03%	-	-12.57%	-
Had4 (imp. amb.)	-7.84%	-	-8.07%	-	-0.44%	-	-7.08%	-
Had5 (p_T squz)	-6.67%	-	-6.77%	-	-0.26%	-	-5.99%	-
Had6 (iso. 2-body dec.)	-7.89%	-	-8.34%	-	-0.77%	-	-7.22%	-
Hadron Mult.	-0.34%	-0.56%	0.41%	-3.56%	-0.80%	-1.23%	-0.21%	-1.34%
INUKE0 (q-exchange)	-0.06%	0.07%	-0.12%	0.12%	-0.19%	0.19%	-0.09%	0.10%
INUKE1 (π elastic)	0.56%	-0.55%	0.50%	-0.49%	-0.32%	0.33%	0.45%	-0.44%
INUKE2 (π inel.)	-0.94%	0.93%	-1.01%	1.08%	0.76%	-0.60%	-0.77%	0.80%
INUKE3 (π abs.)	-0.93%	0.95%	-0.67%	0.68%	0.63%	-0.66%	-0.70%	0.71%
INUKE4 ($\pi \to 2\pi$)	-0.28%	0.29%	-0.25%	0.26%	-0.20%	0.20%	-0.27%	0.27%
INUKE5 (N-knockout)	1.27%	-1.27%	1.60%	-1.60%	2.63%	-2.63%	1.50%	-1.50%
INUKE6 ($N \to (2)\pi$)	-0.53%	0.53%	-0.59%	0.59%	-0.63%	0.63%	-0.56%	0.56%
INUKE7 (form. time)	7.57%	-12.40%	6.97%	-11.97%	-0.39%	-0.00%	6.55%	-10.94%
INUKE8 (π xsec)	-1.00%	1.13%	-0.82%	0.89%	0.04%	-0.05%	-0.85%	0.94%
INUKE9 (N xsec)	-0.25%	0.26%	-0.49%	0.51%	-1.58%	1.59%	-0.45%	0.47%
KNO	6.34%	-8.63%	6.25%	-8.48%	6.82%	-7.16%	6.37%	-8.43%
Linearity	0.05%	-	-0.27%	-	0.28%	-	-0.00%	-
MAQE	0.09%	-0.05%	0.11%	-0.07%	4.72%	-4.53%	0.60%	-0.55%
MARES	2.62%	-1.82%	1.90%	-1.46%	6.18%	-6.03%	2.84%	-2.19%
OptXTalk	-0.55%	-	-1.80%	-	1.73%	-	-0.60%	-
Rel Escale (N $\pm 1\sigma$)	-1.24%	0.89%	-1.38%	1.36%	1.60%	-0.43%	-0.96%	0.86%
SKZP	4.04%	-4.04%	3.68%	-3.68%	5.21%	-5.21%	4.08%	-4.08%
Strip2strip	-0.08%	-	-0.15%	-	0.02%	-	-0.08%	-
TargetDeg	-0.33%	-	-1.52%	-	-1.34%	-	-0.72%	-
Total Extrap	34.07	-35.88	32.59	-34.77	19.46	-19.21	30.47%	-32.12%

Table 9.2: The Near Detector systematics for the ANN11 using the HOOHE decomposition method are shown.

Syst.	NC		ν_μ CC		beam ν_e CC		Total	
Abs Escale	-4.99%	5.27%	-6.69%	6.33%	1.54%	-2.00%	-4.55%	4.59%
Attenuation	0.33%	-	0.68%	-	-0.32%	-	0.33%	-
EMvsHad	-1.83%	2.49%	-1.65%	1.81%	-2.78%	2.93%	-1.91%	2.39%
FLUGG	0.19%	-	0.00%	-	14.02%	-	1.90%	-
Gain (N $\pm 1\sigma$)	2.44%	-1.55%	3.90%	-3.70%	2.82%	-2.42%	2.83%	-2.15%
Had1 (Baryon x_f)	-26.32%	-	-30.15%	-	-1.87%	-	-24.09%	-
Had2 (π^0 sel.)	9.91%	-9.63%	9.85%	-9.67%	0.41%	-0.41%	8.69%	-8.47%
Had3 (mult. corr.)	-18.26%	-	-11.58%	-	-0.95%	-	-14.54%	-
Had4 (imp. amb.)	-9.23%	-	-10.26%	-	-0.64%	-	-8.38%	-
Had5 (p_T squz)	-8.07%	-	-8.86%	-	-0.45%	-	-7.28%	-
Had6 (iso. 2-body dec.)	-9.98%	-	-12.47%	-	-0.84%	-	-9.39%	-
Hadron Mult.	-2.25%	1.91%	-2.61%	-1.79%	-0.50%	-1.44%	-2.11%	0.63%
INUKE0 (q-exchange)	-0.04%	0.05%	-0.25%	0.25%	-0.13%	0.13%	-0.10%	0.11%
INUKE1 (π elastic)	0.39%	-0.39%	0.55%	-0.54%	-0.38%	0.38%	0.33%	-0.32%
INUKE2 (π inel.)	-0.86%	0.88%	-1.18%	1.26%	0.76%	-0.71%	-0.73%	0.77%
INUKE3 (π abs.)	-0.49%	0.49%	-0.52%	0.50%	0.70%	-0.75%	-0.35%	0.33%
INUKE4 ($\pi \to 2\pi$)	-0.31%	0.31%	-0.31%	0.31%	-0.20%	0.20%	-0.29%	0.30%
INUKE5 (N-knockout)	1.33%	-1.34%	1.54%	-1.54%	2.68%	-2.68%	1.55%	-1.55%
INUKE6 ($N \to (2)\pi$)	-0.56%	0.56%	-0.62%	0.62%	-0.62%	0.62%	-0.58%	0.58%
INUKE7 (form. time)	7.99%	-14.40%	7.97%	-14.01%	-0.52%	-0.11%	6.91%	-12.49%
INUKE8 (π xsec)	-0.97%	1.08%	-0.91%	1.00%	0.08%	-0.10%	-0.82%	0.91%
INUKE9 (N xsec)	-0.28%	0.29%	-0.43%	0.46%	-1.65%	1.67%	-0.49%	0.50%
KNO	7.10%	-9.96%	6.99%	-10.01%	6.66%	-6.93%	7.02%	-9.58%
Linearity	0.42%	-	0.42%	-	0.59%	-	0.44%	-
MAQE	0.07%	-0.04%	0.08%	-0.06%	4.88%	-4.75%	0.68%	-0.64%
MARES	2.12%	-1.45%	1.45%	-1.09%	5.98%	-5.93%	2.46%	-1.94%
OptXTalk	-0.54%	-	-1.88%	-	0.64%	-	-0.70%	-
Rel Escale (N $\pm 1\sigma$)	-1.64%	1.95%	-1.95%	3.25%	0.71%	-0.35%	-1.41%	1.96%
SKZP	4.09%	-4.09%	3.75%	-3.75%	5.19%	-5.19%	4.15%	-4.15%
Strip2strip	0.25%	-	0.50%	-	0.28%	-	0.31%	-
TargetDeg	-0.31%	-	-1.62%	-	-1.37%	-	-0.74%	-
Total Extrap	39.53	-41.69	41.20	-43.27	19.22	-19.22	35.33%	-37.27%

Table 9.3: The Near Detector systematics for the ANN14 using the HOOHE decomposition method are shown.

9.6.2 Far Detector

Syst.	NC		ν_μ CC		beam ν_e CC		Total	
Abs Escale	-0.40%	-0.21%	0.55%	-0.94%	-0.59%	1.08%	-0.25%	-0.23%
Attenuation	0.16%	-	0.65%	-	1.84%	-	0.38%	-
EMvsHad	-1.69%	1.87%	-1.87%	2.03%	-0.12%	6.10%	-1.59%	2.24%
FLUGG	0.11%	-	0.00%	-	8.28%	-	0.76%	-
Gain (F $\pm 1\sigma$)	0.58%	0.66%	1.01%	-1.53%	-0.60%	-0.72%	0.56%	0.16%
Had1 (Baryon x_f)	-22.26%	-	-28.55%	-	-3.57%	-	-21.85%	-
Had2 (π^0 sel.)	8.94%	-8.76%	8.87%	-8.69%	0.68%	-0.66%	8.25%	-8.09%
Had3 (mult. corr.)	-14.94%	-	-9.30%	-	-0.28%	-	-12.73%	-
Had4 (imp. amb.)	-7.22%	-	-8.87%	-	-1.60%	-	-7.06%	-
Had5 (p_T squz)	-6.13%	-	-7.68%	-	-1.48%	-	-6.03%	-
Had6 (iso. 2-body dec.)	-6.50%	-	-8.26%	-	-1.66%	-	-6.42%	-
Hadron Mult.	-0.28%	-0.21%	-0.62%	-2.66%	0.67%	-0.23%	-0.27%	-0.65%
INUKE0 (q-exchange)	-0.29%	0.28%	-0.17%	0.18%	0.08%	-0.07%	-0.24%	0.23%
INUKE1 (π elastic)	0.61%	-0.61%	0.47%	-0.47%	-0.08%	0.10%	0.53%	-0.53%
INUKE2 (π inel.)	-0.48%	0.35%	-0.31%	0.10%	0.92%	-0.77%	-0.33%	0.21%
INUKE3 (π abs.)	-1.55%	1.53%	-1.23%	1.22%	0.03%	-0.03%	-1.36%	1.35%
INUKE4 ($\pi \rightarrow 2\pi$)	-0.16%	0.16%	-0.18%	0.19%	-0.36%	0.36%	-0.18%	0.18%
INUKE5 (N-knockout)	1.21%	-1.21%	0.60%	-0.60%	2.64%	-2.64%	1.22%	-1.22%
INUKE6 ($N \rightarrow (2)\pi$)	-0.42%	0.42%	-0.59%	0.59%	-0.56%	0.56%	-0.46%	0.46%
INUKE7 (form. time)	7.66%	-14.04%	6.72%	-13.84%	1.22%	-2.07%	6.97%	-13.02%
INUKE8 (π xsec)	-0.92%	1.02%	-0.99%	1.13%	-0.03%	0.03%	-0.86%	0.96%
INUKE9 (N xsec)	-0.56%	0.59%	0.48%	-0.40%	-1.68%	1.65%	-0.47%	0.50%
KNO	5.87%	-7.98%	5.80%	-8.09%	7.15%	-7.54%	5.96%	-7.96%
Linearity	0.05%	-	0.59%	-	1.44%	-	0.26%	-
MAQE	0.03%	-0.02%	0.08%	-0.05%	4.51%	-4.36%	0.40%	-0.38%
MARES	2.05%	-1.40%	1.36%	-0.94%	5.54%	-5.40%	2.21%	-1.65%
OptXTalk	0.50%	-	0.79%	-	-4.17%	-	0.17%	-
Rel Escale (F $\pm 1\sigma$)	-0.28%	0.05%	1.48%	0.35%	3.32%	1.87%	0.33%	0.26%
SKZP	4.77%	-4.77%	4.60%	-4.60%	10.35%	-10.35%	5.20%	-5.20%
Strip2strip	-0.13%	-	0.20%	-	1.33%	-	0.05%	-
TargetDeg	-0.49%	-	-2.13%	-	-1.69%	-	-0.88%	-
Total Extrap	32.58	-34.97	36.23	-38.57	19.72	-18.87	31.05%	-33.24%

Table 9.4: The systematic effects for the ParticlePID in the Far Detector are shown.

Syst.	NC		ν_μ CC		beam ν_e CC		Total	
Abs Escale	-3.67%	4.06%	-1.27%	1.22%	2.88%	-1.52%	-2.78%	3.19%
Attenuation	-0.33%	-	-0.75%	-	-1.10%	-	-0.45%	-
EMvsHad	-1.68%	1.91%	-1.89%	1.92%	-2.69%	2.96%	-1.79%	2.00%
FLUGG	0.10%	-	0.00%	-	8.89%	-	0.84%	-
Gain (F $\pm 1\sigma$)	1.55%	-0.89%	5.33%	-2.05%	0.35%	-3.60%	1.97%	-1.28%
Had1 (Baryon x_f)	-24.32%	-	-28.08%	-	-2.50%	-	-22.99%	-
Had2 (π^0 sel.)	8.94%	-8.71%	8.50%	-8.30%	0.28%	-0.28%	8.14%	-7.93%
Had3 (mult. corr.)	-16.14%	-	-9.22%	-	0.13%	-	-13.79%	-
Had4 (imp. amb.)	-8.52%	-	-9.27%	-	-1.09%	-	-7.99%	-
Had5 (p_T squz)	-7.41%	-	-8.21%	-	-1.01%	-	-6.98%	-
Had6 (iso. 2-body dec.)	-8.25%	-	-9.16%	-	-2.97%	-	-7.93%	-
Hadron Mult.	0.03%	-0.35%	0.52%	-2.64%	0.87%	-1.31%	0.17%	-0.75%
INUKE0 (q-exchange)	-0.27%	0.25%	-0.03%	0.03%	-0.06%	0.04%	-0.22%	0.20%
INUKE1 (π elastic)	0.38%	-0.37%	0.37%	-0.37%	-0.24%	0.25%	0.32%	-0.32%
INUKE2 (π inel.)	-0.48%	0.30%	-0.55%	0.39%	1.08%	-0.81%	-0.36%	0.21%
INUKE3 (π abs.)	-0.70%	0.66%	-0.46%	0.46%	0.17%	-0.28%	-0.59%	0.55%
INUKE4 ($\pi \to 2\pi$)	-0.28%	0.27%	-0.38%	0.38%	-0.26%	0.26%	-0.29%	0.29%
INUKE5 (N-knockout)	1.80%	-1.80%	1.92%	-1.92%	2.80%	-2.80%	1.90%	-1.90%
INUKE6 ($N \to (2)\pi$)	-0.59%	0.59%	-0.62%	0.62%	-0.63%	0.63%	-0.60%	0.60%
INUKE7 (form. time)	7.22%	-12.85%	4.16%	-9.82%	-0.01%	-1.07%	6.18%	-11.42%
INUKE8 (π xsec)	-0.82%	0.91%	-0.70%	0.79%	0.05%	-0.06%	-0.73%	0.81%
INUKE9 (N xsec)	-0.77%	0.76%	-0.87%	0.87%	-1.53%	1.45%	-0.85%	0.83%
KNO	6.46%	-8.72%	6.08%	-8.35%	6.76%	-6.62%	6.43%	-8.49%
Linearity	0.20%	-	0.37%	-	-0.01%	-	0.21%	-
MAQE	0.10%	-0.05%	0.04%	-0.03%	4.65%	-4.59%	0.48%	-0.43%
MARES	2.71%	-1.85%	1.36%	-0.98%	5.47%	-5.51%	2.75%	-2.04%
OptXTalk	0.69%	-	-2.85%	-	-3.64%	-	-0.17%	-
Rel Escale (F $\pm 1\sigma$)	-0.89%	0.46%	0.50%	-0.24%	1.37%	0.11%	-0.50%	0.33%
SKZP	4.78%	-4.78%	4.46%	-4.46%	10.10%	-10.10%	5.19%	-5.19%
Strip2strip	0.30%	-	-0.03%	-	-0.69%	-	0.17%	-
TargetDeg	-0.59%	-	-2.14%	-	-1.65%	-	-0.90%	-
Total Extrap	35.79	-37.62	36.23	-37.45	18.60	-18.71	33.17%	-34.81%

Table 9.5: The systematic effects for the ANN11 in the Far Detector are shown.

Syst.	NC		ν_μ CC		beam ν_e CC		Total	
Abs Escale	-5.81%	6.00%	-3.57%	4.06%	2.21%	-1.79%	-4.73%	4.98%
Attenuation	-0.46%	-	-0.23%	-	0.91%	-	-0.29%	-
EMvsHad	-2.12%	2.26%	-2.12%	2.19%	-2.81%	3.19%	-2.19%	2.35%
FLUGG	0.10%	-	0.00%	-	8.57%	-	0.91%	-
Gain (F $\pm 1\sigma$)	2.46%	-1.99%	3.34%	-2.34%	1.22%	-0.42%	2.46%	-1.88%
Had1 (Baryon x_f)	-27.92%	-	-34.39%	-	-2.56%	-	-26.31%	-
Had2 (π^0 sel.)	10.31%	-10.00%	10.48%	-10.21%	0.35%	-0.33%	9.36%	-9.08%
Had3 (mult. corr.)	-19.69%	-	-11.96%	-	0.35%	-	-16.70%	-
Had4 (imp. amb.)	-9.96%	-	-12.00%	-	-1.04%	-	-9.36%	-
Had5 (p_T squz)	-8.84%	-	-10.72%	-	-0.98%	-	-8.32%	-
Had6 (iso. 2-body dec.)	-10.88%	-	-13.22%	-	-2.43%	-	-10.37%	-
Hadron Mult.	-2.74%	2.16%	-3.07%	-1.84%	-0.33%	-0.99%	-2.55%	1.32%
INUKE0 (q-exchange)	-0.21%	0.17%	0.02%	-0.03%	-0.01%	-0.02%	-0.16%	0.13%
INUKE1 (π elastic)	0.22%	-0.21%	0.13%	-0.15%	-0.27%	0.30%	0.16%	-0.15%
INUKE2 (π inel.)	-0.14%	-0.14%	-0.69%	0.58%	1.40%	-1.15%	-0.07%	-0.14%
INUKE3 (π abs.)	-0.49%	0.44%	0.36%	-0.54%	0.00%	-0.24%	-0.33%	0.25%
INUKE4 ($\pi \rightarrow 2\pi$)	-0.33%	0.33%	-0.43%	0.43%	-0.26%	0.26%	-0.33%	0.33%
INUKE5 (N-knockout)	1.86%	-1.86%	1.77%	-1.77%	3.12%	-3.12%	1.97%	-1.97%
INUKE6 ($N \rightarrow (2)\pi$)	-0.62%	0.62%	-0.70%	0.70%	-0.62%	0.62%	-0.63%	0.63%
INUKE7 (form. time)	8.31%	-15.49%	4.45%	-12.23%	0.17%	-0.21%	7.00%	-13.56%
INUKE8 (π xsec)	-0.95%	1.07%	-0.68%	0.75%	0.10%	-0.12%	-0.81%	0.91%
INUKE9 (N xsec)	-0.73%	0.70%	-0.68%	0.71%	-1.97%	1.90%	-0.84%	0.82%
KNO	7.61%	-10.73%	6.72%	-9.44%	6.48%	-6.54%	7.38%	-10.15%
Linearity	0.15%	-	-0.14%	-	-0.75%	-	0.02%	-
MAQE	0.07%	-0.04%	0.02%	-0.01%	4.97%	-4.95%	0.54%	-0.52%
MARES	2.01%	-1.37%	1.00%	-0.71%	5.36%	-5.44%	2.20%	-1.68%
OptXTalk	2.08%	-	-0.07%	-	-2.91%	-	1.30%	-
Rel Escale (F $\pm 1\sigma$)	-2.21%	0.73%	0.15%	0.64%	1.92%	0.49%	-1.49%	0.70%
SKZP	4.84%	-4.84%	4.48%	-4.48%	10.01%	-10.01%	5.29%	-5.29%
Strip2strip	0.13%	-	0.53%	-	-0.77%	-	0.10%	-
TargetDeg	-0.58%	-	-2.24%	-	-1.65%	-	-0.91%	-
Total Extrap	42.27	-44.82	44.81	-46.55	18.28	-18.16	38.83%	-41.05%

Table 9.6: The systematic effects for the ANN14 in the Far Detector are shown.

9.6.3 Extrapolation Systematics NC + ν_μ CC + Beam ν_e

Syst.	NC		ν_μ CC		beam ν_e CC		Total	
Abs Escale	-1.11%	1.41%	2.51%	-3.05%	-2.48%	1.94%	-0.71%	0.79%
Attenuation	0.67%	-	0.74%	-	1.66%	-	0.79%	-
EMvsHad	-0.09%	-0.10%	-0.47%	0.20%	3.09%	4.07%	0.18%	0.38%
FLUGG	-0.09%	-	0.00%	-	-4.71%	-	-0.56%	-
Gain (F $\pm 1\sigma$)	0.53%	0.59%	0.80%	-1.42%	-0.38%	-0.56%	0.48%	0.17%
Gain (N $\pm 1\sigma$)	-0.12%	1.09%	-0.99%	0.98%	-2.12%	0.88%	-0.46%	1.05%
Had1 (Baryon x_f)	-0.10%	-	-1.30%	-	-1.55%	-	-0.43%	-
Had2 (π^0 sel.)	-0.01%	0.00%	-0.47%	0.55%	-0.03%	0.04%	-0.08%	0.09%
Had3 (mult. corr.)	0.71%	-	1.82%	-	0.85%	-	0.89%	-
Had4 (imp. amb.)	-0.13%	-	0.38%	-	-0.79%	-	-0.12%	-
Had5 (p_T squz)	-0.28%	-	0.23%	-	-0.91%	-	-0.27%	-
Had6 (iso. 2-body dec.)	0.20%	-	0.60%	-	-1.30%	-	0.10%	-
Hadron Mult.	0.77%	-0.44%	1.64%	-0.26%	2.02%	0.86%	1.03%	-0.27%
INUKE0 (q-exchange)	-0.25%	0.22%	-0.10%	0.10%	0.28%	-0.27%	-0.17%	0.15%
INUKE1 (π elastic)	-0.07%	0.06%	-0.25%	0.25%	0.03%	-0.01%	-0.09%	0.08%
INUKE2 (π inel.)	0.52%	-0.55%	0.85%	-1.07%	0.63%	-0.58%	0.58%	-0.63%
INUKE3 (π abs.)	-0.15%	0.11%	0.20%	-0.17%	-0.36%	0.32%	-0.12%	0.09%
INUKE4 ($\pi \to 2\pi$)	0.06%	-0.06%	-0.00%	0.00%	-0.15%	0.15%	0.03%	-0.03%
INUKE5 (N-knockout)	0.29%	-0.29%	-0.40%	0.40%	0.36%	-0.37%	0.19%	-0.20%
INUKE6 ($N \to (2)\pi$)	0.03%	-0.03%	-0.07%	0.07%	0.05%	-0.05%	0.02%	-0.02%
INUKE7 (form. time)	-0.82%	0.50%	-1.77%	0.29%	1.00%	-1.14%	-0.78%	0.29%
INUKE8 (π xsec)	0.18%	-0.20%	0.09%	-0.05%	0.00%	0.00%	0.15%	-0.15%
INUKE9 (N xsec)	-0.49%	0.47%	0.55%	-0.54%	-0.34%	0.29%	-0.32%	0.30%
Intensity	1.10%	-	1.10%	-	1.10%	-	1.10%	-
KNO	-0.02%	0.18%	-0.17%	0.39%	0.13%	-0.05%	-0.02%	0.19%
Linearity	0.21%	-	0.83%	-	1.45%	-	0.43%	-
MAQE	-0.02%	0.01%	0.04%	-0.02%	0.13%	-0.21%	0.00%	-0.02%
MARES	-0.06%	0.01%	-0.12%	0.13%	-0.38%	0.34%	-0.10%	0.07%
Norm	2.00%	-	2.00%	-	2.00%	-	2.00%	-
OptXTalk	0.32%	-	0.36%	-	-6.46%	-	-0.38%	-
Presel	1.00%	-	1.00%	-	1.00%	-	1.00%	-
Rel Escale (F $\pm 1\sigma$)	-0.36%	0.11%	1.21%	0.34%	3.37%	2.39%	0.27%	0.38%
Rel Escale (N $\pm 1\sigma$)	0.51%	0.81%	1.05%	-0.35%	-0.50%	-0.01%	0.49%	0.55%
SKZP	-0.27%	0.30%	-0.39%	0.45%	3.32%	-3.93%	0.09%	-0.12%
Strip2strip	0.28%	-	0.17%	-	1.39%	-	0.38%	-
TargetDeg	-0.17%	-	-0.08%	-	0.12%	-	-0.13%	-
Total Extrap							3.60%	-3.40%

Table 9.7: The extrapolation effects using the HOOHE Near Detector decomposition method for NC + ν_μ CC + beam ν_e CC are shown for the ParticlePID.

Syst.	NC		ν_μ CC		beam ν_e CC		Total	
Abs Escale	0.03%	0.97%	6.23%	-4.17%	0.72%	-0.05%	0.93%	0.18%
Attenuation	-0.20%	-	-0.47%	-	-1.33%	-	-0.35%	-
EMvsHad	0.10%	0.03%	-0.99%	0.61%	0.09%	0.05%	-0.04%	0.11%
FLUGG	-0.09%	-	0.00%	-	-4.49%	-	-0.53%	-
Gain (F $\pm 1\sigma$)	1.59%	-0.87%	5.15%	-2.04%	0.46%	-3.55%	1.96%	-1.30%
Gain (N $\pm 1\sigma$)	-1.22%	1.21%	-1.14%	2.58%	-1.98%	1.28%	-1.28%	1.40%
Had1 (Baryon x_f)	-1.64%	-	-3.76%	-	-1.09%	-	-1.87%	-
Had2 (π^0 sel.)	0.14%	-0.14%	-0.21%	0.31%	-0.25%	0.25%	0.05%	-0.04%
Had3 (mult. corr.)	-0.77%	-	0.90%	-	0.99%	-	-0.36%	-
Had4 (imp. amb.)	-0.75%	-	-1.06%	-	-0.64%	-	-0.78%	-
Had5 (p_T squz)	-0.84%	-	-1.23%	-	-0.73%	-	-0.88%	-
Had6 (iso. 2-body dec.)	-0.43%	-	-0.45%	-	-2.33%	-	-0.63%	-
Hadron Mult.	0.39%	0.24%	1.51%	0.28%	1.58%	-0.13%	0.66%	0.21%
INUKE0 (q-exchange)	-0.21%	0.18%	0.13%	-0.13%	0.13%	-0.15%	-0.13%	0.10%
INUKE1 (π elastic)	-0.19%	0.19%	-0.10%	0.09%	0.09%	-0.09%	-0.15%	0.15%
INUKE2 (π inel.)	0.48%	-0.64%	0.62%	-0.87%	0.31%	-0.18%	0.48%	-0.62%
INUKE3 (π abs.)	0.25%	-0.31%	0.02%	-0.06%	-0.48%	0.40%	0.15%	-0.21%
INUKE4 ($\pi \rightarrow 2\pi$)	0.01%	-0.01%	-0.16%	0.15%	-0.07%	0.07%	-0.02%	0.02%
INUKE5 (N-knockout)	0.53%	-0.54%	0.29%	-0.30%	0.04%	-0.03%	0.45%	-0.46%
INUKE6 ($N \rightarrow (2)\pi$)	-0.06%	0.06%	-0.02%	0.02%	-0.00%	0.00%	-0.05%	0.05%
INUKE7 (form. time)	-0.30%	-0.50%	-2.43%	2.72%	0.43%	-1.16%	-0.51%	-0.13%
INUKE8 (π xsec)	0.18%	-0.21%	0.10%	-0.09%	0.00%	0.00%	0.16%	-0.17%
INUKE9 (N xsec)	-0.53%	0.50%	-0.36%	0.34%	0.20%	-0.26%	-0.43%	0.40%
Intensity	1.10%	-	1.10%	-	1.10%	-	1.10%	-
KNO	0.11%	-0.09%	-0.13%	0.28%	-0.05%	0.56%	0.07%	0.03%
Linearity	0.16%	-	0.58%	-	-0.34%	-	0.17%	-
MAQE	0.01%	-0.00%	-0.06%	0.04%	-0.07%	-0.07%	-0.01%	-0.00%
MARES	0.08%	-0.04%	-0.27%	0.26%	-0.65%	0.53%	-0.04%	0.06%
Norm	2.00%	-	2.00%	-	2.00%	-	2.00%	-
OptXTalk	1.31%	-	-0.69%	-	-5.04%	-	0.40%	-
Presel	1.00%	-	1.00%	-	1.00%	-	1.00%	-
Rel Escale (F $\pm 1\sigma$)	-0.90%	0.56%	0.27%	-0.09%	1.37%	0.22%	-0.51%	0.44%
Rel Escale (N $\pm 1\sigma$)	1.39%	-0.87%	2.49%	-1.98%	-1.20%	0.25%	1.27%	-0.91%
SKZP	-0.28%	0.32%	-0.29%	0.33%	3.24%	-3.83%	0.07%	-0.10%
Strip2strip	0.37%	-	-0.09%	-	-0.69%	-	0.20%	-
TargetDeg	-0.14%	-	-0.03%	-	0.12%	-	-0.10%	-
Total Extrap							4.70%	-4.38%

Table 9.8: The extrapolation effects using the HOOHE Near Detector decomposition method for NC + ν_μ CC + beam ν_e CC are shown for the ANN11.

Syst.	NC		ν_μ CC		beam ν_e CC		Total	
Abs Escale	-1.21%	0.97%	5.71%	-3.71%	0.43%	0.17%	-0.19%	0.32%
Attenuation	-0.64%	-	-1.02%	-	1.09%	-	-0.47%	-
EMvsHad	-0.25%	-0.20%	-0.87%	0.74%	-0.13%	0.25%	-0.31%	-0.03%
FLUGG	-0.09%	-	0.00%	-	-4.41%	-	-0.60%	-
Gain (F $\pm 1\sigma$)	2.45%	-2.21%	2.95%	-2.71%	1.12%	-0.19%	2.35%	-2.03%
Gain (N $\pm 1\sigma$)	-2.34%	1.62%	-3.84%	4.04%	-2.76%	2.62%	-2.57%	2.03%
Had1 (Baryon x_f)	-2.29%	-	-4.23%	-	-0.79%	-	-2.33%	-
Had2 (π^0 sel.)	0.33%	-0.37%	0.22%	-0.19%	-0.06%	0.07%	0.27%	-0.29%
Had3 (mult. corr.)	-1.74%	-	-0.08%	-	1.14%	-	-1.19%	-
Had4 (imp. amb.)	-0.85%	-	-1.64%	-	-0.42%	-	-0.89%	-
Had5 (p_T squz)	-0.93%	-	-1.72%	-	-0.54%	-	-0.98%	-
Had6 (iso. 2-body dec.)	-1.04%	-	0.08%	-	-1.72%	-	-0.99%	-
Hadron Mult.	-0.39%	0.29%	0.31%	-0.70%	0.13%	0.46%	-0.24%	0.19%
INUKE0 (q-exchange)	-0.17%	0.12%	0.27%	-0.29%	0.14%	-0.16%	-0.08%	0.04%
INUKE1 (π elastic)	-0.19%	0.19%	-0.37%	0.35%	0.13%	-0.11%	-0.17%	0.17%
INUKE2 (π inel.)	0.76%	-1.03%	0.55%	-0.70%	0.64%	-0.43%	0.72%	-0.92%
INUKE3 (π abs.)	0.03%	-0.06%	0.73%	-0.88%	-0.74%	0.58%	0.02%	-0.08%
INUKE4 ($\pi \to 2\pi$)	-0.02%	0.02%	-0.12%	0.12%	-0.06%	0.06%	-0.04%	0.04%
INUKE5 (N-knockout)	0.55%	-0.57%	0.23%	-0.23%	0.42%	-0.44%	0.50%	-0.51%
INUKE6 ($N \to (2)\pi$)	-0.07%	0.07%	-0.07%	0.07%	0.01%	-0.01%	-0.06%	0.06%
INUKE7 (form. time)	0.25%	-1.16%	-3.17%	2.00%	0.80%	-0.24%	-0.09%	-0.67%
INUKE8 (π xsec)	0.03%	-0.01%	0.21%	-0.23%	0.02%	-0.01%	0.05%	-0.04%
INUKE9 (N xsec)	-0.48%	0.44%	-0.28%	0.28%	-0.33%	0.24%	-0.44%	0.40%
Intensity	1.40%	-	1.40%	-	1.40%	-	1.40%	-
KNO	0.46%	-0.83%	-0.32%	0.86%	-0.17%	0.42%	0.29%	-0.48%
Linearity	-0.21%	-	-0.57%	-	-1.41%	-	-0.40%	-
MAQE	-0.00%	-0.00%	-0.05%	0.04%	0.09%	-0.23%	0.00%	-0.02%
MARES	-0.12%	0.10%	-0.28%	0.24%	-0.58%	0.52%	-0.19%	0.16%
Norm	2.00%	-	2.00%	-	2.00%	-	2.00%	-
OptXTalk	2.58%	-	2.41%	-	-3.73%	-	1.80%	-
Presel	1.00%	-	1.00%	-	1.00%	-	1.00%	-
Rel Escale (F $\pm 1\sigma$)	-2.09%	0.70%	-0.27%	0.70%	1.60%	0.61%	-1.42%	0.69%
Rel Escale (N $\pm 1\sigma$)	1.76%	-1.81%	2.89%	-3.55%	-0.05%	-0.13%	1.67%	-1.81%
SKZP	-0.30%	0.34%	-0.33%	0.37%	3.32%	-3.92%	0.14%	-0.17%
Strip2strip	-0.18%	-	-0.18%	-	-0.94%	-	-0.27%	-
TargetDeg	-0.14%	-	0.02%	-	0.15%	-	-0.09%	-
Total Extrap							5.95%	-6.24%

Table 9.9: The extrapolation effects using the HOOHE Near Detector decomposition method for NC + ν_μ CC + beam ν_e CC are shown for the ANN14.

9.6.4 Extrapolation Systematics ν_τ

Syst.	ν_τ CC	
ν_τ xsec	44.49%	-
Abs Escale	-0.40%	-0.69%
Attenuation	-0.32%	-
EMvsHad	-2.02%	2.08%
Gain	-1.67%	-1.71%
Hadron Mult.	-0.54%	-0.37%
Linearity	-0.91%	-
Norm	2.40%	-
OptXTalk	0.32%	-
Presel	1.00%	-
Strip2strip	-1.31%	-
ν_μ FLUGGReweight	0.00%	-
ν_μ KNO	-0.26%	0.11%
ν_μ MAQE	-0.39%	0.39%
ν_μ MARES	-0.68%	0.80%
ν_μ SKZP	0.00%	-
ν_μ Target Deg	0.00%	-
CCEnergyShift	-1.58%	2.25%
CCSigNC	-0.58%	0.58%
Total Extrap	44.75%	-44.72%

Table 9.10: The systematics for the ν_τ CC Far Detector prediction for the ParticlePID are shown.

Syst.	ν_τ CC	
ν_τ xsec	45.50%	-
Abs Escale	-0.70%	1.99%
Attenuation	1.25%	-
EMvsHad	-2.28%	2.38%
Gain	2.66%	-2.43%
Hadron Mult.	-0.38%	-0.21%
Linearity	-0.01%	-
Norm	2.40%	-
OptXTalk	1.48%	-
Presel	1.00%	-
Strip2strip	-0.45%	-
ν_μ FLUGGReweight	0.00%	-
ν_μ KNO	-0.26%	0.10%
ν_μ MAQE	-0.39%	0.40%
ν_μ MARES	-0.68%	0.81%
ν_μ SKZP	0.00%	-
ν_μ Target Deg	0.00%	-
CCEnergyShift	-1.61%	2.35%
CCSigNC	-0.57%	0.58%
Total Extrap	45.87%	-45.79%

Table 9.11: The systematics for the ν_τ CC Far Detector prediction for the ANN11 are shown.

Syst.	ν_τ CC	
ν_τ xsec	45.76%	-
Abs Escale	-3.29%	2.26%
Attenuation	-1.06%	-
EMvsHad	-2.28%	2.41%
Gain	2.39%	-4.19%
Hadron Mult.	-0.39%	-0.35%
Linearity	0.08%	-
Norm	2.40%	-
OptXTalk	-0.47%	-
Presel	1.00%	-
Strip2strip	0.09%	-
ν_μ FLUGGReweight	0.00%	-
ν_μ KNO	-0.26%	0.10%
ν_μ MAQE	-0.40%	0.40%
ν_μ MARES	-0.69%	0.81%
ν_μ SKZP	0.00%	-
ν_μ Target Deg	0.00%	-
CCEnergyShift	-1.66%	2.40%
CCSigNC	-0.57%	0.58%
Total Extrap	46.10%	-46.25%

Table 9.12: The systematics for the ν_τ CC Far Detector prediction for the ANN14 are shown.

9.6.5 Extrapolation Systematics Signal ν_e

Syst.	ν_e CC	
Abs Escale	0.33%	-0.54%
Attenuation	0.01%	-
CalDet	2.60%	-
EMvsHad	-1.47%	1.49%
Gain	0.11%	-0.27%
Had1 (Baryon x_f)	-1.85%	-
Had10	-0.59%	0.00%
Had2 (π^0 sel.)	0.59%	0.00%
Had3 (mult. corr.)	-1.00%	-
Had4 (imp. amb.)	-0.59%	-
Had5 (p_T squz)	-0.44%	-
Had6 (iso. 2-body dec.)	-0.55%	-
Hadron Mult.	-1.67%	-0.61%
INUKE0 (q-exchange)	-0.11%	0.11%
INUKE1 (π elastic)	-0.06%	0.06%
INUKE2 (π inel.)	0.59%	-0.59%
INUKE3 (π abs.)	-0.19%	0.19%
INUKE4 ($\pi \rightarrow 2\pi$)	-0.14%	0.14%
INUKE5 (N-knockout)	2.44%	-2.44%
INUKE6 ($N \rightarrow (2)\pi$)	-0.57%	0.57%
INUKE7 (form. time)	0.51%	-0.48%
INUKE8 (π xsec)	-0.08%	0.10%
INUKE9 (N xsec)	-1.57%	1.61%
Linearity	-0.06%	-
MRE Eff	1.65%	-
Norm	2.40%	-
OptXTalk	0.20%	-
Presel	1.00%	-
Strip2strip	-0.11%	-
ν_μ FLUGGReweight	0.00%	-
ν_μ KNO	0.40%	-0.63%
ν_μ MAQE	-0.25%	0.34%
ν_μ MARES	0.17%	-0.03%
ν_μ SKZP	0.00%	-
ν_μ Target Deg	0.00%	-
CCEnergyShift	3.72%	-2.49%
CCSigNC	-0.50%	0.50%
Total Extrap	7.14%	-6.60%

Table 9.13: The systematics for the signal ν_e CC Far Detector prediction for the ParticlePID are shown.

Syst.	ν_e CC	
Abs Escale	-1.98%	1.52%
Attenuation	-0.12%	-
CalDet	1.55%	-
EMvsHad	-1.74%	1.77%
Gain	0.83%	-0.94%
Had1 (Baryon x_f)	-1.70%	-
Had2 (π^0 sel.)	0.48%	-0.48%
Had3 (mult. corr.)	-0.91%	-
Had4 (imp. amb.)	-0.55%	-
Had5 (p_T squz)	-0.42%	-
Had6 (iso. 2-body dec.)	-0.66%	-
Hadron Mult.	-1.11%	-0.77%
INUKE0 (q-exchange)	-0.13%	0.13%
INUKE1 (π elastic)	-0.17%	0.17%
INUKE2 (π inel.)	0.70%	-0.69%
INUKE3 (π abs.)	0.07%	-0.07%
INUKE4 ($\pi \rightarrow 2\pi$)	-0.15%	0.15%
INUKE5 (N-knockout)	2.84%	-2.84%
INUKE6 ($N \rightarrow (2)\pi$)	-0.60%	0.60%
INUKE7 (form. time)	0.23%	-0.36%
INUKE8 (π xsec)	-0.04%	0.04%
INUKE9 (N xsec)	-1.90%	1.91%
Linearity	0.03%	-
MRE Eff	1.53%	-
Norm	2.40%	-
OptXTalk	0.52%	-
Presel	1.00%	-
Strip2strip	-0.04%	-
ν_μ FLUGGReweight	0.00%	-
ν_μ KNO	0.41%	-0.63%
ν_μ MAQE	-0.24%	0.33%
ν_μ MARES	0.18%	-0.05%
ν_μ SKZP	0.00%	-
ν_μ Target Deg	0.00%	-
CCEnergyShift	3.79%	-2.60%
CCSigNC	-0.50%	0.51%
Total Extrap	7.19%	-6.78%

Table 9.14: The systematics for the signal ν_e CC Far Detector prediction for the ANN11 are shown.

Syst.	ν_e CC	
Abs Escale	-3.17%	2.74%
Attenuation	-0.08%	-
CalDet	5.07%	-
EMvsHad	-1.98%	2.03%
Gain	1.08%	-1.64%
Had1 (Baryon x_f)	-1.58%	-
Had2 (π^0 sel.)	0.45%	-0.45%
Had3 (mult. corr.)	-0.97%	-
Had4 (imp. amb.)	-0.51%	-
Had5 (p_T squz)	-0.38%	-
Had6 (iso. 2-body dec.)	-0.69%	-
Hadron Mult.	-1.32%	-0.80%
INUKE0 (q-exchange)	-0.13%	0.13%
INUKE1 (π elastic)	-0.21%	0.21%
INUKE2 (π inel.)	0.86%	-0.85%
INUKE3 (π abs.)	0.09%	-0.09%
INUKE4 ($\pi \rightarrow 2\pi$)	-0.16%	0.16%
INUKE5 (N-knockout)	2.90%	-2.90%
INUKE6 ($N \rightarrow (2)\pi$)	-0.59%	0.59%
INUKE7 (form. time)	0.15%	-0.29%
INUKE8 (π xsec)	-0.01%	0.02%
INUKE9 (N xsec)	-1.99%	2.01%
Linearity	0.01%	-
MRE Eff	1.51%	-
Norm	2.40%	-
OptXTalk	0.50%	-
Presel	1.00%	-
Strip2strip	-0.05%	-
ν_μ FLUGGReweight	0.00%	-
ν_μ KNO	0.42%	-0.65%
ν_μ MAQE	-0.27%	0.36%
ν_μ MARES	0.17%	-0.03%
ν_μ SKZP	0.00%	-
ν_μ Target Deg	0.00%	-
CCEnergyShift	3.78%	-2.52%
CCSigNC	-0.49%	0.50%
Total Extrap	9.09%	-8.87%

Table 9.15: The systematics for the signal ν_e CC Far Detector prediction for the ANN14 are shown.

9.7 Cosmic Backgrounds

It is possible for events within the spill window to originate from cosmogenic sources. The magnitude of this effect can be calculated with the use of fake spills. Data is taken with the same equipment configurations as during a real spill, except there is no beam. The number of events passing the selection cuts can then be recorded to give an understanding of this cosmic background. This method, as well as suggestions for reducing the cosmic background, are presented in [78] and [118].

After the cosmic cuts, fiducial, preselection, and PID cuts, no events were found the fake spill Far Detector data[119]. This leads to an expected cosmic background in the Far Detector data for all three PIDs of between 0 and 0.331 events at the 90% confidence level.

9.8 Summary

The summary of the effect of the systematics on the background prediction[117] for the ParticlePID, ANN11, and ANN14 are presented in tables 9.16, 9.17, and 9.18. Overall, the ParticlePID has significantly lower systematics than both the ANN11 and ANN14 (about 20% lower than the ANN11 and 34% lower than the ANN14).

The most significant differences are seen in the systematics for the hadronization model ($+1.4\%, -1.1\%$ for the ParticlePID and $\pm 2.3\%$ for the ANN11). While it is expected[120] that the ParticlePID will have larger hadronization model systematics because it is designed to identify and reconstruct changes in the hadronic shower, it is also expected to do so more accurately than the ANN11, and thus the near/far difference in the extrapolation is smaller. Improvements are also noticed in the calibration systematic ($+1.8\%, -1.5\%$ for the ParticlePID and $+2.8\%, -2.3\%$ for the ANN11) which is primarily

due to the gains systematic. This improvement can be explained in part by the fact that the ParticlePID will still find the basic underlying structure of a shower even if the energy of some of the strips are varied, whereas the global EM shower fit employed by the ANN11 can be drastically effected by the variation of the energy deposited in just a single strip. The other categories of systematic error are comparable between ParticlePID and the ANN11, resulting in a total background prediction uncertainty of $+4.4\%, -4.3\%$ for the ParticlePID, $+5.6\%, -5.3\%$ for the ANN11, and $+6.6\%, -6.9\%$ for the ANN14.

The total systematic on the signal ν_e CC events is 7.1% for the ParticlePID, 7.2% for the ANN11, and 9.1% for the ANN14.

Source of Uncertainty	Effect on Background Prediction
Beam Model	±0.6%
Hadronization Model	+1.4%, −1.1%
Crosstalk	±0.4%
Calibration	+1.8%, −1.5%
Far/Near Normalization	±2.4%
Cross Section	+0.2%, −0.1%
Intranuclear Model	+0.7%, −1.1%
ND Decomposition	±2.1%
ν_τ CC component	±1.8%
Total Background Systematic	**+4.4%, −4.3%**

Table 9.16: A summary of the background systematics for the ParticlePID with the HOOHE extrapolation method.

Source of Uncertainty	Effect on Background Prediction
Beam Model	±0.5%
Hadronization Model	±2.3%
Crosstalk	±0.4%
Calibration	+2.8%, −2.3%
Far/Near Normalization	±2.4%
Cross Section	±0.1%
Intranuclear Model	+0.9%, −1.0%
ND Decomposition	±2.8%
ν_τ CC component	±1.7%
Total Background Systematic	**+5.6%, −5.3%**

Table 9.17: A summary of the background systematics for the ANN11 with the HOOHE extrapolation method.

Source of Uncertainty	Effect on Background Prediction
Beam Model	±0.6%
Hadronization Model	±3.0%
Crosstalk	±1.7%
Calibration	+3.5%, −3.9%
Far/Near Normalization	±2.5%
Cross Section	+0.3%, −0.5%
Intranuclear Model	+1.1%, −1.3%
ND Decomposition	±2.9%
ν_τ CC component	±1.9%
Total Background Systematic	**+6.6%, −6.9%**

Table 9.18: A summary of the background systematics for the ANN14 with the HOOHE extrapolation method.

Chapter 10

Verification of the Methods

Three sideband analyses will be examined before unblinding the data in the signal region. The first sideband is called the anti-PID sideband. All standard event selection cuts are applied with the exception of the PID cut, which is instead used to select all events that have a PID value < 0.5. The second sideband is the MRCC sideband. Here, a prediction is made for the number of events that will end up in the Far Detector MRCC Data sample using the Near to Far Detector ratio method that is used in the standard analysis. The third sideband is the MRE sideband. It is identical to the MRCC sideband in application, except that events from the MRE sample instead of from the MRCC sample are used. In each of these tests, agreement between the Far Detector data and the predicted number of events within 2 σ will be accepted as a verification of the methods used.

10.1 Anti-PID

A Far Detector prediction will be compared to the Far Detector data for each of the PIDs for all events passing the standard preselection cuts with a valid PID value < 0.5. This cut value was chosen for simplicity while remaining below the cut value of 0.55 which

was used in this procedure in the last analysis. This cut value is sufficiently low so that even if oscillations occur with $\sin^2(2\theta_{13})$ near the CHOOZ limit, no statistically significant ($< 1\sigma$) oscillated ν_e sample would be visible.

The number of background events expected in the anti-PID sidebands is determined using the full Near Detector data decomposition and far/near extrapolation. The prediction was made with the HOOHE method of decomposition, performed on samples of events passing the anti-PID cut.

The prediction and measured data for each of the PIDs (ParticlePID, ANN11, and ANN14) is presented in tables 10.1, 10.2, and 10.3. The prediction is performed both with the assumption of no ν_e oscillations and with the assumption of ν_e oscillations at the CHOOZ limit.

For all of the PIDs, Run 2 has the largest discrepancy. For ParticlePID, Run 2 assuming no oscillations is beyond the acceptable 2σ threshold. However, at the CHOOZ limit all runs for all PIDs are within the threshold. When the run periods are combined, all PIDs have good agreement at both the CHOOZ limit and in the case of no oscillations.

	$\sin^2 2\theta_{13} = 0$				$\sin^2 2\theta_{13} = 0.15$ and $\delta_{CP} = 0$			
	Run 1	Run 2	Run 3	Total	Run 1	Run 2	Run 3	Total
NC	33.31	52.03	100.75	186.09	33.31	52.03	100.75	186.09
CC	20.82	32.79	62.90	116.51	20.75	32.69	62.72	116.16
B Nue	0.82	1.36	2.86	5.04	0.79	1.30	2.74	4.83
Tau	1.11	1.70	3.28	6.09	1.02	1.56	3.02	5.60
Total Bkgd	56.06	87.87	169.80	313.73	55.87	87.58	169.23	312.68
Nue	0.02	0.03	0.05	0.10	2.32	3.62	6.77	12.71
Data	52	108	162	322	52	108	162	322
σ Diff	-0.54	2.14	-0.60	0.46	-0.81	1.76	-1.06	-0.19

Table 10.1: Anti-ParticlePID (<0.5)

	$\sin^2 2\theta_{13} = 0$				$\sin^2 2\theta_{13} = 0.15$ and $\delta_{CP} = 0$			
	Run 1	Run 2	Run 3	Total	Run 1	Run 2	Run 3	Total
NC	32.94	51.95	100.66	185.55	32.94	51.95	100.66	185.55
CC	21.03	32.76	62.93	116.72	20.96	32.65	62.74	116.35
B Nue	0.87	1.29	2.88	5.04	0.84	1.24	2.77	4.85
Tau	1.14	1.76	3.39	6.29	1.05	1.62	3.12	5.79
Total Bkgd	55.99	87.75	169.86	313.60	55.80	87.45	169.29	312.54
Nue	0.02	0.03	0.05	0.10	2.30	3.58	6.69	12.57
Data	54	106	167	327	54	106	167	327
σ Diff	-0.27	1.94	-0.22	0.75	-0.54	1.57	-0.68	0.10

Table 10.2: Anti-ANN11 (<0.5)

	$\sin^2 2\theta_{13} = 0$				$\sin^2 2\theta_{13} = 0.15$ and $\delta_{CP} = 0$			
	Run 1	Run 2	Run 3	Total	Run 1	Run 2	Run 3	Total
NC	33.49	52.07	101.26	186.82	33.49	52.07	101.26	186.82
CC	21.00	32.81	62.22	116.03	20.93	32.70	62.03	115.66
B Nue	0.87	1.26	2.91	5.04	0.83	1.21	2.80	4.84
Tau	1.15	1.75	3.38	6.28	1.06	1.61	3.11	5.78
Total Bkgd	56.50	87.89	169.77	314.16	56.31	87.59	169.20	313.10
Nue	0.02	0.03	0.05	0.10	2.28	3.53	6.52	12.33
Data	53	102	171	326	53	102	171	326
σ Diff	-0.47	1.50	0.09	0.66	-0.73	1.14	-0.36	0.03

Table 10.3: Anti-ANN14 (<0.5)

10.2 MRCC

The MRCC method (see chapter 7) is used as a way to confirm that the difference seen between data and Monte Carlo in the Near Detector is also seen in the Far Detector. By using the MRCC sample, the standard analysis PID cuts can be applied without the possibility of measuring oscillated ν_e events, since the quantity of events reconstructed from the shower remnant left by the MRCC process is related to the number of ν_μ CC events in the detector. If the difference is seen in both detectors, it indicates a data to Monte Carlo discrepancy which can be accounted for in the near/far extrapolation. If this difference cannot be accounted for, it would indicate a problem isolated to one of the detectors which would require additional steps to be taken in the extrapolation method in order to ensure the validity of the result.

If the discrepancy between Near Detector data and Monte Carlo is also present in the Far Detector, then a prediction, P, made by scaling the Far Detector Monte Carlo by the Near Detector data to Monte Carlo ratio would agree with the observed Far Detector data.

$$P = F^{MC}_{MRCC} \times \frac{N^{data}_{MRCC}}{N^{MC}_{MRCC}} \times C$$

Where F and N are the Far and Near Detectors, and C is an optional ν_μ CC correction factor which will be discussed shortly. This method is sensitive to two different sources of discrepancy, namely those due to differences found in oscillated ν_e-like events and those isolated to long-muon ν_μ CC events from which the MRCC events are generated. The ν_e appearance analysis is concerned only with differences arising from oscillated ν_e-like events which will be present in the actual data sample, so it is desirable to remove residual effects isolated to differences in the sample of long-muon ν_μ CC events.

The MRCC samples are prepared for each run period using the cuts listed in table

10.4, in order of application. Events are checked for data quality and to ensure that the original event (before muon removal) contained a sufficiently long muon track. The sample of reconstructed shower remnants then is filtered by the standard analysis preselection and PID cuts. The ν_μ CC sample is also prepared for each run period using a set of cuts, listed in table 10.5, in order to to select ν_μ CC events corresponding to the same set of cuts used to find the ν_μ CC events which are processed through MRCC. The events used to make the MRCC events is a subset of the ν_μ CC sample at the "CC Cuts" cut, since an additional requirement exists that a shower remnant of significant size remain in the ν_μ CC event once the muon is removed. The ν_μ CC sample is further restricted in an attempt to get a sample most representative of the events used for MRCC at the MRCCPreselection cut level by requiring the event to have a shower with at least 0, 500 MeV or 1 GeV of energy. Since no significant difference was seen with the application of the energy cut on the ν_μ CC event shower, the requirement that the ν_μ CC event has a shower is all that will be shown here. In both samples, a cut requiring event energy to be greater than 210 MeV is used to remove noise and is applied prior to any cuts of interest in this study.

The ν_μ CC correction can be applied to the MRCC events to remove discrepancies arising from differences in ν_μ CC type events, and can be expressed as

$$C = \frac{N_{CC}^{MC}}{N_{CC}^{data}} \times \frac{F_{CC}^{data}}{F_{CC}^{MC}}$$

This ratio can be calculated for each run period and each level of ν_μ CC event cuts. This ratio is used as a correction factor to the predicted MRCCPreselection. Statistical errors arising from the data samples in this ν_μ CC correction are considered. However, uncertainties due to oscillation parameters are not considered when calculating the correction factor error. The ν_μ CC corrected prediction for the Far Detector data MRCC events is sensitive only to discrepancies related to oscillated ν_e-like events, because discrepancies arriving from

Cut Name	Cuts Applied
Data Quality	L010185 running
	Event successfully muon removed
	Shower remnant within Fiducial Volume
	Beam quality cuts (data only)
	Detector quality cuts (data only)
	Largest event in snarl (Far Data/Monte Carlo only)
Cosmic Cuts	Event slope < 10
	If track is present, angle of track w.r.t detector y > 0.6
	If track is present, distance between start and end of track in y < 2 m
Event Energy	Event energy > 210 MeV
MRCCFiducial	Original event within MRCC fiducial volume
MRCCPreselection	Event has a track
	Track pass fit
	Original ν_μ CC PID (roCCPID) > 0.3
Fiducial Volume	Event is in Fiducial Volume
ν_e preselection	Event energy > 1 GeV and < 8 GeV
	Track like planes < 16
	Track planes < 25
	Event has at least 5 contiguous planes
	Event has a shower
	Event is the largest event in the snarl (FD only)
ν_e PID	ANN11 > 0.70
	or ANN14 > 0.75
	or ParticlePID > 0.70

Table 10.4: The sequential cuts applied to create the MRCC sample

Cut Name	Cuts Applied
Data Quality	L010185 running
	Event successfully muon removed
	Shower remnant within Fiducial Volume
	Beam quality cuts (data only)
	Detector quality cuts (data only)
	Event is largest event in snarl (Far Data/Monte Carlo only)
Cosmic Cuts	Event slope < 10
	If track is present, angle of track w.r.t detector y > 0.6
	If track is present, distance between start and end of track in y < 2 m
Fiducial Volume	Event is in Fiducial Volume
Event Energy	Event energy >210 MeV
CC Cuts	Event has a track
	Original ν_μ CC PID (roCCPID) > 0.3
	Track pass fit
HasShw	Event has a shower
HasShw500	Event has shower with energy > 500 MeV
HasShw1000	Event has shower with energy > 1 GeV

Table 10.5: The sequential cuts applied to create the ν_μ CC sample

sources in the ν_μ CC sample are removed by the ν_μ CC correction.

The prediction and correction factor is made in each run period using histograms with 1 GeV bins. The correction histogram records the effective shower energy (event energy - track energy) to make sure that the effect being accounted for in the ν_μ CC events corresponds with the energy of the MRCC event. In the event of no correction factor being used, the entire error is taken as the statistical error on the predicted number of events ($1/\sqrt{\#events}$) and then is compared to the data, assuming no error for the data. In the event that a correction factor is used, there is still no error taken for the data, and the error on the prediction is taken as the binomial error introduced by the correction factor alone on the far data. So, in the case of a correction faction being used, the error taken on the entire prediction is

$$\delta P = \sqrt{F_{CC}^{data} \times \epsilon \times (1 - \epsilon)}$$

where

$$\epsilon = \frac{F_{\alpha}^{data}}{F_{CC}^{data}}$$

and α is the cut (ParticlePID, ANN11, ANN14) at which the prediction is being calculated. Contributions from the statistical uncertainty in the other terms are not included as they are expected to be much smaller.

In addition to statistical errors, the predictions also gain uncertainty from the systematics of each PID selection method (taken to be equal to those found in the standard extrapolation [117]). The oscillation parameters used for the ν_μ oscillation in the Far Detector are $\Delta m^2 = 2.43 \pm 0.13 \times 10^{-3} eV^2$ and $\sin^2(2\theta) > 0.9$ (at 90%C.L.) [121] and give rise to an additional systematic.

The overall Far Detector data and prediction, resulting from the summation of the results from each of the individual run periods, are presented with errors for each of the correction methods in tables 10.6 and 10.7. The same information is repeated, including

the unadjusted Far Detector Monte Carlo and resulting discrepancy for the cases of no ν_μ CC correction and ν_μ CC correction requiring showers in tables 10.8 and 10.9.

In an effort to understand the large discrepancy in the prediction arising without any ν_μ CC correction, the underlying numbers were studied for each run and subrun period as shown in table 10.10 (expressed as raw numbers) or in table 10.11 (expressed as efficiencies with respect to MRCCPreselection), with the discrepancy listed arising from statistical sources only. Run 1 has only one period. Run 2 is split into two subruns (Run 2a and 2b) due to a shutdown. Run 3 is split into three subrun periods (Run 3a, 3b, and 3c) with the first subrun ending with the replacement of Horn 2 and the second subrun ending with the replacement of the bus strips on Horn 1. By chance, all six of these subrun periods represent similar amounts of exposure. Upon splitting the data into subrun periods, it became obvious that the discrepancy seen in the overall Run 1+2+3 numbers was due entirely to an excess of data observed in Run 3b of about 4.4 σ at preselection. It was determined by the scanning of both original ν_μ CC events and the MRCC events that the excess was not due to a reconstruction software problem. Checks of POT counting confirmed the correct normalization. A study looking at the sidereal and real times of these events found no anomalies. Additionally, predictions for the Run 3b data adjusted by the ν_μ CC events with a shower fell well within the desired discrepancy range of 2 σ for all cut levels, as shown in table 10.12 (expressed as raw numbers) or in table 10.13 (expressed as efficiencies with respect to MRCCPreselection), indicating that this large discrepancy has a considerable contribution arising from a source related to ν_μ CC events which is not of interest to the ν_e appearance analysis. Energy distributions for each of the runs are shown at Preselection, ParticlePID ANN11, and ANN14 in figures 10.1, 10.2, 10.3, and 10.4 (without any ν_μ CC correction), and in figures 10.5, 10.6, 10.7, and 10.8 (with the ν_μ CC correction requiring ν_μ CC events having showers). PID distributions are shown for each

PID in figure 10.9. In all of these data to Monte Carlo comparisons, no indication of any underlying structure in the excess is seen.

Sample	Data	Prediction	Errors				σ Diff
			Stat	Sys	$\delta(\Delta m^2_{32})$	$\delta(sin^2(2\theta_{23}))$	
Preselection	534	478.44	21.87	-	$\pm$6.22	$\pm$6.06	2.36
ParticlePID	72	64.33	8.02	2.51	$\pm$0.89	$\pm$0.86	0.90
ANN11	66	53.28	7.30	2.83	$\pm$0.83	$\pm$0.80	1.61
ANN14	41	31.48	5.61	1.83	$\pm$0.47	$\pm$0.46	1.60

Table 10.6: The MRCC sideband with associated errors compared to data obtained by a separate calculation for each run at 6.95×10^{20} POT. No extrapolation systematic is calculated for the preselection sample. This is without any ν_μ CC correction.

Sample	Data	Prediction	Errors				σ Diff
			Stat	Sys	$\delta(\Delta m^2_{32})$	$\delta(sin^2(2\theta_{23}))$	
Preselection	534	535.14	17.58	-	$\pm$6.96	$\pm$6.78	-0.06
ParticlePID	72	73.14	7.41	2.85	$\pm$1.01	$\pm$0.98	-0.14
ANN11	66	60.74	7.01	3.23	$\pm$0.94	$\pm$0.92	0.67
ANN14	41	36.17	5.27	2.10	$\pm$0.54	$\pm$0.52	0.84

Table 10.7: The MRCC sideband with associated errors compared to data obtained by a separate calculation for each run at 6.95×10^{20} POT. No extrapolation systematic is calculated for the preselection sample. This uses the ν_μ CC correction with events having a shower.

Sample	Data	Default MC	Prediction	Errors				σ Diff MC	σ Diff Prediction
				Stat	Sys	$\delta(\Delta m^2_{32})$	$\delta(sin^2(2\theta_{23}))$		
Preselection	534	483.94	478.44	21.87	-	$\pm$6.22	$\pm$6.06	2.28	2.36
ParticlePID	72	71.45	64.33	8.02	2.51	$\pm$0.89	$\pm$0.86	0.06	0.90
ANN11	66	55.44	53.28	7.30	2.83	$\pm$0.83	$\pm$0.80	1.42	1.61
ANN14	41	34.83	31.48	5.61	1.83	$\pm$0.47	$\pm$0.46	1.05	1.60

Table 10.8: The MRCC sideband with associated errors compared to data and original Monte Carlo obtained by a separate calculation for each run at 6.95×10^{20} POT. No extrapolation systematic is calculated for the preselection sample. This is without any ν_μ CC correction.

Sample	Data	Default MC	Prediction	Errors				σ Diff	σ Diff
				Stat	Sys	$\delta(\Delta m^2_{32})$	$\delta(sin^2(2\theta_{23}))$	MC	Prediction
Preselection	534	483.94	535.14	17.58	-	± 6.96	± 6.78	2.28	-0.06
ParticlePID	72	71.45	73.14	7.41	2.85	± 1.01	± 0.98	0.06	-0.14
ANN11	66	55.44	60.74	7.01	3.23	± 0.94	± 0.92	1.42	0.67
ANN14	41	34.83	36.17	5.27	2.10	± 0.54	± 0.52	1.05	0.84

Table 10.9: The MRCC sideband with associated errors compared to data and original Monte Carlo obtained by a separate calculation for each run at 6.95×10^{20} POT. No extrapolation systematic is calculated for the preselection sample. This uses the ν_μ CC correction with events having a shower

Cut	Run 1	Run 2a	Run 2b	Run3a	Run3b	Run3c	Total	Run 1	Run 2	Run 3	Total
POT($\times 10^{20}$)	1.20	1.22	0.71	1.22	1.06	1.55	6.95	1.20	1.92	3.83	6.95
Data											
MRCCPre	139	162	91	157	160	209	918	139	253	526	918
Preselection	71	87	56	91	109	120	534	71	143	320	534
ParticlePID	8	13	8	14	16	13	72	8	21	43	72
ANN11	7	13	7	10	16	13	66	7	20	39	66
ANN14	3	9	5	6	8	10	41	3	14	24	41
Prediction											
MRCCPre	147.96	148.32	85.05	145.05	125.79	183.72	835.90	147.96	233.41	454.63	836.00
Preselection	84.86	84.62	49.06	83.15	72.04	104.73	478.45	84.86	133.60	259.98	478.44
ParticlePID	11.25	11.51	6.60	10.93	9.91	14.24	64.43	11.25	18.11	34.97	64.33
ANN11	9.53	9.50	5.51	9.01	8.14	11.69	53.38	9.53	15.00	28.75	53.28
ANN14	5.55	5.63	3.22	5.33	4.86	6.94	31.53	5.55	8.84	17.08	31.48
σ Diff											
MRCCPre	-0.74	1.12	0.64	0.99	3.05	1.86	2.84	-0.74	1.28	3.35	2.84
Preselection	-1.50	0.26	0.99	0.86	4.35	1.49	2.54	-1.50	0.81	3.72	2.54
ParticlePID	-0.97	0.44	0.55	0.93	1.94	-0.33	0.94	-0.97	0.68	1.36	0.96
ANN11	-0.82	1.13	0.63	0.33	2.76	0.38	1.73	-0.82	1.29	1.91	1.74
ANN14	-1.08	1.42	0.99	0.29	1.42	1.16	1.69	-1.08	1.74	1.67	1.70

Table 10.10: The MRCC sideband without any ν_μ CC correction using bins of width 1.00 GeV. There is a large disagreement in run 3b at all cut levels. All PIDs agree within 2 σ overall, with the best agreement achieved by the ParticlePID.

Cut	Run 1	Run 2a	Run 2b	Run3a	Run3b	Run3c	Total	Run 1	Run 2	Run 3	Total
POT($\times 10^{20}$)	1.20	1.22	0.71	1.22	1.06	1.55	6.95	1.20	1.92	3.83	6.95
Data (% Efficiency to MRCCPre)											
MRCCPre	100.00	100.00	100.00	100.00	100.00	100.00	100.00	100.00	100.00	100.00	100.00
Preselection	51.08	53.70	61.54	57.96	68.12	57.42	58.17	51.08	56.52	60.84	58.17
ParticlePID	5.76	8.02	8.79	8.92	10.00	6.22	7.84	5.76	8.30	8.17	7.84
ANN11	5.04	8.02	7.69	6.37	10.00	6.22	7.19	5.04	7.91	7.41	7.19
ANN14	2.16	5.56	5.49	3.82	5.00	4.78	4.47	2.16	5.53	4.56	4.47
Prediction (% Efficiency to MRCCPre)											
MRCCPre	100.00	100.00	100.00	100.00	100.00	100.00	100.00	100.00	100.00	100.00	100.00
Preselection	57.35	57.05	57.68	57.33	57.27	57.00	57.24	57.35	57.24	57.19	57.23
ParticlePID	7.60	7.76	7.76	7.54	7.88	7.75	7.71	7.60	7.76	7.69	7.69
ANN11	6.44	6.41	6.48	6.21	6.47	6.36	6.39	6.44	6.43	6.32	6.37
ANN14	3.75	3.79	3.78	3.68	3.87	3.78	3.77	3.75	3.79	3.76	3.77
σ Diff											
MRCCPre	-0.74	1.12	0.64	0.99	3.05	1.86	2.84	-0.74	1.28	3.35	2.84
Preselection	-1.50	0.26	0.99	0.86	4.35	1.49	2.54	-1.50	0.81	3.72	2.54
ParticlePID	-0.97	0.44	0.55	0.93	1.94	-0.33	0.94	-0.97	0.68	1.36	0.96
ANN11	-0.82	1.13	0.63	0.33	2.76	0.38	1.73	-0.82	1.29	1.91	1.74
ANN14	-1.08	1.42	0.99	0.29	1.42	1.16	1.69	-1.08	1.74	1.67	1.70

Table 10.11: The MRCC sideband expressed as efficiency without any ν_μ CC correction using bins of width 1.00 GeV. There is a large disagreement in run 3b at all cut levels. All PIDs agree within 2 σ overall, with the best agreement achieved by the ParticlePID.

Cut	Run 1	Run 2a	Run 2b	Run3a	Run3b	Run3c	Total	Run 1	Run 2	Run 3	Total
POT($\times 10^{20}$)	1.20	1.22	0.71	1.22	1.06	1.55	6.95	1.20	1.92	3.83	6.95
Data											
MRCCPre	139	162	91	157	160	209	918	139	253	526	918
Preselection	71	87	56	91	109	120	534	71	143	320	534
ParticlePID	8	13	8	14	16	13	72	8	21	43	72
ANN11	7	13	7	10	16	13	66	7	20	39	66
ANN14	3	9	5	6	8	10	41	3	14	24	41
Prediction											
MRCCPre	144.06	164.15	88.28	156.32	164.83	206.77	924.41	144.06	251.93	528.48	924.48
Preselection	82.28	94.06	52.45	88.85	96.27	121.10	535.02	82.28	146.12	306.74	535.14
ParticlePID	9.86	12.51	7.84	11.89	13.96	17.45	73.51	9.86	20.29	42.99	73.14
ANN11	8.37	10.38	6.52	9.87	11.44	14.38	60.96	8.37	16.90	35.48	60.74
ANN14	4.83	6.16	3.88	5.86	6.91	8.69	36.33	4.83	10.05	21.29	36.17
σ Diff											
MRCCPre	-1.21	-0.52	0.83	0.17	-1.24	0.49	-0.65	-1.21	0.20	-0.34	-0.65
Preselection	-1.52	-0.96	0.63	0.29	1.87	-0.13	-0.06	-1.52	-0.34	1.02	-0.06
ParticlePID	-0.60	0.15	0.07	0.69	0.70	-1.29	-0.20	-0.60	0.18	0.00	-0.15
ANN11	-0.46	0.88	0.21	0.05	1.68	-0.42	0.72	-0.46	0.83	0.69	0.75
ANN14	-0.82	1.26	0.66	0.07	0.53	0.54	0.89	-0.82	1.40	0.70	0.92

Table 10.12: The MRCC sideband corrected to ν_μ CC events having a shower using bins of width 1.00 GeV. The application of the ν_μ CC sample correction results in discrepancies below 2 σ for all run periods at all cut levels. All PIDs agree within 2 σ overall, with the best agreement achieved by the ParticlePID.

Cut	Run 1	Run 2a	Run 2b	Run3a	Run3b	Run3c	Total	Run 1	Run 2	Run 3	Total
POT($\times 10^{20}$)	1.20	1.22	0.71	1.22	1.06	1.55	6.95	1.20	1.92	3.83	6.95
Data (% Efficiency to MRCCPre)											
MRCCPre	100.00	100.00	100.00	100.00	100.00	100.00	100.00	100.00	100.00	100.00	100.00
Preselection	51.08	53.70	61.54	57.96	68.12	57.42	58.17	51.08	56.52	60.84	58.17
ParticlePID	5.76	8.02	8.79	8.92	10.00	6.22	7.84	5.76	8.30	8.17	7.84
ANN11	5.04	8.02	7.69	6.37	10.00	6.22	7.19	5.04	7.91	7.41	7.19
ANN14	2.16	5.56	5.49	3.82	5.00	4.78	4.47	2.16	5.53	4.56	4.47
Prediction (% Efficiency to MRCCPre)											
MRCCPre	100.00	100.00	100.00	100.00	100.00	100.00	100.00	100.00	100.00	100.00	100.00
Preselection	57.11	57.30	59.42	56.84	58.40	58.57	57.88	57.11	58.00	58.04	57.89
ParticlePID	6.84	7.62	8.88	7.61	8.47	8.44	7.95	6.84	8.05	8.13	7.91
ANN11	5.81	6.33	7.38	6.31	6.94	6.96	6.59	5.81	6.71	6.71	6.57
ANN14	3.35	3.75	4.40	3.75	4.20	4.20	3.93	3.35	3.99	4.03	3.91
σ Diff											
MRCCPre	-1.21	-0.52	0.83	0.17	-1.24	0.49	-0.65	-1.21	0.20	-0.34	-0.65
Preselection	-1.52	-0.96	0.63	0.29	1.87	-0.13	-0.06	-1.52	-0.34	1.02	-0.06
ParticlePID	-0.60	0.15	0.07	0.69	0.70	-1.29	-0.20	-0.60	0.18	0.00	-0.15
ANN11	-0.46	0.88	0.21	0.05	1.68	-0.42	0.72	-0.46	0.83	0.69	0.75
ANN14	-0.82	1.26	0.66	0.07	0.53	0.54	0.89	-0.82	1.40	0.70	0.92

Table 10.13: The MRCC sideband expressed as efficiency corrected to ν_μ CC events having a shower using bins of width 1.00 GeV. The application of the ν_μ CC sample correction results in discrepancies below 2 σ for all run periods at all cut levels. All PIDs agree within 2 σ overall, with the best agreement achieved by the ParticlePID.

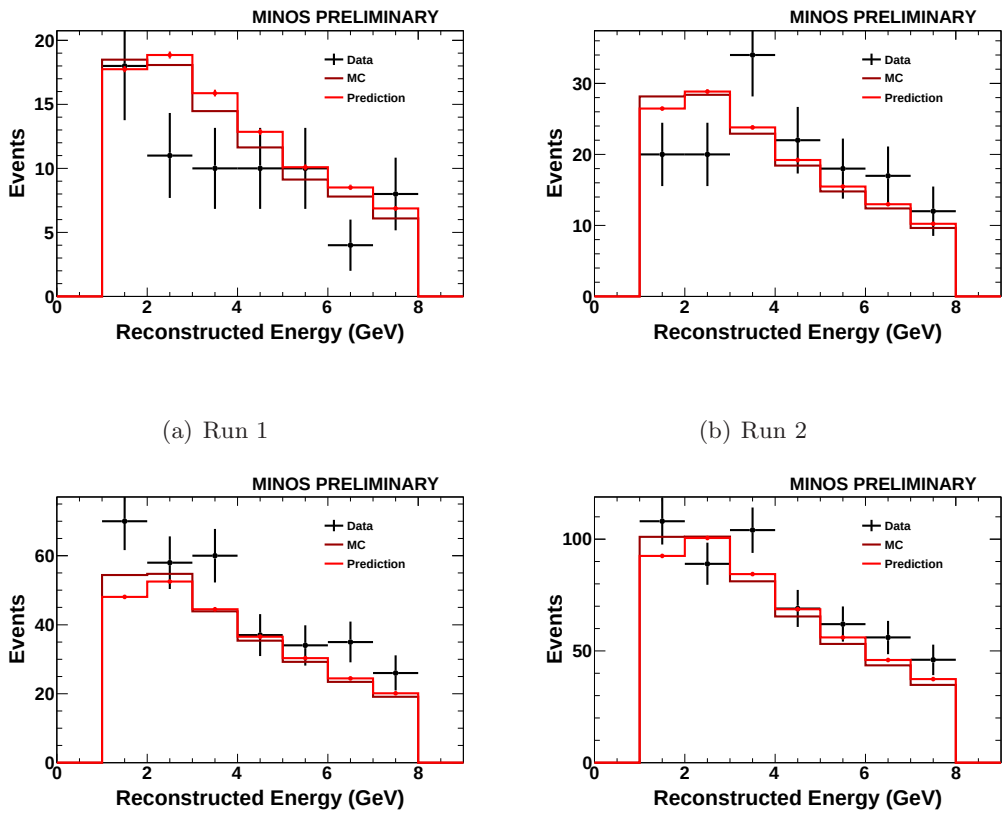

(a) Run 1

(b) Run 2

(c) Run 3

(d) All Runs

Figure 10.1: The MRCC Sideband for separate runs and for all run periods combined after the Preselection cut without any ν_μ CC correction with 1 GeV binning.

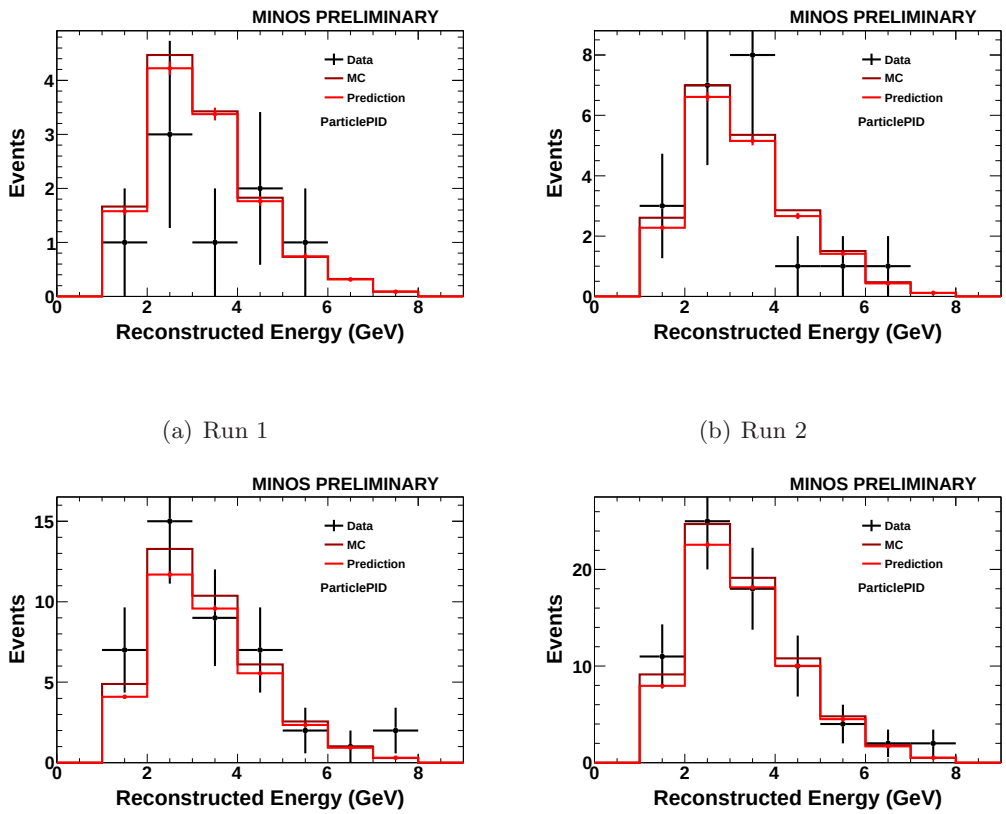

(a) Run 1

(b) Run 2

(c) Run 3

(d) All Runs

Figure 10.2: The MRCC Sideband for separate runs and for all run periods combined after the ParticlePID cut with 1 GeV binning.

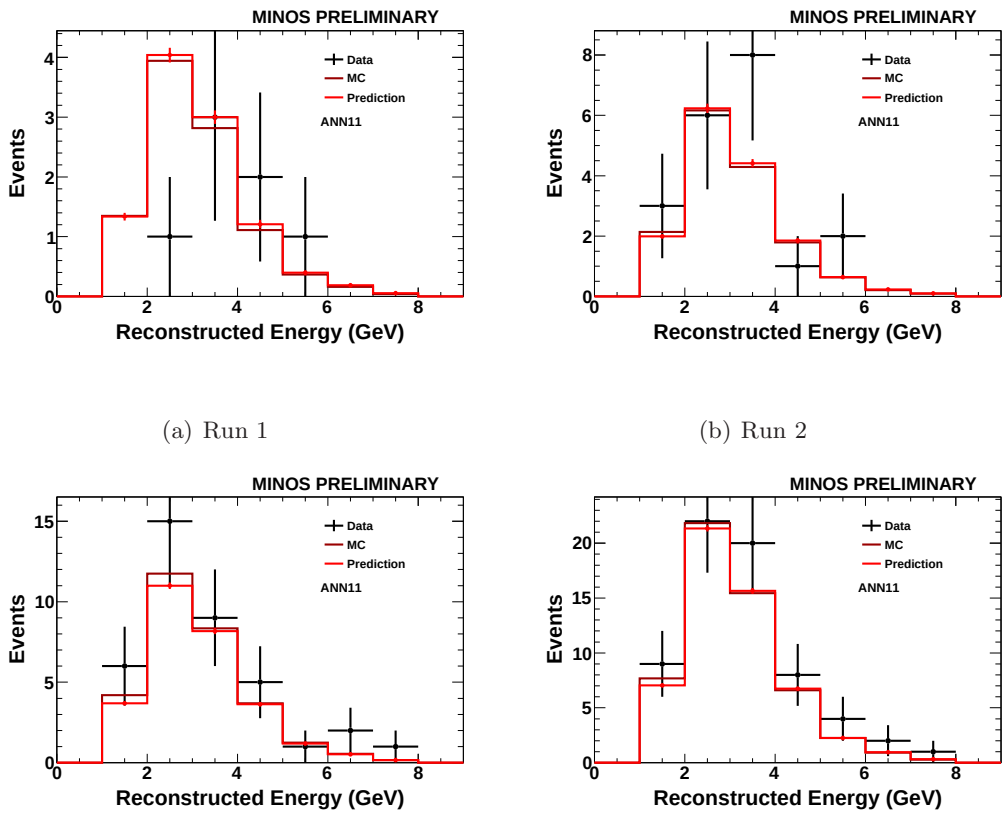

(a) Run 1

(b) Run 2

(c) Run 3

(d) All Runs

Figure 10.3: The MRCC Sideband for separate runs and for all run periods combined after the ANN11 cut with 1 GeV binning.

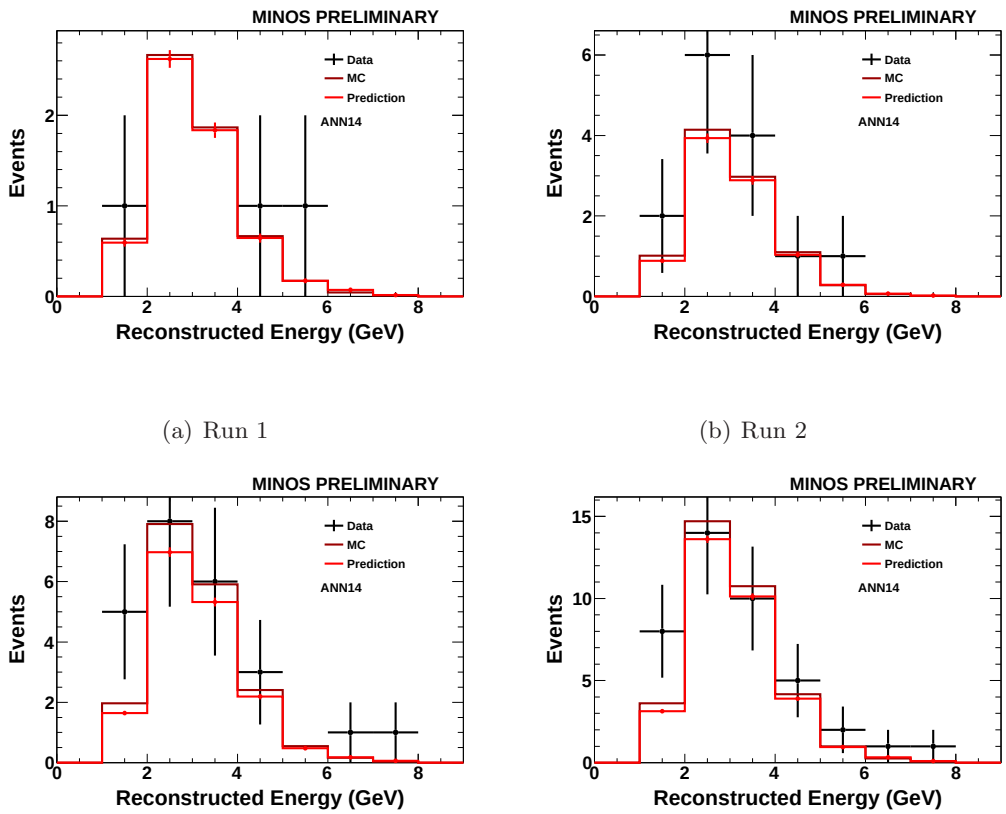

(a) Run 1

(b) Run 2

(c) Run 3

(d) All Runs

Figure 10.4: The MRCC Sideband for separate runs and for all run periods combined after the ANN14 cut with 1 GeV binning.

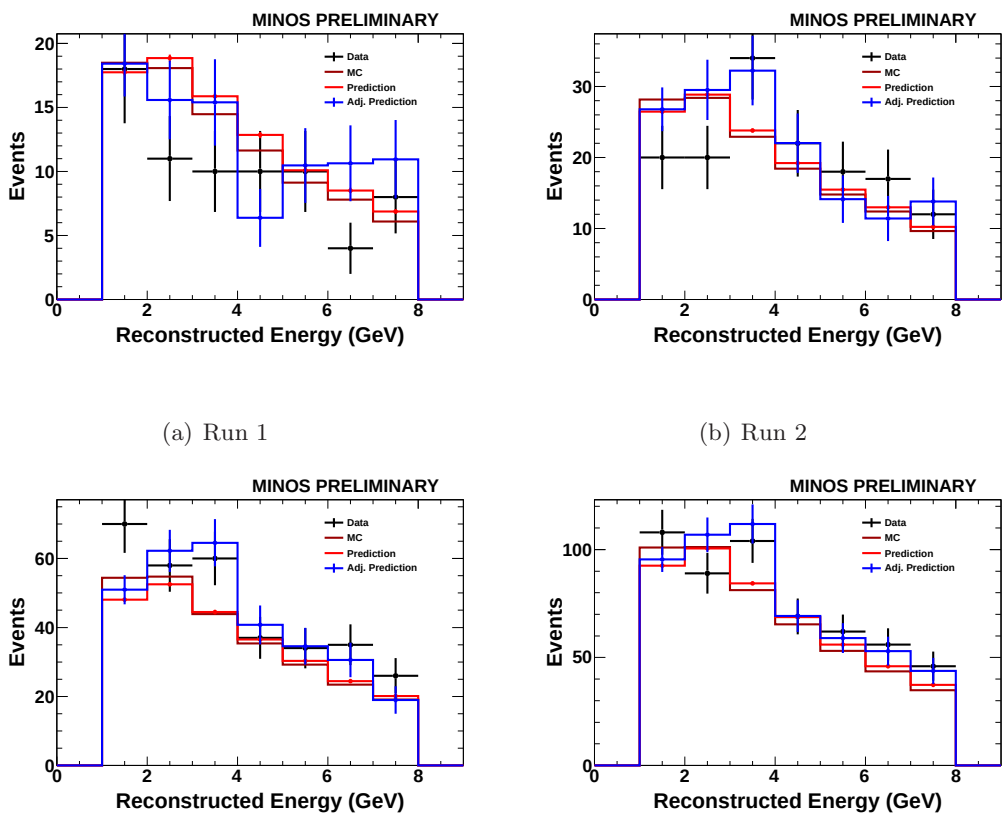

(a) Run 1

(b) Run 2

(c) Run 3

(d) All Runs

Figure 10.5: The MRCC Sideband for separate runs and for all run periods combined after the Preselection cut using a correction from ν_μ CC event having a shower with 1 GeV binning.

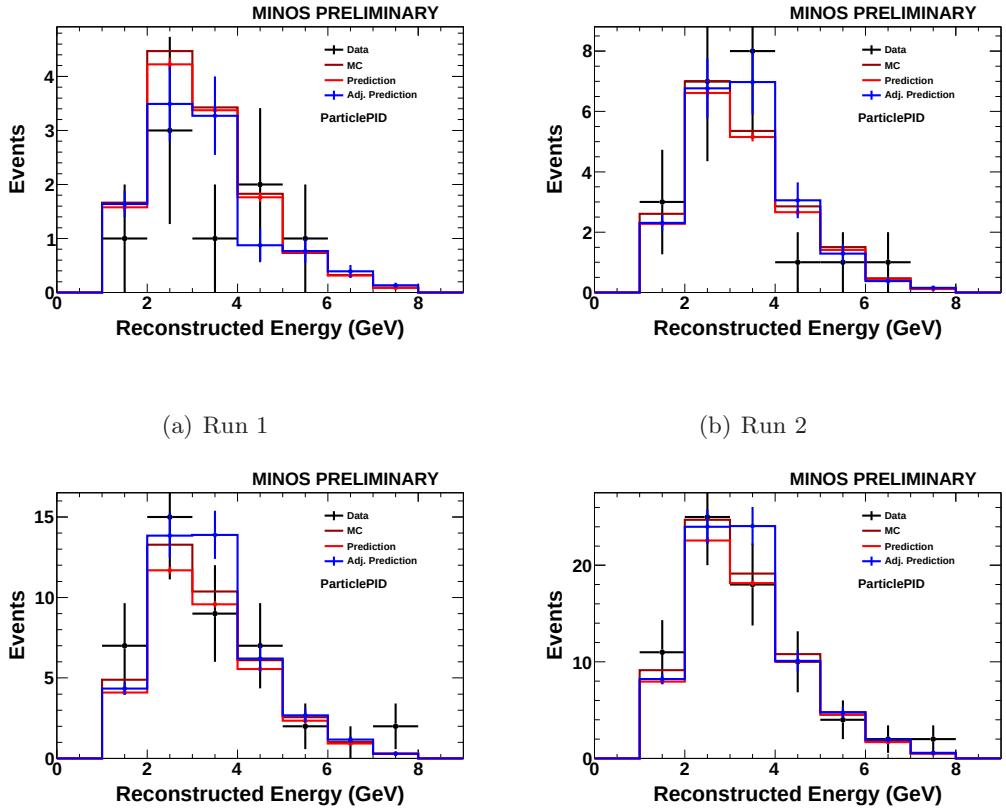

(a) Run 1

(b) Run 2

(c) Run 3

(d) All Runs

Figure 10.6: The MRCC Sideband for separate runs and for all run periods combined after the ParticlePID cut using a correction from ν_μ CC event having a shower with 1 GeV binning.

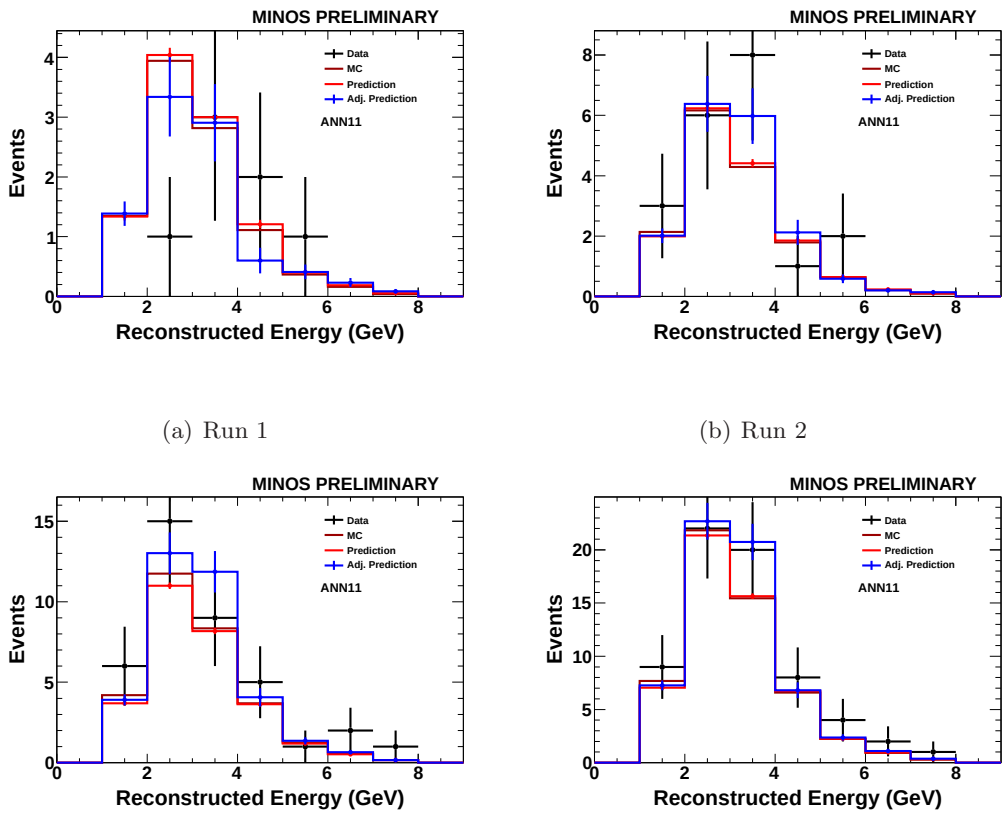

(a) Run 1

(b) Run 2

(c) Run 3

(d) All Runs

Figure 10.7: The MRCC Sideband for separate runs and for all run periods combined after the ANN11 cut using a correction from ν_μ CC event having a shower with 1 GeV binning.

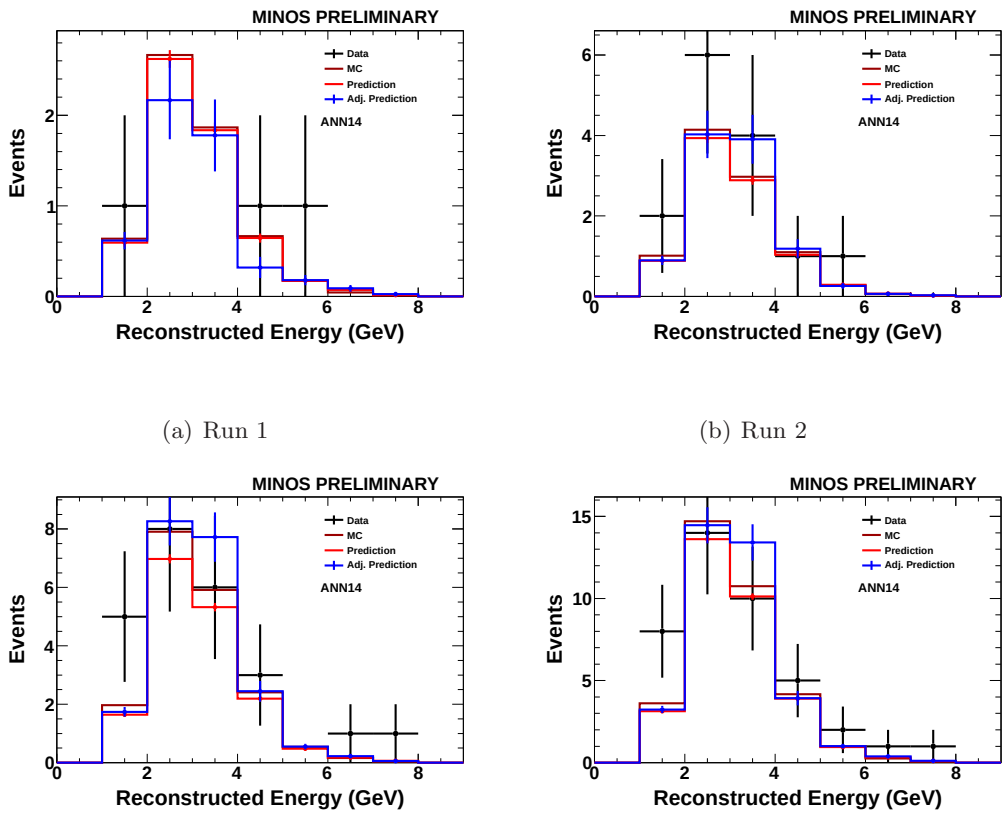

(a) Run 1

(b) Run 2

(c) Run 3

(d) All Runs

Figure 10.8: The MRCC Sideband for separate runs and for all run periods combined after the ANN14 cut using a correction from ν_μ CC event having a shower with 1 GeV binning.

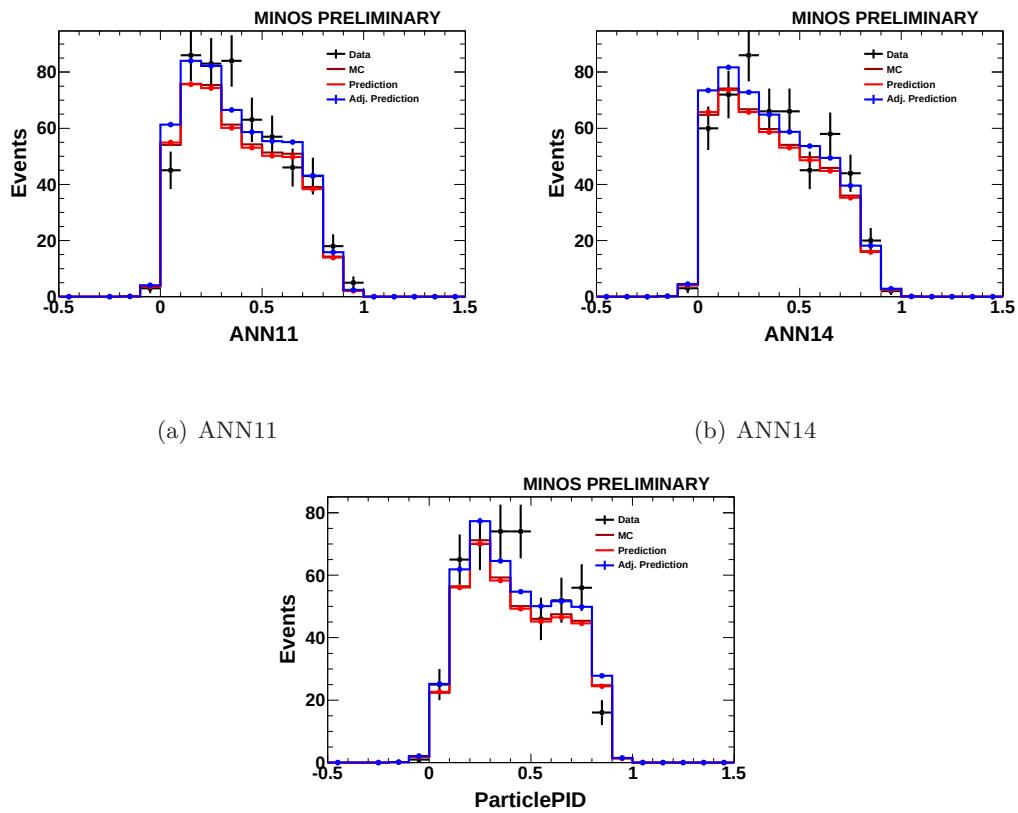

(a) ANN11

(b) ANN14

(c) ParticlePID

Figure 10.9: The MRCC Sideband for each PID after the preselection cut using a correction from ν_μ CC events having a shower with 1 GeV binning.

It is possible to incorporate the ν_μ CC correction directly into the original equation by expressing the prediction as an efficiency with respect to the MRCCPreselection. This is essentially a ν_μ CC correction using all events that have tracks. The results produced by this method are also within the required limits. Here, efficiency is defined as

$$\epsilon_{selection}^{detector,Data/MC} = \frac{detector_{MRCC}^{Data/MC,selection}}{detector_{MRCC}^{Data/MC,MRCCPreselection}}$$

so, for example,

$$\epsilon_{ANN11}^{Far,MC} = \frac{Far_{MRCC}^{MC,ANN11}}{Far_{MRCC}^{MC,MRCCPreselection}}$$

Then, the prediction, P_{ϵ}^{α},at cut α=(ParticlePID, ANN11, or ANN14), becomes

$$P_{\epsilon}^{\alpha} = \epsilon_{\alpha}^{Far,MC} \times \frac{\epsilon_{\alpha}^{Near,data}}{\epsilon_{\alpha}^{Near,MC}}$$

and this gets compared to the data efficiency, $\epsilon_{\alpha}^{Far,data}$. These efficiencies, $\epsilon_{\alpha}^{Far,data}$ and P_{ϵ}^{α} are then each subtracted from 1 to be interpreted as a background rejection efficiency. The results of this method are presented in figure 10.10 and in table 10.14.

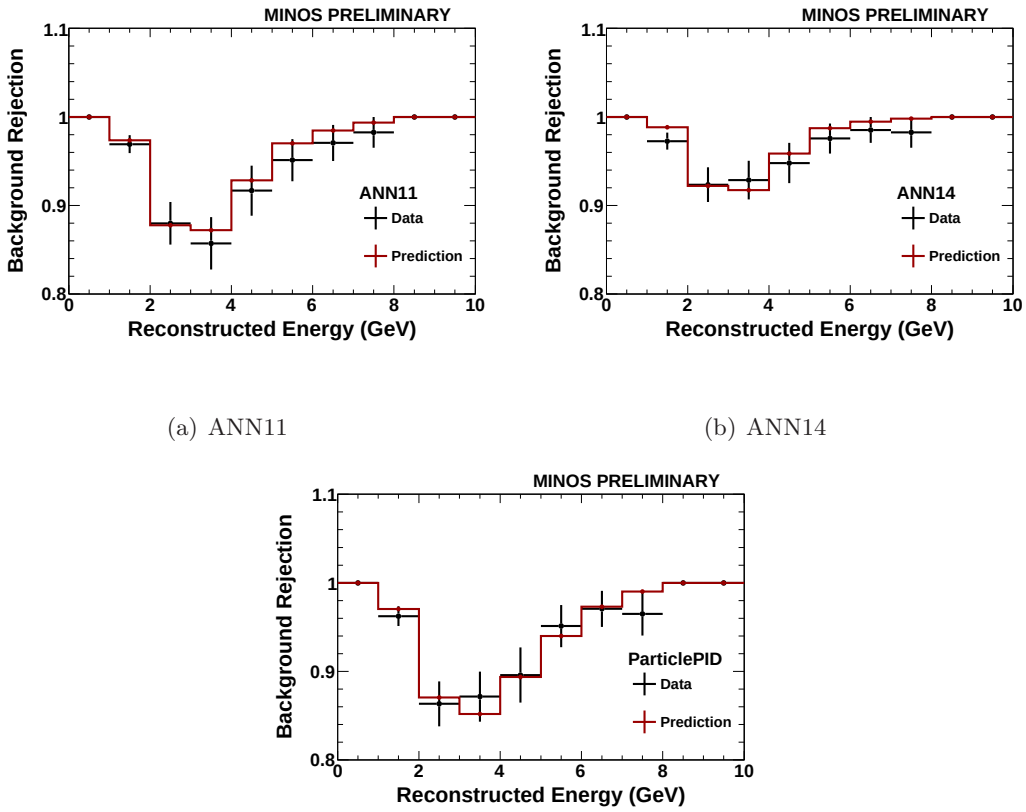

(a) ANN11

(b) ANN14

(c) ParticlePID

Figure 10.10: The MRCC Sideband expressed as a background rejection, comparing the data and prediction as efficiencies of the PID cut to MRCC Preselection.

Cut	Run 1	Run 2a	Run 2b	Run3a	Run3b	Run3c	Run 1	Run 2	Run 3	Total
POT($\times 10^{20}$)	1.20	1.22	0.71	1.22	1.06	1.55	1.20	1.92	3.83	6.95
Data										
MRCCPre	0.00%	0.00%	0.00%	0.00%	0.00%	0.00%	0.00%	0.00%	0.00%	0.00%
Preselection	48.92%	46.30%	38.46%	42.04%	31.87%	42.58%	48.92%	43.48%	39.16%	41.83%
ParticlePID	94.24%	91.98%	91.21%	91.08%	90.00%	93.78%	94.24%	91.70%	91.83%	92.16%
ANN11	94.96%	91.98%	92.31%	93.63%	90.00%	93.78%	94.96%	92.09%	92.59%	92.81%
ANN14	97.84%	94.44%	94.51%	96.18%	95.00%	95.22%	97.84%	94.47%	95.44%	95.53%
Prediction										
MRCCPre	0.00%	0.00%	0.00%	0.00%	0.00%	0.00%	0.00%	0.00%	0.00%	0.00%
Preselection	42.72%	42.99%	42.33%	42.65%	42.72%	43.07%	42.72%	42.80%	42.81%	42.83%
ParticlePID	92.37%	92.21%	92.20%	92.41%	92.05%	92.16%	92.37%	92.21%	92.24%	92.26%
ANN11	93.53%	93.58%	93.49%	93.76%	93.50%	93.60%	93.53%	93.55%	93.64%	93.58%
ANN14	96.23%	96.19%	96.20%	96.29%	96.11%	96.19%	96.23%	96.19%	96.21%	96.20%
σ Diff										
MRCCPre	-	-	-	-	-	-	-	-	-	-
Preselection	1.46	0.84	-0.76	-0.15	-2.93	-0.14	1.46	0.22	-1.71	-0.62
ParticlePID	0.95	-0.11	-0.33	-0.58	-0.86	0.97	0.95	-0.29	-0.34	-0.12
ANN11	0.77	-0.75	-0.42	-0.07	-1.47	0.11	0.77	-0.86	-0.92	-0.91
ANN14	1.31	-0.97	-0.71	-0.07	-0.65	-0.66	1.31	-1.20	-0.85	-0.97

Table 10.14: The MRCC sideband calculated as an efficiency with respect to MRCCPreselection and expressed as a background rejection using a single bin. Errors are calculated using the binomial error method.

It is also possible to compare the data and the Monte Carlo separately. Again, using the definitions of efficiency just described, the data, D_ϵ^α, and Monte Carlo, MC_ϵ^α, ratios are defined as

$$D_\epsilon^\alpha = \frac{\epsilon_\alpha^{Near,data}}{\epsilon_\alpha^{Far,data}} \quad MC_\epsilon^\alpha = \frac{\epsilon_\alpha^{Near,MC}}{\epsilon_\alpha^{Far,MC}}$$

The results of the 1 GeV binned histogram are presented in figure 10.11 and the table for a single bin calculation is table 10.15. The errors presented in this table are simply statistical for both the numerator and denominator of each term of each efficiency ($1/\sqrt{\#\ events}$). While the GeV binned histogram shows some discrepancy (which may or may not be significant), the single bin table shows agreement within the required 2σ. A more correct error calculation is used in table 10.16, where binomial errors are calculated for each of the efficiencies. So for

$$\epsilon = \frac{A}{B}$$

the error is

$$\delta\epsilon = \sqrt{\frac{\epsilon \times (1-\epsilon)}{B}}$$

This method also produces results within the required 2 σ limit.

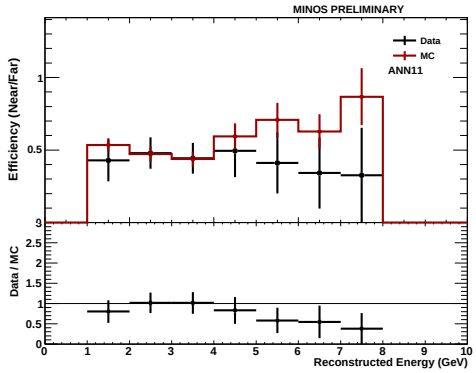

(a) ANN11

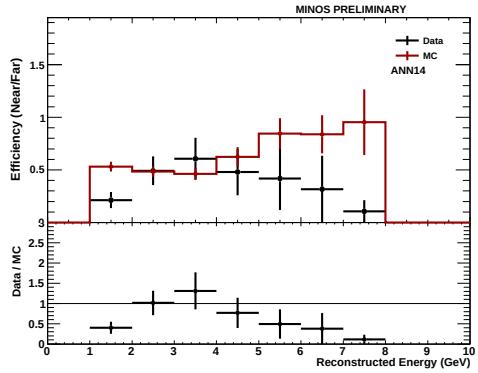

(b) ANN14

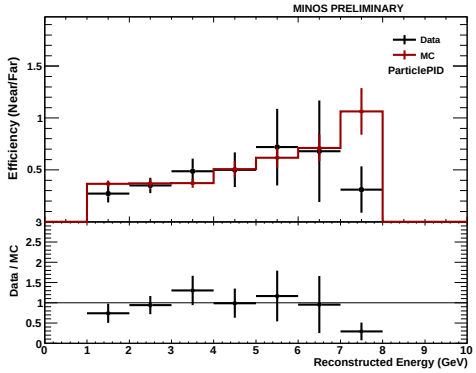

(c) ParticlePID

Figure 10.11: The MRCC Sideband expressed as a data and Monte Carlo near to far efficiencies of the PID cut to MRCC Preselection.

Cut	Run 1	Run 2a	Run 2b	Run3a	Run3b	Run3c	Run 1	Run 2	Run 3	Total
POT($\times 10^{20}$)	1.20	1.22	0.71	1.22	1.06	1.55	1.20	1.92	3.83	6.95
Near Efficiency / Far Efficiency Data										
MRCCPre	100.00	100.00	100.00	100.00	100.00	100.00	100.00	100.00	100.00	100.00
Preselection	45.98	43.39	38.04	40.64	34.09	40.51	45.98	41.28	38.38	40.18
ParticlePID	54.99	39.46	36.07	35.50	31.60	50.31	54.99	38.16	38.58	40.30
ANN11	63.40	39.91	41.95	50.27	31.49	50.69	63.40	40.61	42.74	44.33
ANN14	88.46	34.99	35.86	51.24	38.65	40.80	88.46	35.27	42.67	43.44
Near Efficiency / Far Efficiency Monte Carlo										
MRCCPre	100.00	100.00	100.00	100.00	100.00	100.00	100.00	100.00	100.00	100.00
Preselection	41.00	40.87	40.60	41.07	40.54	40.86	41.00	40.79	40.83	40.89
ParticlePID	41.47	40.66	40.64	41.71	39.75	39.91	41.47	40.65	40.62	40.83
ANN11	49.37	49.90	49.56	51.32	48.44	49.25	49.37	49.80	49.85	49.68
ANN14	50.65	50.97	51.90	52.82	49.73	51.28	50.65	51.24	51.43	51.00
(Near Efficiency / Far Eff) Data/Monte Carlo										
MRCCPre	1.00	1.00	1.00	1.00	1.00	1.00	1.00	1.00	1.00	1.00
Preselection	1.12	1.06	0.94	0.99	0.84	0.99	1.12	1.01	0.94	0.98
ParticlePID	1.33	0.97	0.89	0.85	0.80	1.26	1.33	0.94	0.95	0.99
ANN11	1.28	0.80	0.85	0.98	0.65	1.03	1.28	0.82	0.86	0.89
ANN14	1.75	0.69	0.69	0.97	0.78	0.80	1.75	0.69	0.83	0.85
σ Diff										
MRCCPre	0.00	0.00	0.00	0.00	0.00	0.00	0.00	0.00	0.00	0.00
Preselection	0.74	0.44	-0.39	-0.08	-1.52	-0.07	0.74	0.11	-0.89	-0.32
ParticlePID	0.68	-0.11	-0.34	-0.62	-0.98	0.68	0.68	-0.29	-0.33	-0.11
ANN11	0.57	-0.87	-0.46	-0.06	-2.04	0.09	0.57	-0.97	-0.99	-0.94
ANN14	0.73	-1.33	-0.97	-0.07	-0.79	-0.74	0.73	-1.64	-0.97	-1.08

Table 10.15: The MRCC sideband comparing data and Monte Carlo near to far efficiency ratios (PID to MRCC Preselection). This is calculated using statistical errors ($1/\sqrt{(}N)$). Agreement within 2 σ is seen everywhere except for the ANN11 in run 3b.

Cut	Run 1	Run 2a	Run 2b	Run3a	Run3b	Run3c	Run 1	Run 2	Run 3	Total
POT($\times 10^{20}$)	1.20	1.22	0.71	1.22	1.06	1.55	1.20	1.92	3.83	6.95
Near Efficiency / Far Efficiency Data										
MRCCPre	100.00	100.00	100.00	100.00	100.00	100.00	100.00	100.00	100.00	100.00
Preselection	45.98	43.39	38.04	40.64	34.09	40.51	45.98	41.28	38.38	40.18
ParticlePID	54.99	39.46	36.07	35.50	31.60	50.31	54.99	38.16	38.58	40.30
ANN11	63.40	39.91	41.95	50.27	31.49	50.69	63.40	40.61	42.74	44.33
ANN14	88.46	34.99	35.86	51.24	38.65	40.80	88.46	35.27	42.67	43.44
Near Efficiency / Far Efficiency Monte Carlo										
MRCCPre	100.00	100.00	100.00	100.00	100.00	100.00	100.00	100.00	100.00	100.00
Preselection	41.00	40.87	40.60	41.07	40.54	40.86	41.00	40.79	40.83	40.89
ParticlePID	41.47	40.66	40.64	41.71	39.75	39.91	41.47	40.65	40.62	40.83
ANN11	49.37	49.90	49.56	51.32	48.44	49.25	49.37	49.80	49.85	49.68
ANN14	50.65	50.97	51.90	52.82	49.73	51.28	50.65	51.24	51.43	51.00
(Near Efficiency / Far Eff) Data/Monte Carlo										
MRCCPre	1.00	1.00	1.00	1.00	1.00	1.00	1.00	1.00	1.00	1.00
Preselection	1.12	1.06	0.94	0.99	0.84	0.99	1.12	1.01	0.94	0.98
ParticlePID	1.33	0.97	0.89	0.85	0.80	1.26	1.33	0.94	0.95	0.99
ANN11	1.28	0.80	0.85	0.98	0.65	1.03	1.28	0.82	0.86	0.89
ANN14	1.75	0.69	0.69	0.97	0.78	0.80	1.75	0.69	0.83	0.85
σ Diff										
MRCCPre	-	-	-	-	-	-	-	-	-	-
Preselection	1.30	0.79	-0.80	-0.15	-3.45	-0.13	1.30	0.22	-1.77	-0.62
ParticlePID	0.72	-0.11	-0.37	-0.68	-1.08	0.73	0.72	-0.31	-0.36	-0.12
ANN11	0.60	-0.94	-0.50	-0.07	-2.25	0.10	0.60	-1.05	-1.07	-1.01
ANN14	0.75	-1.41	-1.02	-0.08	-0.83	-0.77	0.75	-1.74	-1.02	-1.13

Table 10.16: The MRCC Sideband expressed as a data and Monte Carlo near to far efficiencies of the PID cut to MRCC Preselection. The error is calculated using the binomial error method. Agreement within 2 σ is seen everywhere except for the preselection and ANN11 in run 3b.

10.3 MRE

The MRE sideband is calculated[89] in a similar way as the MRCC sideband. The prediction is performed for all run periods combined, and is given by the ratio

$$P = F_{MRE}^{MC} \times \frac{N_{MRE}^{data}}{N_{MRE}^{MC}}$$

The results of the test are summarized in table 10.17. The prediction for each of the PIDs agrees with the data within the required 2 σ, with the ParticlePID agreeing at 0.2 σ and the ANN11 and ANN14 agreeing at 0.6 σ.

PID	Prediction	Data	σ difference
ParticlePID	268	271	0.2
ANN11	247	256	0.6
ANN14	202	211	0.6

Table 10.17: The Far Detector prediction, data, and σ difference for the MRE sideband is presented. All PIDs agree within the required 2 σ.

10.4 Summary

The investigations of all three sidebands produced acceptable results. In the anti-PID sideband, the ParticlePID has better agreement at the CHOOZ limit than the ANN11 or ANN14, although for all three samples (both assuming no ν_e oscillations and with oscillations at the CHOOZ limit), the agreement is within 1 σ. In the MRCC sideband, the overall agreement with the CC Analysis correction requiring CC events with showers is also within 1 σ, with the best agreement in ParticlePID (0.21 σ), followed by ANN11 (0.54 σ) and then by ANN14 (0.69 σ). The ParticlePID also has the best agreement in the MRE sideband at 0.2 σ, compared to the 0.6 σ discrepancy seen in both the ANN11 and ANN14.

Chapter 11

Far Detector Signal Region Prediction and Results

After satisfactorily performing all possible known tests for the blind analysis prior to viewing the selected data events (as described in section 10), it is now time to observe the selected data events and to report a result.

11.1 How to Make a Measurement

In an experiment such as this, where the number of observed events could be equal to or less than the predicted background due to statistical fluctuations, it is necessary to use a carefully chosen formalism. The method must always result in a measurement within the physical region. Also, the method must be well defined prior to observing the data, and it must provide a confidence interval in all regions of parameter space, including values at or close to physical boundaries. The Feldman-Cousins Method [122] has been developed for situations such as this, successfully satisfying the mentioned requirements.

The procedure used in this analysis[123] is as follows. The contours that will be

drawn will describe the section of the parameter space (in $\sin^2 2\theta_{13} \sin^2 \theta_{23}$ and δ_{CP}) that could contain the true value capable of giving rise to the observed result within some confidence level. The parameter space of θ_{13}, δ_{CP}, and $sign(\Delta m^2_{23})$ is divided into a 401x401x2 grid with $\sin^2 2\theta_{13} = [0, 0.4]$, $\delta_{CP} = [0, 2\pi]$, and $sign(\Delta m^2_{23}) = \pm$.

Each of these grid points represents a different set of parameters, and so for each, a predicted number of signal (N_{Signal}) and background (N_{Bkgd}) events can be computed based on the oscillation parameters corresponding to that particular grid point.

At each of these grid points, 10,000 individual pseudo experiments are generated to take into account statistical fluctuations on the actual predicted signal and background. To simplify the notation, $R_G(N, \sigma)$ is a function that returns a random number from a Gaussian distribution with a mean of N and a standard deviation of σ, and $R_P(N)$ is a function that returns a random number from a Poisson distribution with a mean of N.

Uncertainties in Oscillation Parameters

The uncertainties in the oscillation parameters will also be taken into account in each of these pseudo experiments. A computationally efficient method was developed[124] which computes the uncertainty due to oscillations in the form of a systematic error, rather than requiring the full computation of the oscillation probability for each of the 10,000 pseudo experiments. This results in an algorithm that completes in roughly 20% of the time needed in the case where the full oscillation probability for each pseudo experiment is individually calculated.

The three oscillation parameters contributing to the oscillation uncertainty are:

- $|\Delta m^2_{23}| = (2.43 \pm 0.13) \times 10^{-3} eV^2$ from MINOS [115]
- $\theta_{23} = \pi/4 \pm 0.122$ from Super-K [125]

- $\Delta m^2_{12} = (8.0 \pm 0.6) \times 10^{-5}$ and $\theta_{12} = 0.594 \pm 0.041$ from solar + KamLand [126]

At each point in the grid, the following procedure is repeated 2,000 times:

- Each parameter (θ_{12}, θ_{23}, Δm^2_{12}, and $|\Delta m^2_{32}|$) is fluctuated within its uncertainty assuming a Gaussian distribution.
- A new prediction for the total expected number of events, N'_{exp} is calculated with the new values of the oscillation parameters.
- The fractional difference, ΔN_{exp}, between the new prediction, N'_{exp}, and the prediction obtained without varying the oscillation parameters, N_{exp}, is calculated and stored: $\Delta N_{exp} = (N'_{exp} - N_{exp})/N_{exp}$

The RMS of the distribution of ΔN_{exp} at each of the grid points is taken as the uncertainty in the total number of predicted events due to oscillation parameter uncertainties ($\sigma_{osc} \equiv \Delta N_{exp}$) at that point.

Calculating the Pseudo Experiments

Each of the pseudo experiments is calculated by the following steps:

1. The number background events for this pseudo experiment, N'_{Bkgd}, is calculated as a systematic fluctuation of the expected number of background events ($N'_{Bkgd} = R_G(N_{Bkgd}, \sigma_{Bkgd})$)
2. The number of signal events for this pseudo experiment, N'_{Signal}, is calculated as a systematic fluctuation of the expected number of signal events

   ($N'_{Signal} = R_G(N_{Signal}, \sigma_{Signal})$)
3. The total number of events for this pseudo experiment is $N_{Total} = N'_{Signal} + N'_{Bkgd}$

4. The total number of events is fluctuated to take into account the systematic uncertainty due to the oscillation parameters ($N'_{Total} = R_G(N_{Total}, \sigma_{osc})$)

5. Statistical fluctuations are considered ($N''_{Total} = R_P(N'_{Total})$)

6. Define $N^{obs} = N''_{Total}$ and $N^{exp} = N_{Signal} + N_{Bkgd}$. Calculate χ^2.

7. Calculate $\Delta\chi^2 = \chi^2 - \chi^2_{min}$ and store this value. χ^2_{min} can also be calculated which is the minimum χ^2 possible for a given number of observed events, N^{obs}. If $N^{obs} \geq N^{exp}_{min}$, so that the number of observed events is larger than the number of events expected with no signal, then $\chi^2_{min} = \chi^2(N^{obs}, N^{exp} \equiv N^{obs}) = 0$. However, if $N^{obs} < N^{exp}_{min}$, then in order to keep the measured answer within the physical region, θ_{13} must be 0 and thus

$$\chi^2_{min} = \chi^2(N^{obs}, N^{exp} \equiv N^{exp}_{min}) = 2\left(N^{exp} - N^{obs} + N^{obs} ln\left(\frac{N^{obs}}{N^{exp}}\right)\right) \neq 0$$

Drawing the Contours

Once the observed number of data events is known, the contours are generated in the following way. For each point on the grid:

1. Calculate $\Delta\chi^2_{data} = \chi^2(N^{obs} \equiv N^{data}, N^{exp}) - \chi^2_{min}$

2. Determine the fraction, f, of the 10,000 pseudo experiments at this point which satisfy $\Delta\chi^2 < \Delta\chi^2_{data}$

3. If $f \leq \alpha\%$, then this grid point is included in the $\alpha\%$ confidence level interval

The grid now contains the contour of the measurement, which is described as being "fuzzy" in appearance due to the discreetness of the grid. The `ROOT` function `Smooth()` is used to smooth the fuzziness of the contours.

11.2 Possible Sensitivities

Prior to looking at the contours for the data, it is useful to asses the potential reach of a given analysis. Considering the ParticlePID, the possible sensitivity assuming that no signal is seen is shown in figure 11.1. A possible contour is shown in figure 11.2 with the assumption that a signal is seen at the best fit from the previous analysis (with $\sin^2 2\theta_{13} = 0.118$ at $\delta_{CP} = 0$).

This tool provides a useful comparison between the different analyses. It is important to note here that possible contours for the ParticlePID and ANN11 match exactly; the gains obtained by reducing the systematic errors in the ParticlePID are offset by the additional number of background events. The sensitivity and the contour from the best fit of the previous analysis for ANN11 are given in figures 11.3 and 11.4.

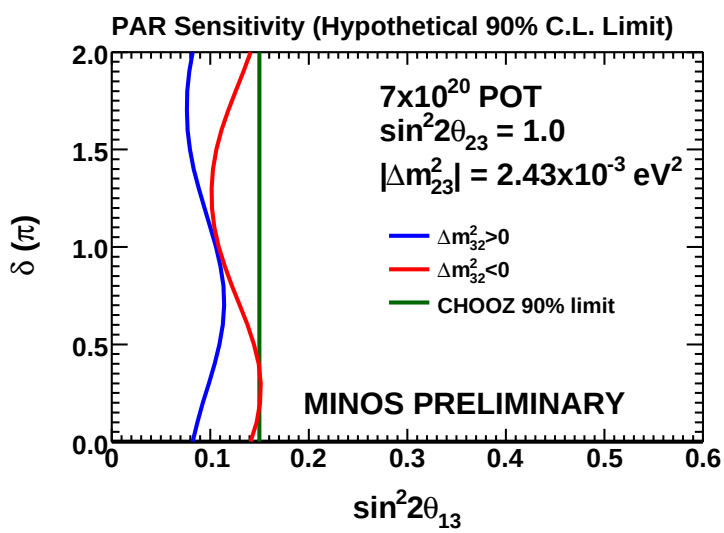

Figure 11.1: The potential sensitivity of the ParticlePID using the HOOHE extrapolation, assuming that the observed total number of events exactly matches the number of expected background at $\sin^2 2\theta_{13} = 0$

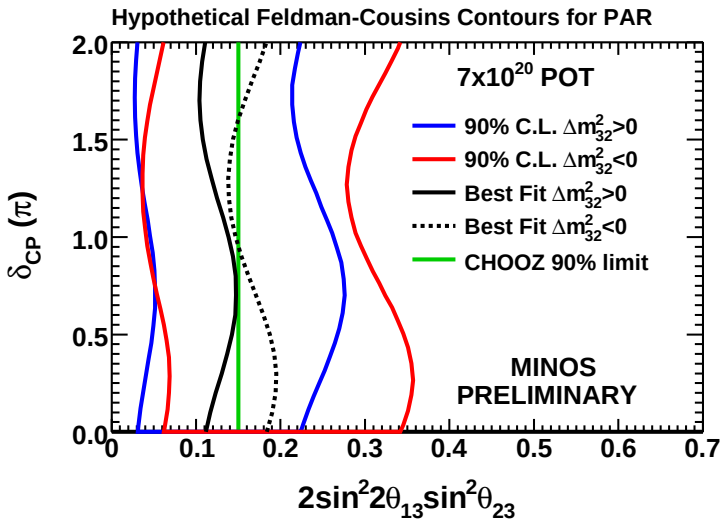

Figure 11.2: The potential sensitivity of the ParticlePID using the HOOHE extrapolation, assuming that the observed total number of events agrees exactly with the best fit of the previous analysis (with $\sin^2 2\theta_{13} = 0.118$ at $\delta_{CP} = 0$)

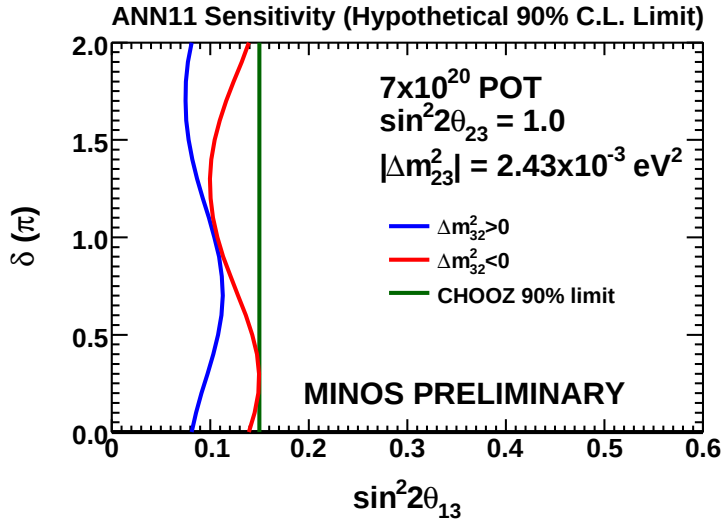

Figure 11.3: The potential sensitivity of the ANN11 using the HOOHE extrapolation, assuming that the observed total number of events exactly matches the number of expected background at $\sin^2 2\theta_{13} = 0$

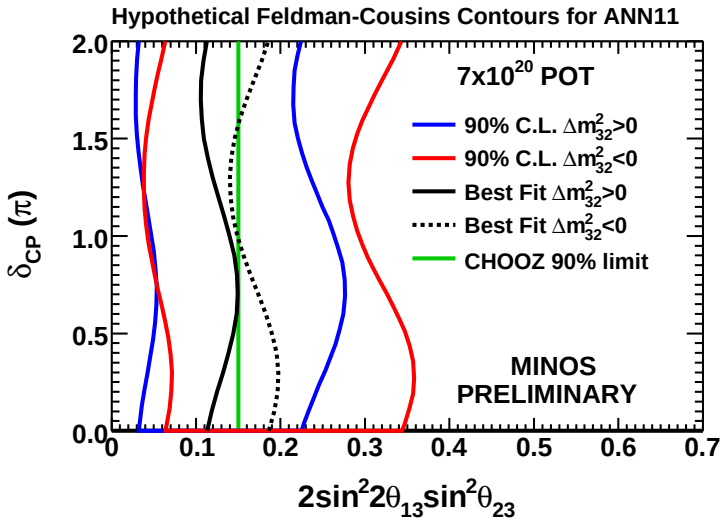

Figure 11.4: The potential sensitivity of the ANN11 using the HOOHE extrapolation, assuming that the observed total number of events agrees exactly with the best fit of the previous analysis (with $\sin^2 2\theta_{13} = 0.118$ at $\delta_{CP} = 0$)

11.3 Results

After all of the cross checking tests were completed and all remaining issues addressed, it was time to look at the actual Far Detector data in the signal region. As a preliminary check, the number of data events present per unit of POT over time was examined at the different cut levels and was found to be acceptable. The event rate is presented in figure 11.5. There appears to be a statistical upward fluctuation in the amount of data recorded in Run 2.

The transverse position of the data events within the Far Detector is shown in figure 11.6. The data events are present throughout the entire detector region, indicating no previously unfound localized detector abnormality.

A comparison between the data events selected by one or both of the ParticlePID and ANN11 methods is shown in figure 11.7. As expected, the number of events selected

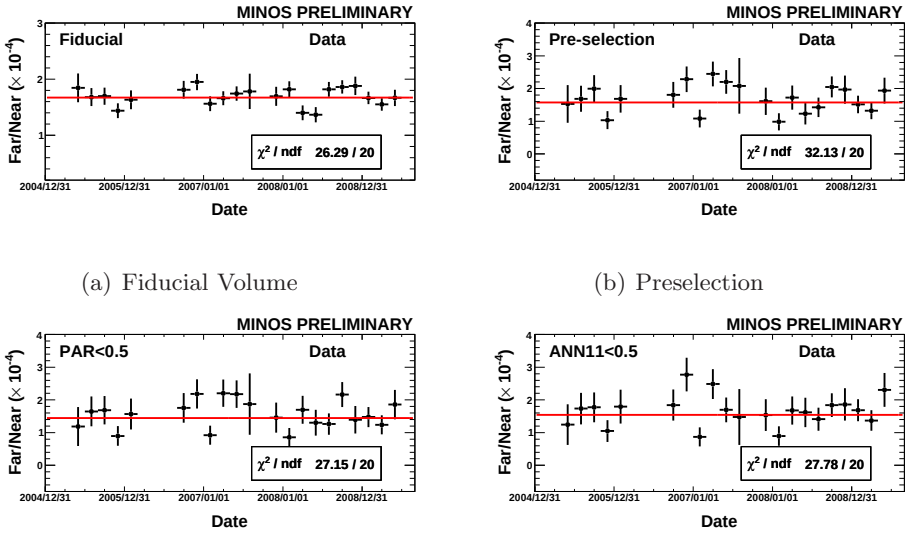

(a) Fiducial Volume

(b) Preselection

(c) ParticlePID

(d) ANN11

Figure 11.5: The number of Far Detector data events per POT over time for each of the samples specified. Note a slightly higher number of events per POT during the period of Run 2 for both the ParticlePID and ANN11 samples.

by the ParticlePID and not by the ANN11 is 42% (compared to an expected 39%). This indicates that the ParticlePID and ANN11 are selecting data events with different topologies.

The number of data events in each run and in total are listed in table 11.1. Note that all PIDs see no statistically significant excess overall, but all do see a statistical fluctuation upward in Run 2, which is consistent with the first analysis and which is also seen in the overall Far Detector event rates during that run.

Selection	Run 1		Run 2		Run 3		Total		
	Data	Prediction	Data	Prediction	Data	Prediction	Data	Prediction	σ excess
ParticlePID	8	9.73	23	15.18	28	29.14	59	54.05	0.7
ANN11	11	8.66	17	13.81	26	26.61	54	49.08	0.7
ANN14	5	5.81	12	9.46	19	18.51	36	33.78	0.4

Table 11.1: The far data event counts by run period are shown. ParticlePID and ANN11 see the same statistical excess of 0.7σ while the ANN11 sees an excess of 0.4σ. The prediction is calculated at $\theta_{13} = 0$.

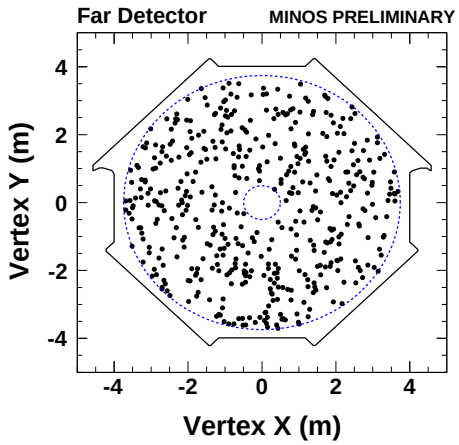

(a) Preselection

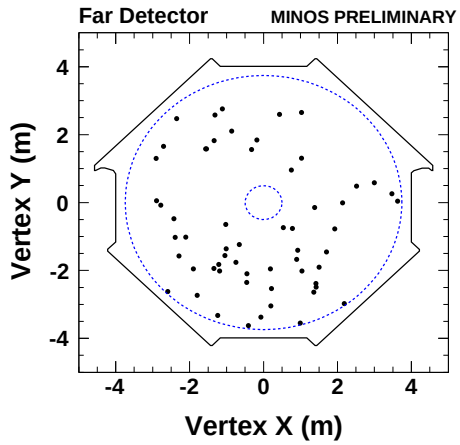

(b) ParticlePID

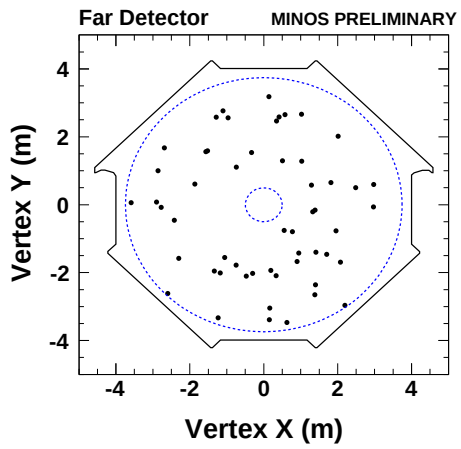

(c) ANN11

Figure 11.6: The location of data events in the Far Detector for each of the samples specified. There are no anomalous spacial gaps in the data for the Far Detector.

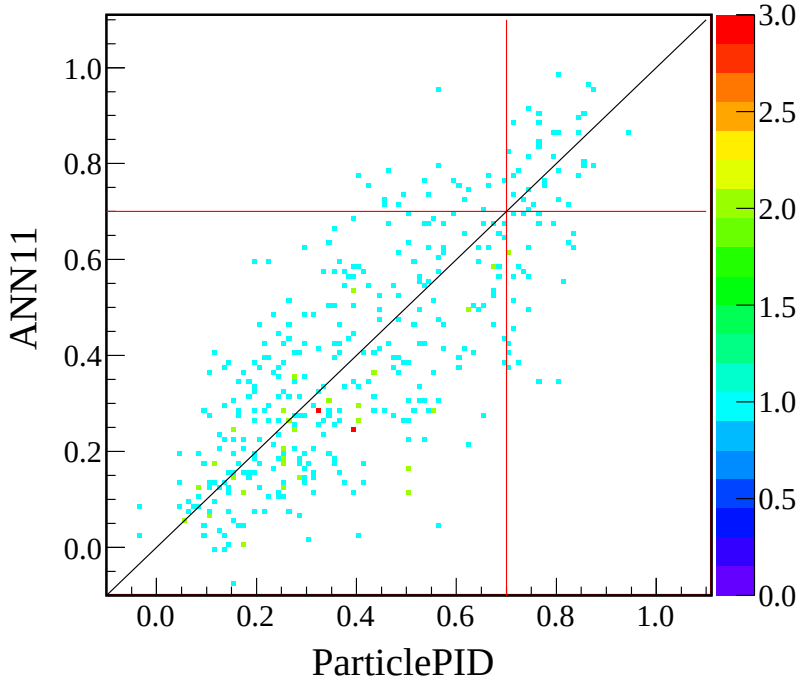

Figure 11.7: The ParticlePID and ANN11 values for each data point is shown. 59 events are selected by the ParticlePID and 54 events are selected by the ANN11. The intersection of selected events by both PIDs includes 34 events, while 24 events are selected by the ParticlePID and not by the ANN11 and 20 events are selected by the ANN11 and not the ParticlePID. The number selected by the ParticlePID and not by the ANN11 is 42% of the total events selected by the ParticlePID, which is consistent with the 39% predicted by Far Detector MC. The red lines indicate the PID cuts applied and the black diagonal line is visual guide for equivalent ParticlePID and ANN11 values.

The resulting contours for the ParticlePID and ANN11 are shown in figures 11.8 and 11.9. As expected, the contours obtained by ParticlePID are identical to those obtained by ANN11 since they both observe the same amount of statistical excess. This is a powerful result, since 42% of the events selected by the ParticlePID are not selected by the ANN11 (compared to an expected 39%). Thus, these two statistically different samples provide the same result, successfully realizing the goal of the ParticlePID acting as a cross check of the primary analysis. Both the ParticlePID and ANN11 analysis methods set limits on $\nu_\mu \rightarrow \nu_e$ oscillations. With 7×10^{20} POT, $\sin^2 2\theta_{13} < 0.12(0.20)$ for the normal (inverted) hierarchy at $\delta_{CP} = 0$ (90%C.L.). The best fit for both methods is at $\sin^2 2\theta_{13} = 0.027(0.055)$ with $\delta_{CP} = 0$.

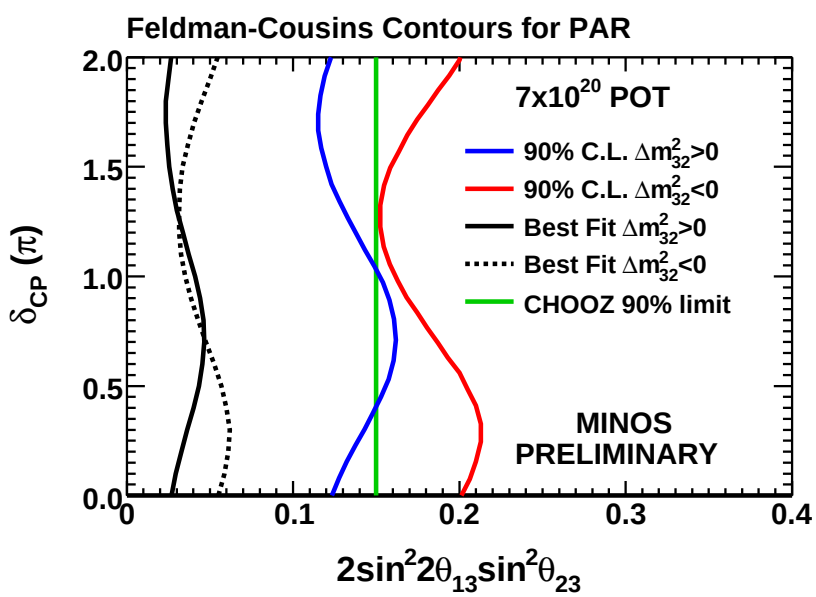

Figure 11.8: The limit on $\sin^2 2\theta_{13}$ obtained with the ParticlePID using the HOOHE extrapolation is shown.

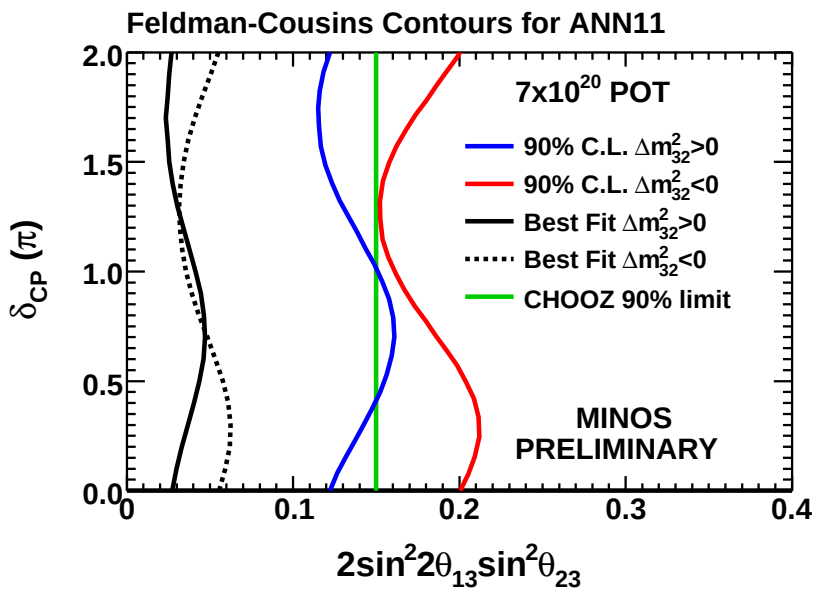

Figure 11.9: The limit on $\sin^2 2\theta_{13}$ obtained with the ANN11 using the HOOHE extrapolation is shown.

11.4 Conclusion

The research presented in this thesis has succeeded in providing an independently set limit on $\sin^2 2\theta_{13}$. The ParticlePID performed the analysis with a sample of events, of which, only about 60% were also used by the ANN11. The ability of the ParticlePID to measure various components of a shower, rather than making measurements of global event properties alone, opened up the possibility of identifying oscillated ν_e events from the background for events having larger hadronic showers. The improved event reconstruction provided for a 27% reduction in the total background prediction systematic error compared to ANN11. This improvement was exactly offset the additional statistical error realized by an increased acceptance of background events. Both the ParticlePID and ANN11 analysis methods set limits on $\nu_\mu \rightarrow \nu_e$ oscillations and found that with 7×10^{20} POT, $\sin^2 2\theta_{13} < 0.12(0.20)$ for the normal (inverted) hierarchy at $\delta_{CP} = 0$ (90%C.L.).

This analysis successfully improves the limit set by the CHOOZ experiment for the normal hierarchy at almost all values of δ_{CP}.

Chapter 12

Future Steps

12.1 The Future of MINOS

The MINOS experiment is expected to continue taking data until 2012. This corresponds to an expected accumulated exposure of 10×10^{20} POT. At the close of the experiment, a final analysis on $\nu_\mu \rightarrow \nu_e$ oscillations will be conducted. While the additional data is not expected to have a large impact on the results, the additional time will allow for the preparation of a complex analysis. This next analysis will use a large library of Monte Carlo events which are matched to the data events through a method of image recognition in a way very similar to facial recognition software. This method has been shown to have a higher FOM compared to methods using ANNs[124].

12.2 Future Experiments

A number of experiments designed especially to perform a measurement of $\nu_\mu \rightarrow \nu_e$ are currently in progress. A few of them will be mentioned here.

The NOνA experiment[127] is beginning construction now and in a few years will

be measuring neutrinos from an upgraded NuMI beam line. The fully active mineral oil based scintillator detector will provide substantial increases in the resolution of ν_e events over the MINOS detector technology. There will be two functionally identical detectors, one situated in the vicinity of the MINOS Near Detector, and another in Ash River, Minnesota at a distance of 810 km away. This experiment is designed to be able to set a sensitivity of $\sin^2 2\theta_{13} < 0.03$.

The T2K experiment[128] in Japan will measure neutrinos from the J-PARC accelerator in Tokai in a detector in Kamioka by reusing the Super Kamiokande Čherenkov detector as the far detector. The near detector is of a very different design, and it uses tracking detectors for a precise measurement of the neutrino flux prior to oscillations. The experiment is expected to have a sensitivity of $\sin^2 2\theta_{13} < 0.01$.

Both of the NOνA and T2K experiments will be located off of the neutrino beam axis. Due to the details of the decay kinematics[129], this results in a neutrino spectrum which is almost entirely from $\pi^{\pm}$ decay with minimal $K^{\pm}$ contamination. Additionally, this configuration results in neutrino energies which are centered around the expected oscillation peak, thus helping to offset the loss of event flux due to the off axis location.

A multiple reactor experiment at Daya Bay, China[130] intends to measure $\overline{\nu}_e$ disappearance to a level of $\sin^2 2\theta_{13} < 0.01$. Comparing precision measurements from both ν_e and $\overline{\nu}_e$ will be necessary to resolve the level of CP violation.

Bibliography

[1] Photograph taken by Alex Sousa.

[2] J. Chadwick. Intensitätsverteilung im magnetischen Spektrum der β-Strahlen von Radium B+C. *Verhandlungen der Deutschen Physikalischen Gesellschaft*, 16:383, 1914.

[3] C. D. Ellis and W. A. Wooster. The Average Energy of Disintegration of Radium E. *Proceedings of the Royal Society of London*, A117:109, 1927.

[4] W. Pauli. Letter to a physicists' gathering at Tubingen. December 4, 1930, reprinted in *Wolfgang Pauli, Collected scientific papers*, edited by R. Kronig and V. Weisskopf, vol. 2, p. 1313, New York, Interscience, 1964.

[5] E. Fermi. An attempt of a theory of beta radiation. 1. *Z. Phys.*, 88:161–177, 1934.

[6] Jr. Cowan, C. L., F. Reines, F. B. Harrison, H. W. Kruse, and A. D. McGuire. Detection of the Free Neutrino: a Confirmation. *Science*, 124(3212):103–104, 1956.

[7] C. S. Wu, E. Ambler, R. W. Hayward, D. D. Hoppes, and R. P. Hudson. Experimental Test of Parity Conservation in Beta Decay. *Phys. Rev.*, 105(4):1413–1415, Feb 1957.

[8] M. Goldhaber, L. Grodzins, and A. W. Sunyar. Helicity of Neutrinos. *Phys. Rev.*, 109(3):1015–1017, Feb 1958.

[9] G. Danby et al. Observation of High-Energy Neutrino Reactions and the Existence of Two Kinds of Neutrinos. *Phys. Rev. Lett.*, 9(1):36–44, Jul 1962.

[10] M. L. Perl et al. Evidence for Anomalous Lepton Production in $e^+ - e^-$ Annihilation. *Phys. Rev. Lett.*, 35(22):1489–1492, Dec 1975.

[11] K. Kodama et al. Observation of tau neutrino interactions. *Physics Letters B*, 504(3):218 – 224, 2001.

[12] K. Kodama et al. Final tau-neutrino results from the DONuT experiment. *Phys. Rev. D*, 78(5):052002, Sep 2008.

[13] The ALEPH Collaboration. Precision electroweak measurements on the Z resonance. *Phys. Rept.*, 427:257, 2006.

[14] B. T. Cleveland et al. Measurement of the solar electron neutrino flux with the Homestake chlorine detector. *Astrophys. J.*, 496:505–526, 1998.

[15] John N. Bahcall, M. H. Pinsonneault, and G. J. Wasserburg. Solar models with helium and heavy-element diffusion. *Rev. Mod. Phys.*, 67(4):781–808, Oct 1995.

[16] J. N. Abdurashitov et al. Measurement of the solar neutrino capture rate by the Russian-American gallium solar neutrino experiment during one half of the 22-year cycle of solar activity. *J. Exp. Theor. Phys.*, 95:181–193, 2002. [arXiv:astro-ph/0204245].

[17] W. Hampel et al. GALLEX solar neutrino observations: results for GALLEX IV. *Physics Letters B*, 447(1-2):127 – 133, 1999.

[18] K. S. Hirata et al. Real time, directional measurement of ^{8}B solar neutrinos in the Kamiokande-II detector. *Phys. Rev.*, D44:2241–2260, 1991.

[19] Y. Fukuda et al. Evidence for Oscillation of Atmospheric Neutrinos. *Phys. Rev. Lett.*, 81(8):1562–1567, Aug 1998.

[20] Q. R. Ahmad et al. Measurement of the Rate of $\nu_e + d \rightarrow p + p + e^-$ Interactions Produced by ^{8}B Solar Neutrinos at the Sudbury Neutrino Observatory. *Phys. Rev. Lett.*, 87(7):071301, Jul 2001.

[21] B. Aharmim et al. Determination of the ν_e and total ^{8}B solar neutrino fluxes using the Sudbury Neutrino Observatory Phase I data set. *Phys. Rev. C*, 75(4):045502, Apr 2007.

[22] W. W. M. Allison et al. Measurement of the atmospheric neutrino flavour composition in Soudan 2. *Physics Letters B*, 391(3-4):491 – 500, 1997.

[23] M. Apollonio et al. Initial results from the CHOOZ long baseline reactor neutrino oscillation experiment. *Physics Letters B*, 420(3-4):397 – 404, 1998.

[24] P. Astier et at. Final NOMAD results on $\nu_\mu \rightarrow \nu_\tau$ and $\nu_e \rightarrow \nu_\tau$ oscillations including a new search for ν_τ appearance using hadronic τ decays. *Nuclear Physics B*, 611(1-3):3 – 39, 2001.

[25] Francis Halzen and Alan D. Martin. Quarks and Leptons. Wiley, 1985.

[26] Michael Edward Peskin and Daniel V. Schroeder. An Introduction to quantum field theory. 1995. Reading, USA: Addison-Wesley (1995) 842 p.

[27] Nicola Cabibbo. Unitary Symmetry and Leptonic Decays. *Phys. Rev. Lett.*, 10(12):531–533, Jun 1963.

[28] Makoto Kobayashi and Toshihide Maskawa. CP-Violation in the Renormalizable Theory of Weak Interaction. *Progress of Theoretical Physics*, 49(2):652–657, 1973.

[29] B. Pontecorvo. Neutrino experiments and the question of leptonic-charge conservation. *Sov. Phys. JETP*, 26:984–988, 1968.

[30] Ziro Maki, Masami Nakagawa, and Shoichi Sakata. Remarks on the unified model of elementary particles. *Prog. Theor. Phys.*, 28:870–880, 1962.

[31] Joshua Adam Alpern Boehm. Measurement of electron neutrino appearance with the MINOS experiment. FERMILAB-THESIS-2009-17.

[32] Evgeny Khakimovich Akhmedov and others. Series expansions for three-flavor neutrino oscillation probabilities in matter. *JHEP*, 04:078, 2004. [arXiv:hep-ph/0402175].

[33] C. Amsler et al. (Particle Data Group). *Physics Letters*, B667:1+, 2008. and 2009 partial update for the 2010 edition.

[34] Evgeny Khakimovich Akhmedov. Three-flavour effects and CP- and T-violation in neutrino oscillations. *Phys. Scripta*, T121:65–71, 2005. [arXiv:hep-ph/0412029].

[35] M. Apollonio et al. Search for neutrino oscillations on a long base-line at the CHOOZ nuclear power station. *Eur. Phys. J.*, C27:331–374, 2003. [arXiv:hep-ex/0301017].

[36] A. D. Sakharov. Violation of CP Invariance, C Asymmetry, and Baryon Asymmetry of the Universe. *Soviet Journal of Experimental and Theoretical Physics Letters*, 5:24–+, January 1967.

[37] Goran Senjanovic. Spontaneous breakdown of parity in a class of gauge theories. *Nuclear Physics B*, 153:334 – 364, 1979.

[38] Frank T. Avignone, III, Steven R. Elliott, and Jonathan Engel. Double Beta Decay, Majorana Neutrinos, and Neutrino Mass. *Rev. Mod. Phys.*, 80:481–516, 2008. [arXiv:nucl-ex/0708.1033].

[39] A. Yu. Smirnov. The MSW effect and solar neutrinos. 2003. [arXiv:hep-ph/0305106].

[40] H. Murayama. Oscillation parameter plots, 2008. `http://hitoshi.berkeley.edu/neutrino/`.

[41] `http://www.fnal.gov/pub/presspass/press_releases/NuMI_photos/`.

[42] P. Adamson et al. Study of muon neutrino disappearance using the Fermilab Main Injector neutrino beam. *Phys. Rev. D*, 77(7):072002, Apr 2008.

[43] Robert Miles Zwaska. Accelerator systems and instrumentation for the NuMI neutrino beam. FERMILAB-THESIS-2005-73.

[44] C C Jensen and G E Krafczyk. NuMI Proton Kicker Extraction System. 2005.

[45] Sacha E. Kopp. Accelerator neutrino beams. *Phys. Rept.*, 439:101–159, 2007. [arXiv:physics/0609129].

[46] R. Zwaska et al. Beam-based alignment of the NuMI target station components at FNAL. *Nuclear Instruments and Methods in Physics Research Section A: Accelerators, Spectrometers, Detectors and Associated Equipment*, 568(2):548 – 560, 2006.

[47] K. Anderson et al. Technical Report. *Fermi National Accelerator Laboratory*, 2002.

[48] V. Bocean. 9th International Workshop on Accelerator Alignment (IWAA 06), Menlo Park, California. 2006.

[49] P. Adamson et al. The MINOS calibration detector. *Nuclear Instruments and Methods in Physics Research Section A: Accelerators, Spectrometers, Detectors and Associated Equipment*, 556(1):119 – 133, 2006.

[50] N. Tagg et al. Performance of Hamamatsu 64-anode photomultipliers for use with wavelength–shifting optical fibres. *Nuclear Instruments and Methods in Physics Research Section A: Accelerators, Spectrometers, Detectors and Associated Equipment*, 539(3):668 – 678, 2005.

[51] D. G. Michael et al. The magnetized steel and scintillator calorimeters of the MINOS experiment. *Nucl. Instrum. Meth.*, A596:190–228, 2008.

[52] The MINOS Off-line Software User's Manual Release R1.28, 2010. `http://www-numi.fnal.gov/offline_software/srt_public_context/doc/UserManual/UserManual.html`.

[53] The MINOS Calibration Group. 2009 Calibration Position Paper on Runs I-II-III. MINOS-DocDB 6717.

[54] The MINOS Calibration Group. January 2008 Position Paper on Calibration of the Pre-Shutdown Data. MINOS-DocDB 3941.

[55] Jeffrey J. Hartnell. Measurement of the calorimetric energy scale in MINOS. FERMILAB-THESIS-2005-51.

[56] D. G. Michael et al. The magnetized steel and scintillator calorimeters of the MINOS experiment. *Nuclear Instruments and Methods in Physics Research Section A: Accelerators, Spectrometers, Detectors and Associated Equipment*, 596(2):190 – 228, 2008.

[57] G. Pawloski and T. Yang. Crosstalk Tuning. Minos-DocDB 5319.

[58] S. Cavanaugh. XTalkFilter. Minos-DocDB 5974.

[59] N. Graf. Optical Cross-Talk First Look. Minos-DocDB 6615.

[60] Retrieving MINOS Data from FNAL. `http://www-numi.fnal.gov/minwork/computing/enstore.html`.

[61] A Ferrari, Paola R Sala, A Fass, and Johannes Ranft. *FLUKA: A multi-particle transport code (program version 2005)*. CERN, Geneva, 2005.

[62] R. Brun et al. CERN Program Library Long Writeup W5013, 1994.

[63] `http://wwwasd.web.cern.ch/wwwasd/geant/`.

[64] Sacha Kopp, Žarko Pavlović, and Patricia Vahle. SKZP2: Update on Fitting the Beam MC to the ND Data. Minos-DocDB 1650.

[65] H. Gallagher. The NEUGEN neutrino event generator. *Nuclear Physics B - Proceedings Supplements*, 112(1-3):188 – 194, 2002.

[66] Serge Rudaz and Pierre Valin. Koba-Nielsen-Olesen scaling, its violation, and the structure of hadrons. *Phys. Rev. D*, 34(7):2025–2042, Oct 1986.

[67] PYTHIA (and JETSET).
`http://home.thep.lu.se/~torbjorn/Pythia.html`.

[68] C. Andreopoulos, H. Gallagher, P. Kehayias, and T. Yang. A Hadronization Model for the MINOS Experiment. Minos-DocDB 5142.

[69] Dieter Rein and Lalit M. Sehgal. Neutrino-excitation of baryon resonances and single pion production. *Annals of Physics*, 133(1):79 – 153, 1981.

[70] C. H. Albright and C. Jarlskog. Neutrino production of M+ and E+ heavy leptons (I). *Nuclear Physics B*, 84(2):467 – 492, 1975.

[71] H. Plothow-Besch. Program PDFLIB in CERN Program Library Pool W5051, 1991.

[72] Dieter Rein and Lalit M. Sehgal. Coherent π^0 production in neutrino reactions. *Nuclear Physics B*, 223(1):29 – 44, 1983.

[73] C. Andreopoulos. The GENIE universal, object-oriented neutrino generator. *Nucl. Phys. Proc. Suppl.*, 159:217–222, 2006.

[74] The FermiGrid.
`http://fermigrid.fnal.gov/`.

[75] P. Adamson et al. Search for muon-neutrino to electron-neutrino transitions in MINOS. *Phys. Rev. Lett.*, 103:261802, 2009. [arXiv:hep-ex/0909.4996].

[76] S. Cavanaugh. Fiducial Volume Selection for NueAna with Cedar-Daikon. Minos-DocDB 3591.

[77] S. Cavanaugh and G. Pawloski. Cedar_phy Daikon Energy Scale Calibration for NueAna. Minos-DocDB 3795.

[78] S. Cavanaugh. A Study of Cosmic Background in the MINOS Far Detector for the ν_e appearance analysis using Cedar_phy data. Minos-DocDB 4145.

[79] K. Hornik et al. Multilayer Feedforward Networks are Universal Approximators. *Neural Networks*, 2:359–366, 1989.

[80] D.W. Ruck et al. *The Multilayer Perceptron as an Approximation to a Bayes Optimal Discriminant Function*, volume 1(4). 1990.

[81] J. Schwindling and B. Mansoulié. MLPFit : a tool for designing and using Multi-Layer Perceptrons. Version 1.40, January 2000, available from: `http://schwind.web.cern.ch/schwind/MLPfit/doc/`.

[82] Christophe Delaere. ROOT Documentation: TMultiLayerPerceptron, July 2003. `http://root.cern.ch/root/html310/TMultiLayerPerceptron.html`.

[83] J. Ling and T. Yang. Retuning of Neural Network for ν_e Identification. Minos-DocDB 6255.

[84] P. V. C. Hough. Machine analysis of bubble chamber pictures. *International Conference on High Energy Accelerators and Instrumentation, CERN, Geneva, Switzerland*, pages 554–556, 1959.

[85] A. Holin. Muon Removal Background Estimation Method. Minos-DocDB 4141.

[86] Rustem Ospanov. A measurement of muon neutrino disappearance with the MINOS detectors and NuMI beam. FERMILAB-THESIS-2008-04.

[87] C. Smith and C. Howcroft. Measuring ν_e CC Selection Efficiency from ν_μ CC Data with Muon Removal and MC Electron Addition. Minos-DocDB 2415.

[88] L. Whitehead. Far Detector Prediction and Sensitivity in the ν_e Analysis. MINOS-DocDB 6697.

[89] X. Huang. Round II MRE Summary. Minos-DocDB 7014.

[90] G. Pawloski, S. Wojcicki, and T. Yang. Estimation of Background Systematic Errors in the $\nu_\mu \to \nu_e$ Analysis With Horn-On and Horn-Off Data. MINOS-DocDB 3461.

[91] G. Pawloski and L. Whitehead. Estimation of the Near Detector NC and CC Spectra for the $\nu_\mu \to \nu_e$ Analysis With Horn-On and Horn-Off Data. MINOS-DocDB 3935.

[92] J. Coelho, G. Pawloski, and S. Swain. Near Detector Beam Decomposition. MINOS-DocDB 6681.

[93] MINOS Nue Analysis Group. Systematic uncertainties on the measurement of ν_e Appearance. Minos-DocDB 5387.

[94] MINOS Nue Analysis Group. Systematic uncertainties for the second nue box opening. Minos-DocDB 6716.

[95] A. A. Himmel. The NuMI Beam Simulation with Flugg. Minos-DocDB 6316.

[96] S. Budd. Beam Systematics for the nue Analysis. Minos-DocDB 6585.

[97] M. Bishai and D. Jaffe. Is there a hole in the NuMI target? Minos-DocDB 4521.

[98] M. Dorman. Target Decay Weighting Function in MCReweight. Minos-DocDB 6477.

[99] C. Andreopoulos, D. Bhattacharya, S. Dytman, H. Gallagher, R. Gran, M. Kordosky, J. Morn, and D. Naples. Updated Cross Section Model Uncertainties for the Charged Current Analysis. Minos-DocDB 2989.

[100] Private phone conversations with Hugh Gallagher.

[101] S. Cavanaugh. ν_τ background estimate and uncertainties in the $\nu_\mu \rightarrow \nu_e$ analysis using Cedar_phy Daikon 00 MC. Minos-DocDB 4140.

[102] S. Cavanaugh. ν_τ background estimate and uncertainties in the $\nu_\mu \rightarrow \nu_e$ analysis using Cedar_phy Daikon 00 MC Firebird NueAna. Minos-DocDB 5271.

[103] J. Boehm, H. Gallagher, and T. Yang. Hadronization Model Uncertainties for the ν_e Analysis. Minos-DocDB 5392.

[104] D. Zieminska et al. Charged-particle multiplicity distributions in νn and νp charged-current interactions. *Phys. Rev. D*, 27(1):47–57, Jan 1983.

[105] H. Gallagher. Hadronization Model Issues for GENIE 2.6.0. Minos-DocDB 5317.

[106] M. Kordosky. A procedure to re-weight events to account for uncertainties in final state interactions. Minos-DocDB 3449.

[107] MINOS Collaboration. 2009 Calibration Position Paper on Runs I-II-III. Minos-DocDB 6717.

[108] J. Nelson. Notes on the N/F relative normalization in the CC analysis. Minos-DocDB 2106.

[109] N. Tagg. Gain Calibration Systematics. Minos-DocDB 4865.

[110] MINOS Collaboration. Calibration Position Paper for Pre-Shutdown Data. Minos-DocDB 3941.

[111] Private Communication with Jeff deJong.

[112] R. Toner. ν_e Analysis Preselection Systematics. Minos-DocDB 5257.

[113] R. Toner. Preselection Systematics. Minos-DocDB 6703.

[114] J. Coelho and G. Pawloski. Incorporating Intensity Prole in Monte Carlo. Minos-DocDB 6032.

[115] P. Adamson et al. Measurement of Neutrino Oscillations with the MINOS Detectors in the NuMI Beam. *Phys. Rev. Lett.*, 101:131802, 2008. [arXiv:hep-ex/0806.2237].

[116] Jiajie Ling and Tricia Vahle. CalDet Signal Efficiency Correction. MINOS-DocDB 6734.

[117] L. Whitehead. Nue Systematics. Minos-DocDB 6629-v2.

[118] S. Cavanaugh. A Study of Cosmic Background in the MINOS Detectors for the ν_e appearance analysis using Cedar_phy data and Firebird. Minos-DocDB 5382.

[119] M. Betancourt. Study of Cosmic Background in the MINOS Far Detector for the ν_e appearance analysis. Minos-DocDB 6698.

[120] Private conversation with David Jaffe.

[121] J. M. Paley for the MINOS Collaboration. Recent Results and Future Prospects from MINOS. [arXiv:hep-ex/0901.2131].

[122] Gary J. Feldman and Robert D. Cousins. Unified approach to the classical statistical analysis of small signals. *Phys. Rev. D*, 57(7):3873–3889, Apr 1998. [arXiv:physics/9711021].

[123] L. Whitehead. θ_{13} Contours for the 7×10^{20} POT ν_e Analysis. Minos-DocDB 7020.

[124] J. P. Ochoa Richoux. A Search for Muon Neutrino to Electron Neutrino Oscillation in the MINOS Experiment. FERMILAB-THESIS-2009-44.

[125] Y. Ashie et al. Evidence for an Oscillatory Signature in Atmospheric Neutrino Oscillations. *Phys. Rev. Lett.*, 93(10):101801, Sep 2004. [arXiv:hep-ex/0404034].

[126] B. Aharmim et al. Electron energy spectra, fluxes, and day-night asymmetries of ^{8}B solar neutrinos from the 391-day salt phase SNO data set. *Phys. Rev.*, C72:055502, 2005. [arXiv:nucl-ex/0502021].

[127] D. S. Ayres et al. The NOvA Technical Design Report. FERMILAB-DESIGN-2007-01.

[128] K. Kaneyuki. T2K experiment. *Nuclear Physics B - Proceedings Supplements*, 145:178 – 181, 2005. NOW 2004.

[129] D. Beavis et al. Long Baseline Neutrino Oscillation Experiment at the AGS (E-889). Physics Design Report. 1995. available from `http://www.hep.princeton.edu/~mcdonald/nufact/e889/`.

[130] Xinheng Guo et al. A precision measurement of the neutrino mixing angle θ_{13} using reactor antineutrinos at Daya Bay. 2007. [arXiv:hep-ex/0701029].